ρ^0(770) vector meson production and elliptic flow measurement in Cu+Cu and Au+Au collisions at $\sqrt{s_{NN}}$ = 200 GeV in STAR at RHIC

Submitted in partial fulfillment of the requirements
for the degree of
Doctor of Philosophy

by

Prabhat R. Pujahari
(Roll No. 07412601)

Supervisor
Prof. Basanta K. Nandi

Department of Physics
INDIAN INSTITUTE OF TECHNOLOGY, BOMBAY, INDIA
2012

Dedicated To

My Parents

&

My Late Grandmother

Thesis Approval

Thesis entitled: ρ^0 (770) **vector meson production and elliptic flow measurement in Cu+Cu and Au+Au collisions at $\sqrt{s_{NN}}$ = 200 GeV in STAR at RHIC** by **Prabhat R. Pujahari** is approved for the degree of Doctor of Philosophy.

Examiners

(1) D. K. Srivastav.

(2) Raghavarun

Supervisor

Chairman

Date : 20/06/2012

Place : IIT Bombay

Declaration

I declare that this written submission represents my ideas in my own words and where others' ideas or words have been included, I have adequately cited and referenced the original sources. I also declare that I have adhered to all principles of academic honesty and integrity and have not misrepresented or fabricated or falsified any idea/data/fact/source in my submission. I understand that any violation of the above will be cause disciplinary action by the Institute and can also evoke penal action from the sources which have thus not been properly cited or from whom proper permission has not been taken when needed.

Prabhat R. Pujahari

Prabhat Pujahari

Roll No. 07412601

Date : 20/06/2012

Place : IIT Bombay

Abstract

The Relativistic Heavy Ion community at the Relativistic Heavy Ion Collider (RHIC) at Brookhaven National Laboratory (BNL), New York, aims to study nuclear matter under extreme condition of temperature and density. This is supported by lattice QCD prediction. The prediction is that at sufficiently high temperature and/or nuclear density, colored quarks and gluons, which are confined in a nucleon become de-confined resulting in a new phase of matter, called the Quark Gluon Plasma (QGP). In a QGP phase, quarks and gluons are able to move over regions larger than a hadronic length. Additionally, QGP is believed to have existed during the first few microseconds after the Big Bang. Understanding the properties of QGP could provide valuable insights on the evolution of our universe. The experimental investigation at RHIC and intensive theoretical calculations with state-of-the-art computers have led to the refinement of the physics goals. The task of the RHIC heavy-ion programme, therefore, will be to investigate the properties of the de-confined matter in much greater details.

Hadronic resonance states have extremely short lifetimes ($\sim$few fm/c) which are comparable to or smaller than the lifetime of the system formed in relativistic heavy-ion collisions. Due to their short lifetimes, hadronic resonances can be used to investigate the freeze-out mechanisms after hadronization. In order to understand the properties of matter formed in relativistic nucleus-nucleus collisions, it is important to understand the production and absorption processes of resonant states created in those collisions. This is attributed to the resonance daughter particles' re-scattering and re-generation effects. Thus, a systematic measurement of the resonances properties such as mass modification and/or width broadening is essential to study the hadronic in-medium effects in heavy-ion collisions. Again, the elliptic flow measurement will extend the sensitivity

of resonance yields to the partonic state through additional information on constituent quark scaling.

So far, RHIC has produced a great amount of data on various resonances. The ρ^0 vector meson (m_{ρ^0} = 775.5 MeV/c^2, Γ_{ρ^0} = 150 MeV/c^2) is one among such resonances through which various properties of the hot and dense medium created in such heavy- ion (i.e. Cu+Cu and Au+Au) collisions can be studied. Because of the broad width, the ρ^0 vector meson is expected to decay, re-scatter, and regenerate all the way from the chemical freeze-out to the kinetic freeze-out. In the context of statistical models, the measured ρ^0 vector meson yield should reflect conditions at kinetic freeze-out rather than at chemical freeze-out. In p+p and d+Au collisions, the ρ^0 vector meson is expected to be produced predominantly by string fragmentation. Therefore, the measurement of the ρ^0 vector meson in p+p and heavy-ions, such as Cu+Cu and Au+Au, collisions at the same nucleon-nucleon center of mass energy can provide insight for the understanding of the dynamics of these systems.

In addition, in-medium modification of the ρ^0 vector meson mass and/or width due to the effects of increasing temperature and density has ben proposed as a possible signal of the phase transition of nuclear matter to a de-confined plasma of quarks and gluons, which is expected to be accompanied by the restoration of chiral symmetry. Therefore, the production of the ρ^0 vector meson is studied and compared with other resonances to investigate the evolution of the fireball. The other important physics goal of this thesis is to study and discuss the results of elliptic flow (v_2) measurement of the ρ^0 vector meson. The number of constituent quark scaling of v_2 for the ρ^0 vector meson will potentially provide information about the ρ^0 production mechanism.

The data used for the analysis in this thesis were taken with the Solenoidal Tracker at RHIC (STAR) detector. Measurement of the ρ^0 vector meson, through the hadronic decay channel $\rho^0 \rightarrow \pi^+ + \pi^-$, in peripheral Cu+Cu and Au+Au collisions and minimum bias p+p and d+Au collisions are presented. The invariant mass spectra of the ρ^0 vector meson are reconstructed using a combinatorial

technique, and the same-event like-sign technique is applied to estimate the uncorrelated background. A line shape analysis is carried out to extract the various information for the ρ^0 vector meson. A much complicated hadronic cocktail function is fit to the background subtracted invariant mass spectra to extract the mass and the uncorrected yield for the ρ^0 vector meson. The corrected p_T spectra, inverse slope parameters, and yields of the ρ^0 vector meson in the mid-rapidity (i.e. -0.5 $<$ y $<$ 0.5) is studied. The average p_T ($< p_T >$) of the ρ^0 vector meson is compared with other particles to investigate effects of radial flow and particle production mechanism. The ρ^0/π^- ratio is studied and compared with K^*/K^- ratio to understand the regeneration vs. re-scattering effects.

In addition, significant amount of the ρ^0 vector meson elliptic flow, $(v_2(p_T))$, has been measured in Au+Au collisions at $\sqrt{s_{NN}}$ = 200 GeV. It has been observed in peripheral, i.e. 40% - 80% Au+Au collisions that in the intermediate p_T (1.5 $< p_T <$ 5 GeV/c), the ρ^0 vector meson elliptic flow coefficient (v_2) followed the number of constituent quark, n=2, meson-scaling. This is a strong evidence for the partonic collectivity of the medium created in the collisions.

Keywords : QGP, Resonances, Vector meson, Chiral symmetry, Freeze-out, Re-scattering, Re-generation, Cocktail fit, Elliptic flow, Quark scaling, Partonic collectivity.

Contents

1 Introduction **1**

1.1 The Standard Model 2

1.2 Confinement and Asymptotic freedom 3

1.2.1 The Quark Gluon Plasma 4

1.3 Lattice QCD and Phase Diagram 5

1.4 Relativistic Heavy-Ion Collisions 7

1.5 Experimental Observables 10

1.5.1 Particle Spectra and Ratios 10

1.5.2 Azimuthal Anisotropy (Collective Flow) 13

1.6 ρ^0 vector meson to study the medium created at RHIC 22

1.7 Scope and Organisation of the thesis 26

2 The Experimental Facilities **29**

2.1 The Relativistic Heavy-Ion Collider 29

2.2 The STAR Detector 31

2.2.1 The Time Projection Chamber (TPC) 33

2.2.2 Particle Identification (PID) 39

2.2.3 Time-Of-Flight Detector 40

2.2.4 Silicon Vertex Tracker 41

2.2.5 Silicon Strip Detector 42

2.2.6 Barrel Electro-Magnetic Calorimeter 42

2.2.7 Endcap Electromagnetic Calorimeter 43

2.2.8 Forward Time Projection Chambers (FTPC) 44

2.2.9 Photon Multiplicity Detector 45

2.3 The STAR Trigger 45

2.3.1 The STAR DAQ 47

2.4 STAR Computing Facilities 49

3 ρ^0 Production in Cu+Cu and Au+Au Collisions at $\sqrt{s_{NN}}$ = 200 GeV **51**
3.1 Trigger for Data 52
3.2 Event Selection 52
3.3 Track Selection 53
3.4 ρ^0 Invariant Mass Reconstruction 58
3.4.1 Mixed-event Technique 58
3.5 Hadronic Cocktail 63
3.6 ρ^0 Mass and Yield Extraction 67
3.7 Other Possible Ways of Cocktail Fit 70
3.8 Efficiency Correction 75

4 ρ^0 Elliptic Flow (v_2) Measurement in Au+Au Collisions at $\sqrt{s_{NN}}$ = 200 GeV **85**
4.1 Data Analysis 86
4.1.1 Event and Track Selection 86
4.2 Reaction Plane Estimation 89
4.3 Removal of Auto-correlations 93
4.4 Extracting ρ^0 Elliptic Flow 94
4.4.1 The Event Plane $(\phi - \Psi_2)$ bin Method 95
4.4.2 The v_2 vs. m_{inv} Method 96
4.5 Event Plane Resolution Correction 101

5 Results and Discussion **113**
5.1 ρ^0 mass vs. transverse momentum 113
5.1.1 In-Medium Effects and Mass Modification 117
5.2 Transverse Momentum Spectra 118
5.3 Mean Transverse Momentum ($< p_T >$) 121
5.4 Particle Ratio 124
5.4.1 Re-Scattering and Re-Generation Effects and Evolution Properties 126
5.5 Azimuthal Anisotropy (v_2) 128
5.5.1 Methods Comparison 129
5.5.2 v_2 vs. Transverse Momentum p_T 132
5.5.3 Number of Constituent Quark Scaling of v_2 137

6 Summary and Outlook **139**
6.1 Summary 139

6.2 Future Prospective 141

A **143**

A.1 Rapidity and Pseudo-rapidity 143

A.2 Energy Density 144

B **145**

B.1 Systematic Uncertainty on the ρ^0 mass and yield 145

C **147**

C.1 Background flow 147

List of Publication **165**

Acknowledgements **168**

List of Figures

1.1 The fundamental particles of Standard Model and the force-mediating bosons. 3

1.2 Summary of measurements of $\alpha_s(Q^2)$ extracted from experimental results compared to QCD predictions (curves) from [18]. 5

1.3 The energy density in QCD from lattice calculations. When the temperature T reaches the critical temperature T_C, the number of degrees of freedom rapidly rises indicating that quarks and gluons become relevant degrees of freedom. The arrows represents the Stefan-Boltzmann values for asymptotically high temperature. The Figure is taken from [13]. 6

1.4 The QCD Phase Diagram. The Figure is taken from [15]. 7

1.5 Compression and heating can produce the QGP phase. 8

1.6 A light-cone diagram of a collision for a case (a) without a QGP and (b) with a QGP. 9

1.7 The χ^2 contours for T_{fo} and $< \beta_T >$ extracted from thermal and radial flow fits for different hadrons produced in Au+Au collisions at $\sqrt{s_{NN}}$ = 200 GeV. The results from p+p collisions are also shown.The Figure is taken from [17]. 11

1.8 p_T integrated ratios of different hadrons at mid-rapidity in central Au+Au collisions at $\sqrt{s_{NN}}$ = 200 GeV in STAR experiment. The horizontal bars represent statistical model fits to the measured yield ratios for stable and long-lived hadrons. The fit parameters are T_{ch} = 163 $\pm$ 4 MeV, μ_B= 24 $\pm$ 4 MeV, γ_S = 0.99 $\pm$ 0.07 [28]. Figure is taken from [17] 12

1.9 Sketch of an almond shaped fireball. z is the beam direction and x is the direction of the impact parameter b. 15

1.10 Coordinates of the almond shaped fireball. The definitions of the reaction plane and participant plane coordinate systems. 15

1.11 STAR experimental results of the transverse momentum dependence of the elliptic flow parameter (v_2) in Au+Au collisions at $\sqrt{s_{NN}}$ = 200 GeV. The hydrodynamic calculations are shown as dot-dashed lines. The Figure is taken from [52]. 18
1.12 v_2 as a function of p_T for various identified particles in Au+Au collisions at $\sqrt{s_{NN}}$ = 200 GeV. The solid and dotted curves represent the hydrodynamical calculations. 19
1.13 **Upper Panel** - v_2/n Vs. p_T/n for identified particles measured by the STAR experiment. n is the number of constituent quarks. The dashed dotted line is the polynomial fit to the data. **Lower Panel** - The data from upper panel is divided by the polynomial fit as a function of p_T/n [54]. 20
1.14 v_2 as a function of p_T for minimum bias events (circle). The error bars represent the statistical errors and the caps show the systematic uncertainty. The data are compared with hydro + pQCD calculations assuming the initial gluon density dN^g/dy = 1000 (dashed line), 500 (dotted line), and 200 (dashed-dotted line). The solid line is pure hydrodynamical calculation. Figure is taken from [59]. . . . 21
1.15 The re-scattering and re-generation effects on measured ρ^0 yields during the time between chemical and kinetic freeze-out times. . . 25

2.1 A schematic view of the collider complex at BNL, USA [83]. 32
2.2 A perspective view of the STAR detector with a cutaway for viewing inner detector systems. 33
2.3 Cross-sectional view of the STAR detector. 34
2.4 The STAR Time Projection Chamber (TPC). 35
2.5 The anode pad plane of one full sector. The inner sector is on the right and it has small pads arranged in widely spaced rows. The outer sector is on the left and it is densely packed with larger pads. 36
2.6 Ionization energy loss as a function of momentum for positively charged particles in TPC. The solid lines superimposed on the scattered points are the Bethe-Bloch function shown in equation 2.1 for different particle species. 40
2.7 $1/\beta$ vs. momentum (p) in p+p collisions at $\sqrt{s}$ = 200 GeV from Run IX. 41
2.8 STAR Barrel Electromagnetic Calorimeter. 43
2.9 Schematic diagram of a FTPC for the STAR experiment. 44
2.10 Correlation between the summed pulse hight of ZDC and CTB. . . 46

2.11 An online display of one central Au+Au collision event recorded in the STAR Time Projection Chamber. 48

3.1 z- vertex distribution at $\sqrt{s_{NN}}$ = 200 GeV. 53
3.2 Reference Multiplicity distributions at $\sqrt{s_{NN}}$ = 200 GeV. 54
3.3 Track quality assurance for Cu+Cu collisions at $\sqrt{s_{NN}}$ = 200 GeV. . 55
3.4 dE/dx as a function of rigidity (momentum $\times$ charge) for all charged particles in Cu+Cu collisions at $\sqrt{s_{NN}}$ = 200 GeV. 56
3.5 $N\sigma$ distributions fit with multi-gaussian functions. 57
3.6 Invariant mass distribution of K^+ and K^- in 40-80% Au+Au collisions at $\sqrt{s_{NN}}$ = 200 GeV. (a) Same-event invariant mass distribution (solid blue closed circles) along with the normalized mixed-event (closed red open circle) invariant mass distribution. (b) Mixed-event background subtracted invariant mass distribution. 59
3.7 (a) The same-event $\pi^+\pi^-$ invariant mass distribution (blue dots) and the mixed-event $\pi^+\pi^-$ invariant mass distribution (red dots). (b) The mixed-event background subtracted $\pi^+\pi^-$ invariant mass distribution. 60
3.8 Invariant mass of K^+K^- after the background subtraction normalized far away from the ϕ mass peak. 61
3.9 The raw $\pi^+\pi^-$ invariant mass, which corresponds to the real pair (red dots) and the like-sign reference distribution, which corresponds to the background (blue dots) in $0.6 \leq p_T < 0.8$ GeV/c at $\sqrt{s_{NN}}$ = 200 GeV. 62
3.10 The normalized geometric mean of the background pair distribution (blue points) and the real pair distribution (red points) in 0.6 $\leq p_T <$ 0.8 GeV/c at $\sqrt{s_{NN}}$ = 200 GeV. 63
3.11 The same event unlike-sign and like-sign invariant mass distributions are normalized in the region 1.5 GeV/$c^2 < M_{\pi\pi} <$ 2.5 GeV/c^2. 64
3.12 The like-sign background subtracted $\pi^+\pi^-$ invariant mass distributions in different collision systems at $\sqrt{s_{NN}}$ = 200 GeV for a particular p_T bin, i.e. $0.6 \leq p_T < 0.8$ GeV/c. 65
3.13 A cocktail function fit to the invariant mass distributions of $\pi^+\pi^-$ after like-sign background subtraction at $\sqrt{s_{NN}}$ = 200 GeV. Different particle contributions in the cocktail are shown in different colors. 66
3.14 The $\pi^+\pi^-$ invariant mass distributions along with the cocktail fit in 40-80% centrality Au+Au collisions at $\sqrt{s_{NN}}$ = 200 GeV for different p_T bins. 69

3.15 The signal-to-background ratio for ρ^0 measurements as a function of p_T for different collision systems at $\sqrt{s_{NN}}$ = 200 GeV. 70
3.16 A cocktail function fit to the invariant mass distributions of $\pi^+\pi^-$ after background subtraction at $\sqrt{s_{NN}}$ = 200 GeV. In these plots, the width of ρ^0 is taken as a free parameter in the cocktail function. 71
3.17 A cocktail function fit to the invariant mass distributions of $\pi^+\pi^-$ after background subtraction at $\sqrt{s_{NN}}$ = 200 GeV. In these plots, the width of ρ^0 is fixed at 0.16 GeV/c^2 in the cocktail function. . . . 73
3.18 A cocktail function fit to the invariant mass distributions of $\pi^+\pi^-$ after background subtraction at $\sqrt{s_{NN}}$ = 200 GeV. In these plots, the σ^0 mass and width are taken as free parameters in the cocktail function. 74
3.19 Input MC ρ^0 p_T vs. reconstructed ρ^0 p_T compared to the case where the most likely associated track candidate is chosen on the basis of most common hits. 75
3.20 The total reconstruction efficiency multiplied with the detector acceptance as a function of transverse momentum of ρ^0 in Cu+Cu collisions at $\sqrt{s_{NN}}$ = 200 GeV. 76
3.21 Detection efficiency as a function of $\pi^+\pi^-$ invariant mass in different p_T bins in Cu+Cu collisions at $\sqrt{s_{NN}}$ = 200 GeV. 78
3.22 Efficiency of measuring a K^* in Cu+Cu collisions at $\sqrt{s_{NN}}$ = 200 GeV in different centralities. 80
3.23 The $\pi^+\pi^-$ invariant mass distributions in minimum bias p+p at 200 GeV for different p_T bins, each having bin width 0.2 GeV/c. The solid black line is the hadronic cocktail fit function discussed in section 3.5 and 3.6. The units of the fit parameters mass and width are in GeV/c^2. 81
3.24 The $\pi^+\pi^-$ invariant mass distributions in minimum bias d+Au at 200 GeV for different p_T bins, each having bin width 0.2 GeV/c. The solid black line is the hadronic cocktail fit function discussed in section 3.5 and 3.6. The units of the fit parameters mass and width are in GeV/c^2. 82
3.25 The $\pi^+\pi^-$ invariant mass distributions in 20-60% centrality in Cu+Cu at 200 GeV for different p_T bins, each having bin width 0.2 GeV/c. The solid black line is the hadronic cocktail fit function discussed in section 3.5 and 3.6. The units of the fit parameters mass and width are in GeV/c^2. 83

3.26 The $\pi^+\pi^-$ invariant mass distributions in 40-80% centrality in Au+Au at 200 GeV for different p_T bins, each having bin width 0.2 GeV/c. The solid black line is the hadronic cocktail fit function discussed in section 3.5 and 3.6. The units of the fit parameters mass and width are in GeV/c^2. 84

4.1 z-vertex distribution in Au+Au $\sqrt{s_{NN}}$ = 200 GeV Run VII data. . . 88

4.2 Reference Multiplicity distribution for minimum bias data in Au+Au collisions at $\sqrt{s_{NN}}$ = 200 GeV. 88

4.3 ϕ and the corresponding ϕ weight distributions in east and west TPC for 40-80% centrality in Au+Au collisions at $\sqrt{s_{NN}}$ = 200 GeV. 91

4.4 The distribution of the 2nd harmonic event plane angle (Ψ_2) from TPC in Au+Au collisions at $\sqrt{s_{NN}}$ = 200 GeV. The red solid line is the result from the fit function mentioned in the text. 92

4.5 The distribution of the 2nd harmonic event plane angle (Ψ_2) from FTPC in Au+Au collisions at $\sqrt{s_{NN}}$ = 200 GeV. The red solid line in the right figure is the result from the fit function mentioned in the text. 93

4.6 (a) The invariant mass of K^+K^- fitted with a BW function after background subtraction, (b) The total v_2 as a function of K^+K^- invariant mass. The red curve is the fitting function mentioned in Equation 4.20. 98

4.7 The 2nd order TPC event plane and FTPC event plane resolution for v_2 in Au+Au collisions for 9 different centrality bins at $\sqrt{s_{NN}}$ = 200 GeV. 102

4.8 The $\pi^+\pi^-$ invariant mass distribution fit with the hadronic cocktail for $0 < \phi - \Psi_2 < \pi/5$ in different p_T windows in Au+Au 40-80% centrality. 104

4.9 The $\pi^+\pi^-$ invariant mass distribution fit with the hadronic cocktail for $\pi/5 < \phi - \Psi_2 < 2\pi/5$ in different p_T windows in Au+Au 40-80% centrality. 105

4.10 The $\pi^+\pi^-$ invariant mass distribution fit with the hadronic cocktail for $2\pi/5 < \phi - \Psi_2 < 3\pi/5$ in different p_T windows in Au+Au 40-80% centrality. 106

4.11 The $\pi^+\pi^-$ invariant mass distribution fit with the hadronic cocktail for $3\pi/5 < \phi - \Psi_2 < 4\pi/5$ in different p_T windows in Au+Au 40-80% centrality. 107

4.12 The $\pi^+\pi^-$ invariant mass distribution fit with the hadronic cocktail for $4\pi/5 < \phi - \Psi_2 < \pi$ in different p_T windows in Au+Au 40-80% centrality. 108
4.13 The ρ^0 yield as a function of $\phi - \Psi_2$ in 40-80% Au+Au collisions in different p_T bins. 109
4.14 The $\pi^+\pi^-$ invariant mass distributions in different p_T bins for 40-80% centrality in Au+Au collisions. These plots are used in the ρ^0 yield extractions for the v_2 measurement in the v_2 vs. m_{inv} method. 110
4.15 The total v_2 as a function of $\pi^+\pi^-$ invariant mass where the event plane is reconstructed from TPC. 111
4.16 The total v_2 as a function of $\pi^+\pi^-$ invariant mass where the event plane is reconstructed from FTPC. 112

5.1 **Upper Panel**-The ρ^0 mass as a function of p_T for minimum bias p+p collisions at $\sqrt{s}$ = 200 GeV. The dashed line represents the ρ^0 mass value from Particle Data Book [127]. **Lower Panel**-The ρ^0 mass as a function of p_T for minimum bias d+Au collisions at $\sqrt{s_{NN}}$ = 200 GeV. The dashed line represents the ρ^0 mass value from Particle Data Book [127]. In both plots, the brackets indicate the systematic uncertainty. The statistical errors are represented by the error bars. 114
5.2 **Upper Panel**-The ρ^0 mass as a function of p_T for 20-60% Cu+Cu collisions at $\sqrt{s_{NN}}$ = 200 GeV. The dashed line represents the ρ^0 mass value from Particle Data Book [127]. **Lower Panel**-The ρ^0 mass as a function of p_T for 40-80% Au+Au collisions at $\sqrt{s_{NN}}$ = 200 GeV. The dashed line represents the ρ^0 mass value from Particle Data Book [127]. In both plots, the brackets indicate the systematic uncertainty. The statistical errors are represented by the error bars. 115
5.3 The detector efficiency and acceptance corrected ρ^0 vector meson transverse momentum spectra for different centralities in Cu+Cu collisions at $\sqrt{s_{NN}}$ = 200 GeV. The error bars shown are statistical only. The solid line represents an exponential function fit to the data points as given by Equation 5.1. 119
5.4 The mean transverse momentum, $< p_T >$, of different particles as a function of number of participants in different collision systems at 200 GeV. 123
5.5 The ρ^0/π^- yield ratio at mid-rapidity as a function of N_{part} for different collision systems. The K^*/K^- yield ratio is plotted for comparison. 125

5.6 **Upper Panel**-The total $\pi^+\pi^-$ scattering cross section as a function of c.m. energy $\sqrt{s}$. Figure is taken from [165]. **Lower Panel**-The total cross section of π^-K^+ scattering as a function of c.m. energy $\sqrt{s}$. Figure is taken from [165]. 127
5.7 **Upper Panel**-The ρ^0 elliptic flow coefficient (v_2) as a function of p_T. The open circles correspond to the $(\phi - \Psi_2)$ bin method and the filled circles correspond to the v_2 vs. M_{inv} method. The error bars shown are statistical only **Lower Panel**-The ρ^0 v_2 measured in TPC and FTPC event plane. Error bars are statistical only. 130
5.8 **Upper Panel**-Elliptic flow (v_2) as a function of transverse momentum. **Lower Panel**-Azimuthal anisotropy (v_2) vs. transverse kinetic energy $(m_T - m_0)$ for ρ^0 vector meson compared with other particles from the same 40-80% hadronic cross-section at $\sqrt{s_{NN}}$ = 200 GeV in Au+Au collisions. 133
5.9 Centrality dependence of ρ^0 elliptic flow (v_2) in Au+Au at $\sqrt{s_{NN}}$ = 200 GeV collisions. The error bars are statistical only. 134
5.10 **Upper Panel**-Number of constituent quark scaling of v_2 (v_2/n_q vs. p_T/n_q) in 40-80% peripheral Au+Au collisions at $\sqrt{s_{NN}}$ = 200 GeV. ρ^0 v_2 scales with n=2 quarks. **Lower Panel**-Transverse kinetic energy scaling of v_2 (v_2/n_q vs. $(m_T - m_0)/n_q$) in 40-80% peripheral Au+Au collisions at $\sqrt{s_{NN}}$ = 200 GeV. ρ^0 v_2 scales with n=2 quarks. 135
5.11 **Upper Panel**-Number of constituent quark scaling of v_2 (v_2/n_q vs. p_T/n_q) in 40-80% peripheral Au+Au collisions at $\sqrt{s_{NN}}$ = 200 GeV. ρ^0 v_2 scales with n=2 quarks. **Lower Panel**-Transverse kinetic energy scaling of v_2 (v_2/n_q vs. $(m_T - m_0)/n_q$) in 40-80% peripheral Au+Au collisions at $\sqrt{s_{NN}}$ = 200 GeV. ρ^0 v_2 scales with n=2 quarks. 136

B.1 The ρ^0 peak is fitted with an exponential plus the BW $\times$ PS function. 145
B.2 Systematic error on the yield by varying the constant according to the statistical error on the constant that gives best χ^2/ndf. 146

C.1 $\pi^+\pi^-$ v_2 as a function of p_T in different mass window. 147

List of Tables

3.1 Centrality definition for different uncorrected multiplicity ranges for Cu+Cu and Au+Au system at $\sqrt{s_{NN}}$ = 200 GeV. 54

3.2 List of dataset used in the analysis. Cuts on V_Z, centrality range selected and number of events used are also shown. 55

3.3 List of track cuts for charged pions ($\pi^{\pm}$) in the ρ^0 analysis for spectra calculation in both Cu+Cu and Au+Au collisions at $\sqrt{s_{NN}}$ = 200 GeV. 57

4.1 Run VII trigger and events selection for minimum bias data in Au+Au collisions at $\sqrt{s_{NN}}$ =200 GeV. 86

4.2 Run VII centrality bins in Au+Au collisions at $\sqrt{s_{NN}}$ = 200 GeV. . . 87

4.3 Track selection criteria for flow analysis used in the event plane reconstruction in Au+Au collisions at $\sqrt{s_{NN}}$ = 200 GeV. 90

4.4 TPC and FTPC event plane resolution in Au+Au collisions at $\sqrt{s_{NN}}$ = 200 GeV for different centralities. 102

5.1 The ρ^0 mass for each p_T bin in minimum bias triggered p+p and d+Au collisions. The unit for p_T is GeV/c and the unit for mass is MeV/c^2. The mass values in p+p and d+Au collisions are listed together with statistical uncertainties and systematic uncertainties. The first error corresponds to the statistical error and the last two errors are the asymmetric systematic errors. 116

5.2 The ρ^0 mass for each p_T bin in 20-60% Cu+Cu collisions and 40-80% Au+Au collisions. The unit for p_T is GeV/c and the unit for mass is MeV/c^2. The mass values in Cu+Cu and Au+Au collisions are listed together with statistical uncertainties and systematic uncertainties. The first error corresponds to the statistical error and the last two errors are the asymmetric systematic errors. 117

5.3 The ρ^0 invariant yields ($d^2N/2\pi p_T dp_T dy$) in different p_T bins and different centralities in Cu+Cu collisions at $\sqrt{s_{NN}}$ = 200 GeV. The errors are statistical only. 120
5.4 The ρ^0 invariant yields ($d^2N/2\pi p_T dp_T dy$) in different p_T bins in different centralities in Cu+Cu collisions at $\sqrt{s_{NN}}$ = 200 GeV. The errors are statistical only. 120
5.5 The ρ^0 dN/dy at $|y| < 0.5$ and the inverse slope parameter (T) measured in Cu+Cu collisions at $\sqrt{s_{NN}}$ = 200 GeV for different centralities. Both statistical and systematic errors are shown. 121
5.6 The ρ^0 average transverse momentum ($< p_T >$) for different collision centralities at $\sqrt{s_{NN}}$ = 200 GeV Cu+Cu collisions. 122
5.7 The ρ^0 v_2 values obtained as a function of p_T in both the methods in Au+Au collisions at $\sqrt{s_{NN}}$ = 200 GeV. Only statistical error is mentioned. 131

Chapter 1

Introduction

"I, a universe of atoms, an atom in the universe."

– Richard P. Feynman

Since ancient times, mankind has been driven by the quest for observing and understanding the vastness of the Universe around. Over times, mankind has developed a systematic and scientific approach to understand the fundamental forces in nature. In conjunction with astrophysics and cosmology, particle physics research seeks answers to the fundamental nature of the physical Universe and its evolution over the last billion of years. Nuclear physics shows how the fundamental building blocks from the early Universe combine to make stable and unstable chemical elements today. With the advancement of technologies, better particle detectors and higher energy particle accelerators, mankind has succeeded to explore the small length scale or sub-atomic level. This exploration has led to a better understanding of the building blocks of matter and their interactions, and eventually ended up with what is today known as "Standard Model" [1, 2].

The Standard Model provides a comprehensive understanding of electromagnetic, weak and strong interactions of the elementary particles and constitutes the

foundation of particle physics. A part of the Standard Model has been validated by the discovery of the $W^{\pm}$ and Z^0 particles at CERN's Super Proton Antiproton collider in 1983 [3, 4] and by the observations of the predicted top quark and tau neutrino at FNAL's Tevatron (USA) in 1995 and 2000 [5, 6]. In spite of this success, the Standard Model of physics cannot explain the origin of mass and has also shown other unexpected flaws [7, 9]. Recent observations in astrophysics indicate that the Universe is mostly made up of "dark" matter and energy, concepts that cannot be modelled with our present theories.

The dearth for understanding the fundamental interactions and its consequences has fascinated the young minds for all the time.

1.1 The Standard Model

There are four fundamental interactions in nature: **Strong, Electromagnetic, Weak and Gravitational**. Each of these interactions are mediated by gauge bosons, i.e. gluons for the strong interaction, photons for the electromagnetic interaction, $W^{\pm}$ and Z^0 for weak interaction and graviton for the gravitational interaction [10]. An attempt has been made to unite all the interactions and to have one model. But so far three fundamental interactions, i.e. Strong, Electromagnetic and Weak, are incroporatd in a model, called the Standard Model, to describe all the properties of elementary particles. The standard model is the best available theory in particle physics till date. In this model, the elementary particles are classified into two groups: quarks and leptons which are spin half particles and are termed as Fermions [11]. Figure 1.1 shows the three generations of quarks and leptons, and the intermediating gauge bosons involved in different interactions.

Among the three interactions incorporated in the Standard Model, Strong interaction is the most challenging one to understand. The theory to describe the strong interactions between quarks and gluons is known as Quantum Chromodynamics (QCD) [7, 12].

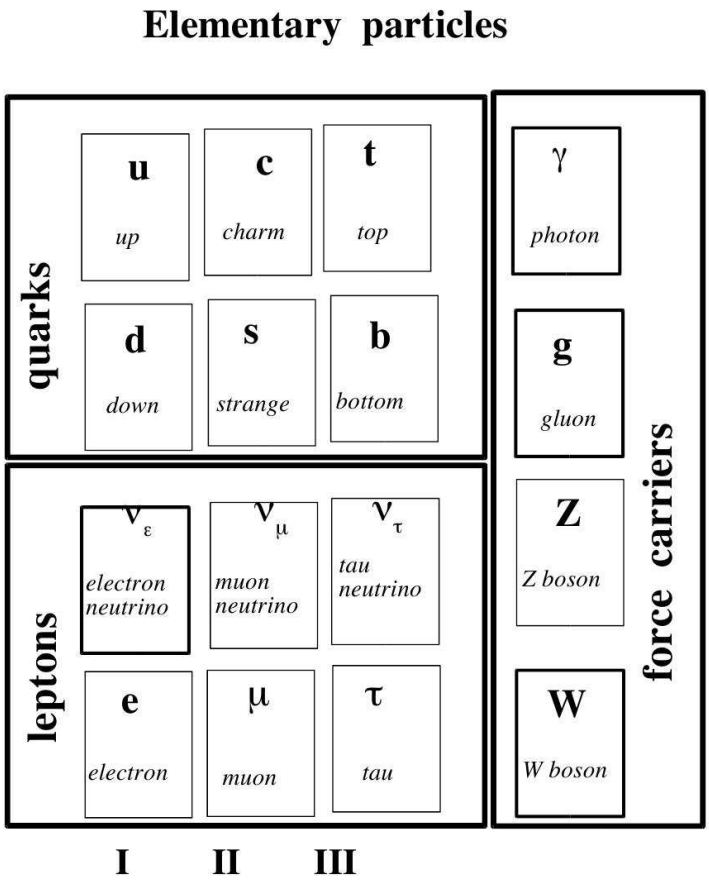

Figure 1.1: The fundamental particles of Standard Model and the force-mediating bosons.

1.2 Confinement and Asymptotic freedom

Theoretical investigations of QCD show a remarkable property of Strong Interaction:- At very high energies, the strength of the interaction between quarks becomes weaker. In other words, the effective coupling constant of strong interactions becomes smaller at higher energies, eventually approaching zero value. This is known as "Asymptotic Freedom". This behavior is opposite to the behavior of Quantum Electrodynamics (QED), where the coupling constant increases with energy. The behavior of asymptotic freedom is well tested in experiments to a high accuracy [8]. However, the understanding of QCD in the domain of low energy remains poor. This is the domain where hadrons form, and quarks are confined into these hadrons. This is called "Colour Confinement".

Apart from this "confinement" there is another domain, where QCD is not well understood. This is the domain of high temperature and high density matter. From theory side this is the expectation based on asymptotic freedom that at high temperature the interactions between quarks will become weak. This leads to an obvious question that whether one should expect an ideal gas of quarks and gluons at such high temperatures or not.

1.2.1 The Quark Gluon Plasma

The coupling constant in QCD is given by [8]:

$$\alpha_s\left(Q^2\right) = \frac{4\pi}{(11 - 2n_F/3)\, lnQ^2/\Lambda^2} \tag{1.1}$$

where Q^2 is the momentum transfer, n_F is the number of quark flavors and Λ is the scaling parameter. The typical value of Λ, obtained from scattering experiments, is about 200 MeV. Equation 1.1 shows that the coupling constant is small when $Q^2 >> \Lambda^2$. This means that the interactions between quarks and gluons become weaker at very high energies, while they are strong at lower energies. Thus, a collection of quarks and gluons interacting with each other with typical momentum transfer much larger than Λ should constitute a weakly interacting system of particles. Perturbative QCD (pQCD) has been very successful in predicting and describing various processes observed in different experiments as illustrated in Figure 1.2 [18]. The value of α_s is extracted from experimental results and compared to pQCD predictions. Thus, if a system of quarks and gluons is at a temperature much higher than several hundred MeV, then coupling constant will be small and the system should behave like an ideal gas. In such a system, one does not expect the effects of confinement of QCD interaction to survive. This system of quarks and gluons, where quarks and gluons are no more confined within the region of a hadron, is called the **Quark Gluon Plasma (QGP)** [16, 17, 22, 23].

Even at sufficiently high density (i.e. compressed baryonic matter), one ex-

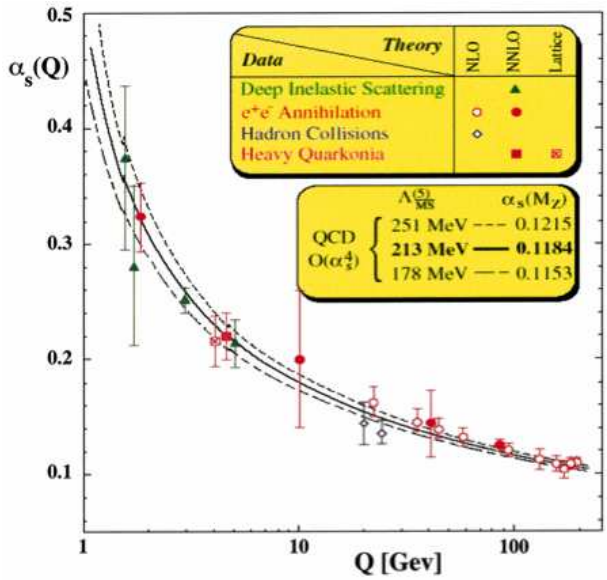

Figure 1.2: Summary of measurements of $\alpha_s(Q^2)$ extracted from experimental results compared to QCD predictions (curves) from [18].

pects that hadrons will overlap. At such high densities, typical separation between constituents quarks of different hadrons become much less than 1 fm, i.e. the typical size of a hadron. This means that at such high densities the effective coupling constant for quark-gluon interaction will be very small. Under such condition, one can also expect a state like QGP.

This expectation is strongly supported by lattice QCD calculations and other phenomenological approaches.

1.3 Lattice QCD and Phase Diagram

The non-perturbative aspects of Quantum Chromodynamics is dealt with the lattice QCD. These lattice QCD calculations are done numerically by putting quarks and gluons on a discrete space-time lattice and many properties like, energy density, pressure etc. are calculated as a function of temperature. The energy density scaled with 4th power of temperature (ϵ/T^4) is calculated in lattice QCD as a function of temperature scaled with the critical temperature (T/T_c) for different quark flavors [13] and the result is shown in Figure 1.3. It is predicted that at

$T = T_c$, ϵ/T^4 rises up and gets saturated below the value of the Stefan-Boltzmann value shown by arrow for different flavors in Figure 1.3. It has been predicted

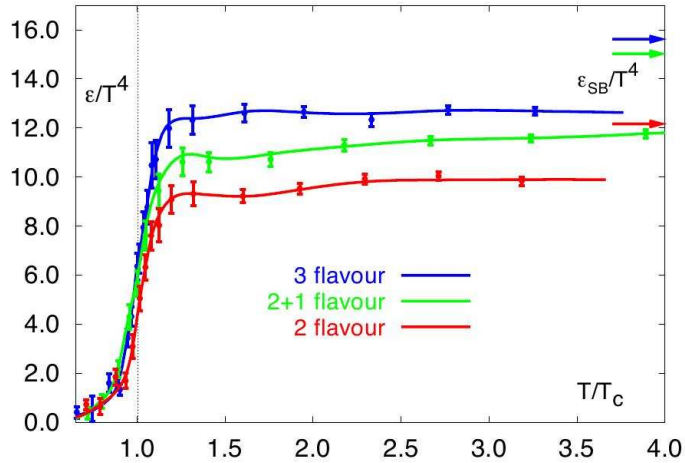

Figure 1.3: The energy density in QCD from lattice calculations. When the temperature T reaches the critical temperature T_C, the number of degrees of freedom rapidly rises indicating that quarks and gluons become relevant degrees of freedom. The arrows represents the Stefan-Boltzmann values for asymptotically high temperature. The Figure is taken from [13].

that at very high temperature the energy density value will finally achieve the ideal Stefan-Boltzmann value [14]. One of the most important observation is that at the critical temperature suddenly the degrees of freedom increase to a larger number indicating a de-confinement phase transition. Although the critical temperature varies with the quark flavors, but the observation of the increase of the degrees of freedom at critical temperature remains valid for all quark flavors.

The QCD phase diagram which maps out the different phases of QCD matter as a function of baryon chemical potential (μ_B) and temperature (T) is shown in Figure 1.4 [15]. If baryon chemical potential increases beyond a critical value keeping the temperature low, there is a possibility of formation of baryon rich plasma, which is produced in Neutron Star. It may so happen that in high baryon rich plasma, there will be attractive force between two quarks leading to the formation of color superconductor phase as shown in Figure 1.4. The phase transition is then predicted to be first order in this region of μ_B and T. If the temperature is increased with zero baryon chemical potential, it has been predicted

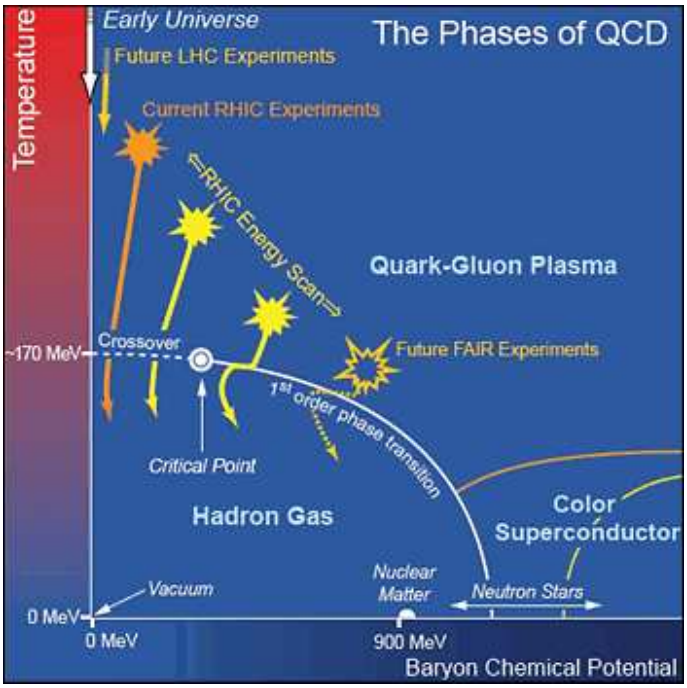

Figure 1.4: The QCD Phase Diagram. The Figure is taken from [15].

by lattice QCD that there will be smooth cross over. This scenario is the early Universe scenario. By suitably changing the baryon chemical potential and the temperature, one can get the point on the phase boundary where first order phase transition stops and beyond that temperature the phase transition will be a cross over. This end point on the phase boundary is known as the Critical point. By suitably tuning the energy of the heavy-ion beam, one can get different combination of baryon chemical potential (μ_B) and the temperature (T) as shown in Figure 1.4. From this one can possibly get some information about the critical point as predicted by the lattice QCD. This is one of the main objectives of the STAR experiment at RHIC to have beam energy scan program that is going on since the year 2010.

1.4 Relativistic Heavy-Ion Collisions

There are two ways, as depicted in Figure 1.5, to create the dense hadronic matter. The first one is by squeezing the nucleus and second one is by heating up

the nucleus. In the first case, the nucleons, i.e. neutrons and protons, inside the nucleus start to overlap when the inter particle distance is smaller than the individual nucleon size. In the second case, number of pions produced is so large that the partons no longer belong to a specific hadron.

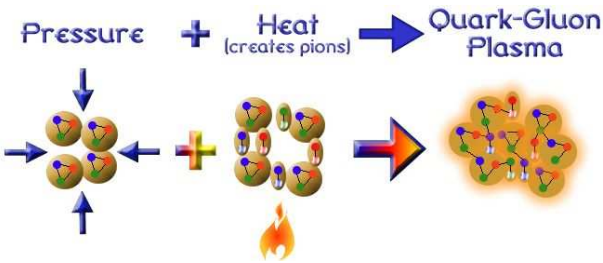

Figure 1.5: Compression and heating can produce the QGP phase.

Relativistic heavy-ion collisions provide a unique opportunity to study the quark gluon plasma in the laboratory experiments. For example, at Relativistic Heavy Ion Collider, beams of Au-Au are collided at 200 GeV per nucleon center of mass energy. At such high energies nuclei, or even protons and neutrons, lose their identity. The density of the secondary partons grows due to multiple scattering among the quarks and gluons initially present in the nucleons. In this case, one could expect a local thermal equilibrium where the quarks and gluons are the degrees of freedom rather than the hadrons.

As the two heavy nuclei approach each other at ultra-relativistic energies, they appear to be Lorentz contracted. Depending on the energy of the nuclei, the nucleons are either opaque or transparent to each other. If the energy is very high, the nucleons pass through each other leaving behind a trail of energy. This energy is confined in a small volume and is called a fireball. Inside the fireball, all quarks and anti-quarks are generated and may lead to locally equilibrated quark gluon plasma, which is shown in Figure 1.6. The fireball expands and cools down. At the same time particle production continues. After certain time, the inelastic process ceases, leading to the Chemical freeze-out. However, the elastic process continue till the mean free path of the particles becomes comparable to the size of the fireball. Then the elastic process stops, leading to the Kinetic Freeze-out. At

this point of time, particles come out of the fireball and hit the detector. Different experimental observables are proposed to extract information about the Kinetic Freeze-out and Chemical Freeze-out.

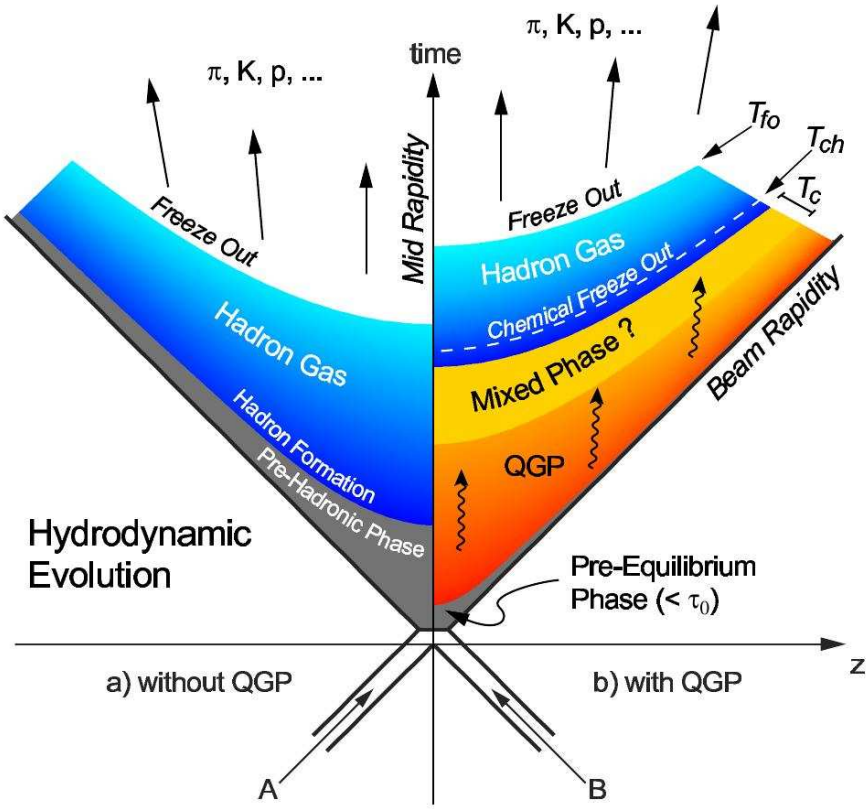

Figure 1.6: A light-cone diagram of a collision for a case (a) without a QGP and (b) with a QGP.

The experimental signatures proposed for the quark matter formation in relativistic heavy-ion collisions can be categorized into two groups, namely - the soft probes and hard probes. The soft probe includes the bulk matter properties such as particle multiplicities, particle yields, transverse momentum spectra and correlations of hadrons especially in the low momentum region ($p_T \leq 1.5$ GeV$/c$). It is also possible to produce energetic particles through hard scattering processes. The interaction of these highly energetic particles with the medium provides a unique set of penetrating probes for the medium, also known as hard probes.

In the following sections, some of the proposed signatures of the QGP phase

are briefly discussed.

1.5 Experimental Observables

1.5.1 Particle Spectra and Ratios

The initial short-lived source in relativistic heavy-ion collisions cannot be measured directly. Therefore, one has to explore different signatures to get the information about different stages of the fireball. The thermal freeze-out temperature is extracted from the transverse momentum (p_T) spectra by fitting an exponential function.

1.5.1.1 Exponential Distribution

The particle production is expected to follow an exponential distribution, as predicted by Hagedorn in the early 1960's [24, 25]. For a thermally equilibrated particle distribution, the p_T spectrum can be described by

$$\frac{1}{2\pi p_T}\frac{d^2N}{dp_T dy} = Ae^{-\frac{m_T}{T}} \tag{1.2}$$

where m_T is the transverse mass, defined as $m_T = \sqrt{p_T^2 + m_0^2}$ and A is the multiplicative constant. The left side of Equation 1.2 can be re-written as,

$$\frac{1}{2\pi p_T}\frac{d^2N}{dp_T dy} = \frac{1}{2\pi m_T}\frac{d^2N}{dm_T dy} \tag{1.3}$$

Substituting Equation 1.3 into Equation 1.2 and integrating over m_T,

$$\int_{m_0}^{\infty}\frac{1}{2\pi m_T}\frac{d^2N}{dm_T dy}dm_T = \int_{m_0}^{\infty} Ae^{\frac{-m_T}{T}}dm_T. \tag{1.4}$$

Equation 1.4 can be re-arranged so that the multiplicative constant, A, can be evaluated directly as,

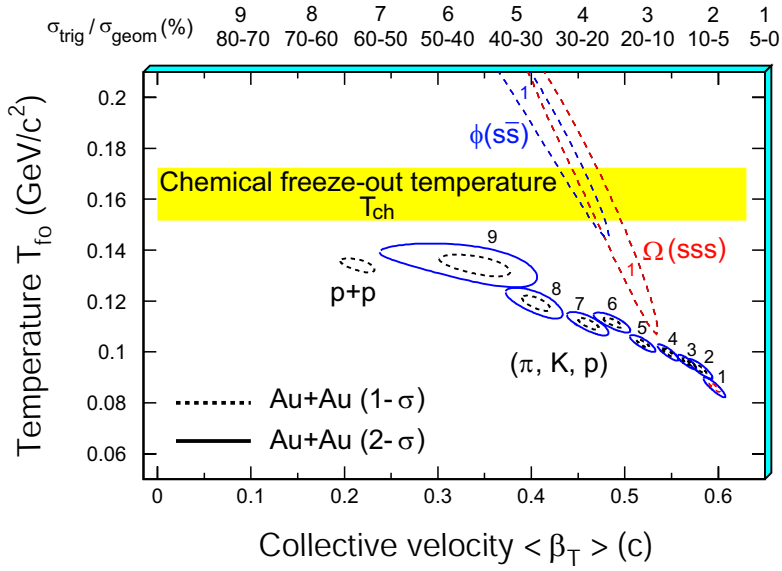

Figure 1.7: The χ^2 contours for T_{fo} and $< \beta_T >$ extracted from thermal and radial flow fits for different hadrons produced in Au+Au collisions at $\sqrt{s_{NN}}$ = 200 GeV. The results from p+p collisions are also shown.The Figure is taken from [17].

$$A = \frac{dN/dy}{\int_{m_0}^{\infty} 2\pi e^{\frac{-m_T}{T}} m_T dm_T} = \frac{dN/dy}{2\pi T\,(m_0 + T)\, e^{\frac{-m_0}{T}}}. \tag{1.5}$$

Now Equation 1.2 can be expressed as,

$$\frac{1}{2\pi m_T}\frac{d^2N}{dm_T dy} = \frac{dN/dy}{2\pi T\,(m_0 + T)} e^{\frac{-(m_T - m_0)}{T}}. \tag{1.6}$$

Equation 1.6 is used to describe the p_T spectra of the particles that are measured. The temperature parameter T, commonly referred as the inverse slope parameter, was initially expected to be directly related to the freeze-out temperature ($T_{f.o.}$). However, in presence of the transverse flow in the system, T is written as [27]:

$$T_{eff} = T\sqrt{\frac{1 + \beta_T}{1 - \beta_T}} \tag{1.7}$$

where T_{eff} is the effective temperature of the fireball and for a given m_0 it is obtained from the p_T spectrum for that m_0. By measuring T_{eff} for various m_0, one can extract $T_{f.o.}$. In Equation 1.7, β_T is the transverse velocity.

Figure 1.7 shows the values of T_{fo} and $< \beta_T >$ extracted from hydrodynamics-

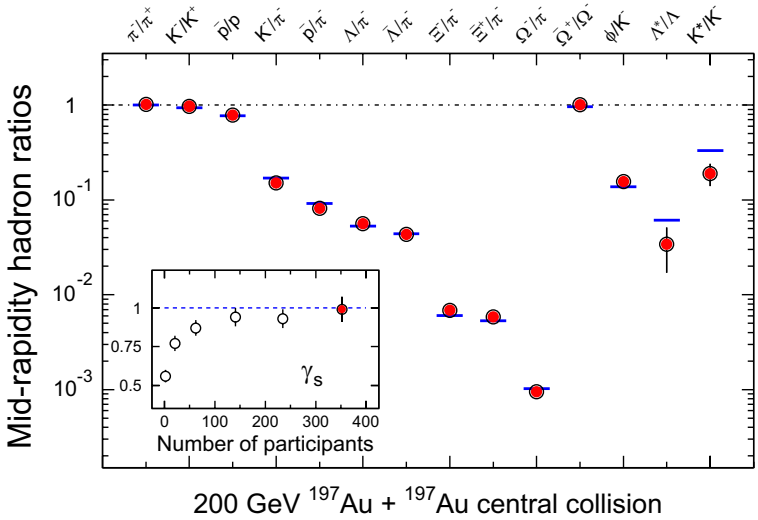

Figure 1.8: p_T integrated ratios of different hadrons at mid-rapidity in central Au+Au collisions at $\sqrt{s_{NN}}$ = 200 GeV in STAR experiment. The horizontal bars represent statistical model fits to the measured yield ratios for stable and long-lived hadrons. The fit parameters are T_{ch} = 163 $\pm$ 4 MeV, μ_B= 24 $\pm$ 4 MeV, γ_S = 0.99 $\pm$ 0.07 [28]. Figure is taken from [17]

motivated fits [27] to the p_T spectra of identified hadron species for different centrality in Au+Au collisions at $\sqrt{s_{NN}}$ = 200 GeV. Also in the same Figure, the result from p+p collisions is shown. It is clear from Figure 1.7 that the flow velocity increases with the size of the system. This is argued in favor of more re-scattering in a larger system, which allows larger collective flow velocities to develop. This is also supported by the drop in the thermal freeze-out temperature with system size, which suggests that larger systems are in thermal contact for a longer time period. Interestingly, the Ω-baryon and ϕ-meson have highest kinetic freeze-out temperatures which suggests that these particles thermally decoupled from the expanding fireball at an early stage. In case of p+p data in Figure 1.7, one should be careful in interpreting the parameters, i.e. T_{fo} and $\langle\beta_T\rangle$, as these collisions are not expected to produce a thermalized medium under collective flow.

1.5.1.2 Statistical Model

The basic ingredient required to compute the thermal composition of particle yields measured in heavy-ion collisions is the partition function. The statistical

model [29–31] is based on a grand canonical ensemble to describe the partition function. Hence, the density of particle species in an equilibrated fireball is written as:

$$n_i = \frac{g_i}{2\pi^2} \int_0^\infty \frac{p^2 dp}{e^{(E_i(p)-\mu_i)/T_{ch}} \pm 1} \tag{1.8}$$

where T_{ch} is the chemical freeze-out temperature, n_i is the particle density, g_i is the spin degeneracy, p is the momentum, E_i is the total energy and μ_i is the chemical potential and equals to $\mu_B B_i - \mu_S S_i - \mu_{I^3} I_i^3$. The quantities B_i, S_i and I_i^3 are the baryon number, the strangeness number and the third component of the isospin quantum number of the particle of species i. In the above equation, the temperature T_{ch} and the baryon chemical potential μ_B are two independent parameters of the model. The volume of the fireball, V, is fixed and the strangeness chemical potential μ_S, and the isospin chemical potential μ_{I^3} are fixed by the conservation laws as follows:

$$V \sum_i n_i B_i = Z + N \tag{1.9}$$

$$V \sum_i n_i S_i = 0 \tag{1.10}$$

$$V \sum_i n_i {I_i}^3 = \frac{Z - N}{2} \tag{1.11}$$

This statistical model has been applied to fit the STAR data in Au+Au collisions at $\sqrt{S_{NN}}$ = 200 GeV [17]. By using various particle ratios obtained from STAR, the best agreement of the model and the data is achieved with minimum χ^2 at the baryon chemical potential $\mu_B \simeq 24 \pm 4$ MeV and the temperature $T_{ch} \simeq 163 \pm 4$ MeV. The comparison of the STAR experimental particle ratios and the statistical model calculations is shown in Figure 1.8.

1.5.2 Azimuthal Anisotropy (Collective Flow)

In a non-central heavy-ion collision, the initial state is characterized by a spatial anisotropy in the azimuthal plane. In such collisions, the overlapping reaction

zone of two colliding nuclei is not spherical and has rather an almond shape as shown in Figure 1.9. The initial momenta of the produced particles are predominantly longitudinal. Transverse momenta, if any, are isotropically distributed. On the other hand, if these particles interact with each other frequently and with an adequate strength, then local thermal equilibrium is likely to be reached. In that case, the system can be described in terms of thermodynamical quantities such as temperature, pressure, etc [32]. The spatial anisotropy of the almond-shaped overlap zone via sufficient interactions among the produced particles ensures anisotropic pressure gradient in the transverse plane. This leads to a final state, characterized by a momentum anisotropy in the $P_x P_y$ plane as shown in Figure 1.9.

The measurement of the azimuthal anisotropy, resulting from non-central nuclear collisions, appears to be one of the most informative directions in studying the nature and properties of matter created in high energy nuclear collisions. The main importance of this study lies in its sensitivity to the system properties very early in its evolution. The flow refers to a collective expansion of the bulk matter. Because the spatial asymmetries rapidly decrease with time, "self-quenching", anisotropic flow can develop only in the first few fm/c. Therefore, the momentum anisotropy is particularly sensitive to the early stages of the system evolution [36]. Thus, the azimuthal anisotropy is a measure of the degree of thermalization of the matter produced in a non-central heavy-ion collision and hence, is sensitive to the equation of state (EoS) of the expanding matter [32–37].

In heavy-ion collisions, the size and shape of the colliding region depend on the distance between the centers of the nuclei in the transverse plane, which is called impact parameter and is denoted by b. The plane spanned by the impact parameter (b) vector and the beam direction is known as reaction plane. The overlap zone in the transverse plane has a short axis parallel to the impact parameter and a long axis perpendicular to the impact parameter. Due to the pressure gradient, this almond shape is converted into a momentum asymmetry and thus more particles are emitted along the short axis [37], as shown in Figure 1.9.

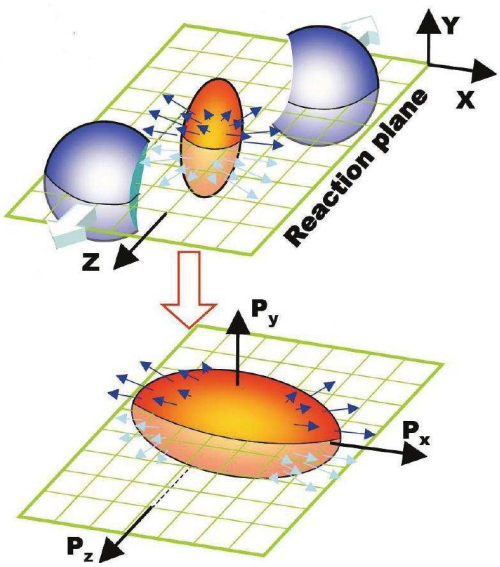

Figure 1.9: Sketch of an almond shaped fireball. z is the beam direction and x is the direction of the impact parameter b.

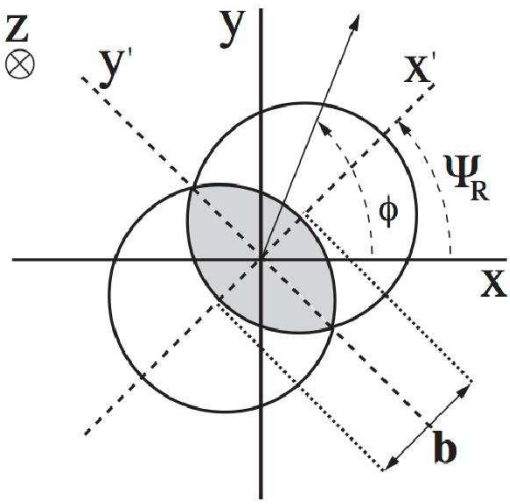

Figure 1.10: Coordinates of the almond shaped fireball. The definitions of the reaction plane and participant plane coordinate systems.

As the elliptic flow should be zero for a totally azimuthally symmetric system, for small anisotropies in the initial geometry, elliptic flow is proportional to this spatial anisotropy. The initial spatial anisotropy in the reaction zone can be characterized by the eccentricity defined as:

$$\epsilon_{std} = \frac{\langle Y^2 - X^2 \rangle}{\langle Y^2 + X^2 \rangle}, \tag{1.12}$$

where X and Y are the spatial coordinates in overlapping region as shown in Figure 1.10. The average in Equation 1.12 is taken over the initial geometry with some weight. However, the participating nucleons in the collisions fluctuate from event to event at a fixed impact parameter. In this case, the center of the overlap zone is shifted, and the orientation of the principal axis of the interaction zone is rotated with respect to the initial coordinate system. Then the anisotropy develops along the plane spanned by the minor axis of the participant zone and the beam direction. This is called the participant plane. The eccentricity in the participant plane, i.e. ϵ_{part} is defined as:

$$\epsilon_{part} = \frac{\langle Y'^2 - X'^2 \rangle}{\langle Y'^2 + X'^2 \rangle}, \tag{1.13}$$

where X' and Y' are the shifted coordinates with respect to X and Y coordinates respectively, as shown in Figure 1.10.

Except for the most peripheral heavy-ion collisions such as Au+Au, the average values of ϵ_{std} and ϵ_{part} are similar. However, in case of smaller systems fluctuations in the nucleon positions become important for all centralities and the average eccentricity can vary significantly [38].

The triple differential invariant distribution of the produced particles with respect to the reaction plane can be written in term of a Fourier series [37, 40] as follows:

$$E\frac{d^3N}{dp^3} = \frac{1}{2\pi}\frac{d^2N}{p_T dp_T dy}(1 + \sum_{n=1}^{\infty} 2v_n cos[n(\phi - \Psi_r)]), \tag{1.14}$$

where the coefficients v_n $(= \langle cos\,[n\,(\phi_i - \Psi_r)]\rangle)$ are used for a quantitative char-

acterization of the event anisotropy, ϕ is the azimuthal angle of the produced particles and Ψ_r is the reaction plane angle. The angle brackets mean an average over all particles in all events. The sine terms are not present because of the symmetry with respect to the reaction plane. In the above expansion, the Fourier coefficient v_1 represents the directed flow and v_2 is the elliptic flow. The elliptic flow coefficient, v_2, is expected to be dominant because of the geometry of the collisions.

1.5.2.1 Mass Ordering of v_2

At low p_T (≤ 2 GeV/c), the differential elliptic flow ($v_2(p_T)$) for different hadrons has been observed to scale with particle mass. Figure 1.11 shows the STAR experimental results of v_2 at low p_T in Au+Au collisions at $\sqrt{s_{NN}}$ = 200 GeV for different charged particles. This can be explained in a hydrodynamical picture [47, 51] assuming the system is in thermal equilibrium. The systematic dependence of v_2 on particle mass is a strong indicator of a common transverse velocity field for all particles [45].

Ideal hydrodynamics assumes that matter is in local thermal equilibrium and, therefore, is most likely to be applicable for the low p_T particles. The higher p_T particles are produced in hard scattering which are unlikely to reach thermal equilibrium with the surrounding medium over the lifetime of the system. Hydrodynamical models based on initial conditions including a QGP equation of state have been able to successfully describe the result obtained for RHIC elliptic flow at low p_T, as shown in Figure 1.12.

In ideal hydrodynamics the mass ordering of v_2 persists up to larger p_T, although less pronounced because of the v_2 of the different particles start to approach each other [45]. It is observed that as the p_T of the particle goes beyond 1.5 GeV/c, the v_2 values of different hadrons deviate from the expected hydrodynamics behavior. This mass dependence behavior is the reverse of the behavior observed at low p_T. This is not expected for hadrons in hydrodynamics and is also not expected, if the v_2 is caused by a parton energy loss. An elegant explanation

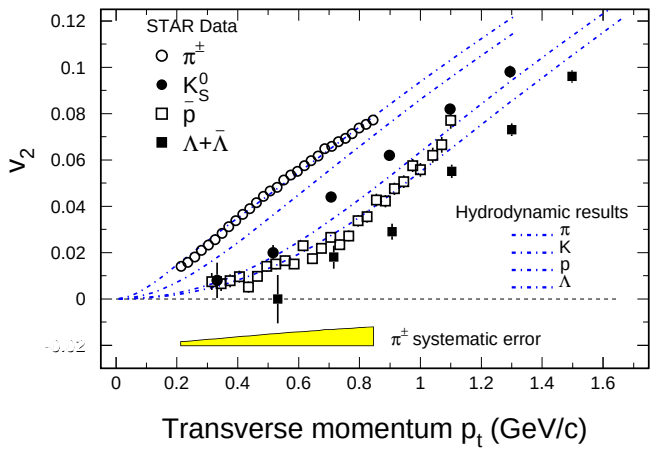

Figure 1.11: STAR experimental results of the transverse momentum dependence of the elliptic flow parameter (v_2) in Au+Au collisions at $\sqrt{s_{NN}}$ = 200 GeV. The hydrodynamic calculations are shown as dot-dashed lines. The Figure is taken from [52].

of the unexpected particle type dependence and magnitude of v_2 at intermediate p_T is provided by the coalescence picture [50].

1.5.2.2 Number of Constituent Quark Scaling of v_2

Figure 1.12 represents the v_2 measurement of identified hadrons in Au+Au minimum bias collisions at $\sqrt{s_{NN}}$ = 200 GeV in STAR and PHENIX experiments. For $p_T > 2$ GeV/c, one can see that the observed values of v_2 saturate and there is a substantial difference between the saturation levels for baryons and mesons. This provides some important information regarding the origin of baryon-meson difference [45]. The hydrodynamic calculations overpredict the data for $p_T >$ 2 GeV/c. However, if we divide the v_2 value with the number of constituent quarks, we observe a scaling for $p_T/n > 1$ GeV/c. The observation of number of constituent quark scaling is of particular interest and importance. It indicates that the system is in a de-confined stage. If hadrons are formed via the coalescence of the constituent quarks, then there should be a region in the transverse momentum space where particle yield would be proportional to the quark density to the

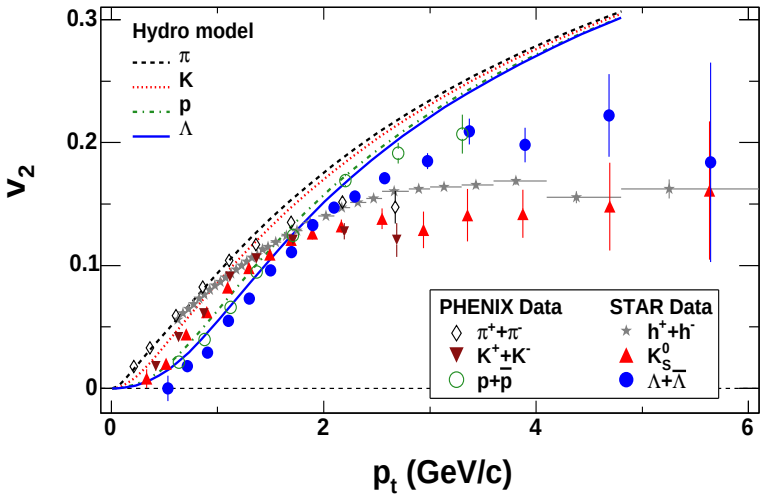

Figure 1.12: v_2 as a function of p_T for various identified particles in Au+Au collisions at $\sqrt{s_{NN}}$ = 200 GeV. The solid and dotted curves represent the hydrodynamical calculations.

power equal to the number of constituent quarks in the produced hadron, 2 for meson and 3 for baryons [50]. Besides other important consequences, such as enhanced relative production of baryons in this transverse momentum region, this picture leads to the constituent quark scaling of elliptic flow, $v_2(p_T) \sim nv_2(p_T/n)$, where n is the number of constituent quarks in the hadron [50, 53]. Figure 1.13 shows this scaling holds good. It is important to note that this scaling is limited to a specific region in the transverse momentum. The reason for the scaling violation at lower momenta might be due to the break down of coalescence picture. For identified particles the scaling for mesons and baryons is based on the equations:

$$\frac{d^3n_M}{d^3p_M} \propto \left[\frac{d^3n_q}{d^3p_q}(p_q \approx p_M/2)\right]^2 \tag{1.15}$$

$$\frac{d^3n_B}{d^3p_B} \propto \left[\frac{d^3n_q}{d^3p_q}(p_q \approx p_B/3)\right]^3 \tag{1.16}$$

where M stands for mesons and B stands for baryons. These equations are valid only if the probability of coalescence is relatively low. According to these equations the hadron yield scales with power 2 or 3 of the quark density. Elliptic flow of identified particles measured in Au+Au collisions at RHIC exhibits a

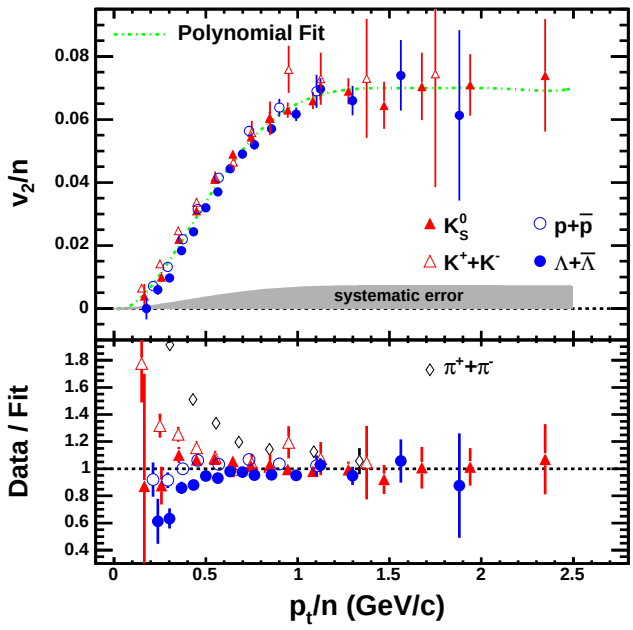

Figure 1.13: **Upper Panel** - v_2/n Vs. p_T/n for identified particles measured by the STAR experiment. n is the number of constituent quarks. The dashed dotted line is the polynomial fit to the data. **Lower Panel** - The data from upper panel is divided by the polynomial fit as a function of p_T/n [54].

remarkable scaling with the number of constituent quarks at intermediate p_T.

The upper panel in Figure 1.13 shows the STAR experimental results on v_2/n vs. p_T/n for identified hadrons in Au+Au collisions at $\sqrt{s_{NN}}$ = 200 GeV. Here n stands for the number of constituent quarks. The dashed-dotted line denotes a polynomial fit to the data. In the intermediate p_T range, the apparent scaling behavior points towards the quark degrees of freedom as the most effective one determining the hadron flow. It indicates that hadron formation at intermediate p_T proceeds via quark coalescence. The constituent quarks carry their own substantial azimuthal anisotropy which is later summed up to give the flow of hadrons.

1.5.2.3 High p_T region

At high transverse momentum ($p_T > 5$ GeV/c), measurement of azimuthal anisotropy is an interesting observable to study the path length dependence of energy loss of

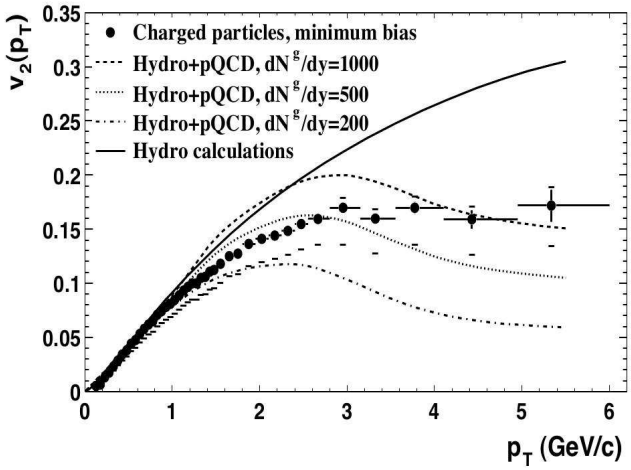

Figure 1.14: v_2 as a function of p_T for minimum bias events (circle). The error bars represent the statistical errors and the caps show the systematic uncertainty. The data are compared with hydro + pQCD calculations assuming the initial gluon density dN^g/dy = 1000 (dashed line), 500 (dotted line), and 200 (dashed-dotted line). The solid line is pure hydrodynamical calculation. Figure is taken from [59].

high p_T parton [45, 55]. At sufficiently high transverse momentum, hadron yields are thought to contain a significant fraction of hadrons coming from the fragmentation of high energy partons produced in the initial hard scatterings. Calculations based on perturbative QCD (pQCD) predict that high energy partons traversing nuclear matter lose energy through induced gluon radiation [56, 57]. The energy loss is expected to depend strongly on the color charge density of the created system and the traversed path length of the propagating parton. In non-central heavy-ion collisions, the geometrical overlap region has an almond shape in the transverse plane. Depending on the azimuthal emission angle, So partons traversing in such a system will travel different path lengths depending on the azimuthal angle of emission. Therefore, they lose different energy. This mechanism of energy loss introduces an elliptic flow at high transverse momenta of hadrons [55, 57, 58].

The first quantitative theoretical predictions based on energy-loss calculations in a static medium is shown as the dashed lines in Figure 1.14 [58]. The theoretical predictions are compared with the STAR data points [59]. It is clear from

the picture that the predictions are not perfectly matching with the data points. This could be realized that in the p_T range of 2 - 6 GeV/c hadron yields might not dominantly originate from the fragmentation of high energy partons, but are produced by quark coalescence. Therefore, in order to compare the data to the predictions of parton energy loss, v_2 has to be measured above $p_T = 6$ GeV/c.

1.6 ρ^0 vector meson to study the medium created at RHIC

Resonances are strongly decaying particles having an extremely short lifetime. The lifetime of the resonance is of the order of 10^{-23} seconds. These are also known as the excited states of stable particles. Because of the short lifetime they can only travel about 10^{-15} meters before decaying. That is why it is very challenging to identify resonances produced in the collisions. These particles cannot be measured directly. Therefore, resonances are measured indirectly from their decayed daughters through the reconstruction of invariant mass.

- **In-medium Effects:**

  The in-medium effects related to the high density and/or high temperature of the medium can modify the properties of short-lived resonances, such as their masses, widths, and even their spectral shapes [75].

  One of the important approaches on this study of the hadrons in-medium effects was theoretically addressed by G.E. Brown and M. Rho in 1991, which is well known as Brown-Rho scaling [71]. Considering an effective Lagrangian, dictated by symmetries of QCD, at low energy and zero density, they studied how the theory evolves with the increase of density and/or temperature by embedding a hadron in a dense medium. They observed that the mass of the embedded hadron in the dense medium had been modified. Finally, they established the famous approximation in-medium scaling law:

$$m^*_\sigma/m_\sigma \sim m^*_N/m_N \sim m^*_\rho/m_\rho \sim m^*_\omega/m_\omega \tag{1.17}$$

where the masses with the asterisks stand for the values in the dense medium and the masses without asterisks are for free space values.

Ralf Rapp also started the work on thermal $\pi^+\pi^-$ emission spectra [72] from the late stages of the heavy-ion reactions at relativistic energies considering the hadronic in-medium effects. He started with the ρ propagator, D_ρ, at finite temperature. The ρ-propagator is given as:

$$D_\rho = \frac{1}{M^2 - (m^0_\rho)^2 - \sum_{\rho\pi\pi} - \sum_{\rho M} - \sum_{\rho B}} \tag{1.18}$$

The in-medium self-energy terms consist of three parts: (1) $\sum_{\rho\pi\pi}$ represents the free decay width into 2-pion states, (2) $\sum_{\rho M}$ describes resonance ρ-interaction with surrounding π, K and ρ mesons, (3) $\sum_{\rho B}$ accounts for the resonance ρ-interactions with surrounding nucleons, hyperons and baryon resonances. Finally, the in-medium ρ spectral function is given as:

$$\frac{dR_{\rho\to\pi\pi}}{dM} = \frac{6}{\pi}\frac{g^2_\rho}{6\pi}\frac{k^3}{M}F_{\rho\pi\pi}(k)^2 \times ImD_\rho(M;\mu_B,\,T)(\frac{MT}{2\pi})^{3/2}e^{-(M-\mu_\rho)/T} \tag{1.19}$$

Thus, the spectral function of the ρ resonance in a medium with finite density and finite temperature would have a peak at smaller mass and wider width than the spectral function of the ρ in a free space.

E. V. Shuryak and G. E. Brown have also studied the resonance in-medium effects in *t*-channel $\rho - \pi$ interactions[73]. The ρ can scatter with a pion in the medium to temporarily form a_1 resonance. After the a_1 resonance decays to a ρ and a π, the ρ properties might have been modified by this *t*-channel interactions. They predicted a downward mass shift for the ρ in the hot-dense medium.

Thus, a systematic measurement of various properties of resonances, such

as, their masses, widths and line shapes, in relativistic heavy-ion collisions will provide sufficient information regarding the in-medium effects of the hadrons.

- **Re-scattering and Re-generation effects:**
  ρ_0 vector meson, being a short-lived resonance, decays to $\pi^+\pi^-$ inside the medium created in the heavy-ion collisions. The decay pions go through multiple re-scattering in the hadron gas phase [74, 76, 77]. In order to understand the properties of matter formed in ultra-relativistic nucleus-nucleus collisions, it is important to understand the production and absorption processes of resonant states created in those collisions. In general, when a resonance decays before kinetic freeze-out, elastic interactions of the decay daughters with the medium particles will change the momenta of these particles. This is called re-scattering effect and this causes the loss of resonance signal. However, there is another competing scenario. That is the medium particles may interact among themselves and produce a part of the resonance signal. This effect is known as re-generation effect. Due to this effect there will be an enhancement in resonance signal. Figure 1.15 shows the schematic representation of the ρ^0 re-scattering and re-generation effects between chemical freeze-out (T_{ch}) and kinetic freeze-out (T_{fo}). The contribution of re-scattering and re-generation to the signal yields depends on the following factors:

  (1) Time span between chemical and kinetic freeze-out and lifetime of each resonance.

  (2) the interaction cross-section of the decay particles

  By studying the particle ratios , like ρ^0/π, and comparing with K^*/K, one can get the information about the re-scattering and re-generation effects, which are good probes to shed light on the evolution of the fireball between chemical freeze-out and kinetic freeze-out, and the time scale between the two freeze-outs.

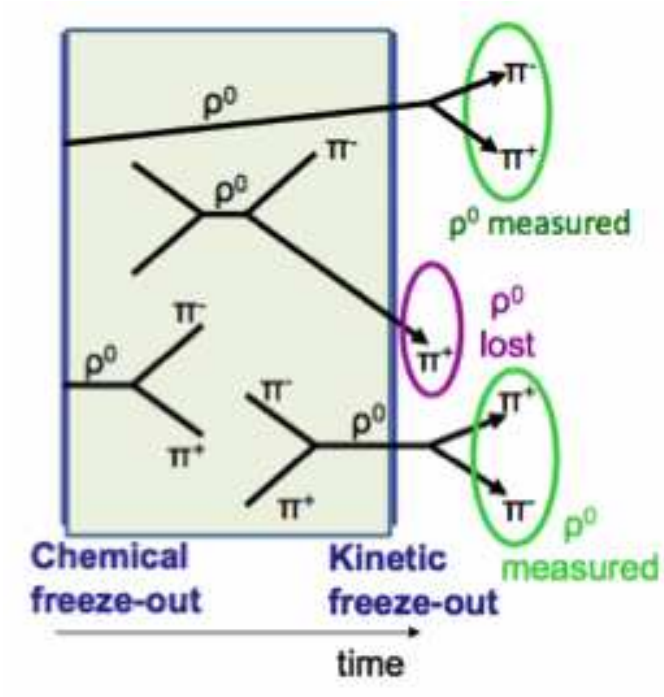

Figure 1.15: The re-scattering and re-generation effects on measured ρ^0 yields during the time between chemical and kinetic freeze-out times.

- **Collectivity:**

  The degree of collectivity of the medium created in the heavy-ion collisions can be proved by studying the elliptic flow (v_2) of ρ^o vector meson. The ρ^0 vector meson can be produced either in the de-confined phase or in the hadronic phase. If it is produced in the de-confined phase, the elliptic flow in the intermediate p_T region will scale with n_q=2. If ρ^0 vector meson is produced in the hadronic phase via $\pi^+\pi^-$ re-scattering, it will scale with n_q=4. The elliptic flow measurement of ρ^0 vector meson will certainly shed light on the medium produced in the heavy-ion collisions at RHIC.

1.7 Scope and Organisation of the thesis

The main focus of this thesis is to discuss how the resonance, in particular the ρ^0 vector meson, increases our understanding of the evolution of the fireball in heavy-ion collisions at RHIC energies.

The present thesis investigates the production of the ρ^0 vector meson through its hadronic decay mode ($\rho^0 \rightarrow \pi^+ + \pi^-$) at mid-rapidity in minimum bias p+p, d+Au, Cu+Cu and Au+Au collisions at $\sqrt{s_{NN}}$ = 200 GeV. It also addresses the measurement of ρ^0 elliptic flow in Au+Au collisions at $\sqrt{s_{NN}}$ = 200 GeV.

The analysis part of this thesis is mainly divided into two parts. In the first part, the ρ^0 production and possible in-medium modifications of its properties are discussed in minimum bias p+p, d+Au, Cu+Cu and Au+Au collisions. Although, the main objective of the thesis is to study ρ^0 production in Cu+Cu and Au+Au collision systems, we have tried to measure the same in p+p and d+Au as a baseline for the heavy-ion study in terms of number of participating nucleons. In particular, looking at the data in terms of N_{part} offers the possibility of studying system size dependence of various bulk properties and in particular, the ρ^0 mass vs. p_T, particle ratios, mean transverse momentum ($\langle p_T \rangle$), etc. This may help to disentangle the initial state versus final state interactions at RHIC. The second part of the thesis covers the elliptic flow measurement of the ρ^0 vector meson. This measurement is done by using the Au+Au collisions data at $\sqrt{s_{NN}}$ = 200 GeV taken during the year 2007 by the STAR experiment at RHIC. The motivation behind the ρ^0 elliptic flow measurement is to understand the ρ^0 production mechanism in such heavy-ion collisions.

The organization of the thesis is as follows: The RHIC complex and the STAR detector systems are presented briefly in Chapter 2. Since, the main sub-detector system used in the analysis is the STAR Time Projection Chamber (TPC), it has been discussed in detail. As I have mentioned, the analysis part of the thesis is basically divided into two parts. Chapter 3 deals with the first part which includes the methods and analysis techniques used for the ρ^0 production along with a detailed description of the data set used for the study. In Chapter 4, the second part of the analysis is mentioned which deals with the data set and various methods used for the ρ^0 elliptic flow measurement. Results of the presented analysis which includes both the parts are described in Chapter 5 and this is followed by the physics discussion based on the results obtained in this study.

Chapter 2

The Experimental Facilities

2.1 The Relativistic Heavy-Ion Collider

The Relativistic Heavy Ion Collider (RHIC) at Brookhaven National Laboratory (BNL) is the first collider to accelerate two counter-rotating heavy ion beams and is capable of accelerating any combination of ion species, such as p+p, d+Au, Cu+Cu, Au+Au and so on, with varying center-of-mass energy per nucleon-nucleon pair. Each ion can be accelerated to 99.995% of the speed of light. In addition to the heavy-ion programs, there is also an active spin physics program at RHIC, which aims at studying the spin structure of nucleon. Therefore, RHIC is designed to run polarized proton-proton collisions as a part of the spin physics program.

The various facilities required to produce collisions of heavy-ions at top RHIC energy of $\sqrt{s_{NN}}$ = 200 GeV are briefly described in this chapter and are outlined schematically in Figure 2.1 [81, 82].

- **Tandem Van de Graaff:**
  The Tandem uses static electricity to accelerate atoms removing some of their electrons, which are in a cloud around the nucleus. What remains is a charged atom called an ion. A partial lack of electrons gives each ion a strong positive charge. The Tandem gives billions of these ions a boost of

energy, sending them on their way towards the Booster.

- **Tandem-to-Booster line (TTB):**
  At the exit of the Tandem, the bunches of ions enter the Tandem-to-Booster beam line, which carries them through a vacuum via magnetic field to the Booster. At this point they are traveling at about 5% of the speed of light.

- **Linear Accelerator (Linac):**
  In addition to heavy-ions, experiments at RHIC use colliding beams of protons. For this, energetic protons are supplied by the 200 MeV Linac. Protons from the Linac are transferred to the Booster.

- **Booster Synchrotron:**
  The Booster synchrotron is a powerful circular accelerator that provides the ions more energy by having them surf ride on the downhill slope of radio frequency electromagnetic waves. The ions are propelled forward at higher and higher speeds and getting closer and closer to the speed of light. The Booster then feeds the beam into the Alternating Gradient Synchrotron.

- **Alternating Gradient Synchrotron (AGS):**
  As ions enter the Alternating Gradient Synchrotron (AGS) from the Booster, they are traveling at about 37% of the speed of light. As they whirl around the AGS and are accelerated in the Booster, the ions get even more energy and are traveling at 99.7% of the speed of light.

- **AGS-to-RHIC Line:**
  When the ion beam is traveling at top speed in AGS, it is taken down to another beam line called the AGS-to-RHIC (ATR) transfer line. At the end of this line, a switching magnet sends the ion bunches down to one of the two beam lines. Bunches are directed either left to the clockwise RHIC ring or right to travel counter-clockwise in the second RHIC ring.

- **RHIC Rings:**
  The Relativistic Heavy Ion Collider consists of two independent rings of

superconducting magnets which bend and focus the ion beams. The rings are approximately circular in shape (3.8 km circumference), are positioned in the same horizontal plane and intersect at six points which allows six interaction points for particle collisions. Each of the rings consists of six arc sections and six straight insertion sections. The beam pipe runs through the centre of the magnets which are kept cooled at $T < 4.6^0$ K. The RHIC rings have dual functions. They operate as accelerator ring and storage ring once the beams reach full colliding energy. One bunch of ions at a time is filled into the RHIC ring from AGS. The nominal configuration of 56 bunches in the 360 radio frequency (RF) buckets per ring is achieved through 14 AGS cycles. The ions are accelerated to the top energy of 100 GeV/A in a period of approximately 2 minutes by the acceleration RF-system. Once the top energy is reached, the storage RF-system (which has a higher frequency than the acceleration RF-system for limiting the growth of bunch length from intra-beam scattering) maintains cycles at the top energy. Once the required energy is achieved, oppositely rotating beams are collided at the interaction points.

RHIC has six interaction points, out of which four are occupied. BRAHMS, STAR, PHENIX and PHOBOS experiments are located at 2 o'clock, 6 o'clock, 8 o'clock and 10 o'clock, respectively.

2.2 The STAR Detector

The Solenoidal Tracker at RHIC (STAR) [84] is one of the four detector systems at RHIC. It was constructed to investigate the behavior of strongly interacting matter at high energy density through the simultaneous measurement of multiple observables. In order to achieve these goals, STAR was constructed to measure hadron production over a large acceptance.

The layout of the STAR detector is shown in Figure 2.2. A cross sectional view of the STAR detector as configured for the RHIC 2001 run is displayed in Figure

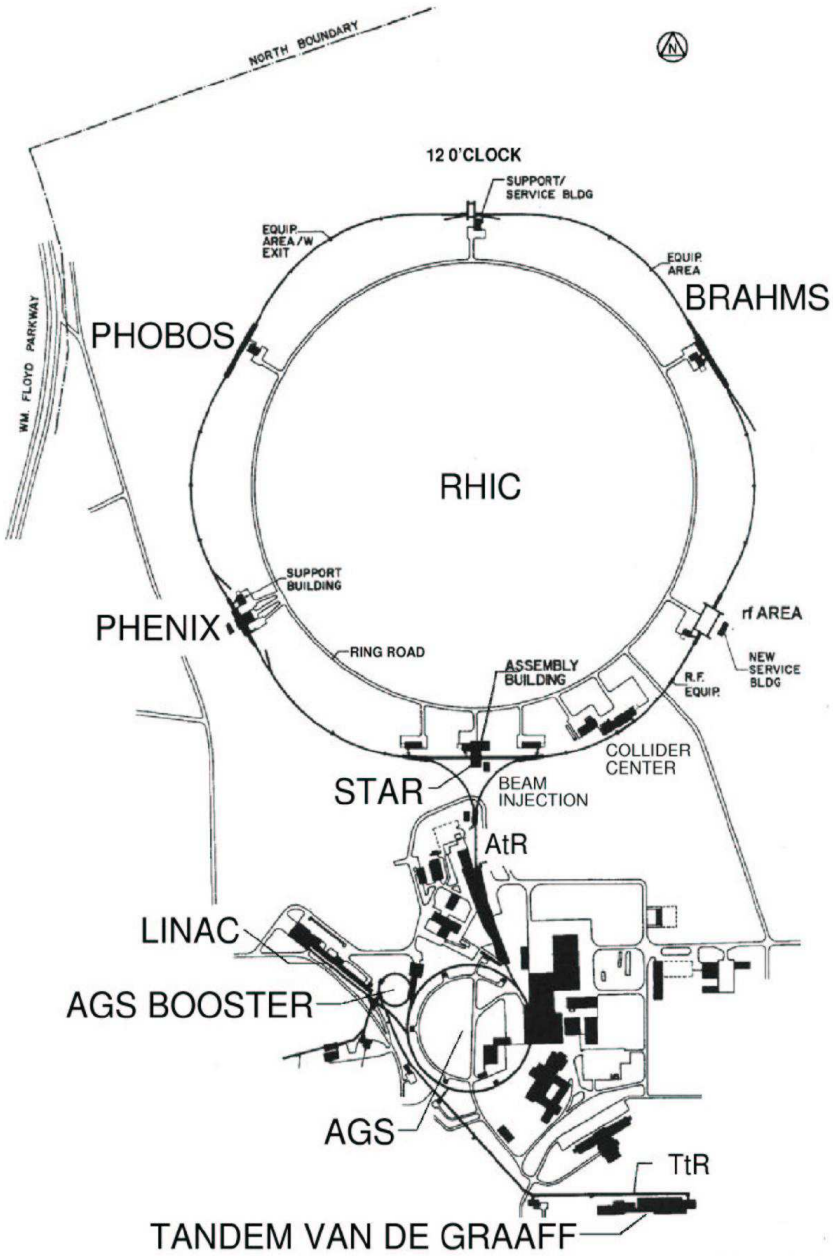

Figure 2.1: A schematic view of the collider complex at BNL, USA [83].

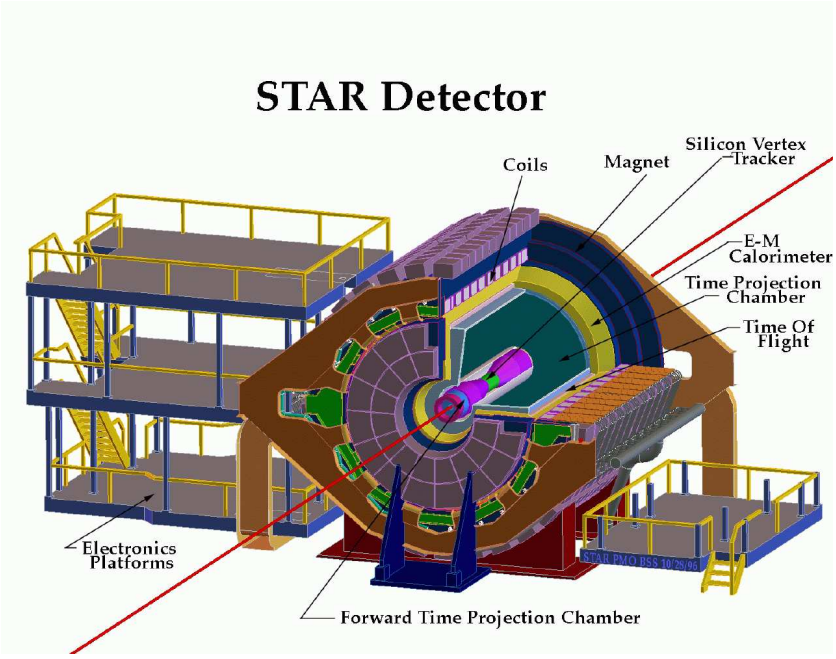

Figure 2.2: A perspective view of the STAR detector with a cutaway for viewing inner detector systems.

2.3.

The STAR detector system is enclosed inside a solenoidal magnet, maintained at room temperature. The solenoidal magnet produces a uniform magnetic field of maximum value 0.5 T [85]. The detector consists of various detector sub-systems for high precision tracking, good momentum resolution, and good particle identification at mid-rapidity. There are also few sub-detector systems at forward rapidity region. The various sub-detectors are discussed briefly in this section.

2.2.1 The Time Projection Chamber (TPC)

The Time Projection Chamber (TPC) [86] is the primary tracking as well as particle identification detector at mid-rapidity. This is a large volume gas detector. It covers the pseudo-rapidity from -1.8 to +1.8 with full azimuthal coverage. The STAR TPC is shown schematically in Figure 2.4. It is a 4 meter long cylinder surrounding the beam pipe with inner radius 50 cm and outer radius 200 cm. It

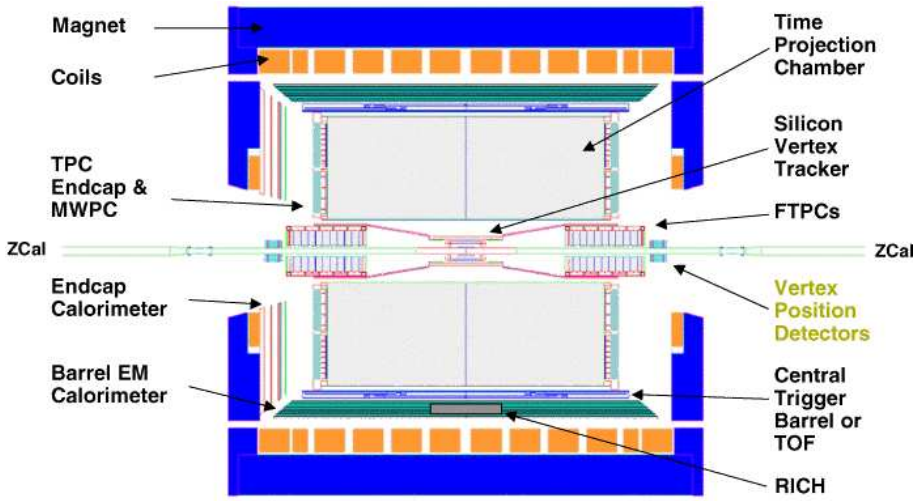

Figure 2.3: Cross-sectional view of the STAR detector.

is filled with P10 gas (10% methane and 90% argon), regulated at 2 mbar above atmospheric pressure [86]. It is surrounded by a magnet that produces a uniform magnetic field of 0, ± 0.25 or ± 0.5 Tesla in the z-direction depending on the physics goal. It is divided into two halves by a thin central membrane which provides the high voltage (28 kV) to maintain a uniform electric field of $\sim$ 135 V/cm between the membrane and the read-out endcaps placed at both the ends of the TPC. The read-out endcaps are maintained at ground potential. When a charged particle enters through the TPC, it ionizes the gas. There will be primary as well as secondary ionization. The electrons, released in the secondary ionization, drift in the direction of the electric field to the read-out endcaps located at each end of the TPC. The maximum drift length for an electron is half of the entire TPC length.

The central membrane, acting like a cathode, consists of 70 μm thick carbon-loaded Kapton film. The membrane is secured under tension to an outer support hoop which is mounted inside the outer field cage cylinder. It has also 36 aluminium strips attached to each side which are used as targets for the TPC laser calibration system.

The TPC endcap read-out planes are multi-wire proportional counter (MWPC) with pad read-out and are positioned on the support wheels. Each MWPC cham-

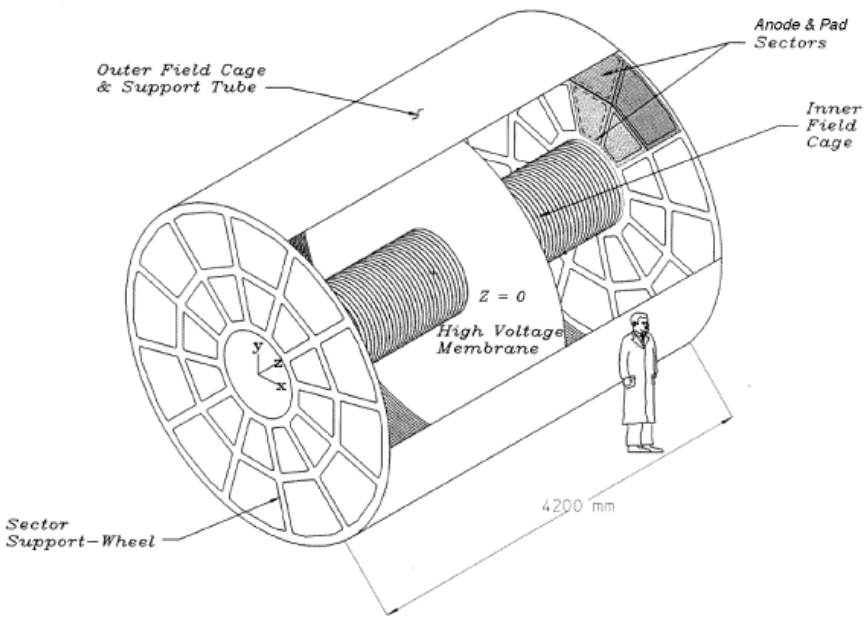

Figure 2.4: The STAR Time Projection Chamber (TPC).

bers consists of three wire planes and a pad plane. For each endcap, there are 12 read-out sectors which are positioned radially with respect to the hole defined by the inner field cage with 3 mm gap between each sector. One full sector of the anode pad is shown in Figure 2.5.

The outer sub-sectors have continuous pad coverage with no spaces between the pad rows to optimise dE/dx resolution by maximizing the measurement of the ionization electrons. The inner sub-sectors are in the high track density region. So they are optimized for two hit resolution by reducing the size of the pads. The space available for front end electronics limits the number of possible pad rows on the inner sub-sectors. Therefore, maximum 45 times a TPC track can be sampled if it crosses all 45 pad rows.

Charged particles traversing the TPC follow a curved trajectory in the $(x - y)$ plane due to the presence of magnetic field and subsequently leave a trail of ionized atoms in the active volume. Under the influence of the electric field, the liberated electron clouds drift with an average velocity 5.45 cm/μs towards the read-out plane which is divided into 24 sectors, 12 at each end of the read out

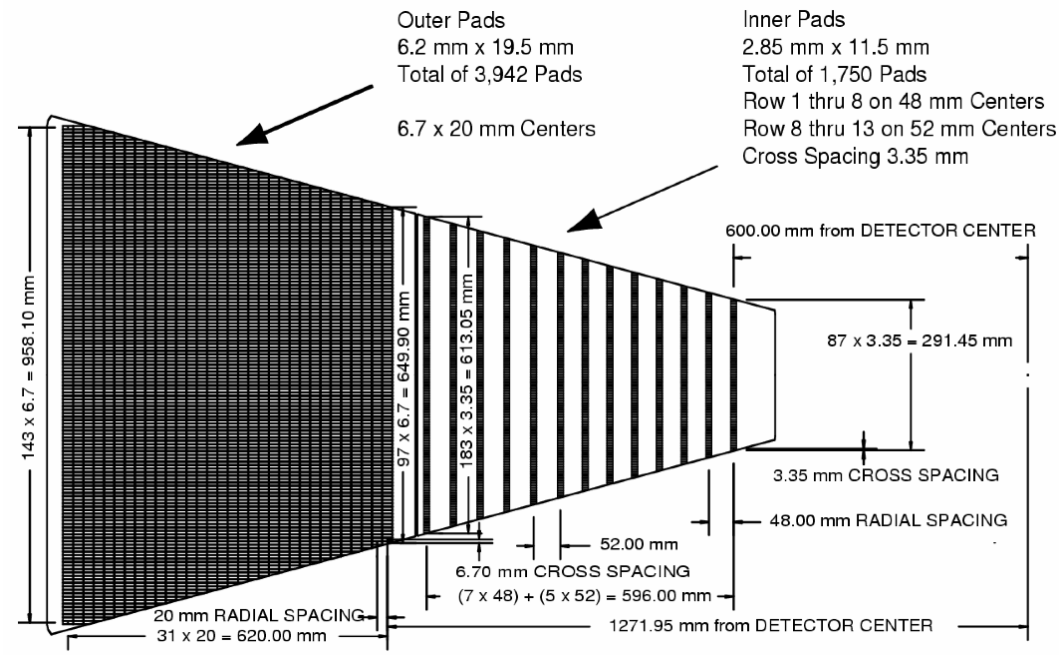

Figure 2.5: The anode pad plane of one full sector. The inner sector is on the right and it has small pads arranged in widely spaced rows. The outer sector is on the left and it is densely packed with larger pads.

plane, while positive ions drift towards the membrane. The maximum drift time is $\sim 40\ \mu s$. At the read-out plane, the electrons encounter a gating grid. Depending on the trigger, the gating grid will either allow the electrons to pass through or stop. After this the electrons will pass through a shielding grid which marks the start of the proportional region. The inner and the outer sectors in this region contain anode grids maintained at 1.1 kV and 1.39 kV, respectively, which serve to amplify the drift electrons by accelerating them and creating an avalanche of electrons via secondary ionization. The number of avalanche electrons is proportional to the number of drift electrons where the ratio is referred to as the gain, and for inner and outer sectors this is approximately 3770 and 1230, respectively [86].

The positive ions created in this process induce an image charge on cathode pads. The charge is digitized to give an ADC value for every pad. The dimensions of the rectangular pads are optimized to give the best position resolution perpendicular to the stiff tracks. The width of the pad along the wire direction is

chosen such that the induced charge from an avalanche point on the wire shares most of it's signal with only 3 pads. This is to say that the optimum pad width is set by the distance from the anode wire to the pad plane. Concentrating the avalanche signal to 3 pads gives the best centroid reconstruction using either a 3-point gaussian fit or a weighted mean. Accuracy of the centroid determination depends on signal-to-noise ratio and track angle, but it is typically better than 20% of the narrow pad dimension. The x and y positions of the cluster are determined by the radial distance of the pad row and the centroid from the Gaussian fit. For triggered collisions, each pad is read 512 times which leads to a time interval of 100 ns. As the signal from a drifting electron will often cover several time intervals due to diffusion, a weighted average is taken, and the extracted mean is used to determine the z position of the electron. The recorded x, y and z values are assigned to the hit position. The hit position is not quite the true position of the particle. The position is getting distorted due to the motion of the drifting electron and also due to the non-uniformities in the electric and magnetic field [88]. This hit position needs to be corrected before the track reconstruction takes place.

- Field misalignment : There is a small, but finite $\left(\vec{E} \times \vec{B}\right)$ term, and the TPC z direction is not exactly parallel to both the $\vec{E}$ and $\vec{B}$ fields [86, 89].
- Space charge distortion: The liberated ions can perturb the $\vec{E}$ and $\vec{B}$ fields in the drift volume [86, 87, 89].
- Grid leak: A thin sheet of avalanche electrons enter the drift volume from a region between the inner and outer sectors which again bias the E and B fields [86, 89].

All the three items mentioned above are corrected for by mapping the fields with further measurements and applying the necessary corrections to the trajectories of drift electrons. Another process which can affect the motion of the drift electrons is natural diffusion due to the interactions with the gas. However, as this is a random process, no systematic correction can be applied.

2.2.1.1 The TPC Track Reconstruction

During the track reconstruction, hits are connected to reconstruct the 3D trajectory of the charged tracks. The maximum number of TPC hits in a track can have 45 as this corresponds to the number of pad rows. Tracking starts at the outermost pad row where the hit density is lowest. Firstly, a set of 3 hits, close in space, selected and fitted with a straight line. Then the inward extrapolation is being used to find additional hits. If additional hits are found, a helix is formed with all the connected hits. Collectively, this is known as a segment. The hits associated with the segment are then removed from the hit pool, and the process is repeated until all possible segments are exhausted. Starting with the largest segments, the helix is projected inwards and outwards in order to find additional hits which were not removed from the pool previously. Segments are then merged, if they result from the splitting of a track. After this, the segments are simply known as tracks. The curvature of the track is used to determine the transverse momentum of the track using the expression:

$$p_T = 0.3BRq(GeV/c) \tag{2.1}$$

where B is the magnetic field, R is the radius of the curvature and q is the charge of the track (units of electron charge). Using the track azimuthal and dip angles (i.e. the angle between the particle momentum and the drift direction, $\theta = \cos^{-1}(p_z/p)$), all three momentum components can be found out. The finite spatial resolution and track length lead to a finite momentum resolution. In order to provide a better estimate of track momentum, a Kalman Filter is used to fit the hits in a uniform magnetic field to form a global track. Once all the global tracks in an event are reconstructed, the trajectories of selected global tracks are extrapolated to the beam axis at $x = y = 0$ and thus, the z-position of the primary collision vertex of this event is found out. Then the global tracks with a 3-dimensional distance of closest approach (DCA) to the primary vertex less than 3 cm are chosen for a re-fit by forcing a new track helix ending at the primary

vertex. These newly reconstructed helix is called primary tracks.

2.2.2 Particle Identification (PID)

Charged particles passing through the TPC will lose energy via ionization energy loss. The total ionized charges collected from each hit of a track are proportional to the energy loss of the particle. For a particle with charge z (in the units of e) and speed $\beta = v/c$ passing through a medium with density ρ, the mean energy loss it suffers can be described by the Bethe-Bloch formula

$$\left\langle \frac{dE}{dx} \right\rangle = 2\pi N_0 r_e^2 m_e c^2 \rho \frac{Zz^2}{A\beta^2} \left[ln \frac{2m_e \gamma^2 v^2 E_M}{I^2} - 2\beta^2 \right] \tag{2.2}$$

where N_0 is Avogadro's number, m_e is the electron mass, r_e is the classical electron radius, c is the speed of light, Z is the atomic number of the absorbing material, A is the atomic weight of the absorbing material, $\gamma = 1/\sqrt{(1-\beta^2)}$, I is the mean excitation energy, and $E_M (= 2m_e c^2 \beta^2/(1-\beta^2))$ is the maximum transferable energy in a single collision [90].

From the above equation, we can see that different charged particles (electron, muon, pion, kaon, proton and deuteron) with the same momentum p passing through the TPC gas can cause different amount of mean energy loss. Figure 2.6 shows the energy loss (dE/dx) as a function of momentum (p) for different charged particles.

It is clear from Figure 2.6 that different charged particles have their own dE/dx vs. momentum band. That is why the energy loss of a charged particles is used to identify different particles, like π, K and p. Pions and Kaons are identified up to the momentum 0.75 GeV/c and protons and anti-protons up to 1.1 GeV/c. A dE/dx resolution of $\sim 8\%$ can be achieved by requiring the tracks of charged particles to have at least 20 out of a maximum of 45 hits in the TPC [91].

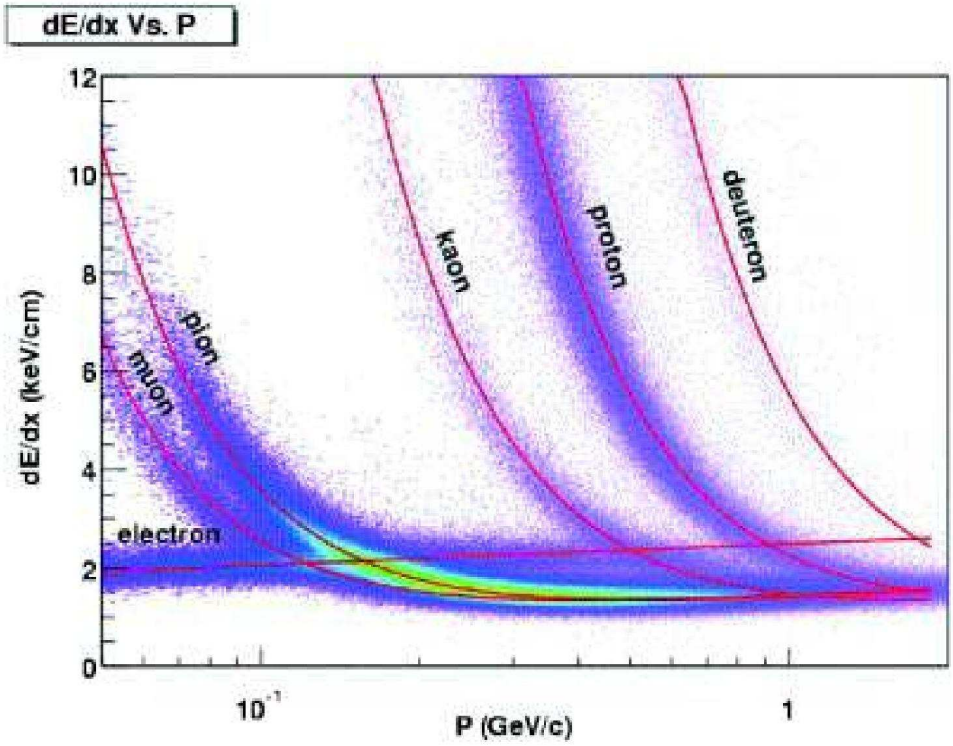

Figure 2.6: Ionization energy loss as a function of momentum for positively charged particles in TPC. The solid lines superimposed on the scattered points are the Bethe-Bloch function shown in equation 2.1 for different particle species.

2.2.3 Time-Of-Flight Detector

The STAR Time-Of-Flight (TOF) is a Multigap Resistive Plate Chamber (MRPC). It is located between TPC and Barrel Electromagnetic Calorimeter (BEMC). It covers $|\eta| < 1$ with 100% azimuthal coverage. The intrinsic time resolution is less than 100 ps and the detection efficiency of charged particles is more than 95% with $p_T > 0.5$ GeV/c. It identifies π, K and p up to the momentum ~1.8 GeV/c and can separate p from π and K up to momentum ~3 GeV/c [91]. It also identifies electron above the transverse momentum (p_T) 0.2 GeV/c.

The trigger system of the TOF detector is the two upgraded pseudo Vertex Position Detectors (upVPD), each staying 5.7 m away from the TPC centre along the beam. The upVPD provides the starting time information for the TOF detector and pseudo vertex position in the beam direction of each event. The TOF hit provides the stop time of each particle. The difference of this two is the time of

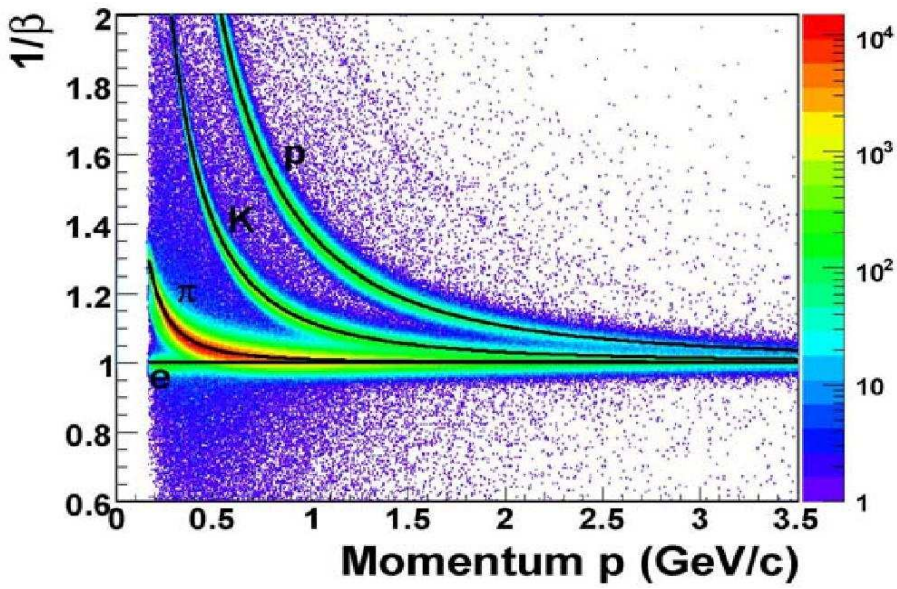

Figure 2.7: $1/\beta$ vs. momentum (p) in p+p collisions at $\sqrt{s}$ = 200 GeV from Run IX.

flight of the associated track corresponding to a particle. The velocity of the track is found from the momentum and mass of the track. In Figure 2.7, the hadron identification capability of TOF system in Run IX is shown for p+p collisions at $\sqrt{s}$ = 200 GeV.

2.2.4 Silicon Vertex Tracker

The Silicon Vertex Tracker (SVT) is placed around the interaction region [92]. The main objective of this detector is to improve the resolution of primary vertex, reconstruct secondary vertex and improve the low-momentum tracking capabilities. It is a barrel micro-vertex detector based upon silicon drift detector technology. It enables the reconstruction of very short-lived particles (primarily the strange as well as multi-strange baryons and D-mesons) through secondary vertex close to the interaction point. The SVT expands the kinematical acceptance by using independent tracking to very low momentum particles those do not reach the active volume of TPC because of the magnetic field. In addition to the position resolution, the detector also provides an energy measurement on the basis

of the charged particle energy loss (dE/dx) in each layer. Position resolution of 20 μm as well as energy loss (dE/dx) measurement with a resolution of about 7$\%$ are achieved with the STAR-SVT.

2.2.5 Silicon Strip Detector

The STAR Silicon Strip Detector (SSD) is placed in between the SVT and the TPC [93]. It is a cylindrical structure with a radius 230 mm. and covers a pseudo-rapidity range of $|\eta| < 1.2$ with 100 $\%$ azimuthal coverage. It has a total silicon surface area of $\sim$1 m^2. This detector enhances the tracking capabilities of STAR by providing two-dimensional hit position and energy loss measurement for charged particles. It improves the extrapolation of TPC tracks through SVT hits, increasing the average number of space points measured near the collision point. This ensures better detection efficiency for long-lived meta-stable particles, like Λ hyperon.

2.2.6 Barrel Electro-Magnetic Calorimeter

The STAR Barrel Electro-Magnetic Calorimeter (BEMC) is positioned inside the aluminium coil of the STAR solenoid and spans a pseudo-rapidity range -1$< \eta <$+1 with full azimuthal coverage. It has the same acceptance as the TPC. This is shown schematically in Figure 2.8. The front face of the calorimeter is at a radius of $\approx$ 220 cm from nominal vertex and parallel to the beam axis.

The BEMC allows the STAR experiment to trigger on and study rare high p_T processes such as jets, direct photons and heavy quark. It provides large acceptance for photons, electrons, π^0, and η mesons in all collision systems spanning from polarized p+p to Au+Au collisions [94]. The BEMC design includes 120 calorimeter modules and is segmented into a total of 4800 towers. Each of the towers is projective and pointing back to the centre of the interaction point. Each of the module consists of a lead-scintillator stack and a set of Shower Maximum Detector (SMD), situated approximately 5.6 radiation length (X_0) away

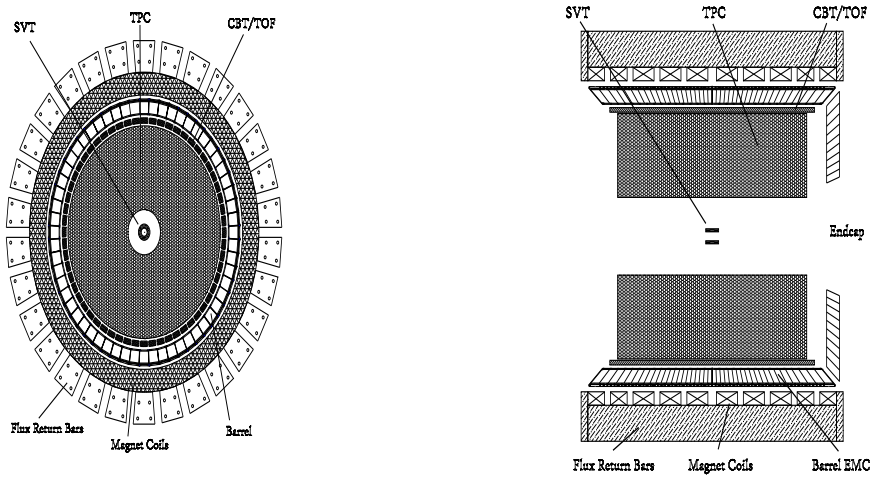

(a) X-Y view (b) Y-Z view

Figure 2.8: STAR Barrel Electromagnetic Calorimeter.

from the front of the stack. The SMD is used to provide fine spatial resolution in the calorimeter. The high spatial resolution provides by the SMD is essential for direct γ, electron identification and π^0 reconstruction.

2.2.7 Endcap Electromagnetic Calorimeter

The Endcap Electro-magnetic Calorimeter (EEMC) is situated in the west pole-tip of the STAR detector. It has a pseudo-rapidity coverage of $1 < \eta < 2$ over full azimuthal range, supporting the barrel EMC (BEMC). It is capable of detecting photons and electromagnetically decaying mesons (π^0, η). It also identifies electrons and positrons and acts to trigger on high energy particles [95]. The triggering capabilities and its coverage are crucial for the spin physics program in polarized p+p collisions. It includes a scintillating-strip Shower Maximum Detector (SMD) to provide fine granularity. This helps to distinguish the transverse shower characteristic of a photon and π^0. It is also useful to discriminate between electron and hadron by correlating with TPC tracks.

2.2.8 Forward Time Projection Chambers (FTPC)

The Forward Time Projection Chambers (FTPC) were constructed to extend the acceptance of the STAR experiment [96]. They cover the pseudo-rapidity range of $2.5 < |\eta| < 4.0$ on both sides of the TPC. The increased acceptance improves the event characterization and allows the study of asymmetric systems. The full two-component system measures the momenta and production rates of charged particles. Each of the units is a 120 cm cylindrical structure, 75 cm in diameter with a radial drift field. It has read-out chambers located in five rings on the outer cylindrical surface. This radial configuration improves the two track separation in the highest particle density region (close to the beam pipe). The Front End Electronics (FEE) boards are mounted on the back of the read-out chambers. The ionization electrons drift to the anode sense wires. The induced signals on the adjacent cathode surface are read-out by 9600 pads. The low electron diffusion and the radial drift principle results in the required 2-track separation of about 1 mm. The two FTPC's have 19200 channels of electronics, capable of measuring the charge drifting to read-out chambers in short time. A schematic diagram of STAR FTPC is shown in Figure 2.9.

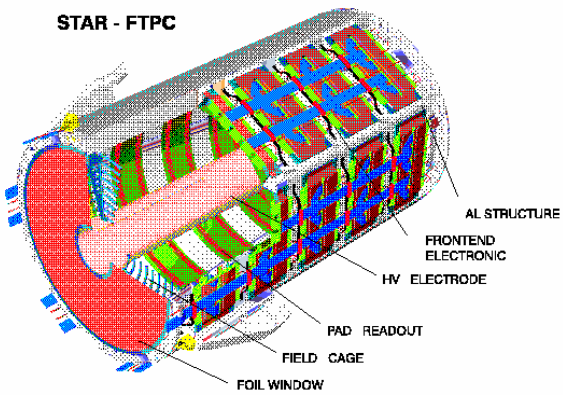

Figure 2.9: Schematic diagram of a FTPC for the STAR experiment.

The FTPC uses a mixture of Ar and CO_2 with a ratio of 50%:50% by volume. The track points are calculated from the charge distribution measured by read-out electronics. These track points are grouped to tracks which together with mag-

netic field maps, can be used to get the particle momenta. Due to the high multiplicity, in a central Au+Au event, the event-by-event observables like $< p_T >$ and fluctuations of charged particle multiplicity can be studied.

2.2.9 Photon Multiplicity Detector

The Photon Multiplicity Detector (PMD) is installed in the forward region to measure photon multiplicity produced in the heavy-ion collisions. The inclusion of the PMD enhances the phase space coverage of STAR for photons considerably, in pseudo-rapidity range of $-3.7 \leq \eta \leq -2.4$ with full azimuthal acceptance [97]. The detector is based on a proportional counter design using $Ar + CO_2$ gas mixture (70% Ar and 30% Co_2 by volume). It measures the spatial distribution and multiplicity of photons on an event-by-event basis. This can probe critical phenomena near the phase boundary, leading to fluctuation in global observables like multiplicity and pseudo-rapidity distributions.

2.3 The STAR Trigger

There are four primary trigger detectors in the STAR experiment: the Zero Degree Calorimeters (ZDCs), the Central Trigger Barrel (CTB), the Electromagnetic Calorimeter (EMC) and a Beam-Beam Counter (BBC). The purpose of the STAR trigger is to instruct the slower detectors on when to record data. The trigger can be used to select central ion-ion collisions, events with high energy particles with EMC data, or ultra peripheral collisions which involve photon exchanges that excite the nuclei and produce only a few particles. The most commonly used configuration is the minimum bias trigger which selects hadronic events with a range of centralities without any deliberate preference. This configuration was used for Cu+Cu at $\sqrt{s_{NN}}$ = 200 GeV events in this analysis. The two ZDCs are positioned at ± 18.25 meters along the beam axis relative to $z = 0$. Their purpose is to determine the energy of the spectator neutrons resulting from a heavy-ion collision. For a minimum bias trigger, a coincidence between the two ZDCs is

required with a summed signal greater than $\sim 40\%$ of a single neutron signal. Because of the required coincidence, the timing difference allows for an event's z-position to be determined online. An online z-vertex cut is often placed to ensure triggered events roughly occur in the middle of the TPC ($z = 0$) where typical detector acceptance is most favorable. The CTB which encircles the TPC has an acceptance of $|\eta| < 1$ and consists of an array of 240 scintillator slats. The signal of each slat is approximately proportional to the number of charged particles that have traversed through it. The centrality of an event is determined online taking the signal from CTB and ZDC. Figure 2.10 shows the correlation between the ZDC and CTB signals.

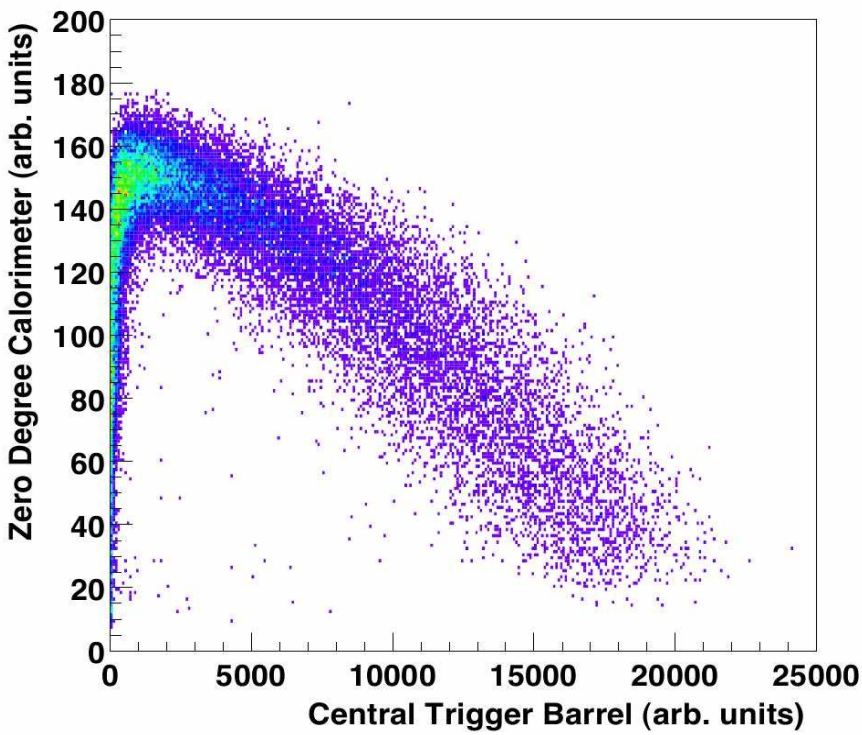

Figure 2.10: Correlation between the summed pulse hight of ZDC and CTB.

Peripheral events (large impact parameters) typically correspond to a high ZDC sum and a low CTB sum. This is simply because the number of spectator neutrons is large, and the number of charged particles produced is small. Conversely, central collisions will have high CTB sum and a low ZDC sum because of high number of charged particles produced, and a low number of spectator

neutrons involved. This allows the trigger to be configured in order to select the centrality. The Electromagnetic Calorimeter (EMC) can be used to select events with rare probes such as high energy γ and π^0 particles or electrons from J/Ψ and Υ decay.

The algorithm which instructs the slow detectors to record data consists of four levels of different timing constraints. The configuration of all four levels depends on the trigger requirements. Level 0 receives information from ZDCs, CTB and EMC for every bunch crossing, thus has a timing constraint of ~ 106 ns (for 120 bunches). The ZDC sum, CTB sum, and the z-position are available at this level as well as EMC information on high energy hits. If interaction passes the event selection, a trigger is issued to the slow detectors. Level 1 and Level 2 will then carry out further processing and work with the larger time constraints of 100 μs and 5 ms, respectively. Full EMC information is available at Level 2. For a minimum bias trigger, both levels are not required for further event selections. Beyond Level 2, the data acquisition (DAQ) system is responsible for the collection of data from all detectors. Before this is transfered to a hard disk and/or data tape, Level 3 can then be used for further event selection with information from all the available STAR detectors. It is also used to create an online event display as shown in Figure 2.11.

2.3.1 The STAR DAQ

The design and implementation of the STAR Data Acquisition System (DAQ) [98] was driven by the characteristics of STAR's main detectors, i.e. TPC, FTPC and SVT. If all channels in every detector is read-out, then the event size of one event becomes 200 MB. The data are produced at 100 Hz. This implies that the data are produced 20,000 MB per sec. The main task of the STAR DAQ system is to read 20,000 MB data in one second and to store in the RHIC facility.

The large input data rate to the DAQ system demands parallel processing at the DAQ front end. Multiple Receiver Boards receive data in parallel through separate optical fibers from the detectors. The Receiver Boards are grouped to-

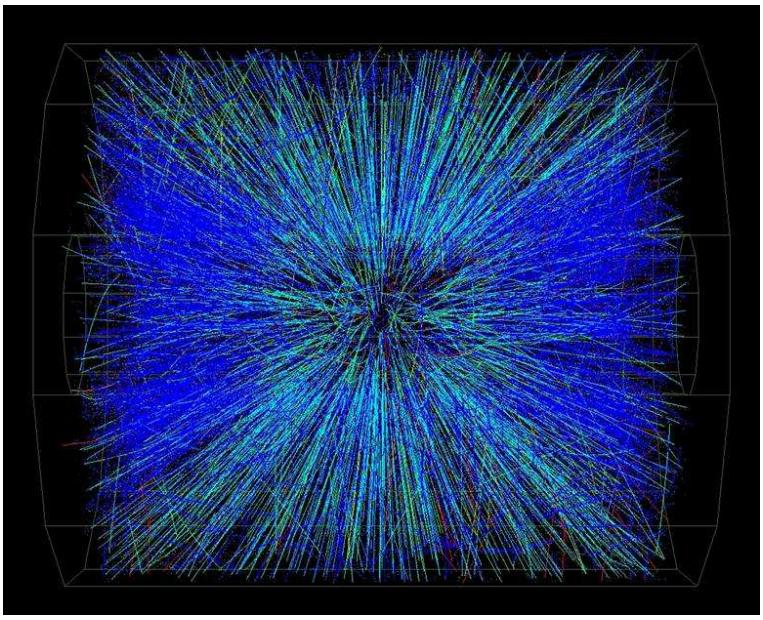

Figure 2.11: An online display of one central Au+Au collision event recorded in the STAR Time Projection Chamber.

gether in VME crates. Each crate is controlled by a Detector Broker CPU, called DET. There are 12 DETs for TPC, two for SVT, two for FTPC, and one for each additional detectors. Two strategies are used to reduce the data volume. Firstly, the channels with zero values are removed from the data stream to reduce the data volume drastically. This is called zero-suppression and the event size after the zero-suppression comes down to 10MB approximately. Secondly, a physics-based filter, known as Level 3 (L3) Trigger, is applied to choose the events to write to the tape. The L3 must find on the order of 1500 tracks in the TPC and make trigger decisions based on that within 200 ms. This limits the time available for DAQ front-end processing, and creates the need for a farm of $\sim$50 CPUs integrated within DAQ dedicated to tracking. The delay between receiving the event and the build/reject decision from the L3 trigger makes it necessary for the system to manage multiple events at the same time.

Event Building is performed on a Sun Solaris 450 workstation which is called Buffer Box (BB). It has 140GB of buffer disk for use when the RHIC HPSS system becomes temporarily unavailable. The BB also writes summary data to the tag database, which contains a short descriptor record for each event as well as

summary information for each run and for each data file.

2.4 STAR Computing Facilities

Computational facilities are an integral part of the high energy physics experiments. The huge data volume (of the order of many TB) recorded by the experiments needs enough computing facility to do the reconstruction and to write the reconstructed output in an user friendly format for further analysis. The need for first access to these data volumes for data analysis has helped to drive the high performance computing in terms of more robust storage and disk access technology in hardware and software. Without robust storage and computing capacity for parallel data processing, analysis of data from heavy-ion experiments in any reasonable time-frame would be impossible.

During a run period, the data captured by RHIC experiments will be directly transferred to RHIC computing facility (RCF) at BNL for storage, processing and further analysis. RCF is a distributed and centralized facility for all its users. Another computing facility in data reconstruction, storage and processing for STAR experiment is the NERSC at Lawrence Berkeley National Laboratory (LBNL), USA.

Chapter 3

ρ^0 Production in Cu+Cu and Au+Au Collisions at $\sqrt{s_{NN}}$ = 200 GeV

The ρ^0 is a resonance with a large width. Because of its large width, i.e. 150 MeV, the life time is very small and approximately 1.3 fm/c. This life time is smaller than the life time of a fire ball formed in the heavy-ion collisions. That is why the ρ^0 decays to pions inside the fire ball. These decay daughter pions suffer scattering with other particles inside the fireball. And there is also a finite probability that a ρ^0 is produced from two pions during the evolution of the fireball. Apart from this, it has also been predicted that there is an in-medium modification of the properties of ρ^0 vector meson such as mass and/or width of ρ^0 [99–104].

In this chapter, the detailed analysis method, i.e. trigger selection, event selection, track selection, invariant mass reconstruction, background subtraction etc., used to extract various parameters of ρ^0 vector meson in Cu+Cu and Au+Au collisions at $\sqrt{s_{NN}}$ = 200 GeV using the STAR experiment at RHIC are described. Although, the main focus of this chapter is the ρ^0 production in heavy-ion collisions, as a baseline we have studied the production in minimum bias p+p and d+Au collisions and compared with the results obtained in heavy ion collisions. The measurement of the ρ^0 vector meson in p+p, d+Au and in heavy-ion collisions, such as Cu+Cu and Au+Au interactions, at the same nucleon-nucleon c.m. system energy can provide insight for the understanding of the dynamics of these

systems.

3.1 Trigger for Data

The data set used in the present analysis is from Au+Au and Cu+Cu collisions at $\sqrt{s_{NN}}$ = 200 GeV. The data were taken from the 2004 Au+Au Run IV and 2005 Cu+Cu RunV at RHIC using the STAR detector [84]. Minimum Bias (MB) data were used for both Au+Au and Cu+Cu systems. The MB trigger, requiring coincidences between the two Zero Degree Calorimeters (ZDC) located in the beam direction at $\theta < 2$ mrad, was used in the data selection. In both Au+Au and Cu+Cu collisions, a minimum bias trigger was defined using coincidences between two ZDCs that measured the spectator neutrons. The MB events were chosen according to the raw charged track multiplicity within a pseudo-rapidity window $|\eta| < 0.5$, corresponding to 0-80% of the total measured cross section.

3.2 Event Selection

In order to achieve uniform acceptance in the pseudo-rapidity range, the collision vertex was required to be within ± 30 cm along the beam line. Figure 3.1 (a) and (b) show the z-vertex distribution of Cu+Cu and Au+Au collisions, respectively.

The collision centrality is defined in accordance with the fraction of the charged particle reference multiplicity distribution within the pseudo-rapidity window $|\eta| < 0.5$ for all events. Figure 3.2 (a) represents the charged particles reference multiplicity distribution in Cu+Cu collisions at $\sqrt{s_{NN}}$ = 200 GeV, whereas Figure 3.2 (b) represents for Au+Au collisions.

In this analysis, four centrality bins, i.e. 20-30%, 30-40%, 40-50% and 50-60%, for Cu+Cu collisions and two centrality bins, i.e. 40-60% and 60-80%, for Au+Au collisions are considered. The central collisions (0-20%) in Cu+Cu and ($0 - 40\%$) in Au+Au were not analysed due to very poor signal to background ratio. The uncorrected reference multiplicity ranges for different centrality bins for both the

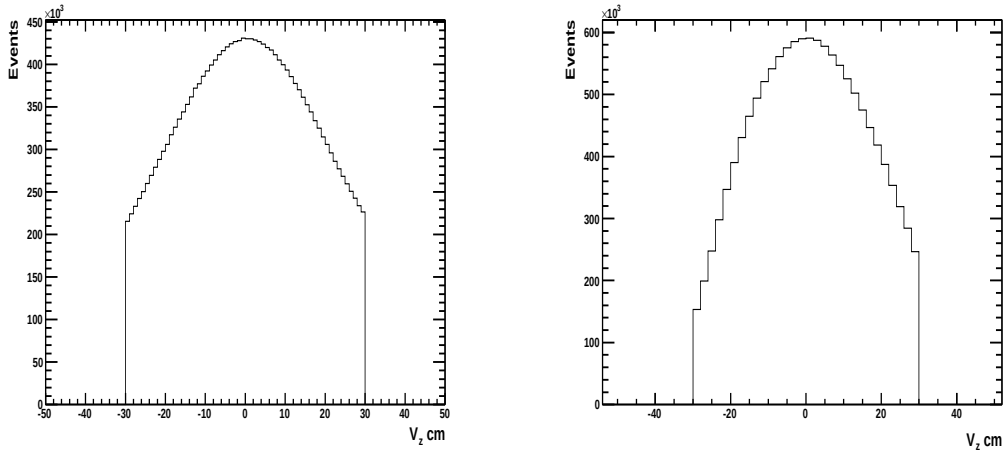

(a) Cu+Cu collisions (b) Au+Au collisions

Figure 3.1: z- vertex distribution at $\sqrt{s_{NN}}$ = 200 GeV.

systems are given in Table 3.2. The approximate number of events analysed in each centrality bins in both Cu+Cu and Au+Au systems after imposing the z-vertex cuts, i.e. $|z|$-vertex $<$ 30 cm, are listed in Table 3.2.

3.3 Track Selection

The main focus of this analysis is to study the hadronic decay channel of ρ^0 vector meson where ρ^0 decays to $\pi^+\pi^-$. The ρ^0 vector meson, being a short lived particle, decays inside the fireball and the decayed pions appear to be coming from the collision vertex. In order to ensure the tracks originating from the collision vertex, only charged pions whose distance of closest approach (DCA) to the primary interaction vertex was less than 3 cm were selected. Such candidate tracks are referred to as primary tracks. Figure 3.3 (a) shows a typical DCA distribution after the cut for π^+ and π^- tracks in minimum bias 200 GeV Cu+Cu collisions where the transverse momentum (p_T) of the candidate pions are in the range of $0.2 \leq p_T < 4.0$ GeV/c. In order to avoid the acceptance drop in the high η range, all track candidates were required to have $|\eta| < 0.8$.

Further to assure good momentum as well as dE/dx resolution, the TPC tracks

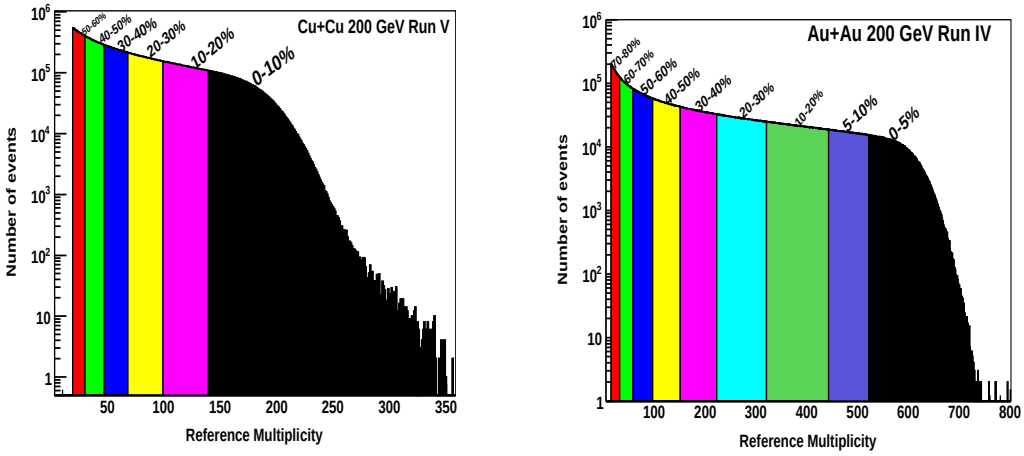

(a) Cu+Cu collisions (b) Au+Au collisions

Figure 3.2: Reference Multiplicity distributions at $\sqrt{s_{NN}}$ = 200 GeV.

Collision System	Centrality Bin	Uncorrected RefMult Range
Cu+Cu (200 GeV)	0-10%	TPC RefMult. $\geq$ 139
	10-20%	98 $\leq$ TPC RefMult. $<$ 138
	20-30%	67 $\leq$ TPC RefMult. $<$ 97
	30-40%	46 $\leq$ TPC RefMult. $<$ 66
	40-50%	30 $\leq$ TPC RefMult. $<$ 45
	50-60%	19 $\leq$ TPC RefMult. $<$ 29
$Au + Au$ (200 GeV)	0-5%	TPC RefMult. $\geq$ 520
	5-10%	441 $\leq$ TPC RefMult. $<$ 519
	10-20%	319 $\leq$ TPC RefMult. $<$ 440
	20-30%	222 $\leq$ TPC RefMult. $<$ 318
	30-40%	150 $\leq$ TPC RefMult. $<$ 221
	40-50%	96 $\leq$ TPC RefMult. $<$ 149
	50-60%	57 $\leq$ TPC RefMult. $<$ 95
	60-70%	31 $\leq$ TPC RefMult. $<$ 56
	70-80%	14 $\leq$ TPC RefMult. $<$ 30

Table 3.1: Centrality definition for different uncorrected multiplicity ranges for Cu+Cu and Au+Au system at $\sqrt{s_{NN}}$ = 200 GeV.

Collision System	Centrality Bin	$\lvert V_Z \rvert$ cm	Number of Events
Cu+Cu (200 GeV)	0-60%	30	2.059×10^7
	20-30%	30	1.057×10^6
	30-40%	30	9.150×10^5
	40-50%	30	9.082×10^5
	50-60%	30	8.241×10^5
	20-60%	30	3.871×10^6
Au+Au (200 GeV)	0-80%	30	1.322×10^7
	40-60%	30	1.491×10^6
	60-80%	30	1.451×10^6
	40-80%	30	3.023×10^6

Table 3.2: List of dataset used in the analysis. Cuts on V_Z, centrality range selected and number of events used are also shown.

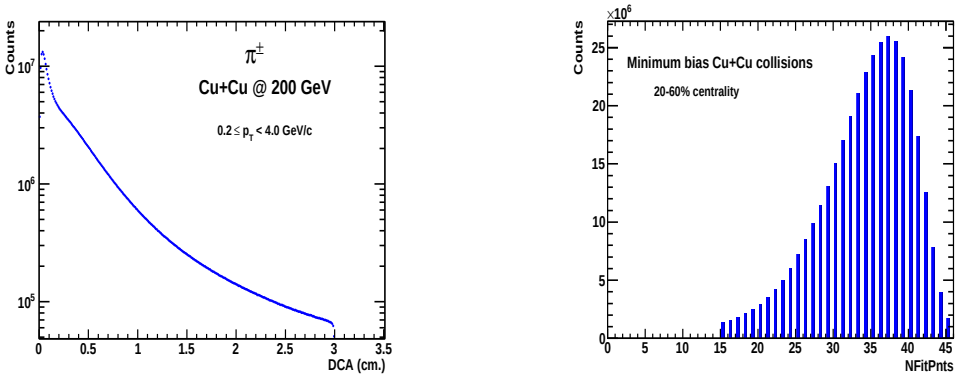

(a) DCA distribution of pion candidates (b) NFitPnts of pion candidates

Figure 3.3: Track quality assurance for Cu+Cu collisions at $\sqrt{s_{NN}}$ = 200 GeV.

were required to have at least 15 fit points out of maximum 45 fit points of the TPC. Figure 3.3 (b) shows a typical distribution of the fit points that is used in the analysis. Also the ratio of the number of fit points to the number of maximum possible fit points was required to be greater than 0.55. This was applied to remove any split tracks.

In order to describe the particle identification, the variable N_σ is defined. This N_σ corresponds to the standard deviation of a Gaussian distribution resulting from the difference between the measured energy loss of a track and its theoretical expected value. In case of pion, ($N_{\sigma\pi}$) is defined as:

$$N_{\sigma\pi} = \frac{1}{R} log \frac{(dE/dx)_{measured}}{< dE/dx >_{\pi}} \tag{3.1}$$

where $(dE/dx)_{measured}$ is the measured energy loss of a pion track, $< dE/dx >_{\pi}$ is the theoretical expected mean energy loss of a pion track at a given momentum [105–107] and R is the dE/dx resolution which is around 8.1%.

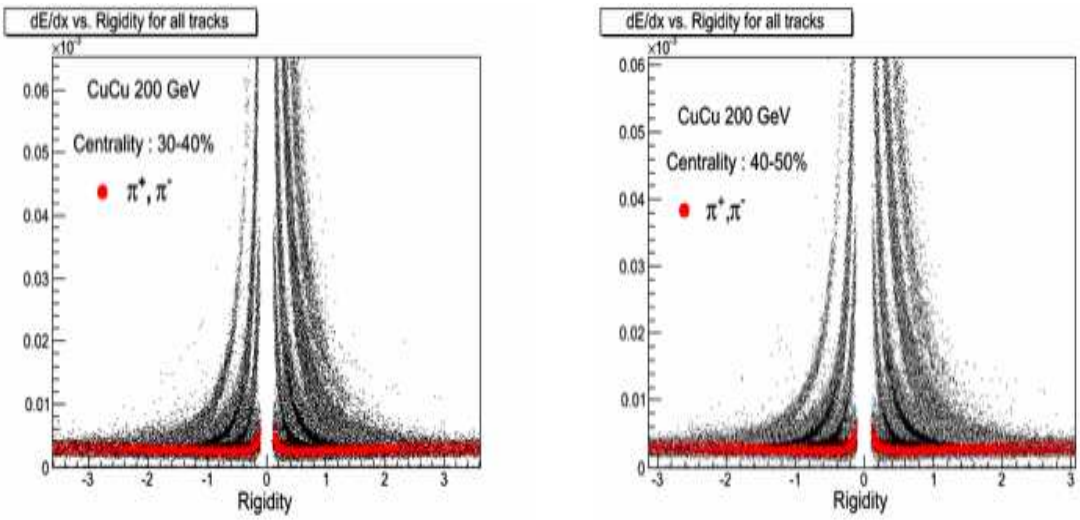

(a) 30-40% centrality (b) 40-50% centrality

Figure 3.4: dE/dx as a function of rigidity (momentum $\times$ charge) for all charged particles in Cu+Cu collisions at $\sqrt{s_{NN}}$ = 200 GeV.

In order to identify charged kaons, protons etc. similar definition of $N_{\sigma K}$ and $N_{\sigma p}$ are defined. Thus, a suitable cut on the variables $N_{\sigma\pi}$, $N_{\sigma K}$ and $N_{\sigma p}$ are applied to select π, K and p, respectively. In this analysis, the charged pions are selected by taking the track dE/dx within three standard deviations (3σ) of the expected value ($|N_{\sigma\pi}| < 3$). Figure 3.4 (a) and (b) show the typical dE/dx distribution as a function of rigidity (momentum $\times$ charge) for all charged particles measured in the TPC for Cu+Cu collisions at $\sqrt{s_{NN}}$ = 200 GeV in 30-40% and 40-50% centrality, respectively. The charged pions within 3σ of the energy loss parameterization are identified with red color. Figure 3.5 (a) represents a typical $N_{\sigma\pi^+}$ distribution and (b) represents $N_{\sigma\pi^-}$ in the range $0.6 < p_T < 0.8$ GeV/c in Cu+Cu collisions at $\sqrt{s_{NN}}$ = 200 GeV.

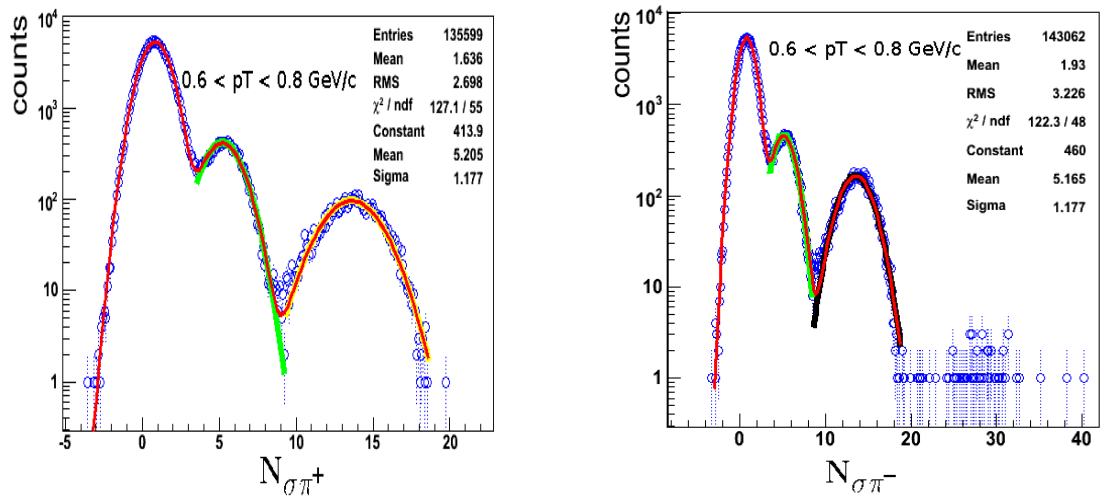

(a) $N\sigma\pi^+$ (b) $N\sigma\pi^-$

Figure 3.5: $N\sigma$ distributions fit with multi-gaussian functions.

In addition, a minimum p_T cut was applied to maintain reasonable momentum resolution. To improve statistics, pions are selected with both momentum and transverse momentum up to 10 GeV/c. A compilation of the cuts used in the ρ^0 analysis is given in Table 3.3.

Analysis Cuts	**Values**
$N_{\sigma\pi^\pm}$	(-3.0, +3.0)
Pion p (GeV/c),	(0.2, 10.0)
Pion p_T (GeV/c),	(0.2, 10.0)
NFitPnts,	> 15
NFitPnts/MaxPnts,	0.55
Pseudo-rapidity (η),	$\lvert\eta\rvert < 0.8$
DCA	< 3.0 cm.
Rapidity (y) of pion pair	$\lvert y\rvert < 0.5$

Table 3.3: List of track cuts for charged pions ($\pi^\pm$) in the ρ^0 analysis for spectra calculation in both Cu+Cu and Au+Au collisions at $\sqrt{s_{NN}}$ = 200 GeV.

3.4 ρ^0 Invariant Mass Reconstruction

The most challenging part of the analysis is to find out the number of ρ^0 produced in the collisions. This is done using the invariant mass technique. The invariant mass of ρ^0 is calculated from the energies and momenta of the decayed pions and is defined as:

$$M_{\pi^+\pi^-} = \sqrt{(E_{\pi^+} + E_{\pi^-})^2 - (\vec{p}_{\pi^+} + \vec{p}_{\pi^-})^2} \tag{3.2}$$

where E_{π^+} and E_{π^-} are the energies of π^+ and π^-, and $\vec{p}_{\pi^+}$ and $\vec{p}_{\pi^-}$ are the 3-momenta of π^+ and π^- ($|\vec{p}| = \sqrt{{p_x}^2 + {p_y}^2 + {p_z}^2}$), respectively. Since it is not known in the experiment which pions are coming from the ρ^0 decay, that is why all the possible combinations of π^+ and π^- are considered for the invariant mass reconstruction. In this way, not only the ρ^0s are reconstructed, but also a huge combinatorial background is reconstructed. Unless the combinatorial background is removed, the signal, i.e. the ρ^0 peak, will not be visible. There are two possible ways of reconstructing the background: One is the mixed-event technique and the other one is same-event like sign technique.

3.4.1 Mixed-event Technique

The mixed-event technique has been widely used in extracting the signal for many resonance particles like ϕ [108, 109], Δ^{++} [110], K^* [111], etc. Figure 3.6 (a) shows the invariant mass distribution of K^+ and K^-. The blue solid circles represent the invariant mass obtained from K^+ and K^- in the same event and the red open circles represent the invariant mass of K^+ K^- in the mixed-event in Au+Au collisions at $\sqrt{s_{NN}}$ = 200 GeV. A clear peak is seen at ϕ mass. After proper normalization and background subtraction a clean ϕ signal is obtained which is shown in Figure 3.6 (b).

The same technique is adopted to calculate the combinatorial background for the ρ^0 signal extraction. The mixed-event sample pair is formed taking the first partner from one event and the second partner from another event. For example,

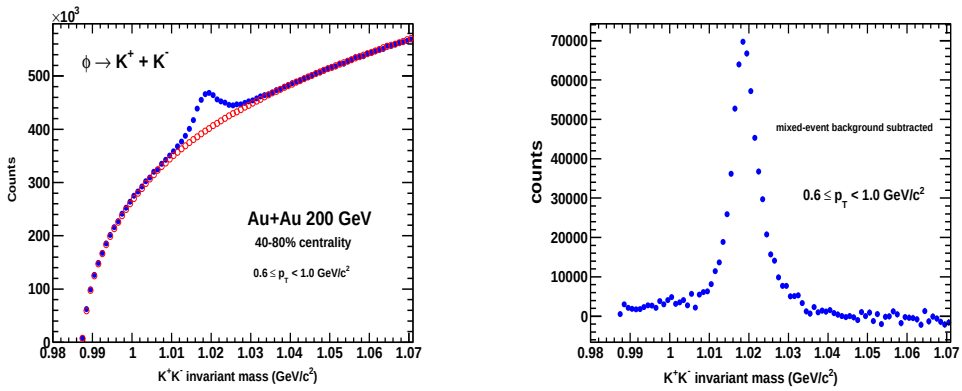

(a) Before background subtraction (b) After background subtraction

Figure 3.6: Invariant mass distribution of K^+ and K^- in 40-80% Au+Au collisions at $\sqrt{s_{NN}}$ = 200 GeV. (a) Same-event invariant mass distribution (solid blue closed circles) along with the normalized mixed-event (closed red open circle) invariant mass distribution. (b) Mixed-event background subtracted invariant mass distribution.

if a π^+ is taken from event # 1, the π^- is taken from event # 2. For mixed event, a pool of events of similar event structure are considered. This is done by taking a small bin of z-vertex and the centrality. In this calculation, the data sample was divided into 10 bins in multiplicity and 10 bins of collision vertex position. In the present analysis, the number of events used for mixing is 10. In doing so, it is assured that the event structure is maintained and the correlations are lost.

Figure 3.7 (a) shows the same event $\pi^+\pi^-$ spectrum and the mixed event $\pi^+\pi^-$ spectrum before normalization. In order to get the ρ^0 signal, the combinatorial background is subtracted from the same event π^+ and π^- invariant mass spectrum after normalization of both the spectra in the invariant mass region from 1.5 GeV/c^2 to 2.5 GeV/c^2.

Figure 3.7 (b) shows the ρ^0 signal after the mixed-event combinatorial background subtraction. The tail portion of the invariant mass, i.e. $M_{\pi^+\pi^-} > 0.9$ GeV/c^2, does not remain flat and also the distribution becomes negative. This could be because of the normalization being carried out far away from the ρ^0 mass region. In order to check the behavior of the tail portion in the mixed-event

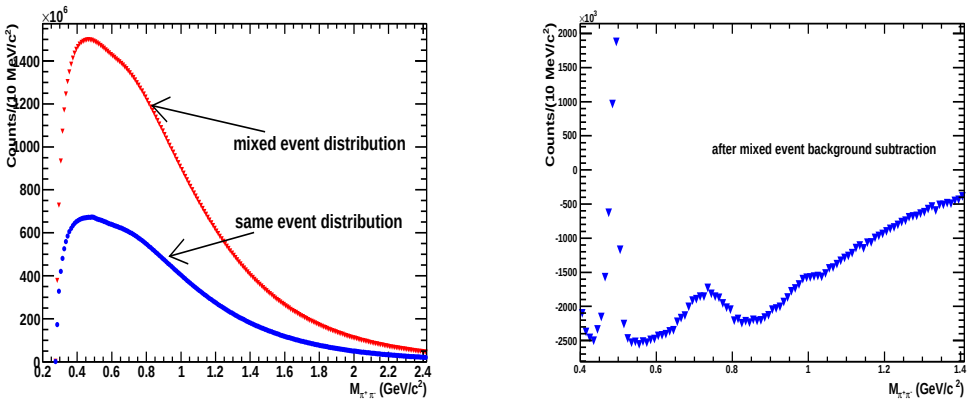

(a) Before normalization (b) After normalization

Figure 3.7: (a) The same-event $\pi^+\pi^-$ invariant mass distribution (blue dots) and the mixed-event $\pi^+\pi^-$ invariant mass distribution (red dots). (b) The mixed-event background subtracted $\pi^+\pi^-$ invariant mass distribution.

background subtraction, the same study is investigated in ϕ meson via K^+ and K^- decay and is shown in Figure 3.8. The normalization is done in the region from 1.5 GeV/c^2 to 2.0 GeV/c^2. It is also clear from the Figure 3.8 that the mixed-event technique does not work nicely when normalized in a region far away from the ϕ-meson mass peak.

Hence, the mixed-event technique is not used for ρ^0 analysis.

3.4.1.1 Like-Sign Technique

The same event like-sign approach is adopted to subtract the background from the same-event unlike-sign ($\pi^+\pi^-$) pair invariant mass spectrum. The advantage of like-sign technique is the like-sign pairs are taken from the same event so that there is no event structure difference between the like-sign spectrum and the unlike-sign spectrum. There is no bias due to the multiplicity and the z-vertex of the event.

In this measurement, the real pair represents all the possible combinations of $\pi^+\pi^-$ invariant mass distributions in an event and the total background is calculated from the geometric mean of the invariant mass distribution obtained from

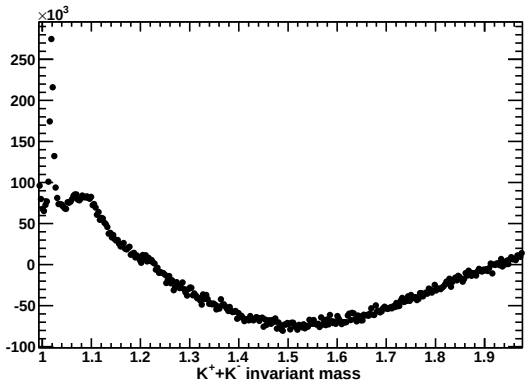

Figure 3.8: Invariant mass of K^+K^- after the background subtraction normalized far away from the ϕ mass peak.

the uncorrelated $\pi^+\pi^+$ and $\pi^-\pi^-$ pairs from the same event.

Real pair = $\pi^+\pi^-$.

Background pair = 2 $\times\sqrt{\pi^+\pi^+ \times \pi^-\pi^-}$.

The invariant mass distribution of real pair and the like-sign combinatorial background are represented in Figure 3.9 by red and blue solid dots, respectively. Figure 3.9 (a) represents the invariant mass distribution of correlated and uncorrelated pions for Au+Au at $\sqrt{s_{NN}}$ = 200 GeV, whereas Figure 3.9 (b) represents for Cu+Cu at same energy. Both the figures are in $0.6 \leq p_T < 0.8$ GeV/c. The factor 2 in the background pair is not taken while constructing the combinatorial background just to clearly distinguish the real pair and background pair distributions.

The ρ^0 signal is extracted after properly normalizing the background with the signal. Since there are many resonances coming from the π^+ and π^- up to the mass 1.25 GeV/c^2, it is safer to do the normalization after 1.5 GeV/c^2. In this analysis, the $\pi^+\pi^-$ invariant mass distribution ($M_{\pi\pi}$) and the like-sign reference background distribution were normalized to each other at 1.5 GeV/$c^2 < M_{\pi\pi} <$ 2.5 GeV/c^2. The normalization was done by taking the ratio of the counts obtained from the unlike-sign distribution to the counts obtained from the like-sign distribution in the mass region 1.5 GeV/$c^2 < M_{\pi\pi} <$ 2.5 GeV/c^2. The normalization factor is calculated in each transverse momentum bins.

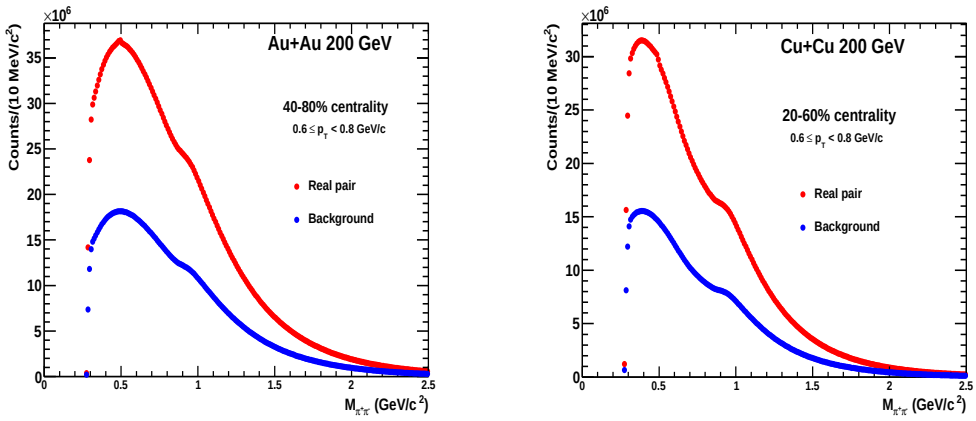

(a) 40-80% Au+Au collisions (b) 20-60% Cu+Cu collisions

Figure 3.9: The raw $\pi^+\pi^-$ invariant mass, which corresponds to the real pair (red dots) and the like-sign reference distribution, which corresponds to the background (blue dots) in $0.6 \leq p_T < 0.8$ GeV$/c$ at $\sqrt{s_{NN}}$ = 200 GeV.

Figure 3.10 shows the same event unlike-sign $\pi^+\pi^-$ invariant mass spectrum and the same event like-sign ($\sqrt{\pi^+\pi^+ \times \pi^-\pi^-}$) invariant mass spectrum after normalization.

The normalization and background subtraction of the unlike and like-sign invariant mass spectrum to get the true resonance signal, as mentioned above, can be written in the following form:

$$N_{\rho^0}(m_{\pi\pi}) = N_{\pi^+\pi^-}(m_{\pi\pi}) - N_{\left(R\times 2\times\sqrt{\pi^+\pi^+\times\pi^-\pi^-}\right)}(m_{\pi\pi}) \tag{3.3}$$

where, N stands for the number of $\pi^+\pi^-$ pairs in a bin, having bin center at $m_{\pi\pi}$. R represents the normalization factor and ($2 \times \sqrt{\pi^+\pi^+ \times \pi^-\pi^-}$) represents the total geometric mean of the like-sign pairs. Figure 3.11 shows the normalization region which is obtained by dividing the yields for the real pair and the background pair in the invariant mass $1.5 < M_{\pi\pi} < 2.5$ GeV$/c$. The red solid line is the fit to a straight line which tells about the flatness of the invariant mass in this region.

After properly normalizing and subtracting the like-sign background from the

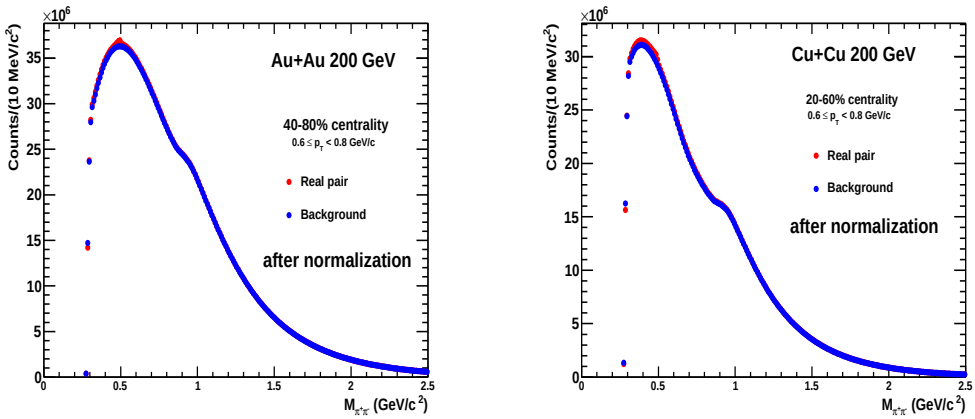

(a) 40-80% Au+Au collisions (b) 20-60% Cu+Cu collisions

Figure 3.10: The normalized geometric mean of the background pair distribution (blue points) and the real pair distribution (red points) in $0.6 \leq p_T < 0.8$ GeV/c at $\sqrt{s_{NN}}$ = 200 GeV.

unlike-sign distribution, the ρ^0 signal is observed. A typical result is shown in Figure 3.12. Figure 3.12 (a) and (b) represent the ρ^0 signals for minimum bias p+p and d+Au collisions at $\sqrt{s}$ = 200 GeV, whereas Figure 3.12 (c) and (d) represent the same for 20-60% centrality in Cu+Cu collisions and 40-80% centrality in Au+Au collisions at $\sqrt{s_{NN}}$ = 200 GeV, respectively.

Throughout this thesis, the same event like-sign technique is used for the background estimation and ρ^0 signal extraction.

3.5 Hadronic Cocktail

Figure 3.12 shows the ρ^0 signal after the combinatorial background subtraction. In Figure 3.12, the ρ^0 signal is not very clean. This is because ρ^0 has a large width. This makes the ρ^0 mass from 0.28 GeV/c^2 to 1.2 GeV/c^2. There are few more resonances lying in this mass region. For example, K^0_s, ω, f_0, σ^0 and f_2 are contributing to the ρ^0 signal. Therefore, a different analysis technique, known as line shape analysis, is adopted to extract the ρ^0 contribution from the entire spectrum of two pion invariant mass. A cocktail of all these mentioned short lived res-

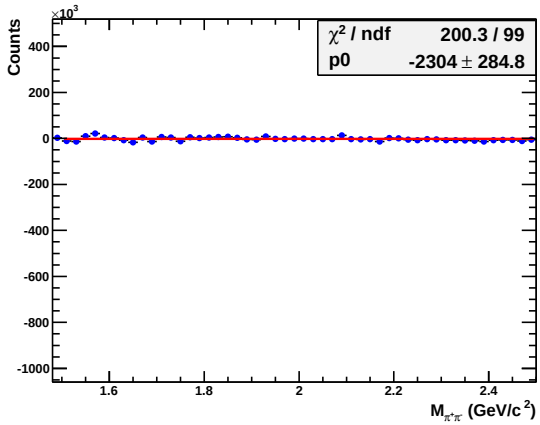

Figure 3.11: The same event unlike-sign and like-sign invariant mass distributions are normalized in the region 1.5 GeV/c^2 $< M_{\pi\pi} <$ 2.5 GeV/c^2.

onances are made with some fixed parameters and some free parameters. The different parameters of the short lived resonances are described below:

- The K_s^0 in PDG has a very negligible width. Whatever width we obtain in our analysis for $\pi^+\pi^-$ invariant mass spectrum in the K_s^0 mass region is due to the momentum resolution of the detector. Therefore, in the cocktail, the K_s^0 was fit to a Gaussian function. The mass and width are set as free parameters in between 0.47 to 0.5 GeV/c^2 and 0.004 to 0.025 GeV/c^2, respectively.
- $\omega \rightarrow \pi^+ + \pi^-$ has a very small branching ratio ($\sim$2%). Therefore, it appears to be a very small signal peak under the true ρ^0 signal. On the other hand, $\omega \rightarrow \pi^+ + \pi^- + \pi^0$ has almost 90% branching ratio. In the later case, when the π^0s are missing in the detector there is a mass shift towards the lower invariant mass region. Therefore, in the $\pi^+\pi^-$ continuum, we observe a huge contribution from the ω Dalitz decay in the low mass range. In this analysis, the ω shape is obtained from the HIJING event generator [112, 113]. The mass and width of the ω are fixed according to the PDG value [161].
- The K^* shape was obtained from the HIJING event generator [112, 113], with the kaon being misidentified as a pion. When the pions being misiden-

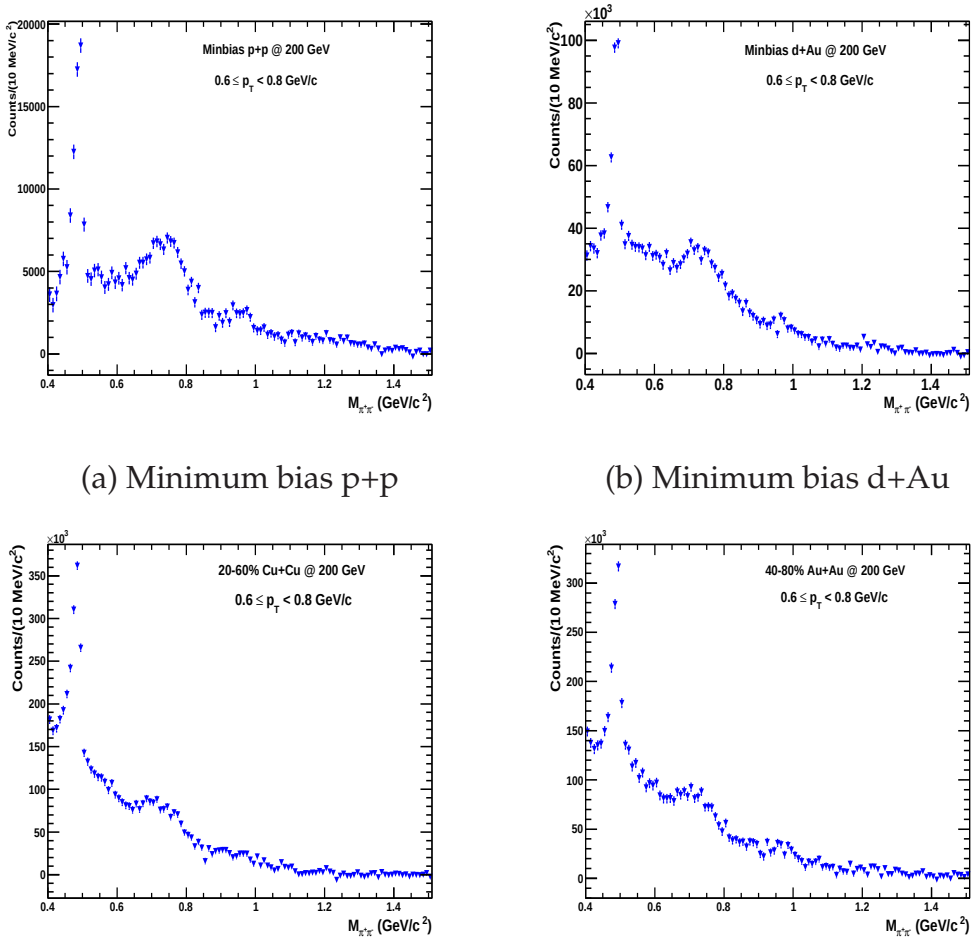

(a) Minimum bias p+p

(b) Minimum bias d+Au

(c) 20-60% centrality Cu+Cu

(d) 40-80% centrality Au+Au

Figure 3.12: The like-sign background subtracted $\pi^+\pi^-$ invariant mass distributions in different collision systems at $\sqrt{s_{NN}}$ = 200 GeV for a particular p_T bin, i.e. $0.6 \leq p_T < 0.8$ GeV/c.

tified as kaons they give rise to a distribution near the K^* mass region. In this study, the number of such misidentified K^*s were calculated and then subtracted out from the cocktail contributions. How the fraction of uncorrected K^* yield was calculated is discussed later in this chapter.

- The f_0(980), σ^0(400-1200) and f_2(1270), being scalar mesons with $J = 0$ for the first two and $J = 2$ for the last one, are fit to s-wave and d-wave relativistic Breit-Wigner function [114, 115] respectively. The detail of the functional form used for the Breit-Wigner function is discussed below. Because

of the experimental uncertainty in the measurement of mass and width of scalar particles, we always fix these parameters for f_0 and f_2 according to the PDG [127]. Because of the huge uncertainty in both the mass and width of σ^0 scalar meson in the PDG, we have fixed the mass and width of σ^0 at 630 MeV/c^2 and 600 MeV/c^2, respectively.

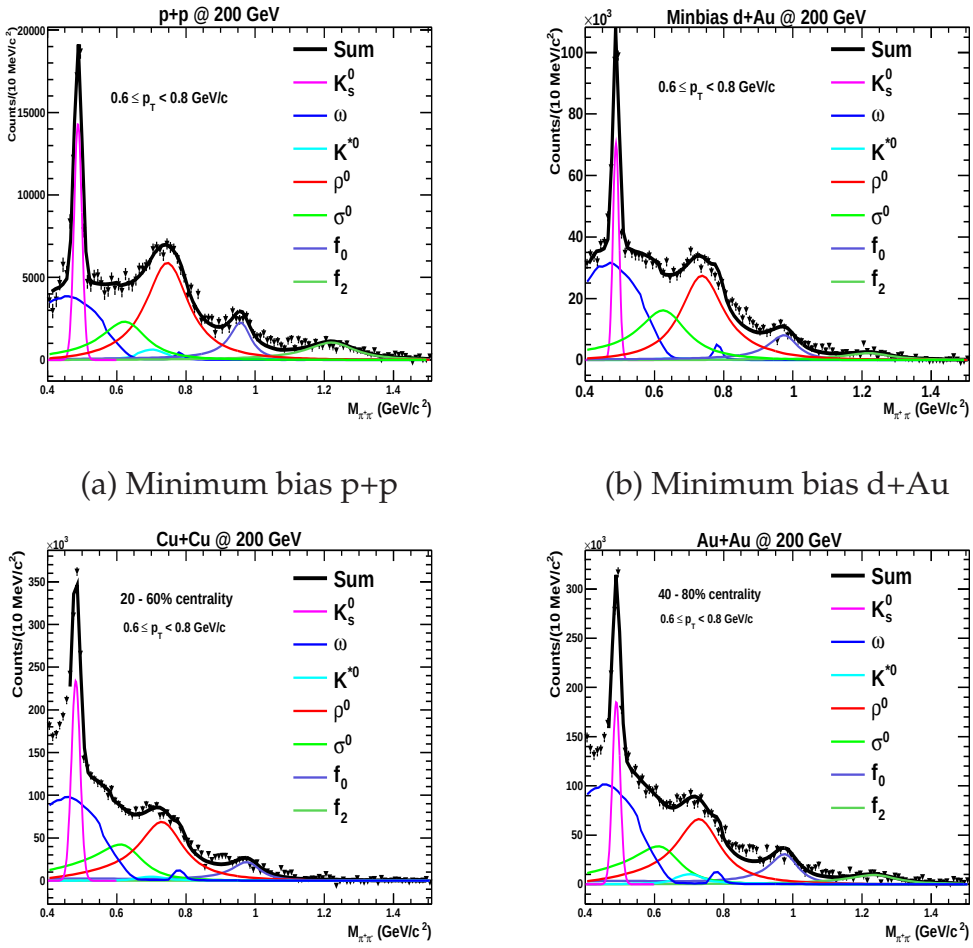

(a) Minimum bias p+p

(b) Minimum bias d+Au

(c) 20-60% centrality Cu+Cu

(d) 40-80% centrality Au+Au

Figure 3.13: A cocktail function fit to the invariant mass distributions of $\pi^+\pi^-$ after like-sign background subtraction at $\sqrt{s_{NN}}$ = 200 GeV. Different particle contributions in the cocktail are shown in different colors.

Figure 3.13 represents the hadronic cocktail fit to the background subtracted invariant mass distributions for different collision systems, i.e. minimum bias p+p, d+Au, 20-60% Cu+Cu and 40-80% Au+Au, at $\sqrt{s_{NN}}$ = 200 GeV. The solid

black line in Figure 3.13 is the sum of all the contributions in the hadronic cocktail and the different individual particle's contribution is shown in different colors.

3.6 ρ^0 Mass and Yield Extraction

The ρ^0(770), a resonance vector meson, has $J = 1$. The $\pi^+\pi^-$ invariant mass distribution for ρ^0 is therefore fitted to a p-wave relativistic Breit-Weigner (BW) function [114] of the form:

$$BW\left(M_{\pi\pi}\right) = \frac{AM_{\pi\pi}M_0\Gamma\left(M_{\pi\pi}\right)}{\left[\left({M_0}^2 - {M_{\pi\pi}}^2\right)^2 + {M_0}^2\Gamma^2\left(M_{\pi\pi}\right)\right]} \tag{3.4}$$

where A is a constant parameter proportional to the yield of the ρ^0, $M_{\pi\pi}$ is the $\pi^+\pi^-$ invariant mass, M_0 is the PDG ρ^0 mass, and $\Gamma\left(M_{\pi\pi}\right)$ is the momentum dependent width [114, 116].

$$\Gamma\left(M_{\pi\pi}\right) = \left[\frac{\left(M_{\pi\pi}^2 - 4m_\pi^2\right)}{\left(M_0^2 - 4m_\pi^2\right)}\right]^{(2J+1)/2} \times \Gamma_0 \times \left(M_0/M_{\pi\pi}\right) \tag{3.5}$$

In Equation 3.5, Γ_0 is the ρ^0 full width at half maximum and m_π is the pion mass in PDG.

In heavy-ion collisions, besides the direct production of ρ^0 from partons [117, 118], a ρ^0 can also be produced through $\pi^+\pi^-$ scattering in the hadronic medium via $\pi^+ + \pi^- \rightarrow \rho^0 \rightarrow \pi^+\pi^-$ [119, 120]. The $\pi^+\pi^-$ invariant mass distribution for the ρ^0 generated in this way might be modified by the initial pions phase space distribution. Thus, the relativistic Breit-Wigner function should be multiplied by a Boltzmann factor [121–123] to account for Phase Space (PS). In case of p+p collisions, the hadronic medium is much smaller than that formed in heavy-ion collisions, but still the ρ^0 can be produced in the same process [110]. The functional form of the PS can be written as:

$$PS\left(M_{\pi\pi}\right) = \frac{M_{\pi\pi}}{\sqrt{M_{\pi\pi}^2 + p_T^2}} \times exp(-\sqrt{M_{\pi\pi}^2 + p_T^2}/T) \tag{3.6}$$

where p_T is the transverse momentum of the ρ^0 and T is the temperature at

which the resonance is emitted [121]. In case of heavy-ions, i.e. Au+Au and Cu+Cu, the observed ρ^0 is emitted at the kinetic freeze-out stage and the hadronic medium has already cooled down and the temperature is lower than the chemical freeze-out stage [120, 121]. That is why in heavy-ion the temperature used in the phase space factor is 120 MeV. In p+p and d+Au collisions, the temperature used is T=160 MeV according to a statistical model calculation [124–126] which reasonably reproduces particle compositions.

Thus, the ρ^0 mass was obtained by fitting the data to a relativistic p-wave Breit-Weigner function times a factor which accounts for the phase space (BW $\times$ PS) in the hadronic cocktail. The parameters A and M_0 are two free parameters, whereas the parameter Γ_0 is fixed at 160 MeV/c^2 in the fit function. Then the mass of ρ^0 is extracted from the fit.

Since the PS factor modifies the position of the peak for the BW function, the mass derived from the BW$\times$PS fit may be shifted compared to the peak of the BW function alone. To check this, the ρ^0 peak was also fitted to a BW function excluding the PS factor in the hadronic cocktail. However, the fit failed to reproduce the ρ^0 line shape, and underestimated the position of the peak in general, particularly at low p_T.

This measurement does not have sufficient sensitivity to permit a systematic study of the ρ^0 width. Therefore, for the cocktail fits in this analysis, the ρ^0 width was fixed at $\Gamma_0 = 160$ MeV/c^2 which is consistent with the convoluted ρ^0 natural width (150.9 $\pm$ 2.0 MeV/c^2 [127]) with the intrinsic resolution of the detector [128]. The ρ^0, ω, K^{*0}, f_0, σ^0 and f_2 distributions were corrected for the detector acceptance and efficiency determined from a detailed simulation of the TPC response using GEANT [128] in the STAR environment and is explained later in this chapter.

In order to extract the raw ρ^0 yield in certain transverse momentum range, the background subtracted $\pi^+\pi^-$ invariant mass distribution was fit to the cocktail function as discussed above. Then the specific ρ^0 raw yield from the cocktail was obtained by taking the area under the red curve which represents the BW

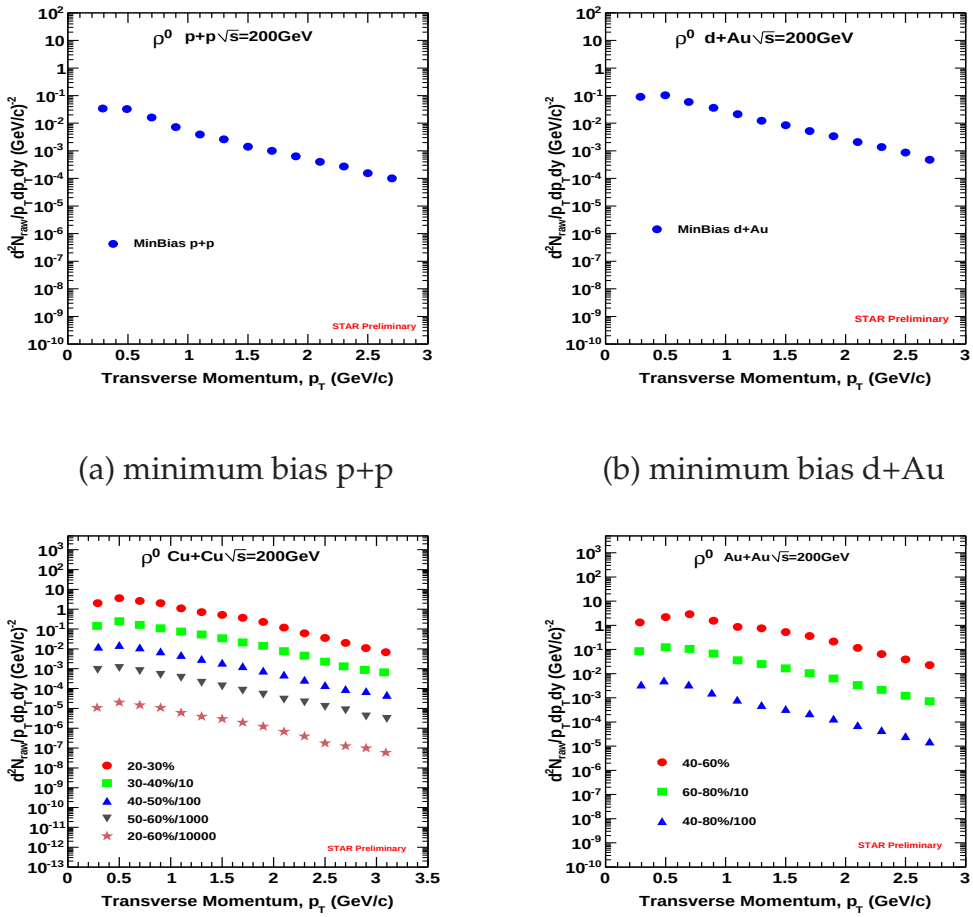

(a) minimum bias p+p

(b) minimum bias d+Au

(c) minimum bias Cu+Cu

(d) minimum bias Au+Au

Figure 3.14: The $\pi^+\pi^-$ invariant mass distributions along with the cocktail fit in 40-80% centrality Au+Au collisions at $\sqrt{s_{NN}}$ = 200 GeV for different p_T bins.

function times the PS factor as shown in Figure 3.13. Figure 3.14 shows the ρ^0 raw invariant yields $[1/(2\pi)d^2N_{raw}/p_T dp_T dy]$, normalized by the total number of collision events at mid-rapidity $|y| < 0.5$ as a function of p_T in minimum bias p+p, d+Au, five centralities (20-30%, 30-40%, 40-50%, 50-60% and 20-60%) in minimum bias Cu+Cu and 3 centralities (40-60%, 60-80% and 40-80%) in minimum bias Au+Au collisions.

The signal-to-background ratio as a function of $\pi^+\pi^-$ pair p_T for minimum bias p+p, minimum bias d+Au, 20-60% peripheral Cu+Cu and 40-80% peripheral Au+Au collisions at $\sqrt{s_{NN}}$ = 200 GeV is shown in Figure 3.15. The ratio is

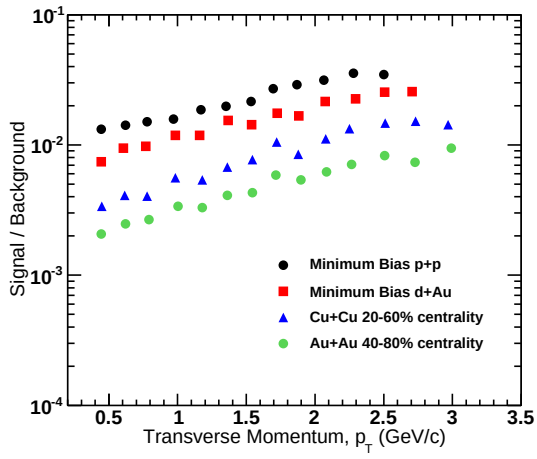

Figure 3.15: The signal-to-background ratio for ρ^0 measurements as a function of p_T for different collision systems at $\sqrt{s_{NN}}$ = 200 GeV.

observed to increase with increasing p_T for all systems.

Figure 3.23 shows the background subtracted $\pi^+\pi^-$ invariant mass distribution in eight different p_T bins (with each p_T bin width 0.2 GeV/c) in the p_T range between 0.2 and 2.6 GeV/c in minimum bias p+p collisions at $\sqrt{s}$ = 200 GeV. Figure 3.24 shows the same invariant mass distribution in the p_T range between 0.2 and 2.8 GeV/c.

Figure 3.25 and 3.26 show the background subtracted $\pi^+\pi^-$ invariant mass distribution in nine different p_T bins (with each p_T bin width 0.2 GeV/c) in the p_T range between 0.2 and 2.6 GeV/c in 20-60% Cu+Cu and 40-80% Au+Au collisions at $\sqrt{s_{NN}}$ = 200 GeV, respectively. In case of Cu+Cu and Au+Au collisions, the hadronic cocktail fit range has been slightly changed in order to get a better fit.

3.7 Other Possible Ways of Cocktail Fit

One of the very important parts of this analysis is to extract the fitting parameters for various particles used in the cocktail. For this one has to be very careful while fitting the data points with a much complicated cocktail functions with multi parameters.

As we have mentioned earlier in this chapter, for our analysis in Cu+Cu RunV and Au+Au RunIV at $\sqrt{s_{NN}}$ = 200 GeV, we are dealing with a much higher statistics than the published data for Au+Au 200 GeV Run II [104], the cocktail itself has to be redefined to get a better fit to extract the information properly. Below, we have mentioned three different possible ways that we have studied and tried to put the physics argument for and against each of the possibilities.

- **Cocktail Possibility I**

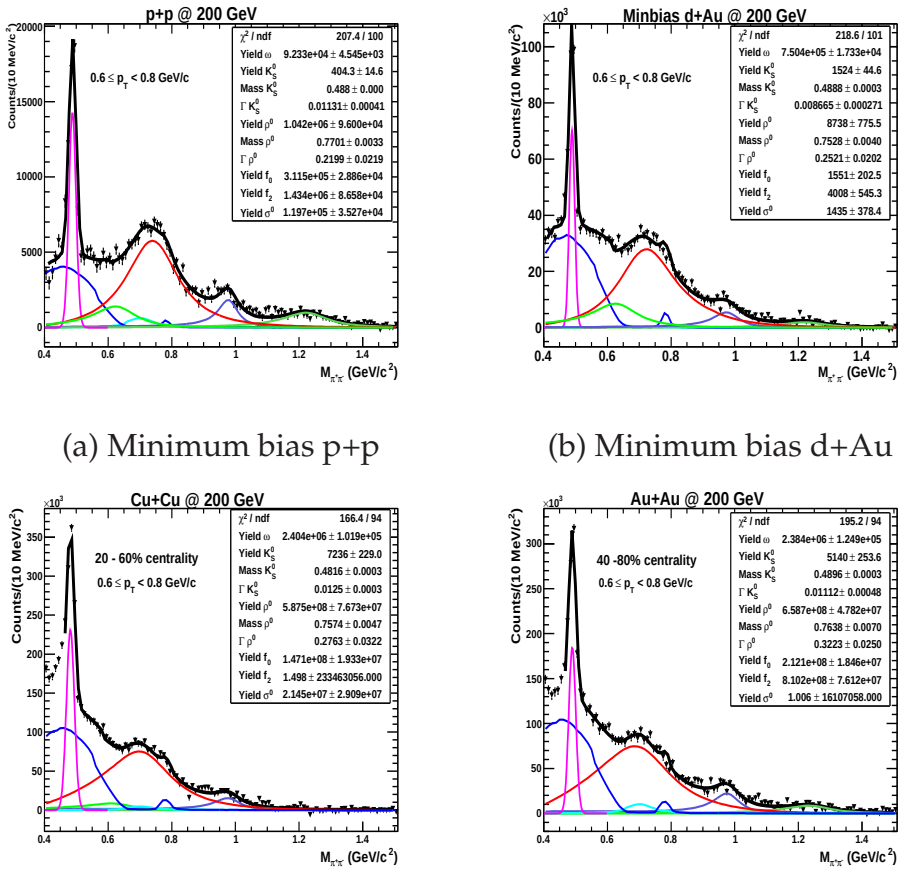

(a) Minimum bias p+p

(b) Minimum bias d+Au

(c) 20-60% Cu+Cu

(d) 40-80% Au+Au

Figure 3.16: A cocktail function fit to the invariant mass distributions of $\pi^+\pi^-$ after background subtraction at $\sqrt{s_{NN}}$ = 200 GeV. In these plots, the width of ρ^0 is taken as a free parameter in the cocktail function.

One of the very obvious question is why not the ρ^0 width is a free parameter in the fit function and to justify this argument we have done the following study.

The background subtracted invariant mass distribution was fitted with a cocktail function with the following:

1) ρ^0 mass is a free parameter, but constrained between 0.6 GeV/c^2 and 0.8 GeV/c^2.

2) ρ^0 width is free.

3) Temperatures used in the Phase Space (PS) factor is 160 MeV for minimum bias p+p and d+Au collisions, whereas for Cu+Cu and Au+Au collisions it is 120 MeV.

Figure 3.16 shows the cocktail fit with ρ^0 width as a free parameter for p+p, d+Au, Cu+Cu and Au+Au collisions at 200 GeV.

From Figure 3.16, it is very clear that the ρ^0 width is very high and can go up to ~350 MeV/c^2 in peripheral Au+Au collisions, which seems to be unphysical. The temperature used in the phase space is not sufficient enough to produce such width for ρ^0 [129]. Therefore, although this fitting gives better χ^2/ndf, we are not following this way of the cocktail fit where the ρ^0 width is a free parameter.

- **Cocktail Possibility II**

We have observed in possibility-I that the ρ^0 width cannot be a free parameter in the fitting function. Therefore, we are trying to understand the goodness, i.e. χ^2/ndf, of the cocktail by fixing the width of ρ^0 vector meson.

In this case, the background subtracted invariant mass distribution was fitted with a cocktail function with the following description:

1) ρ^0 mass is a free parameter, but constrained between 0.6 GeV/c^2 and 0.8 GeV/c^2.

2) ρ^0 width is fixed at 0.16 GeV/c^2.

3) Temperatures used in the Phase Space (PS) factor are 160 MeV and 120 MeV for p+p, d+Au and Cu+Cu, Au+Au collisions at $\sqrt{s_{NN}}$ = 200 GeV, respectively.

Figure 3.17 shows the cocktail fit with ρ^0 width fixed at 0.16 GeV/c^2.

As we have mentioned earlier, because of the larger event statistics, the above cocktail is not representing the data points well and therefore, we have a poor

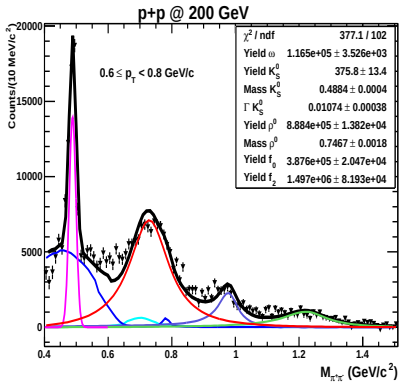

(a) Minimum bias p+p

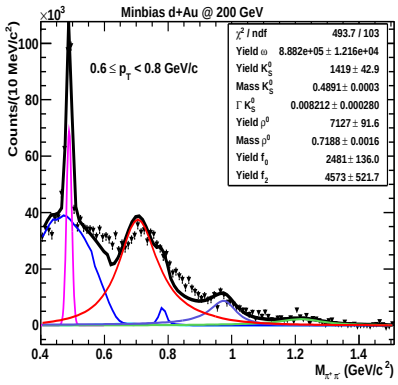

(b) Minimum bias d+Au

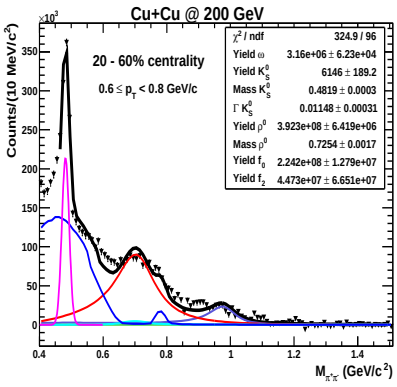

(c) 20-60% Cu+Cu

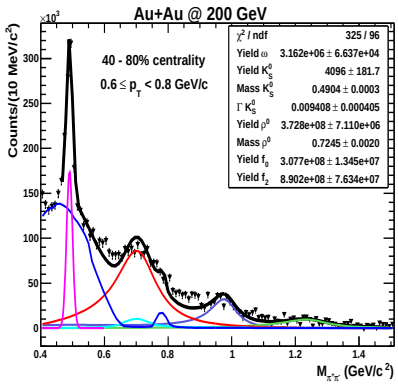

(d) 40-80% Au+Au

Figure 3.17: A cocktail function fit to the invariant mass distributions of $\pi^+\pi^-$ after background subtraction at $\sqrt{s_{NN}}$ = 200 GeV. In these plots, the width of ρ^0 is fixed at 0.16 GeV/c^2 in the cocktail function.

χ^2/ndf. We believe that this is not a good idea to carry on the analysis with such a fit function which may affect the yield extraction of the ρ^0.

- **Cocktail Possibility III**

In our analysis, we have observed that there is a bump around 600 MeV/c^2 in background subtracted $\pi^+\pi^-$ invariant mass distribution. The cocktail is not well explaining the data points in this mass region. Therefore, we tried to include σ^0 meson in the cocktail. Although there is a huge uncertainty in the mass and width of the σ^0 in the PDG. but after including in the cocktail it gives a better fit. The different parameters in the cocktail are mentioned below.

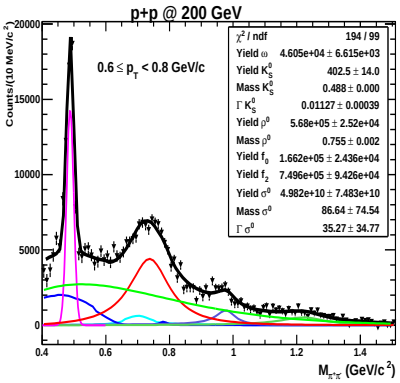

(a) Minimum bias p+p

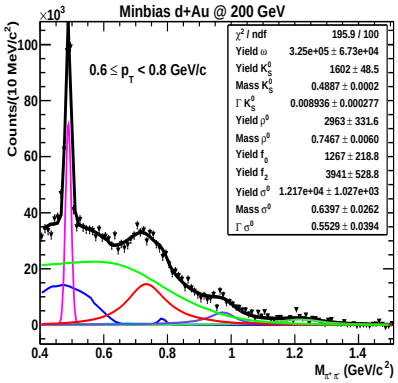

(b) Minimum bias d+Au

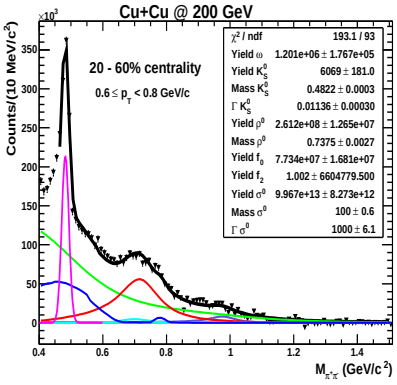

(c) 20-60% Cu+Cu

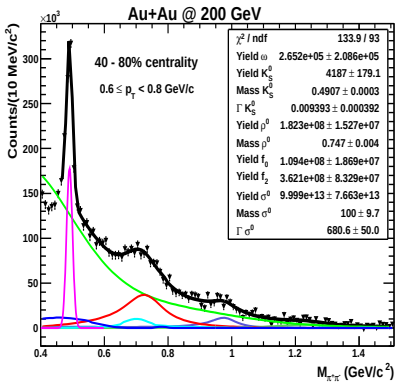

(d) 40-80% Au+Au

Figure 3.18: A cocktail function fit to the invariant mass distributions of $\pi^+\pi^-$ after background subtraction at $\sqrt{s_{NN}}$ = 200 GeV. In these plots, the σ^0 mass and width are taken as free parameters in the cocktail function.

1) ρ^0 mass is a free parameter between 0.6 and 0.8 GeV$/c^2$.

2) ρ^0 width is fixed at 0.16 GeV$/c^2$

3) σ^0 mass is a free parameter.

4) σ^0 width is free.

It is observed from Figure 3.18 that if we make the σ^0 mass and width free, then it dominates in the continuum and kills the other signals contribution. Since σ^0 is not a well detected particle in experiments, it looks unphysical to get such a huge yield contributions from these fits. Therefore, the mass and width of σ^0 are not taken free in the fit and henceforth this way of cocktail fit is discarded.

Since these three possibilities did not give either good χ^2/ndf or physical results, the entire ρ^0 analysis was done taking the cocktail mentioned in the section 3.5.

3.8 Efficiency Correction

After obtaining the ρ^0 raw yields in each p_T bins, corrections for the detector acceptance and tracking efficiency are applied. Although the STAR TPC has a full 2π azimuthal acceptance, there are some gaps between the TPC sectors which cause some loss of particle identification and measurement. The tracking efficiency is also inverse function of momentum since high momentum particles have almost straight trajectories in the 0.5 T magnetic field and it is therefore more difficult to reconstruct the momenta of these particles. These effects are

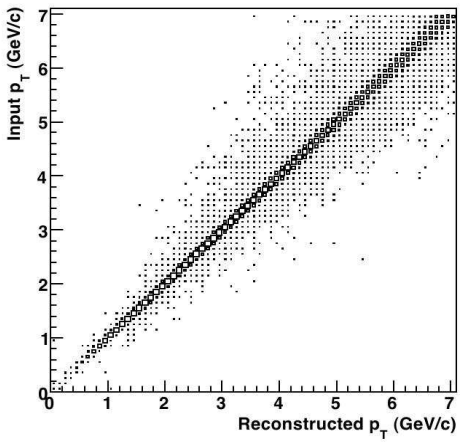

Figure 3.19: Input MC ρ^0 p_T vs. reconstructed ρ^0 p_T compared to the case where the most likely associated track candidate is chosen on the basis of most common hits.

corrected by comparing with MC simulations. MC simulated ρ^0 mesons are generated using a flat p_T and rapidity distribution. They are then passed through GSTAR [130] (the STAR framework software package to run the simulation using GEANT [131, 132] and TRS (TPC Response Simulator) [130]. The ρ^0 mesons are then decayed by GEANT through their hadronic decay channel, $\rho^0 \rightarrow \pi^+ + \pi^-$. The simulated ρ^0 mesons and their decayed daughters are then embedded into

the real raw events. This combination of real and simulated data was then passed through the standard STAR reconstruction chain subject to the same analysis cuts that were applied in the real data analysis. After reconstruction of the complete event, known as reconstructed event, we move towards "Association". The process of matching or associating the reconstructed information of decay daughters of ρ^0 meson with the MC information is called Association. A cut of 15 common hit points was applied on the number of common hit points in the TPC for both the reconstructed and input simulated tracks. The ratio of the reconstructed ρ^0 mesons to the input ρ^0 meson is the (efficiency $\times$ acceptance).

The correlation of input p_T and the reconstructed p_T of ρ^0 is shown in Figure 3.19. Figure 3.19 represents a nice correlation between the input p_T and the reconstructed p_T of ρ^0 suggesting that the embedding is working as expected. As we go to higher p_T bin, the resolution of single track becomes worse. This produces some outliers on both the sides of the correlation plot as shown in Figure 3.19. Therefore, the reconstruction efficiency for a given p_T bin can be determined as

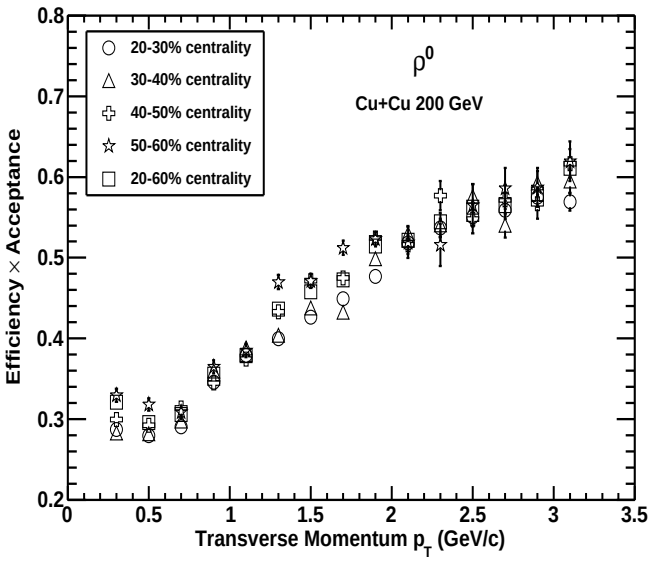

Figure 3.20: The total reconstruction efficiency multiplied with the detector acceptance as a function of transverse momentum of ρ^0 in Cu+Cu collisions at $\sqrt{s_{NN}}$ = 200 GeV.

follows. First we obtained the total number of simulated ρ^0 meson in the above

mentioned p_T bin. Then we obtain the associated decay daughter information in the reconstructed event and subject them to the same dynamical cuts to get the number of reconstructed ρ^0 mesons in that particular bin. The ratio of the above two quantities is known as reconstruction efficiency. The reconstruction efficiency as derived above has been studied as a function of collision centrality for various p_T bin in Cu+Cu collisions and is shown in Figure 3.20.

3.8.0.2 ρ^0 Efficiency

The ρ^0 correction factor (reconstruction efficiency multiplied by the detector acceptance) as a function of invariant mass for different p_T bins is shown in Figure 3.21 in Cu+Cu collisions at $\sqrt{s_{NN}}$ = 200 GeV. In general, the correction factor increases as a function of transverse momentum. The fact that the correction factor is larger at low values of $M_{\pi\pi}$ and large values of p_T is simply due to kinematics. In case of narrow resonances, such as K^*, Σ^*, and Λ^*, the correction factor is dependent only on the p_T bin being analyzed. Therefore, the correction is performed as a function of p_T only. On the other hand, for wider resonances, such as ρ^0 and Δ^{++}, the correction factor depends on the invariant mass for each p_T interval that is being analyzed. In this case, the correction is applied as a function of the invariant mass for each p_T bin.

In this analysis, the correction factors as a function of invariant mass for different p_T bins are obtained from minimum bias Cu+Cu collisions for different centralities. The correction factors for Au+Au collisions could not be obtained because of the time constraint. Therefore, the same correction factors obtained in Cu+Cu are used for Au+Au system. Before using the same correction factors in Au+Au data, we have done a systematic study of the validity of the correction factors obtained in different centrality bins Cu+Cu collisions.

Figure 3.21 shows the acceptance $\times$ efficiency as a function of $\pi^+\pi^-$ invariant mass for different p_T bins obtained from 40-50% centrality in Cu+Cu collisions and represented by the green line, plotted together with the acceptance $\times$ efficiency obtained from the minimum bias Cu+Cu and scaled up by an arbitrary

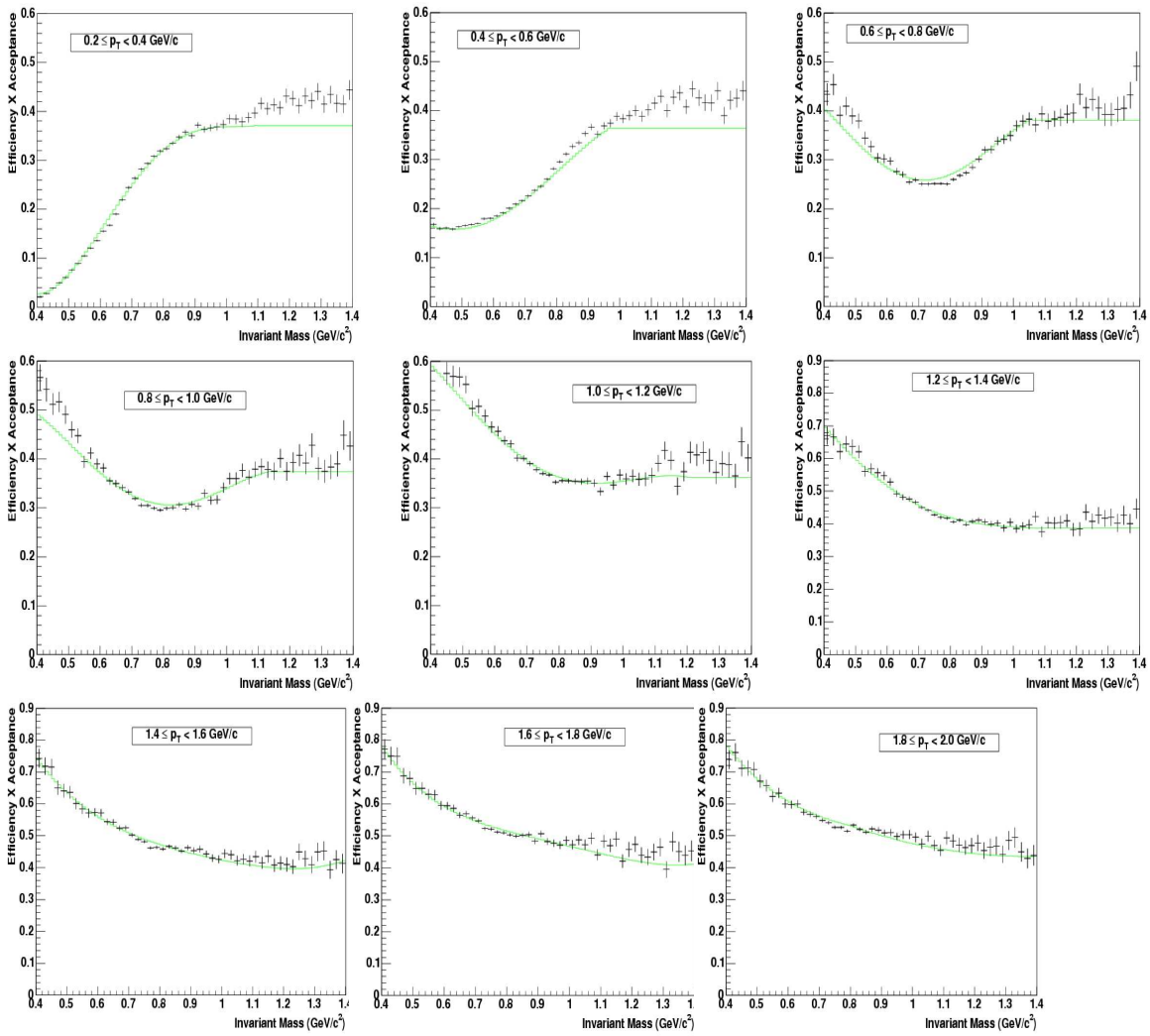

Figure 3.21: Detection efficiency as a function of $\pi^+\pi^-$ invariant mass in different p_T bins in Cu+Cu collisions at $\sqrt{s_{NN}}$ = 200 GeV.

normalization. It is shown from Figure 3.21 that the acceptance $\times$ efficiency obtained from Cu+Cu minimum bias scaled up by an arbitrary normalization are in good agreement with the acceptance $\times$ efficiency obtained from the 40-50% centrality. So, the idea is to use the "shape" of the acceptance $\times$ efficiency as a function of invariant mass for different p_T bins obtained from Cu+Cu minimum bias to fit the invariant mass distributions of different collision centralities in Cu+Cu as well as in Au+Au systems.

3.8.0.3 K^{*0} Mis-Identification

In the STAR TPC, the particle identification is done through the energy loss (dE/dx). Kaons and pions are identified only when their momenta are less than 0.7 GeV/c and protons are identified only when their momenta are less than 1.1 GeV/c. In our analysis, we have selected the pion candidates with their momenta between 0.2 GeV/c and 10.0 GeV/c. Thus, it is clear that a pion track with momentum greater than 0.7 GeV/c can be mis-identified as a kaon track. A proton track with momentum greater than 1.1 GeV/c can be mis-identified as either a pion or a kaon track or both. In case of ρ^0 vector meson, where $\rho^0 \rightarrow \pi^+\pi^-$, if its positive pion daughter has a momentum greater than 0.7 GeV/c, then it can be mis-identified as a kaon and thus it can be falsely reconstructed as a K^{*0} or $\bar{K^{*}}0$. If both the daughters have momenta greater than 0.7 GeV/c, it can be mis-identified twice as both a K^{*0} or $\bar{K^{*}}0$. So, in order to get the contamination for each p_T bin and each centrality. the following procedure has been adopted.

First, the K^* efficiency of being mis-identified (EffMis) as a function of p_T is calculated and this is same for all centralities. Then, the efficiency of measuring the K^* (EffK*) with our analysis cuts, which is similar to the ρ^0 analysis, is calculated. Figure 3.22 shows the efficiency of measuring a K^* with our analysis cuts for Cu+Cu collisions in different centralities.

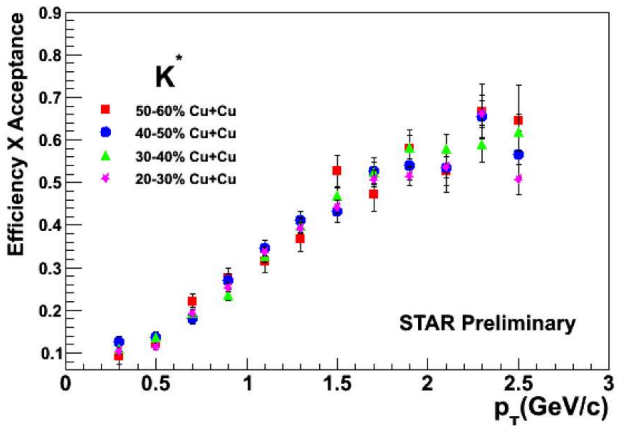

Figure 3.22: Efficiency of measuring a K^* in Cu+Cu collisions at $\sqrt{s_{NN}}$ = 200 GeV in different centralities.

Finally, the contamination is calculated using the following formula:

$$\left(K^* + \bar{K^*}\right) counts = p_T \times dp_T \times \frac{dN}{2\pi p_T dy dp_T} \times 2 \times \frac{2}{3} \times EffMis \times N_{event} \times 2\pi \times EffK* \tag{3.7}$$

where $\frac{2}{3}$ is the branching ratio correction for the K^{*0} yields, N_{event} is the number of events used in the corresponding centrality. The quantity $\frac{dN}{2\pi p_T dy dp_T}$ is calculated for each p_T bin and each centrality, and this is given by [133, 134]:

$$\frac{dN}{2\pi p_T dy dp_T} = \frac{N}{(2\pi T\,(m_0 + T))} \times exp\left(-\left(m_T - m_0\right)/T\right) \tag{3.8}$$

where, T = inverse slope parameter,

N = yield of K^{*0},

m_T = $\sqrt{p_T^2 + m_0^0}$ and m_0 = 0.896 GeV/c^2 (K^{*0} mass).

Also to check the purity of the sample, we have done the study with various values of $N_{\sigma\pi}$ cut. In our analysis, the charged pions are selected by requiring their dE/dx to be within three standard deviations (3σ) of the expected value. In order to test the purity of the selected pion candidates, we have checked with more tighter values of the $N_{\sigma\pi}$ cut as well as pair p_T cut.

Invariant mass distributions in p+p 200 GeV:

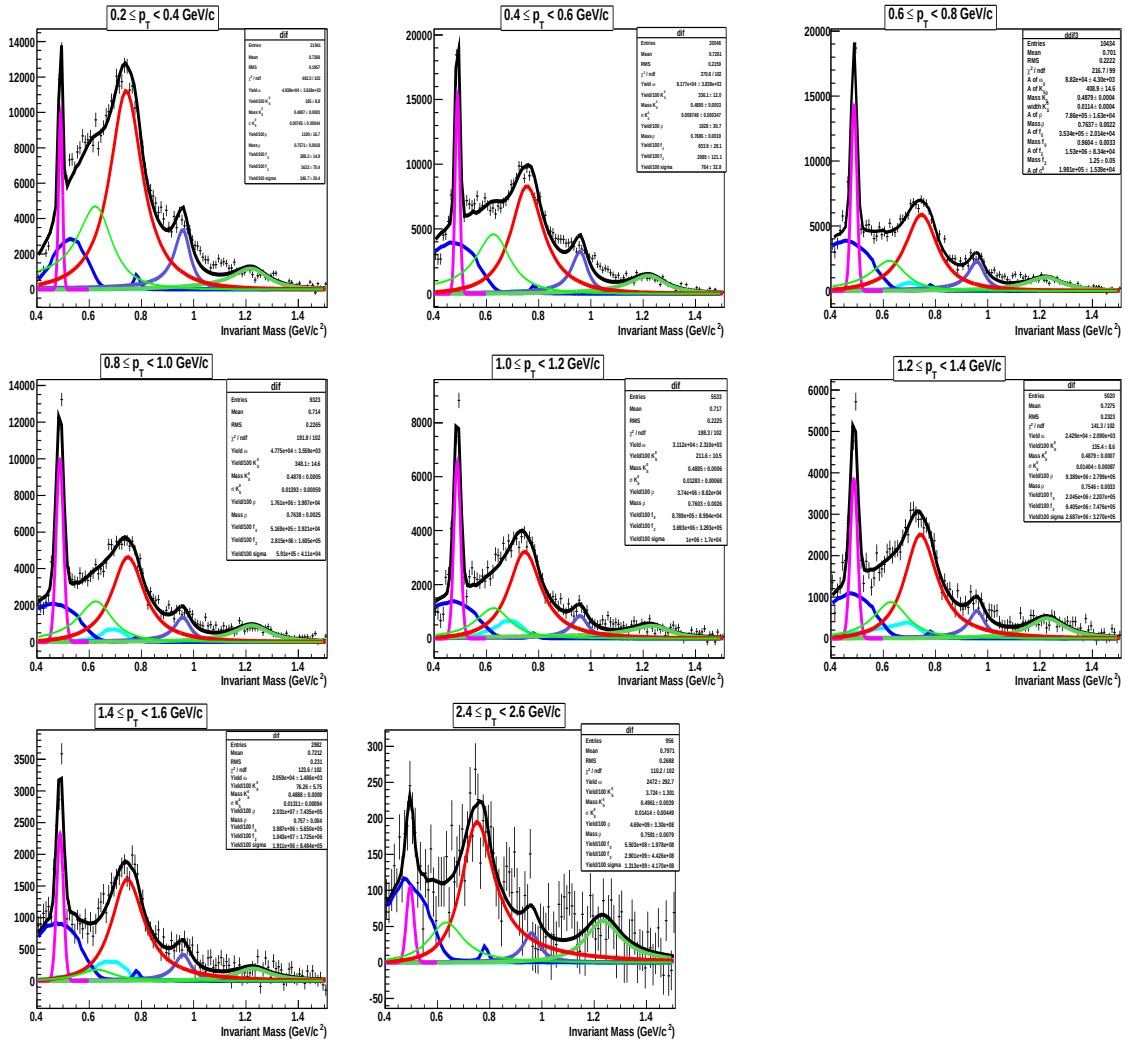

Figure 3.23: The $\pi^+\pi^-$ invariant mass distributions in minimum bias p+p at 200 GeV for different p_T bins, each having bin width 0.2 GeV/c. The solid black line is the hadronic cocktail fit function discussed in section 3.5 and 3.6. The units of the fit parameters mass and width are in GeV/c^2.

Invariant mass distributions in d+Au 200 GeV:

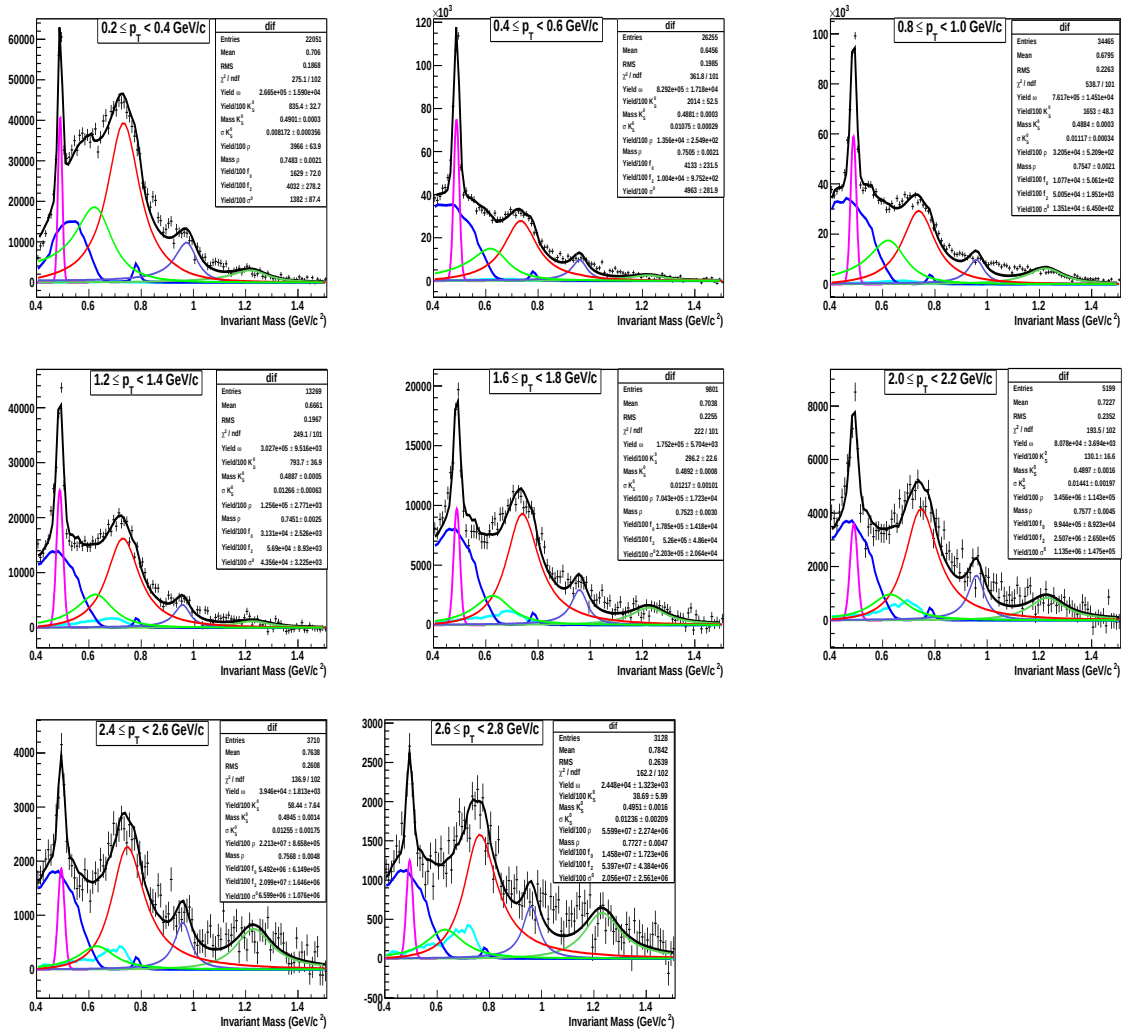

Figure 3.24: The $\pi^+\pi^-$ invariant mass distributions in minimum bias d+Au at 200 GeV for different p_T bins, each having bin width 0.2 GeV/c. The solid black line is the hadronic cocktail fit function discussed in section 3.5 and 3.6. The units of the fit parameters mass and width are in GeV/c^2.

Invariant mass distributions in Cu+Cu (20-60% Cent.) 200 GeV:

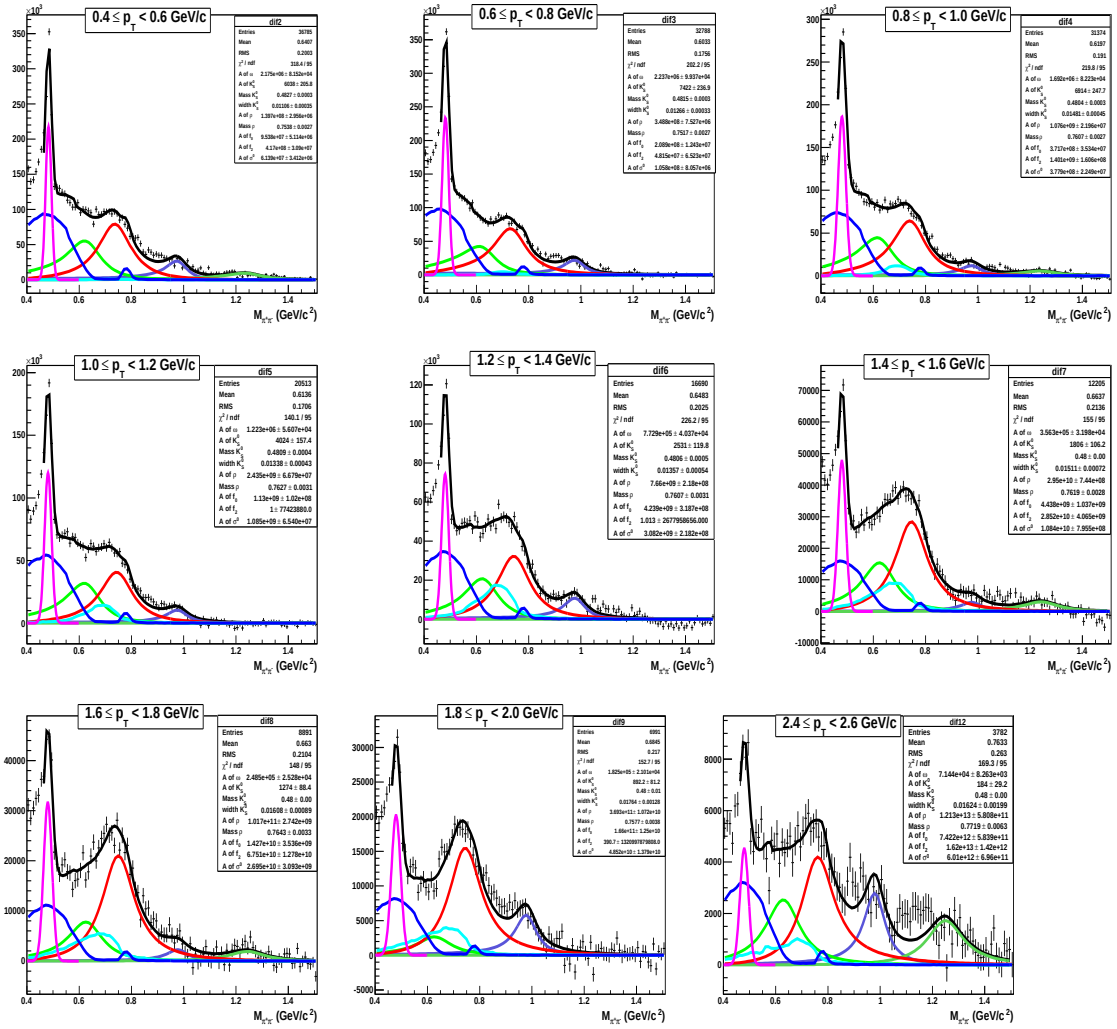

Figure 3.25: The $\pi^+\pi^-$ invariant mass distributions in 20-60% centrality in Cu+Cu at 200 GeV for different p_T bins, each having bin width 0.2 GeV/c. The solid black line is the hadronic cocktail fit function discussed in section 3.5 and 3.6. The units of the fit parameters mass and width are in GeV/c^2.

Invariant mass distributions in Au+Au (40-80% Cent.) 200 GeV:

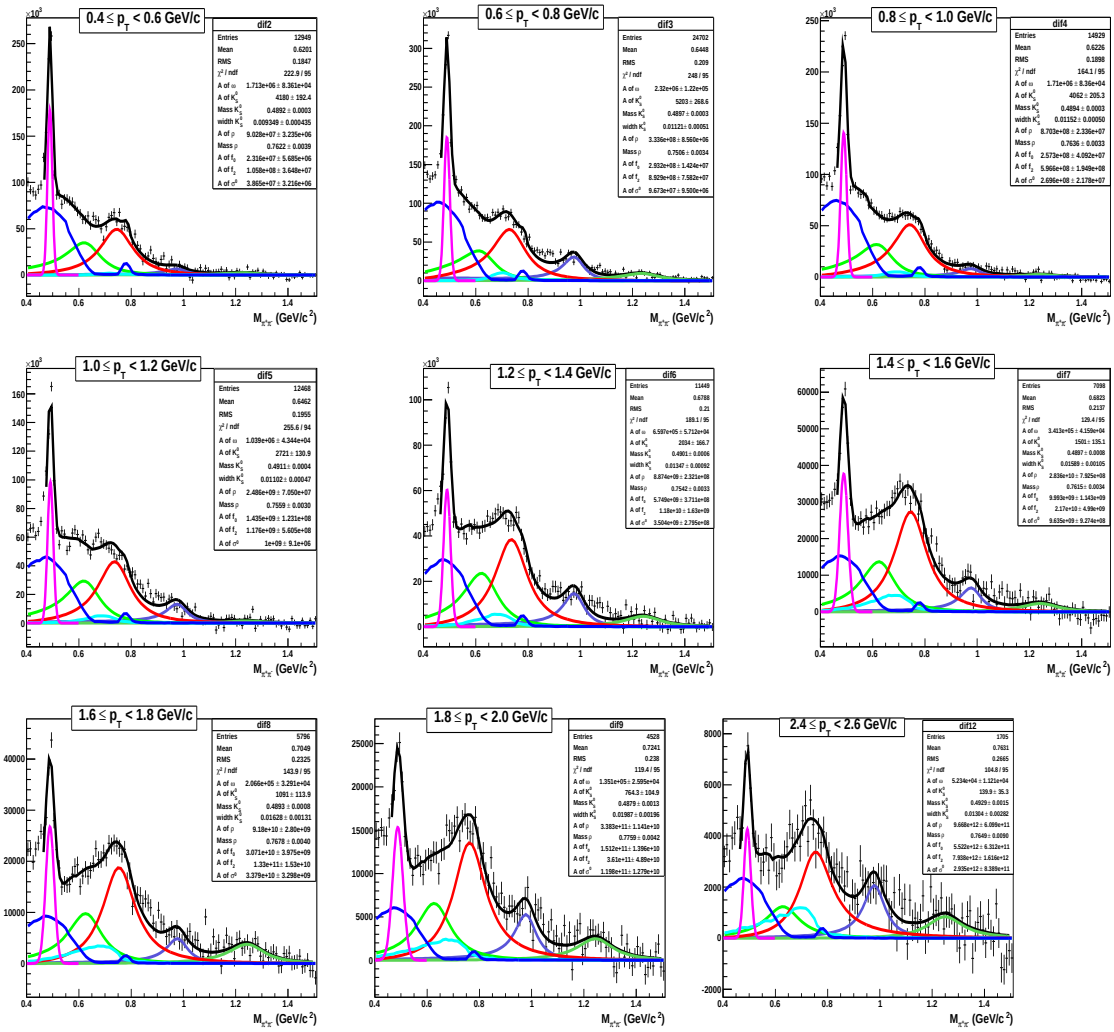

Figure 3.26: The $\pi^+\pi^-$ invariant mass distributions in 40-80% centrality in Au+Au at 200 GeV for different p_T bins, each having bin width 0.2 GeV/c. The solid black line is the hadronic cocktail fit function discussed in section 3.5 and 3.6. The units of the fit parameters mass and width are in GeV/c^2.

Chapter 4

ρ^0 Elliptic Flow (v_2) Measurement in Au+Au Collisions at $\sqrt{s_{NN}}$ = 200 GeV

The elliptic flow of any specific particle is nothing but the azimuthal anisotropy of the corresponding particle. In non-central nucleus-nucleus collisions, there is initial spatial anisotropy. This spatial anisotropy is transformed into an anisotropy in momentum space because of sufficient interactions among the constituents within the system. Once the system is expanded enough to quench the spatial anisotropy, further development of momentum anisotropy ceases. Because of this reason the signal of azimuthal anisotropy is self-quenching in nature and sensitive to the very early stages of the collisions. This phenomenon is called anisotropic flow [135–139], where the azimuthal angles of the outgoing particles are correlated with the impact parameter direction[140].

The elliptic flow (v_2) of hadrons shows a universal nature when scaled with the number of constituent quarks[141]. It has also been proposed that the measurement of elliptic flow of short-lived resonances can shed light on their production mechanism. That means, whether the short-lived resonances are produced during hadronization via quark-quark coalescence or later in the collision via hadron re-scattering [142]. Here, the measurement of elliptic flow (v_2) of the

ρ^0 ($\rho^0 \rightarrow \pi^+ + \pi^-$) vector meson can potentially provide more information in this direction [143].

4.1 Data Analysis

In this chapter, the elliptic flow (v_2) measurement of ρ^0 vector meson is discussed. For the differential measurement of elliptic flow, i.e. $v_2\,(p_T)$, of ρ^0 vector meson, a good amount of event statistics is required. That is why for this analysis, a higher statistic Au+Au data at $\sqrt{s_{NN}}$ = 200 GeV, taken during the year 2007, was used. The measurement of v_2 of ρ^0 was carried out in the peripheral, i.e. 40-80% centrality, events. Also, the v_2 measurement of ρ^0 was carried out in three different centrality bins, i.e. 20-30%, 40-60% and 60-80%, in Au+Au collisions. Though the current statistics did not allow us to make any conclusive statement on the centrality dependence of ρ^0 elliptic flow, but a systematic trend is observed similar to other identified particles, like π, K, p etc.

4.1.1 Event and Track Selection

The STAR experiment collected about 64 million minimum bias events during RHIC Run VII for Au+Au collisions at $\sqrt{s_{NN}}$ = 200 GeV. The details of the trigger and event selection for this data set are summarized in Table 4.1.

Trigger Set-up Name	Production	Vertex Cut	Trigger ID	No. of Events
2007ProductionMinBias	P08ic	$\pm$ 30 cm	200001, 200003	$\sim$ 50 M
2007Production2	P08ic	$\pm$ 30 cm	200013	$\sim$ 10 M

Table 4.1: Run VII trigger and events selection for minimum bias data in Au+Au collisions at $\sqrt{s_{NN}}$ =200 GeV.

Earlier the reference multiplicity was used to determine the centrality of the event. But in Run VII, because of the inclusion of inner tracking, the reference multiplicity could not be used to determine the centrality. This was because the reconstruction efficiency became a function of z-vertex position even if $|z|$-vertex

$<$ 30 cm. This was highly undesirable. This was not the case with the TPC tracks only. In order to avoid this problem, a new variable, called global reference multiplicity, was used to determine the centrality in Run VII data.

Global reference multiplicity is the number of global tracks, lying within the pseudo-rapidity coverage from -0.5 to 0.5, with TPC hits more than 10 and the distance of closest approach (DCA) to the primary vertex less than 3 cm. The nine centrality bins and the corresponding geometric cross-sections for Au+Au collisions are listed in Table 4.2.

Centrality Bin	Global Reference Multiplicity	Geometric Cross Section
1	10 - 20	70% - 80%
2	21 - 38	60% - 70%
3	39 - 68	50% - 60%
4	69 - 113	40% - 50%
5	114 - 177	30% - 40%
6	178 - 268	20% - 30%
7	269 - 398	10% - 20%
8	399 - 484	5% - 10%
9	$\geq$485	0% - 5%

Table 4.2: Run VII centrality bins in Au+Au collisions at $\sqrt{s_{NN}}$ = 200 GeV.

The remaining issues are biases on multiplicity distribution introduced by the main online Vertex Position Detector (VPD) trigger-setup (200013). The biases come from two sources. Firstly, the VPD is more efficient in triggering central events than peripheral events. This leads to a general deficit of peripheral events in a given data sample. Secondly, the online z-vertex resolution of VPD is worse for peripheral events compared to the central events.

The z-vertex dependent biases in multiplicity distribution requires a re-weighting correction to be applied for all analysis. For any analysis with a "signal" summed up over a range of global reference multiplicity, events at $|z|$-vertex ~ 0 cm will have their peripheral contribution scaled up in order to restore the unbiased case via the correction. The opposite will be true for events at higher $|z|$-vertex where the peripheral contribution will be scaled down again to restore the unbiased

case. The correction has to be applied as a function of z-vertex in 2 cm bins for acceptance reasons.

In a given z-vertex bin, the weights are determined by normalizing the global reference multiplicity distribution by the number of events with global reference multiplicity larger than 500. The Monte Carlo (MC) Glauber histogram is then divided by the normalized global reference multiplicity distribution to calculate the weights. Finally in each event, we multiply the event quantities by its weight which is obtained according to the z-vertex and global reference multiplicity in this event.

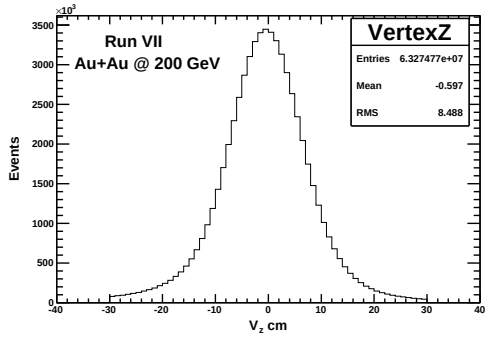

Figure 4.1: z-vertex distribution in Au+Au $\sqrt{s_{NN}}$ = 200 GeV Run VII data.

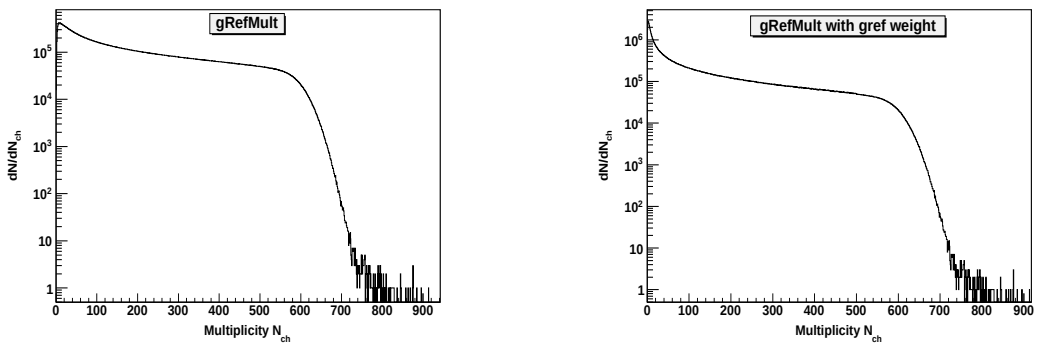

(a) Global reference multiplicity (b) Weighted global reference multiplicity

Figure 4.2: Reference Multiplicity distribution for minimum bias data in Au+Au collisions at $\sqrt{s_{NN}}$ = 200 GeV.

Figure 4.1 represents the z-vertex distribution in Au+Au at $\sqrt{s_{NN}}$ = 200 GeV RunVII data in the range between -30 cm. to +30 cm. Figure 4.2 (a) shows global

reference multiplicity distribution and (b) shows the global reference multiplicity distribution after the correction.

In this analysis, we have used wider centrality bin (40% - 80%) in peripheral Au+Au data to get better statistics. Thus, the four narrow centrality bins, i.e. 40%-50%, 50%-60%, 60%-70%, 70%-80%, are used to combine to a wider centrality bin. Approximately 30 M events in the peripheral Au+Au collisions are used for the v_2 measurement of ρ^0 in 40-80% centrality bins and pions are identified with a cut of $|N_{\sigma\pi}| < 3$.

4.2 Reaction Plane Estimation

In order to calculate the elliptic flow as described in section 1.5, the reaction plane angle (Ψ_r) which is unknown apriori has to be estimated on an event-by-event basis. The estimated reaction plane is known as event plane. The first step of the flow analysis is to determine the flow vector of each event. It is a two-dimensional vector known as event flow vector $Q = (Q_x, Q_y)$ and is defined as [144, 145]

$$Q_x = Qcos(n\Psi_n) = \sum_{i=1}^{M} \omega_i cos(n\phi_i), \tag{4.1}$$

$$Q_y = Qsin(n\Psi_n) = \sum_{i=1}^{M} \omega_i sin(n\phi_i), \tag{4.2}$$

where the sum goes over all detected particles in an event [144]. M is the observed multiplicity of the event, ϕ_i are the azimuthal angles of the produced particles measured with respect to a fixed direction in the laboratory. The coefficients ω_i in Equations 4.1 and 4.2 are the weights. Usually, the weights are assigned with the transverse momentum. The choice of weights is to make the event plane resolution the best by maximizing the flow contributions to the flow vector. The track selection criteria to reconstruct the event plane are listed in Table 4.3. The event plane angle can be calculated for each harmonic as follows:

$$\Psi_n = \frac{1}{n}\left[tan^{-1}\left(\frac{\sum_i \omega_i sin(n\phi_i)}{\sum_i \omega_i cos(n\phi_i)}\right)\right]. \tag{4.3}$$

Flow track selection criteria	TPC	FTPC
nHits	> 15	> 15
nHits/nMax	> 0.52	> 0.52
DCA	< 2 cm	< 2 cm
transverse momentum (GeV/c)	(0.15, 2)	(0.1, 2.0)
eta	< 1.0	(2.5, 4.0)

Table 4.3: Track selection criteria for flow analysis used in the event plane reconstruction in Au+Au collisions at $\sqrt{s_{NN}}$ = 200 GeV.

In this analysis, the weighting is done by taking the p_T and ϕ of each particle in each event and is defined as $\omega_i = p_T \times \omega_\phi$, where ω_ϕ is the ϕ-weight factor. The ϕ-weight correction is necessary to take care of the detector effects which can lead to anisotropic particle distributions in the lab frame. This anisotropic distribution can result a fake flow. Therefore, it is necessary to ensure the event plane angle distribution over all events to be isotropic, i.e. flat with respect to the azimuthal angle ϕ.

In order to calculate ω_ϕ, tracks from all events are distributed as a function of ϕ. Then, ω_ϕ is given as:

$$\omega_\phi = \frac{< N(\phi) >}{N(\phi)} \tag{4.4}$$

where $N(\phi)$ is the count in an azimuthal angle bin with its bin center at ϕ and $< N(\phi) >$ is the average of $N(\phi)$ over all the bins of ϕ. It is also important to perform the correction for the positive and negative η regions separately since the acceptance in the STAR TPC is different in the two regions.

Figure 4.3 (a) and (b) show the ϕ distributions of east ($\eta < 0$) and west ($\eta > 0$) TPC for 40-80% centrality in Au+Au collisions at $\sqrt{s_{NN}}$ = 200 GeV. The ϕ weights corresponding to east and west TPC are shown in Figure 4.3 (c) and (d), respectively.

Figure 4.4 shows the distribution of the event plane angle in Au+Au collisions at $\sqrt{s_{NN}}$ = 200 GeV. This distribution is supposed to be flat. So it is essential to test

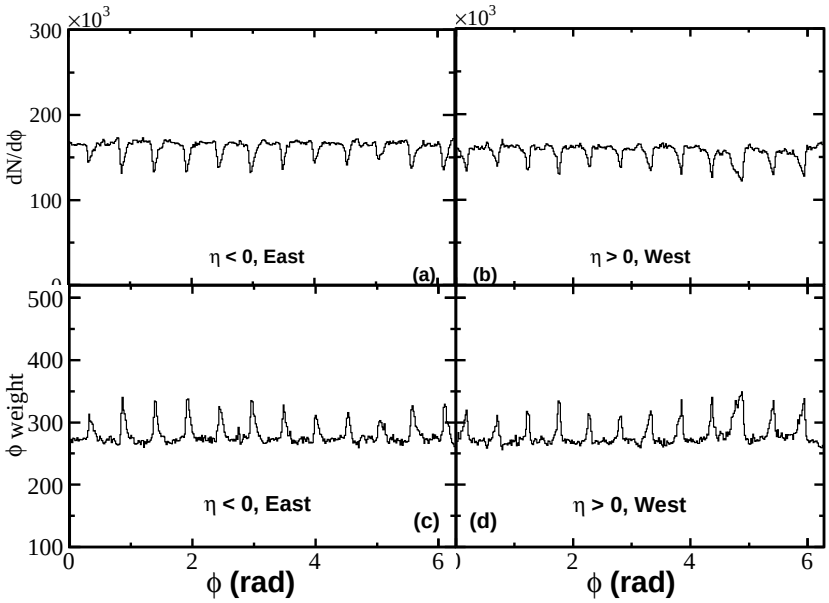

Figure 4.3: ϕ and the corresponding ϕ weight distributions in east and west TPC for 40-80% centrality in Au+Au collisions at $\sqrt{s_{NN}}$ = 200 GeV.

the flatness of the distribution. That is why this distribution is fitted to a function as follows:

$$p0\left[1 + p1 \times cos(2\Psi_2)\right]. \tag{4.5}$$

In Equation 4.5, the value of p_1 corresponds to the contribution from v_2. From the fitting, it is clear that there is negligible contribution (0.047%) from the non-flatness of the event plane in our study.

We have also used both the Forward Time Projection Chambers (FTPCs) to determine an event plane for each event. Since the FTPCs cover pseudo-rapidity from 2.5 to 4.0 and -2.5 to -4.0, it helps to reduce the non-flow contributions. These non-flow effects refer to the correlations those are not associated with the event plane.

Due to several acceptance loss for FTPC, the ϕ weight method alone is not sufficient enough to generate the flat event plane distribution for FTPC. Thus the shifting method [146] is applied in this analysis to make the event plane distribu-

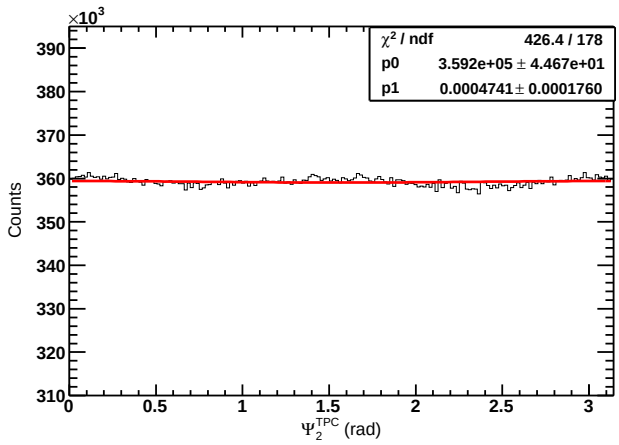

Figure 4.4: The distribution of the 2nd harmonic event plane angle (Ψ_2) from TPC in Au+Au collisions at $\sqrt{s_{NN}}$ = 200 GeV. The red solid line is the result from the fit function mentioned in the text.

tion flat. The corrected new angle is defined as:

$$\Psi' = \Psi + \delta\Psi \tag{4.6}$$

here $\delta\Psi$ is written in the form

$$\delta\Psi = \sum_n \left[A_n cos(n\Psi) + B_n sin(n\Psi)\right]. \tag{4.7}$$

Requiring the vanishing of the nth Fourier moment of the new distribution, the coefficients A_n and B_n can be evaluated by the original distributions

$$A_n = \frac{2}{n}\left\langle cos(n\Psi)\right\rangle, \tag{4.8}$$

$$B_n = -\frac{2}{n}\left\langle sin(n\Psi)\right\rangle, \tag{4.9}$$

where $\langle ... \rangle$ is the average over the whole event sample. Putting Equation 4.8 and 4.9 in Equation 4.7, the formula for the shift correction can be written as

$$\Psi' = \Psi + \sum_n \frac{1}{n} \left[- < sin\,(2n\Psi) > cos\,(2n\Psi) + < cos\,(2n\Psi) > sin\,(2n\Psi) \right]. \quad (4.10)$$

The average in Equation 4.10 goes over a large sample of events. In this analysis, the distributions of Ψ_2^{East} and Ψ_2^{West} are treated separately and then the full event plane distributions are constructed.

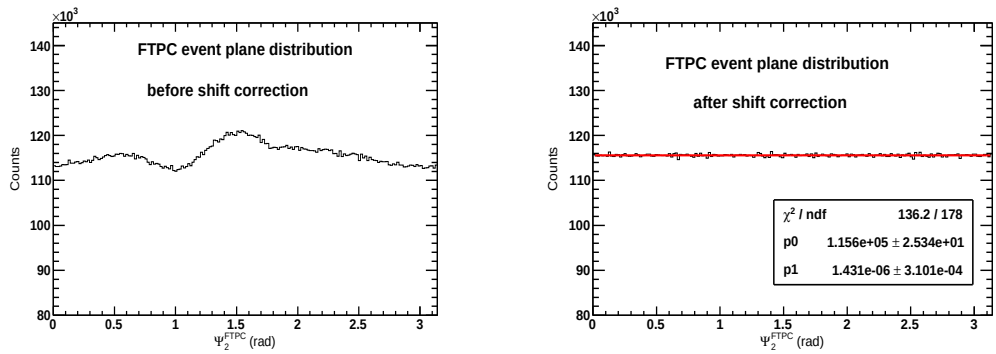

(a) Before shift correction (b) After shift correction

Figure 4.5: The distribution of the 2nd harmonic event plane angle (Ψ_2) from FTPC in Au+Au collisions at $\sqrt{s_{NN}}$ = 200 GeV. The red solid line in the right figure is the result from the fit function mentioned in the text.

Figure 4.5 (a) shows the second harmonic event plane azimuthal distribution only with the FTPC ϕ weight correction and Figure 4.5 (b) shows the FTPC event plane distribution after shift correction. The histogram in Figure 4.5 (b) is fitted to a function mentioned in Equation 4.5. From the fit parameter $p1$, it is very clear that the contribution of event plane itself towards the v_2 measurement is very negligible while considering the FTPC event plane.

4.3 Removal of Auto-correlations

While calculating the elliptic flow (v_2) in a specific psseudo-rapidity coverage, it is good to find out the event plane from a completely different pseudo-rapidity range to avoid the auto-correlations. For this, FTPC event plane would be the

ideal one. But because of the bad FTPC event plane resolution, due to less number of particles detected, in this analysis it is decided to consider the event plane from TPC. Hence, it is required to remove the auto-correlations while calculating the elliptic flow of ρ_0 vector meson in the mid-rapidity. To remove auto-correlations one has to subtract the Q-vector of the particle of interest from the total event Q-vector and obtain a Ψ_n to correlate with the particle [145, 147]. A bit detail of the procedure for removal of auto-correlations is discussed below.

Strong auto-correlations exist when tracks used to calculate the ρ^0 vector meson invariant mass are also used to calculate the reaction plane angle. These auto-correlations are eliminated by excluding those tracks already been used for the ρ^0 invariant mass calculation from the reaction plane angle estimation. In order to avoid the auto-correlations between tracks and to measure the ρ^0 elliptic flow correctly, the following technique has been followed. For each $\pi^+\pi^-$ pair in an event, we calculate the event plane angle by using all other primary tracks except these π^+ and π^- candidates. Now the original event plane angle in Equation 4.3 will become

$$\Psi_2' = \frac{1}{2}tan^{-1}\frac{\sum_i \omega_i sin(2\phi_i) - \omega_{\pi^+} sin(2\phi_{\pi^+}) - \omega_{\pi^-} sin(2\phi_{\pi^-})}{\sum_i \omega_i cos(2\phi_i) - \omega_{\pi^+} cos(2\phi_{\pi^+}) - \omega_{\pi^-} cos(2\phi_{\pi^-})} \tag{4.11}$$

The subscripts π^+ and π^- stand for positive pion and negative pion tracks, respectively. Using this method, the auto-correlations between $\pi^+\pi^-$ azimuthal angle ($\phi_{\pi^+\pi^-}$) and the event plane angle is avoided.

4.4 Extracting ρ^0 Elliptic Flow

The are several methods to calculate the elliptic flow coefficient (v_2). In our analysis, two different methods are adopted to extract the differential elliptic flow of ρ^0 vector meson. The most obvious one is the standard reaction plane method or known as ($\phi - \Psi_2$ bin) method [145] and the other one is called invariant mass method or known as (v_2 vs. m_{inv}) method [140]. Both the methods are based on the definition of $v_2 \equiv \langle cos2\,(\phi - \Psi_2)\rangle$ where both ϕ and Ψ_2 are measured with

respect to a lab-fixed frame of reference. The details of each method are outlined in the following subsections.

4.4.1 The Event Plane $(\phi - \Psi_2)$ bin Method

The standard $(\phi - \Psi_2)$ binning method of v_2 extraction of identified particles involves the measurement of the raw yield of the chosen particle in bins of the $(\phi - \Psi_2)$. Here, ϕ is the azimuthal angle of the particle in the lab-frame and Ψ_2 is the 2nd harmonic event plane angle. In order to have a better statistics, we have taken 5 bins of the $(\phi - \Psi_2)$ distribution in each of the p_T bin. After the like-sign background subtraction and the cocktail fit to the background subtracted invariant mass distribution as described in chapter 3, the ρ^0 yield has been obtained in each p_T and in each $(\phi - \Psi_2)$ bin. The extracted ρ^0 yield as a function of $(\phi - \Psi_2)$ can then be fitted by the following functional form to get the observed v_2 value:

$$\frac{dN}{d\,(\phi - \Psi_2)} = A[1 + 2v_2^{observed} cos2(\phi - \Psi_2)], \tag{4.12}$$

Figure 4.8 represents the $\pi^+\pi^-$ invariant mass distribution in six different p_T bins in the angle between $0 < \phi - \Psi_2 < \pi/5$ for Au+Au collisions at $\sqrt{s_{NN}}$ = 200 GeV. Figure 4.9 shows the same distribution in the angle between $\pi/5 < \phi - \Psi_2 < 2\pi/5$. Figure 4.10, Figure 4.11, Figure 4.12 are the same $\pi^+\pi^-$ invariant mass distributions in angles $2\pi/5 < \phi - \Psi_2 < 3\pi/5$, $3\pi/5 < \phi - \Psi_2 < 4\pi/5$, $4\pi/5 < \phi - \Psi_2 < \pi$, respectively.

Once the ρ^0 counts are obtained from each $(\phi - \Psi_2)$ bins for a particular p_T bin, the ρ^0 counts are plotted as a function of $(\phi - \Psi_2)$. Figure 4.13 represents $(\phi - \Psi_2)$ distributions for different p_T bins used in this analysis. The solid line is the fit result to the data with Equation 4.12 where the two free fitting parameters P_0 corresponds to the constant of proportionality A and P_1 corresponds to $v_2^{0observed}$.

Especially for the case of resonances, where the signal typically consists of a very small mass peak sitting above a large combinatorial background, i.e. the signal to background ratio is very poor, it is a difficult task to extract the raw

yields accurately. Again, the $(\phi - \Psi_2)$ bin method of extracting v_2 requires that for each p_T bin, the already small signal is further divided into bins of $(\phi - \Psi_2)$ angle. This can lead to a large systematic errors in the final v_2 measurement as the systematic (or statistical) error in extracting the raw yield is large. Because of this reason, another method (v_2 vs. m_{inv}), described in the following section, is used to extract the resonance v_2 coefficient.

4.4.2 The v_2 vs. m_{inv} Method

A different method, i.e. v_2 vs. m_{inv}, is applied to extract the v_2 of ρ^0 meson. This method is inspired by "Azimuthally sensitive correlations in nuclus-nucleus collisions" proposed by N. Borghini and J.O. Ollitraut [140]. A brief description taken from the referenced paper, is mentioned below.

The probability distribution in terms of the azimuthal angle ϕ can be written as:

$$P(\phi - \Psi_r) = \frac{1}{2\pi} \sum_{n=-\infty}^{+\infty} v_n e^{in(\phi - \Psi_r)} \tag{4.13}$$

where ϕ is the azimuthal angle of the particle and Ψ_r is the reaction plane angle. In case of a symmetric system with real v_n, Equation 4.13 reduces to:

$$P(\phi - \Psi_r) = \frac{1}{2\pi} \left[1 + 2 \sum_{n=1}^{\infty} v_n cos(n(\phi - \Psi_r)) \right]. \tag{4.14}$$

Equation 4.13, can be extended for pair of particles as:

$$P(\phi_{pair} - \Psi_r) = \frac{1}{2\pi} \sum_{n=-\infty}^{+\infty} v_n^{pair} e^{in(\phi_{pair} - \Psi_r)} \tag{4.15}$$

where ϕ is replaced by ϕ_{pair}. In case of resonances, ϕ_{pair} is the azimuthal angle of the parent resonance particle. v_n^{pair} are called the pair-flow coefficients. But unlike in the previous case of single particles, here v_n^{pair} are not necessarily real numbers [140]. Hence, both cosine and sine terms exist in the Fourier expansion. Now the probability becomes

$$P(\phi_{pair} - \Psi_r) = \frac{1}{2\pi}\left(1 + 2\sum_{n=1}^{+\infty}[v_{c,n}^{pair} cos\left(n(\phi_{pair} - \Psi_r)\right) + v_{s,n}^{pair} sin\left(n(\phi_{pair} - \Psi_r)\right)]\right), \tag{4.16}$$

where the real coefficients $v_{c,n}^{pair} = < cos[n(\phi_{pair} - \Psi_r)] >$ and $v_{s,n}^{pair} = < sin[n(\phi_{pair} - \Psi_r)] >$ are related to the complex v_n^{pair} by the relation $v_n^{pair} = v_{c,n}^{pair} - iv_{s,n}^{pair}$.

In experimental analysis, any method that can be used to measure the single-particle flow v_n can be applied to extract the cosine terms $v_{c,n}^{pair}$. Without any modification one can simply consider the pair as a single particle with azimuthal angle ϕ_{pair} [140]. A resonance particle, identified through its mass peak in an invariant mass distribution, consists of signal and background in its mass peak region. The invariant mass distribution can be separated into:

$$N_{pair}\left(m_{inv}\right) = N_{Bg}\left(m_{inv}\right) + N_{Sig}\left(m_{inv}\right) \tag{4.17}$$

where N_{Bg} is the number of combinatorial background pairs and N_{Sig} is the number of signal pairs (the number of real pairs). One then performs a decomposition similar to Equation 4.17 for the azimuthally dependent part of the pair-flow coefficients. In a similar way, for a resonance particle, we can write the contributions to the pair-flow coefficients as:

$$N_{pair}\left(m_{inv}\right) v_{c,n}\left(m_{inv}\right) = N_{Bg}\left(m_{inv}\right) v_{c,n}^{Bg}\left(m_{inv}\right) + N_{Sig}\left(m_{inv}\right) v_{c,n}^{Sig} \tag{4.18}$$

$$N_{pair}\left(m_{inv}\right) v_{s,n}\left(m_{inv}\right) = N_{Bg}\left(m_{inv}\right) v_{s,n}^{Bg}\left(m_{inv}\right) + N_{Sig}\left(m_{inv}\right) v_{s,n}^{Sig}. \tag{4.19}$$

Because of the symmetry of the particle with respect to the reaction plane, $v_{s,n}^{Sig} = 0$ and if the background is composed of uncorrelated particles, then $v_{s,n}^{Bg} = 0$ [140]. Based on Equation 4.18, the v_2 distribution as a function of invariant mass (m_{inv}) can be fitted using:

$$v_2^{Sig+Bg}(m_{inv}) = v_2^{Sig} \times \frac{N_{Sig}}{N_{Sig+Bg}}(m_{inv}) + v_2^{Bg}(m_{inv}) \times \frac{N_{Bg}}{Sig+Bg}(m_{inv}) \tag{4.20}$$

The v_2 of all resonance candidates is divided into two parts, one is the signal v_2 multiplied with the signal yields, and the other is background v_2 multiplied with the background yields as shown in Equation 4.20.

Before applying this technique to extract the v_2 of ρ^0, it was checked with a narrow resonance such as ϕ meson where the background is nicely explained by a polynomial function. Figure 4.6 (a) shows one example plot for the ϕ meson invariant mass distribution in our calculation for RunVII Au+Au collisions at $\sqrt{s_{NN}}$ = 200 GeV, where the signal is fit with a BW function and the background is fit with a polynomial function. By fitting the signal and background, as shown in Figure 4.6 (a), $\frac{N_{Sig}}{N_{Sig+Bg}}$ and $\frac{N_{Bg}}{N_{Sig+Bg}}$ can be obtained. Here, we assume that v_2^{Bg} is a linear function of invariant mass (m_{inv}).

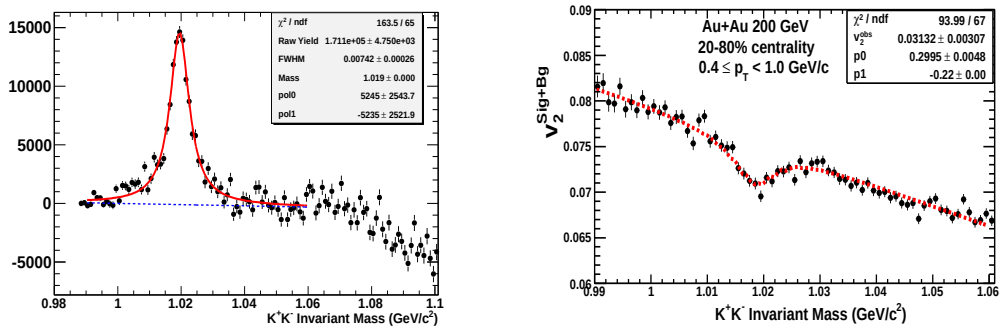

(a) K^+K^- invariant mass

(b) v_2^{Total} vs. m_{inv}

Figure 4.6: (a) The invariant mass of K^+K^- fitted with a BW function after background subtraction, (b) The total v_2 as a function of K^+K^- invariant mass. The red curve is the fitting function mentioned in Equation 4.20.

A 3rd order polynomial fit to describe the background distribution is shown as solid dotted line. $\frac{N_{Sig}}{N_{Sig+Bg}}(m_{inv})$ is obtained by dividing the BW fit line by data. $\frac{N_{Sig}}{N_{Sig+Bg}}(m_{inv})$ is calculated as $\left(1 - \frac{N_{Sig}}{N_{Sig+Bg}}\right)$. Then the total v_2 which is v_2^{Sig+Bg} is plotted as a function of m_{inv} and fitting with Equation 4.20 will give rise to the

observed v_2 parameter for ϕ meson. Figure 4.6 (b) shows one such example of the fitting result.

For a broad resonance, such as ρ^0 ($\rho^0 \rightarrow \pi^+ + \pi^-$), the v_2 of $\pi^+\pi^-$ pairs is composed of the v_2 of the background, the v_2 of the ρ^0 signal and the v_2 for all other particles used in the cocktail. Since our main focus is to find out the v_2 of ρ^0, we shall be only discussing the v_2 contribution coming from ρ^0 in the whole $\pi^+\pi^-$ continuum in this analysis. In this way, the invariant mass distribution can be separated into:

$$N_{\pi^+\pi^-}(m_{inv}) = N_{Sig}(m_{inv}) + N_{Bg}(m_{inv}) \tag{4.21}$$

where $N_{\pi^+\pi^-}(m_{inv})$ is the total number of $\pi^+\pi^-$ pairs in each invariant mass bin, $N_{Sig}(m_{inv})$ is the number of signals and $N_{Bg}(m_{inv})$ is the background pairs in the particular invariant mass bin. So the total v_2 of the $\pi^+\pi^-$ pairs vs. invariant mass can be described by the function:

$$v_2^{Sig+Bg}(m_{inv}) = v_2^{Sig} \times \frac{N_{Sig}}{N_{Sig+Bg}}(m_{inv}) + v_2^{Bg}(m_{inv}) \times \left[1 - \frac{N_{Sig}}{N_{Sig+Bg}}\right](m_{inv}). \tag{4.22}$$

The right hand side of Equation 4.22 is used to fit the data obtained from the v_2^{Sig+Bg} as a function of invariant mass to extract the observed v_2 signal, which is one of the free parameters in the fitting function. Also, for a narrow resonance signal (for example ϕ-meson), the v_2^{Bg} is assumed to be a polynomial function which makes the calculation much simpler. In case of ρ^0 vector meson v_2 analysis, the background is much more complicated and many resonance particles are contributing to the background within the ρ^0 mass range. That is why the v_2 of the background is estimated from the data instead of just assuming a polynomial function. Therefore, in our analysis, the above Equation 4.22 is modified to

extract the v_2 of ρ^0 vector meson as follows:

$$\begin{aligned} v_2^{Sig+Bg}(m_{inv}) &= v_2^{\rho^0} \times \frac{N_{\rho^0}}{N_{Sig+Bg}}(m_{inv}) \\ &+ v_2^{\sigma^0} \times \frac{N_{\sigma^0}}{N_{Sig+Bg}}(m_{inv}) \\ &+ v_2^{\omega^0} \times \frac{N_{\omega^0}}{N_{Sig+Bg}}(m_{inv}) \\ &+ v_2^{K_S^0} \times \frac{N_{K_S^0}}{N_{Sig+Bg}}(m_{inv}) \\ &+ v_2^{f_0} \times \frac{N_{f_0}}{N_{Sig+Bg}}(m_{inv}) \\ &+ v_2^{f_2} \times \frac{N_{f_2}}{N_{Sig+Bg}}(m_{inv}) \end{aligned} \tag{4.23}$$

where $N_{Bg} = N_{Sig+Bg} - (N_{\rho^0} + N_{\sigma^0} + N_{\omega^0} + N^0_{K_S} + N_{f_0} + N_{f_2})$.

Figure 4.14 represents few example plots of the cocktail fitting to the background subtracted invariant mass distributions in different transverse momentum bins in Au+Au RunVII data at $\sqrt{s_{NN}}$ = 200 GeV in 40-80% centrality. In Figure 4.15, the v_2^{Sig+Bg} vs. m_{inv} distribution is fitted to a function described in Equation 4.23 for different p_T bins. The fitting results for the observed v_2 parameters of ρ^0 are shown in each plot along with the observed v_2 parameters of other particles in the cocktail function.

In case of FTPC event plane, we have merged few p_T bins into one to get better statistics and therefore, we have less number of data points. Figure 4.16 shows the results of the fit to extract the v_2 of ρ^0 meson for FTPC event plane.

As the fitting covers a wider range of m_{inv} for ρ^0, the data points far from the mass peak region come from background contributions. Thus, in this case $\frac{N_{Bg}}{N_{Sig+Bg}}(m_{inv})$ is equal to 1. v_2^{Sig+Bg} data points in this region have strong constraint on v_2^{Bg} while doing the fitting.

4.5 Event Plane Resolution Correction

There is a limited number of tracks in each event to estimate the reaction plane. Therefore, there is a finite resolution of the estimated event plane angle. In order to calculate the true value of the elliptic flow coefficient (v_2), the observed v_2 value obtained using the described methods in section 4.4.1 and 4.4.2 must be corrected for the event plane resolution factor. The non-zero resolution factor always makes the observed v_2 value smaller than the true v_2. So the final v_2 in this case will be written as:

$$v_2 = \frac{v_2^{observed}}{< cos[2\,(\Psi_2 - \Psi_r)] >} \tag{4.24}$$

The event plane resolution for v_2 can be expressed as [145]:

$$< cos(2(\Psi_2 - \Psi_r)) >= \frac{\sqrt{\pi}}{2\sqrt{2}}\chi_2 exp(-\chi_2^2/4)[I_0(\chi_2^2/4) + I_1(\chi_2^2/4)], \tag{4.25}$$

where I_0 and I_1 are the modified Bessel function of order 0 and 1, respectively.

The resolution can be estimated using the correlation of the event planes calculated using independent sub-events. For this analysis, the sub-events were reconstructed by randomly dividing particles (which satisfy the condition to be used in the event plane calculation) into two groups, (A) and (B). Then, the correlation between flow angles of independent sets of particles can be written in the simple relation:

$$\left\langle cos\left[2\left(\Psi_2^A - \Psi_2^B\right)\right]\right\rangle = \left\langle cos\left[2\left(\Psi_2^A - \Psi_r\right)\right]\right\rangle \times \left\langle cos\left[2\left(\Psi_2^B - \Psi_r\right)\right]\right\rangle. \tag{4.26}$$

Since the multiplicity of each sub-event A and B should be approximately same and their respective resolutions should be equal, the resolution of each sub-events is given by:

$$\left\langle cos\left(2\left(\Psi_2^A - \Psi_r\right)\right)\right\rangle = \sqrt{\langle cos\left(2\left(\Psi_2^A - \Psi_2^B\right)\right)\rangle}. \tag{4.27}$$

Now, the event plane resolution determined in the above way is the event plane resolution of the sub events. Then, the full event plane resolution can be calcu-

lated from the sub-event resolution using Equation 4.25 taking into account that the multiplicity of the full event is twice as large as the multiplicity of the sub-event. Because $\chi_2 = v_2/\sigma$ is proportional to $\sqrt{N}$, Equation 4.27 reduces to

$$\langle cos\left(2\left(\Psi_2 - \Psi_r\right)\right)\rangle = \sqrt{2}\left\langle cos\left(2\left(\Psi_2^A - \Psi_r\right)\right)\right\rangle . \tag{4.28}$$

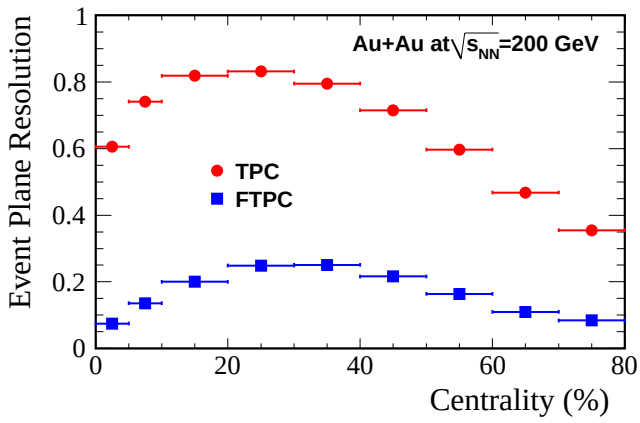

Figure 4.7: The 2nd order TPC event plane and FTPC event plane resolution for v_2 in Au+Au collisions for 9 different centrality bins at $\sqrt{s_{NN}}$ = 200 GeV.

Centrality (%)	**Ψ_2 Resolution (TPC)**	**Ψ_2 Resolution (FTPC)**
0-5%	0.605164 ± 0.000537	0.074567 ± 0.000600
5-10%	0.740933 ± 0.000360	0.135662 ± 0.000503
10-20%	0.818574 ± 0.000188	0.200273 ± 0.000430
20-30%	0.831454 ± 0.000184	0.248951 ± 0.000385
30-40%	0.794789 ± 0.000224	0.250984 ± 0.000349
40-50%	0.714916 ± 0.000310	0.216444 ± 0.000325
50-60%	0.596990 ± 0.000466	0.163508 ± 0.000318
60-70%	0.467668 ± 0.000755	0.109759 ± 0.000476
70-80%	0.354777 ± 0.001241	0.084352 ± 0.002105

Table 4.4: TPC and FTPC event plane resolution in Au+Au collisions at $\sqrt{s_{NN}}$ = 200 GeV for different centralities.

The event plane resolution for TPC and FTPC as a function of centrality is shown in Figure 4.7. The event plane resolution increases from central to mid-central and then it decreases towards peripheral. This is because the event plane

resolution depends on the multiplicity taken in the calculation and the strength of the anisotropic flow. Although in the central event, the multiplicity is high, the anisotropic flow is very very small and vice versa in the peripheral events. That is why the event plane resolution is small at both central as well as peripheral events. The red solid circles in Figure 4.7 represents the event plane resolution of TPC, whereas the blue solid squares represent the event plane resolution of FTPC. The values of the event plane resolution are given in Table 4.4. Since the multiplicity of FTPC is small compared to TPC, the event plane resolution of FTPC is small compared to TPC. The event plane resolution for wider centrality bins for ρ^0 analysis is calculated by weighting the event plane resolution with the corresponding ρ^0 yield. The event plane resolutions of TPC and FTPC in 40-80% centrality Au+Au collisions are 0.5964 and 0.1493, respectively.

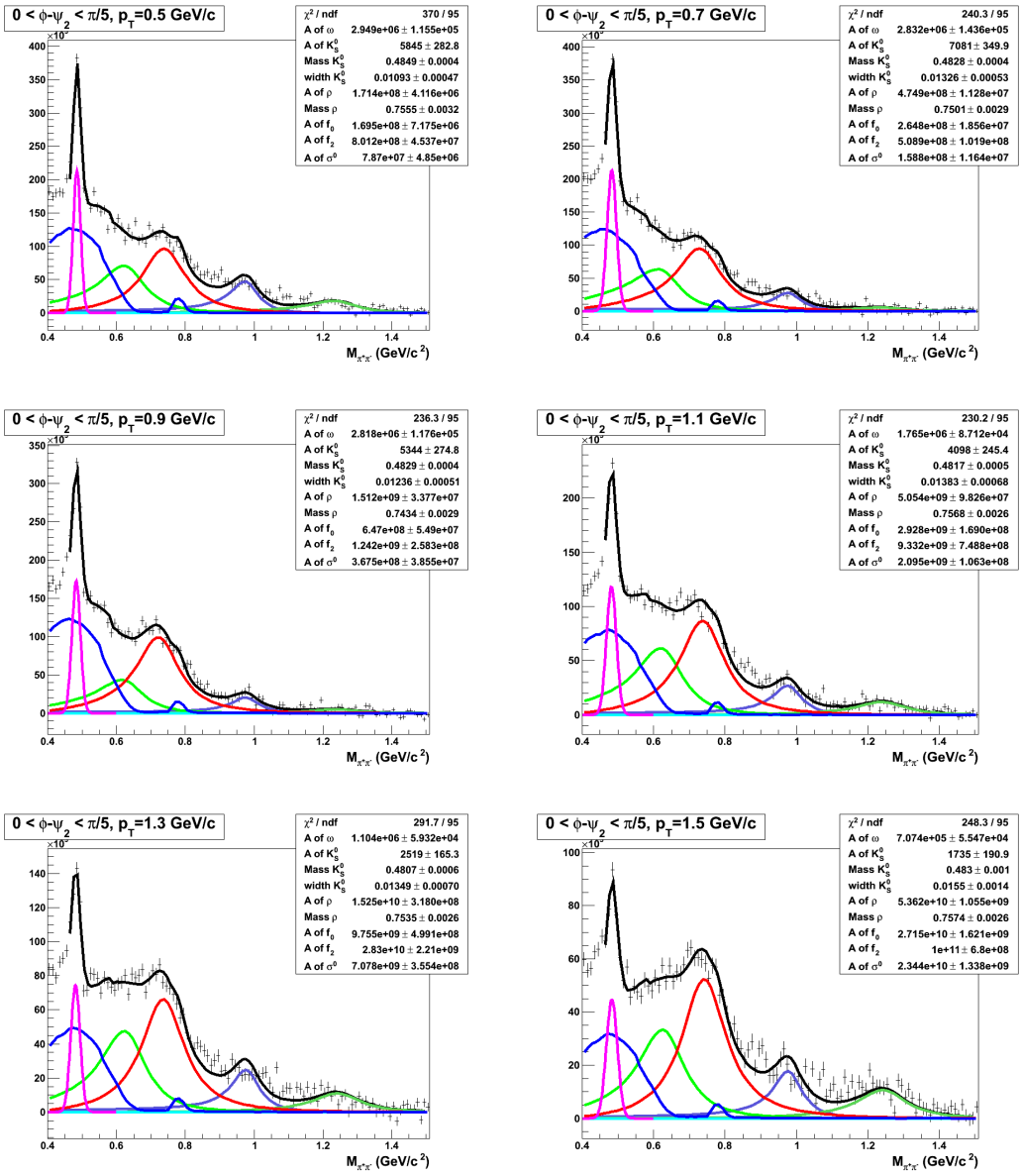

Figure 4.8: The $\pi^+\pi^-$ invariant mass distribution fit with the hadronic cocktail for $0 < \phi - \Psi_2 < \pi/5$ in different p_T windows in Au+Au 40-80% centrality.

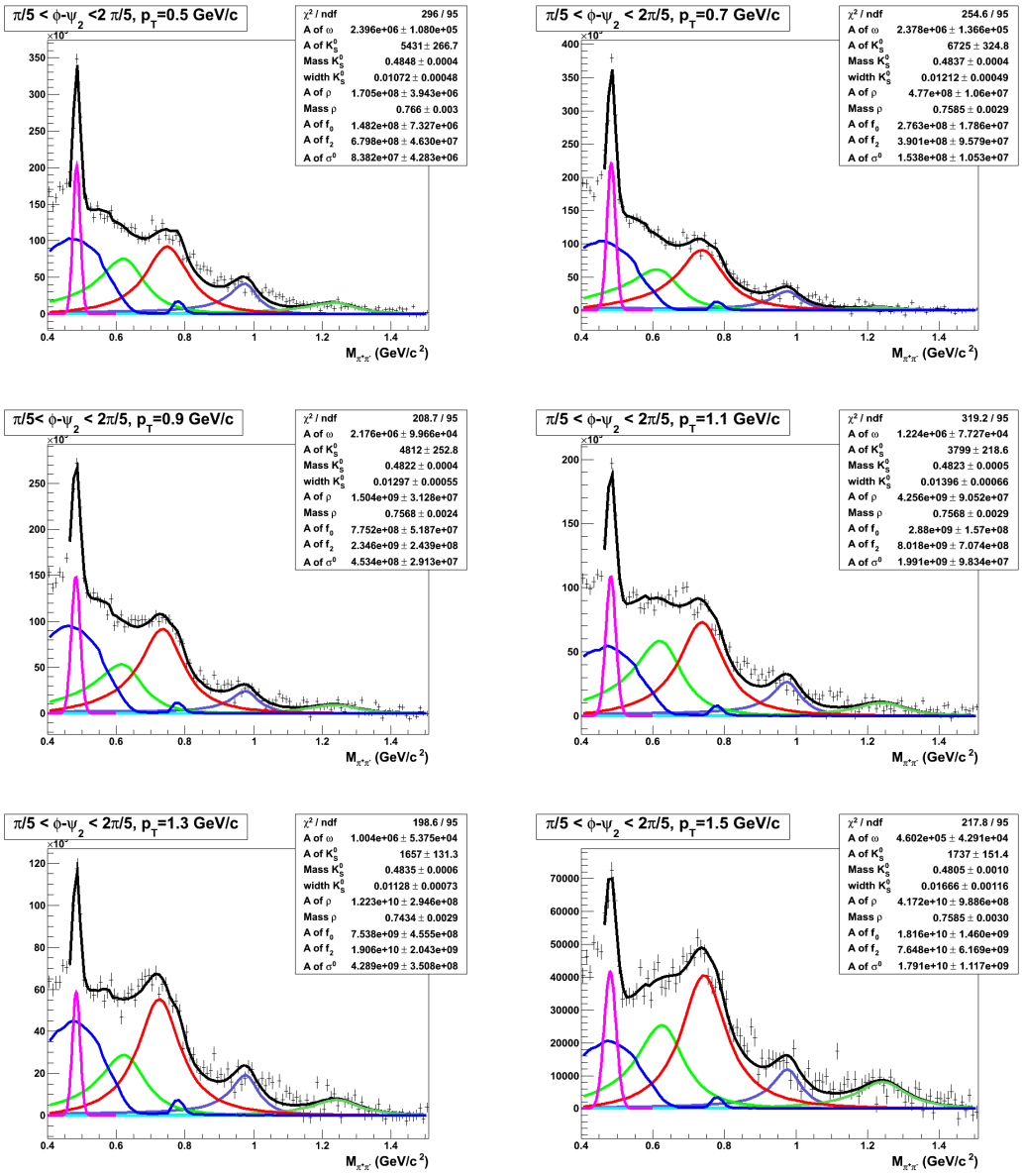

Figure 4.9: The $\pi^+\pi^-$ invariant mass distribution fit with the hadronic cocktail for $\pi/5 < \phi - \Psi_2 < 2\pi/5$ in different p_T windows in Au+Au 40-80% centrality.

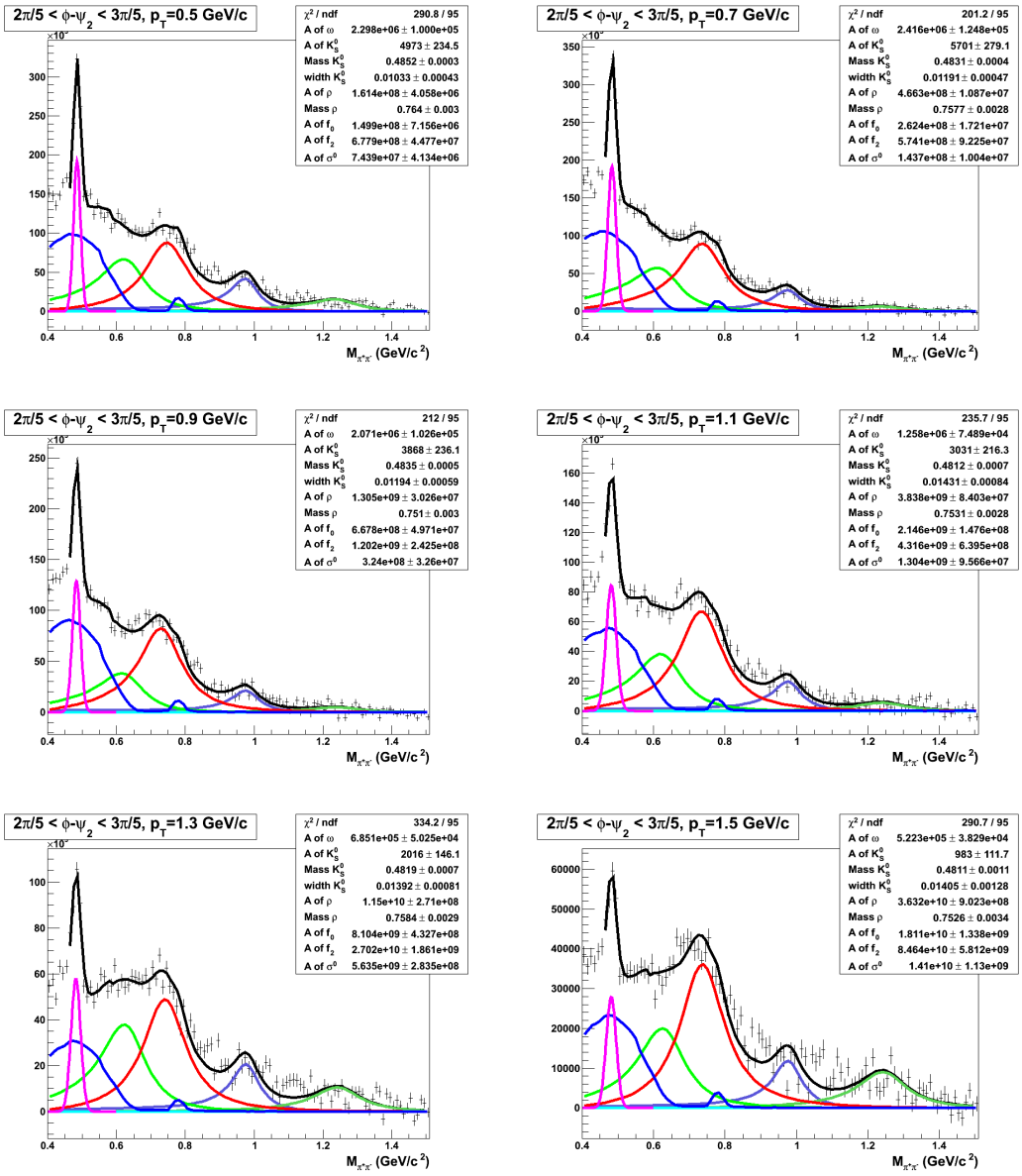

Figure 4.10: The $\pi^+\pi^-$ invariant mass distribution fit with the hadronic cocktail for $2\pi/5 < \phi - \Psi_2 < 3\pi/5$ in different p_T windows in Au+Au 40-80% centrality.

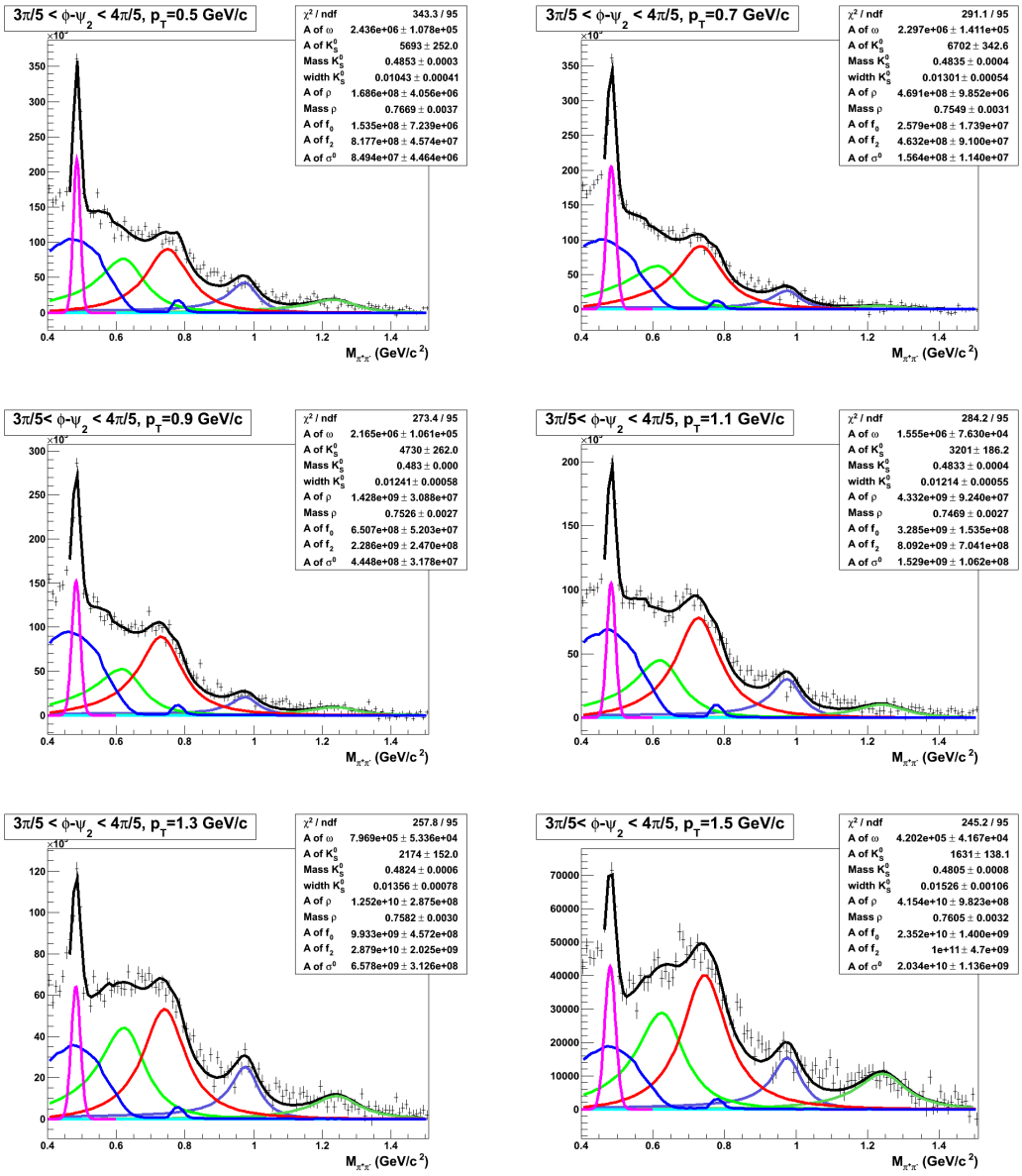

Figure 4.11: The $\pi^+\pi^-$ invariant mass distribution fit with the hadronic cocktail for $3\pi/5 < \phi - \Psi_2 < 4\pi/5$ in different p_T windows in Au+Au 40-80% centrality.

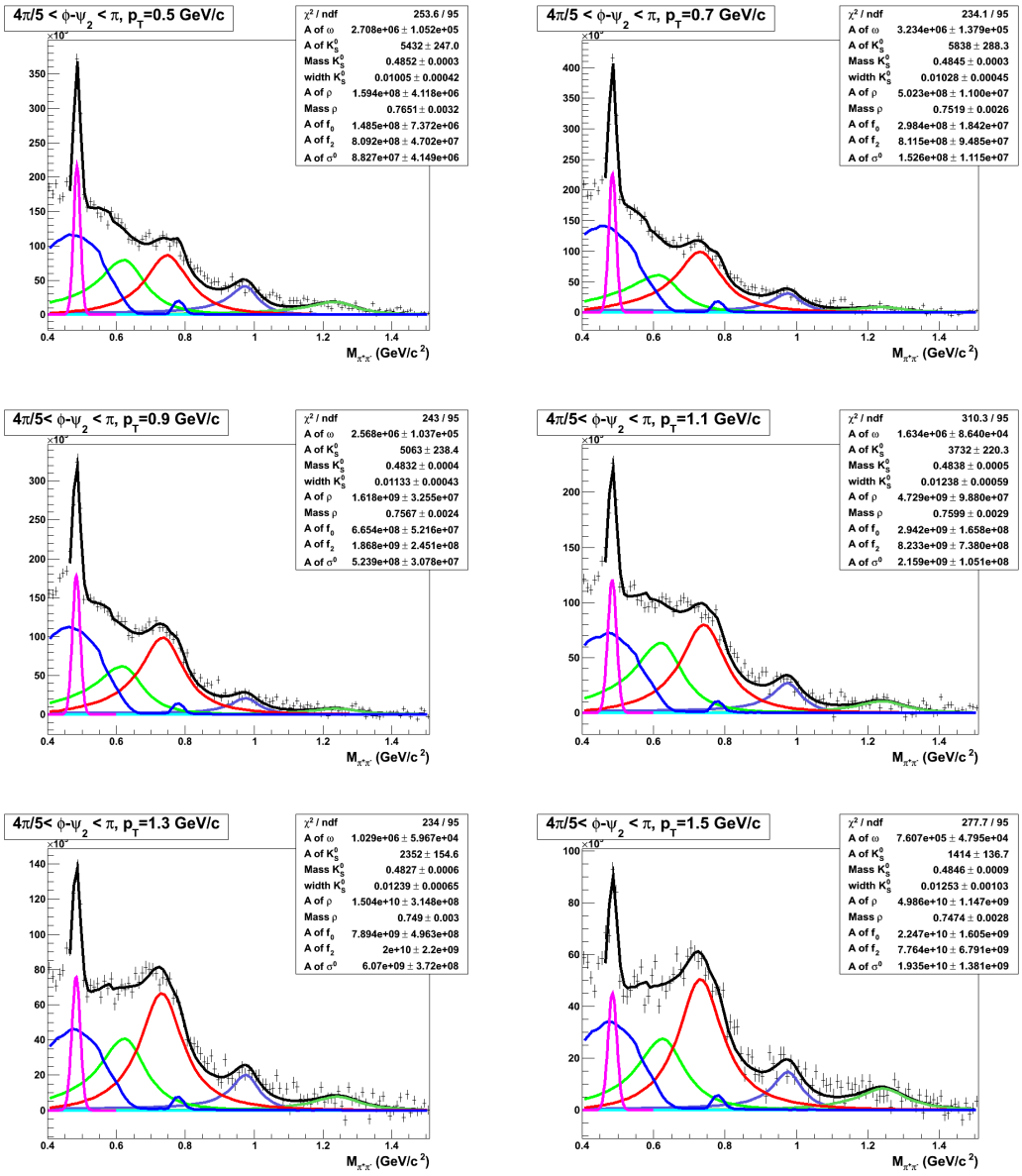

Figure 4.12: The $\pi^+\pi^-$ invariant mass distribution fit with the hadronic cocktail for $4\pi/5 < \phi - \Psi_2 < \pi$ in different p_T windows in Au+Au 40-80% centrality.

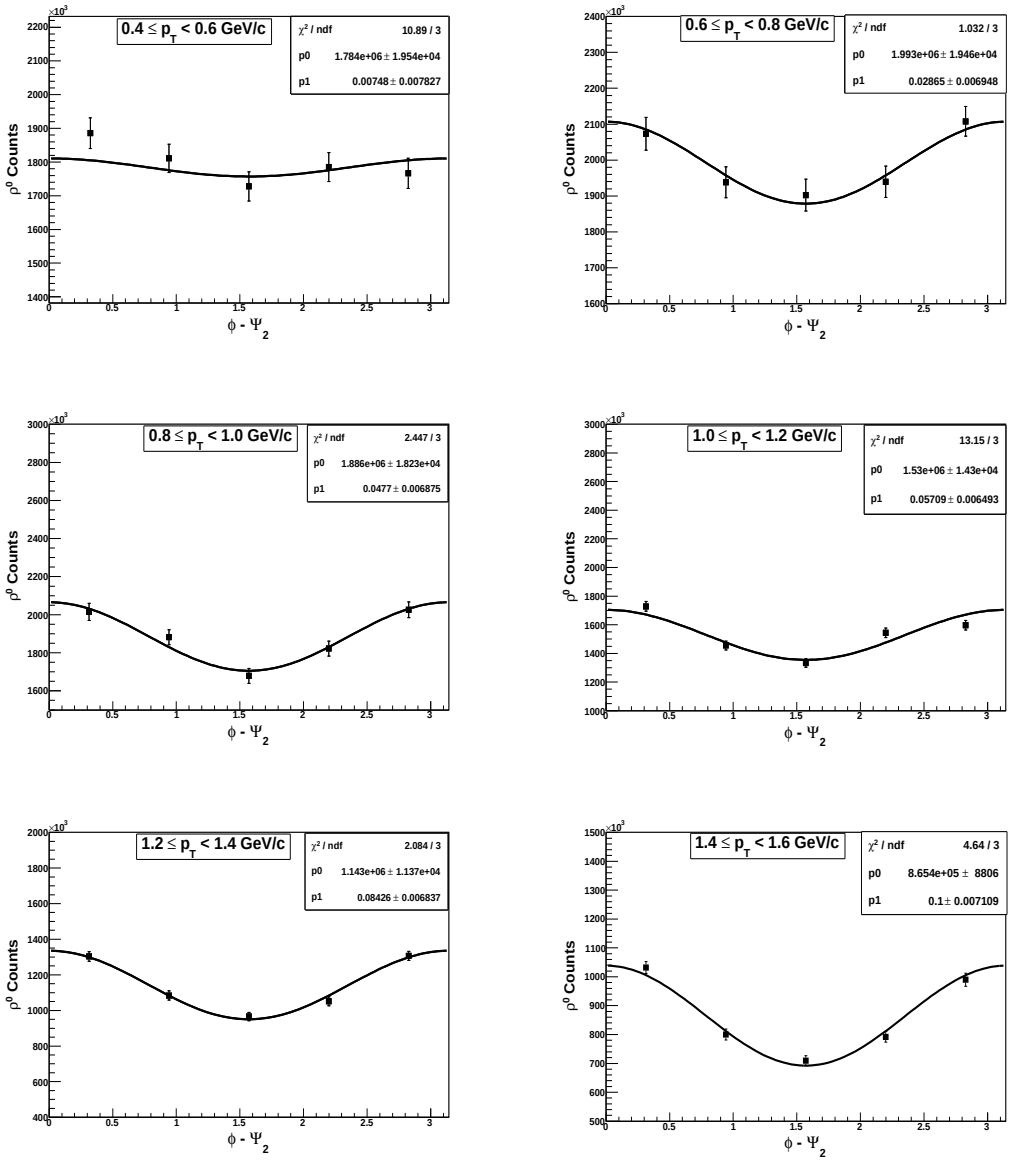

Figure 4.13: The ρ^0 yield as a function of $\phi - \Psi_2$ in 40-80% Au+Au collisions in different p_T bins.

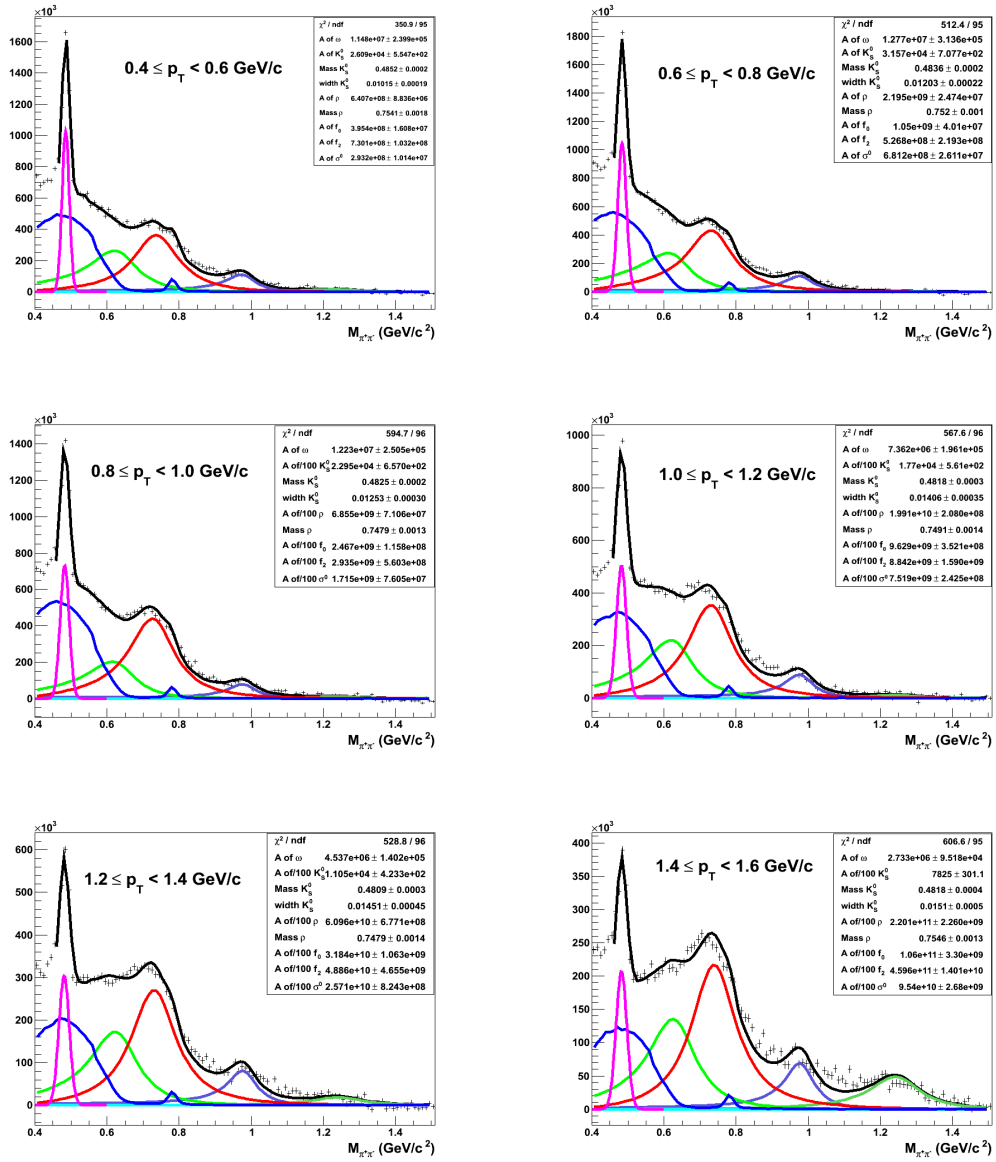

Figure 4.14: The $\pi^+\pi^-$ invariant mass distributions in different p_T bins for 40-80% centrality in Au+Au collisions. These plots are used in the ρ^0 yield extractions for the v_2 measurement in the v_2 vs. m_{inv} method.

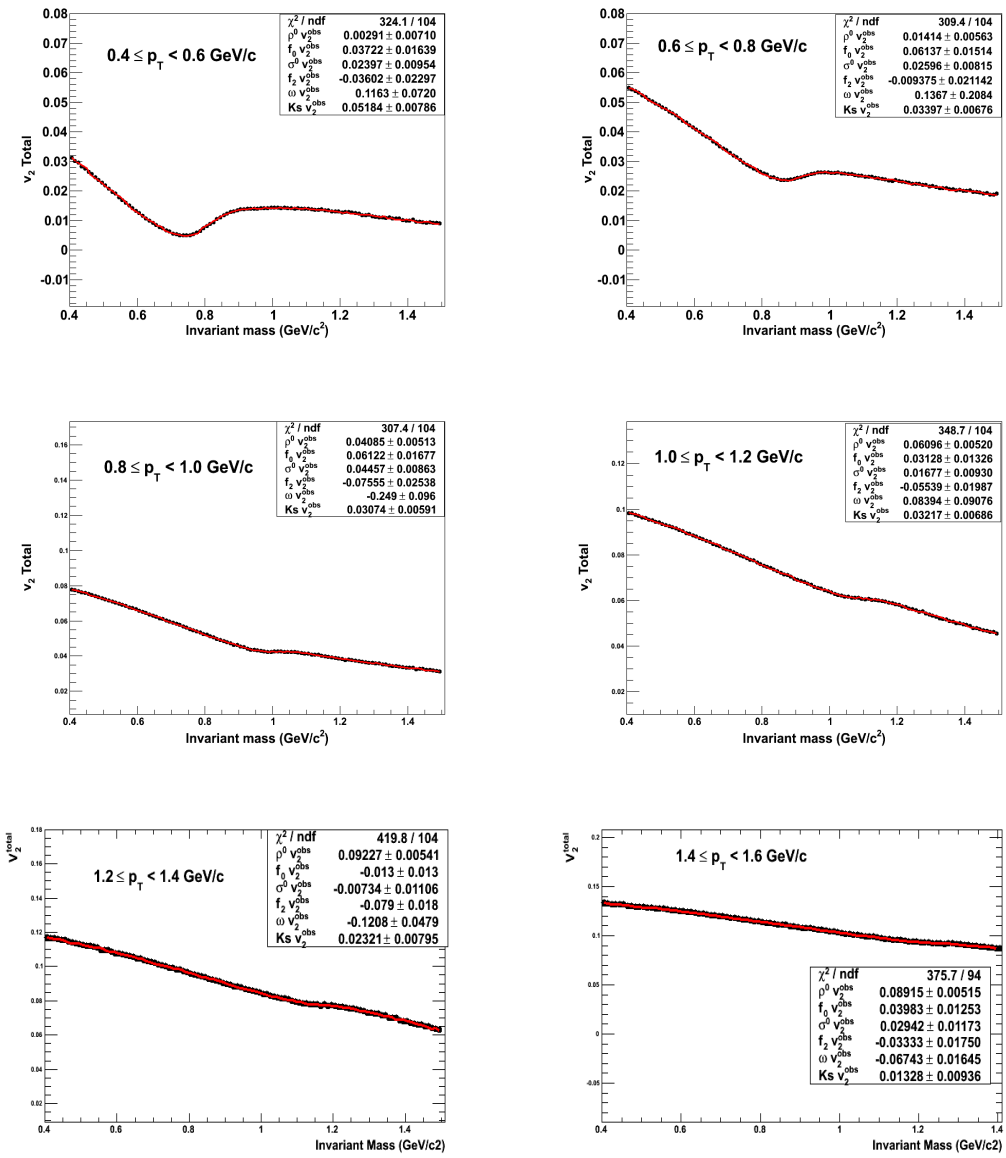

Figure 4.15: The total v_2 as a function of $\pi^+\pi^-$ invariant mass where the event plane is reconstructed from TPC.

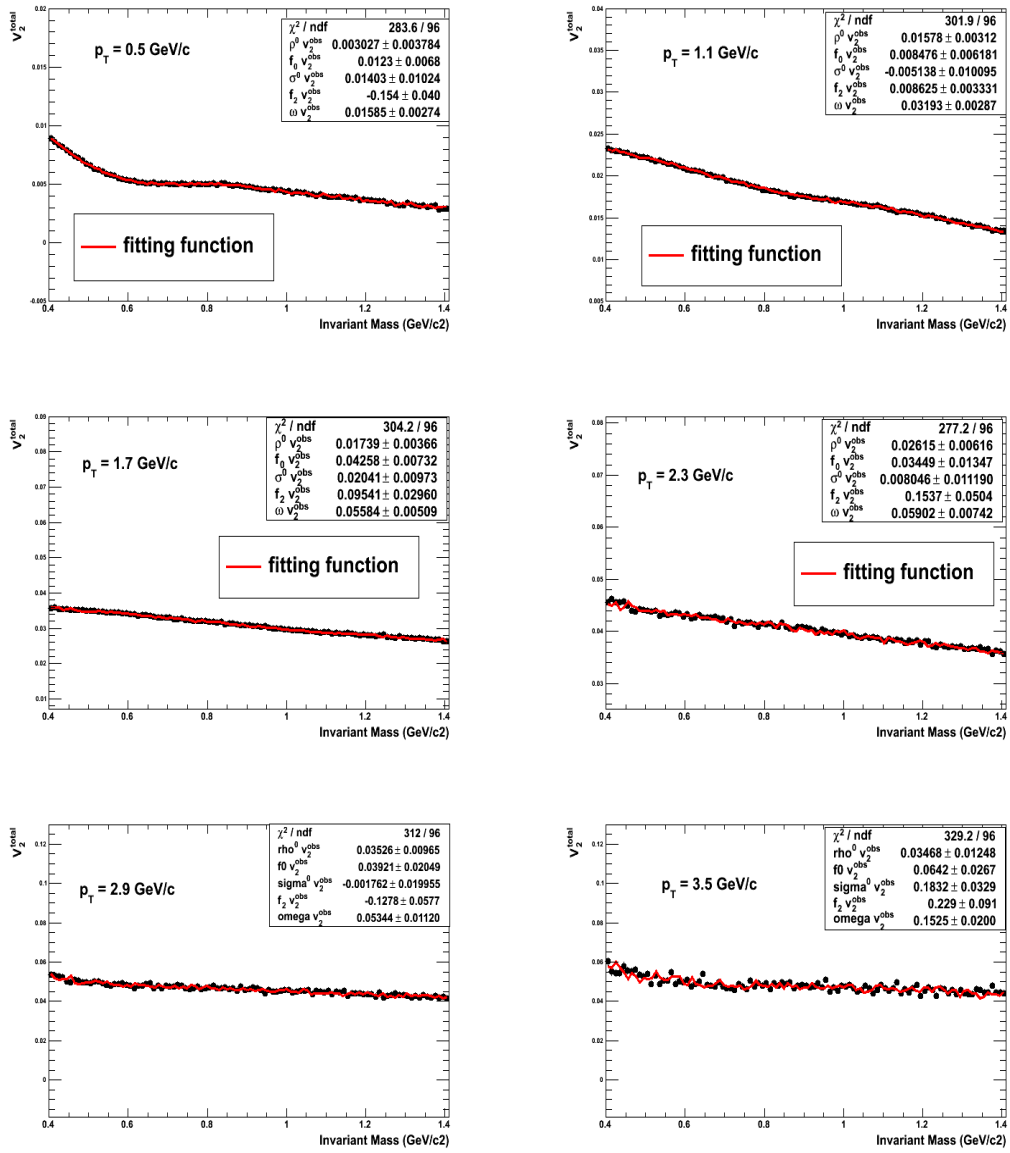

Figure 4.16: The total v_2 as a function of $\pi^+\pi^-$ invariant mass where the event plane is reconstructed from FTPC.

Chapter 5

Results and Discussion

In this chapter, the results on ρ^0 vector meson mass for minimum bias p+p, d+Au, Cu+Cu and Au+Au events as a function of transverse momentum (p_T) are presented. This has been done to look at the medium induced modification of the ρ^0 mass parameter. The p_T distributions of ρ^0 yields for different systems have also been studied. This is expected to provide valuable information on particle production mechanism. The ρ^0/π^- yield ratios are compared with the K^*/K^- yield ratios to look at the effects of re-generation and re-scattering. In the end, the result on ρ^0 vector meson elliptic flow (v_2) in Au+Au collisions at $\sqrt{s_{NN}}$ = 200 GeV with high statistics data is presented. The number of constituent quark scaling of v_2 of ρ^0 will potentially provide information about the ρ^0 production mechanism.

5.1 ρ^0 mass vs. transverse momentum

In a strongly interacting matter at high temperature and/or high density, dynamical interactions of the ρ^0 with the surrounding matter may cause the modification of the ρ^0 mass and/or width due to the so-called in-medium effect [101, 103, 148, 149]. In case of a hadron gas, $\pi^+\pi^-$ can re-generate ρ^0 through $\pi^+ + \pi^- \rightarrow \rho^0 \rightarrow \pi^+ + \pi^-$ so that ρ^0 resonance line shape might be affected by the pions initial phase space distributions [121–123, 150–152].

The upper panel of Figure 5.1 shows variation of the ρ^0 mass as a function

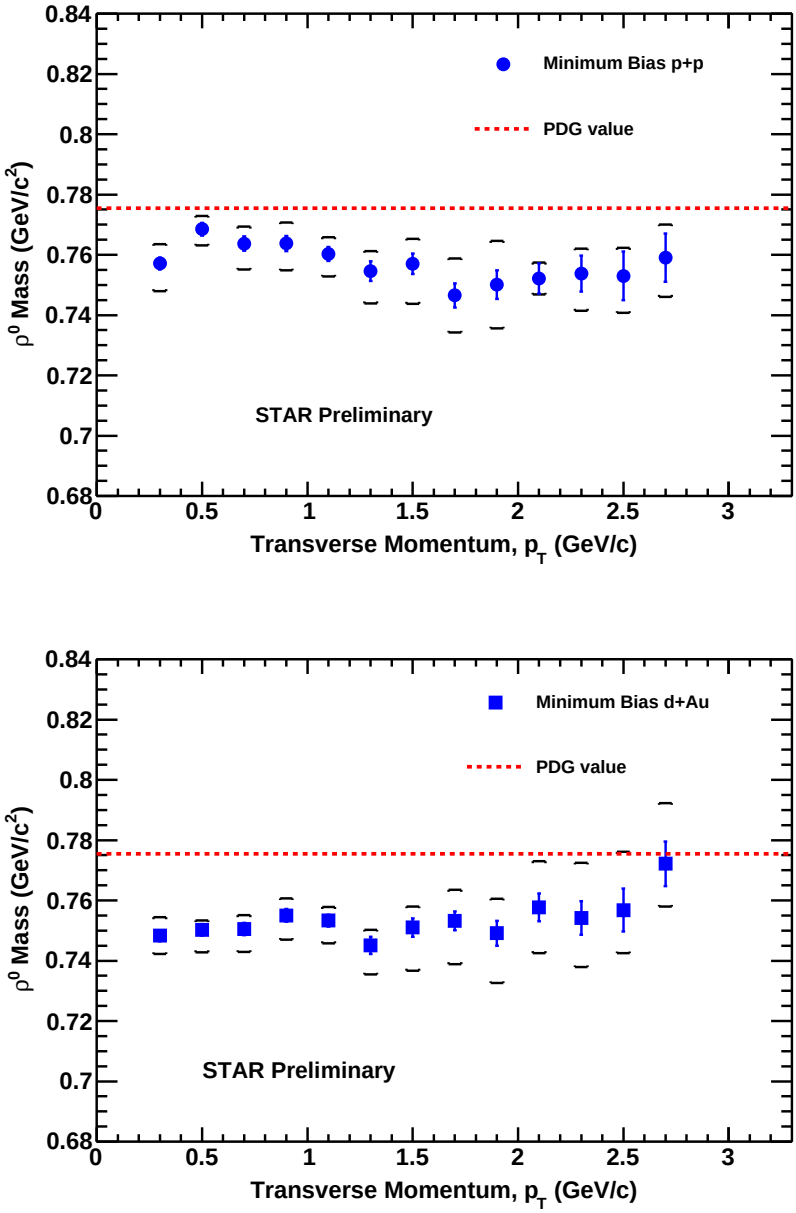

Figure 5.1: **Upper Panel**-The ρ^0 mass as a function of p_T for minimum bias p+p collisions at $\sqrt{s}$ = 200 GeV. The dashed line represents the ρ^0 mass value from Particle Data Book [127]. **Lower Panel**-The ρ^0 mass as a function of p_T for minimum bias d+Au collisions at $\sqrt{s_{NN}}$ = 200 GeV. The dashed line represents the ρ^0 mass value from Particle Data Book [127]. In both plots, the brackets indicate the systematic uncertainty. The statistical errors are represented by the error bars.

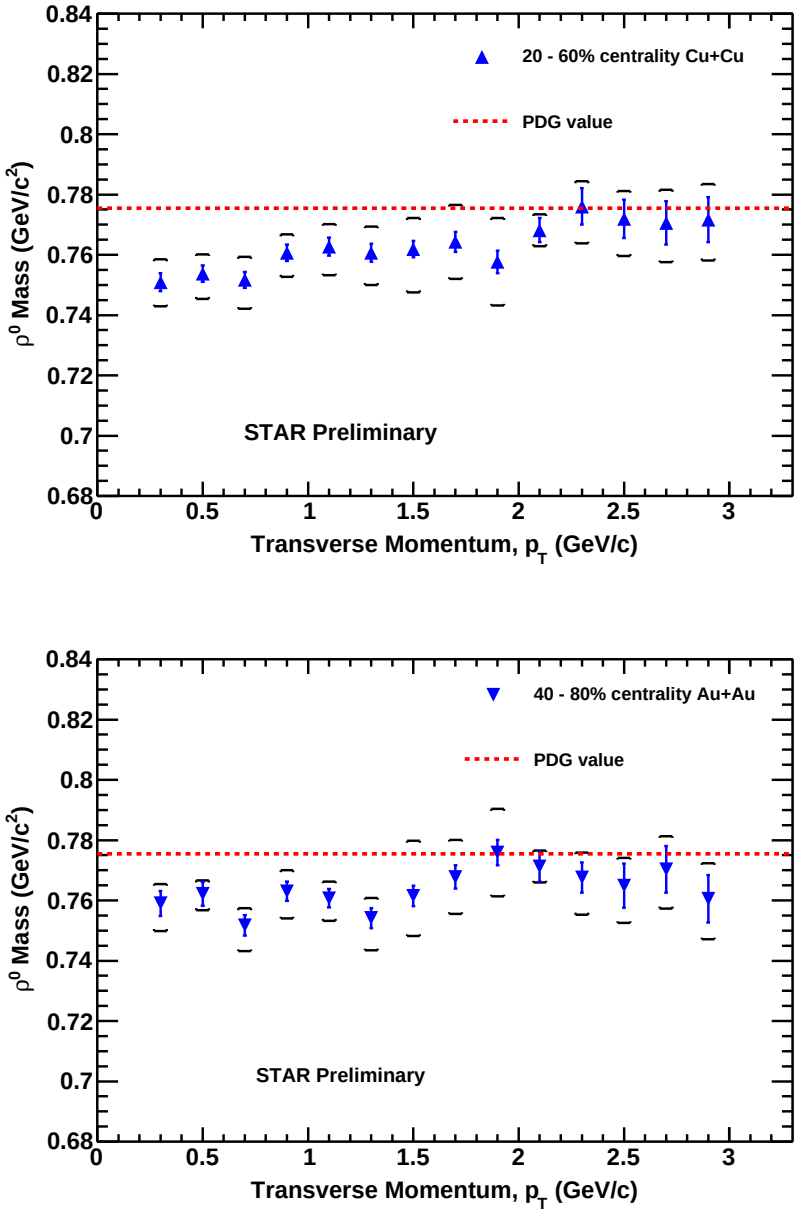

Figure 5.2: **Upper Panel**-The ρ^0 mass as a function of p_T for 20-60% Cu+Cu collisions at $\sqrt{s_{NN}}$ = 200 GeV. The dashed line represents the ρ^0 mass value from Particle Data Book [127]. **Lower Panel**-The ρ^0 mass as a function of p_T for 40-80% Au+Au collisions at $\sqrt{s_{NN}}$ = 200 GeV. The dashed line represents the ρ^0 mass value from Particle Data Book [127]. In both plots, the brackets indicate the systematic uncertainty. The statistical errors are represented by the error bars.

of p_T for minimum bias p+p collisions at 200 GeV and the lower panel of Figure 5.1 shows the same for minimum bias d+Au collisions. The dotted straight line represents the standard mass value as given in the Particle Data book for ρ^0 (775.5 MeV/c^2). The error bars correspond to statistical errors, while the brackets represent systematic uncertainties.

The upper panel of Figure 5.2 shows variation of the ρ^0 mass as a function of p_T for 20-60% centrality in minimum bias Cu+Cu collisions at $\sqrt{s_{NN}}$ = 200 GeV. The lower panel of Figure 5.2 shows the same for peripheral 40-80% centrality in minimum bias Au+Au collisions. The dotted straight line represents the standard mass value as given in the Particle Data book for ρ^0 (775.5 MeV/c^2). The error bars correspond to statistical errors, while the brackets represent systematic uncertainties.

The ρ^0 invariant masses for different p_T bins for minimum bias p+p and d+Au collisions are listed in Table 5.1 and for peripheral, i.e. 20-60% Cu+Cu and 40-80% Au+Au collisions, these values are listed in Table 5.1.

Minimum Bias p+p		**Minimum Bias d+Au**	
p_T	Mass ± Stat. + Sys. - Sys.	p_T	Mass ± Stat. + Sys. - Sys.
0.2 - 0.4	757.1 ± 2.0+6.5-9.1	0.2 - 0.4	748.3 ± 1.8+6.1-6.3
0.4 - 0.6	768.5 ± 2.1+4.4-5.4	0.4 - 0.6	750.2 ± 1.9+3.2-7.4
0.6 - 0.8	763.7 ± 2.4+5.6-8.6	0.6 - 0.8	750.5 ± 2.0+4.6-7.6
0.8 - 1.0	763.7 ± 2.5+7.0-9.0	0.8 - 1.0	755.0 ± 2.1+5.7-8.7
1.0 - 1.2	760.3 ± 2.3+5.5-7.5	1.0 - 1.2	753.3 ± 2.0+4.5-7.5
1.2 - 1.4	754.5 ± 3.3+6.7-9.0	1.2 - 1.4	745.1 ± 2.9+5.2-9.7
1.4 - 1.6	757.0 ± 3.4+8.3-10.	1.4 - 1.6	751.0 ± 3.0+7.0-14.3
1.6 - 1.8	746.5 ± 4.0+12.-13.	1.6 - 1.8	753.2 ± 3.1+10.3-16.5
1.8 - 2.0	750.1 ± 4.8+14.-12.	1.8 - 2.0	749.1 ± 4.1+11.5-15.3
2.0 - 2.2	752.1 ± 5.0+5.3-5.5	2.0 - 2.2	757.7 ± 4.3+15.3-16.3
2.2 - 2.4	753.8 ± 6.0+8.3-12.	2.2 - 2.4	754.2 ± 5.6+18.3-14.3
2.4 - 2.6	753.0 ± 8.1+9.3-12.	2.4 - 2.6	756.8 ± 3.4+19.1-19.2
2.6 - 2.8	759.1 ± 8.0+11.-13.	2.6 - 2.8	772.2 ± 4.4+17.1-19.3

Table 5.1: The ρ^0 mass for each p_T bin in minimum bias triggered p+p and d+Au collisions. The unit for p_T is GeV/c and the unit for mass is MeV/c^2. The mass values in p+p and d+Au collisions are listed together with statistical uncertainties and systematic uncertainties. The first error corresponds to the statistical error and the last two errors are the asymmetric systematic errors.

Cu+Cu (20-60% centrality)		**Au+Au (40-80% centrality)**	
p_T	Mass ± Stat. + Sys. - Sys.	p_T	Mass ± Stat. + Sys. - Sys.
0.2 - 0.4	750.9 ± 3.0+7.5-8.1	0.2 - 0.4	758.9 ± 2.0+6.5-9.1
0.4 - 0.6	753.8 ± 2.7+6.4-8.4	0.4 - 0.6	762.1 ± 4.1+4.4-5.4
0.6 - 0.8	751.6 ± 2.6+7.6-9.6	0.6 - 0.8	751.7 ± 3.9+5.6-8.6
0.8 - 1.0	760.7 ± 2.7+6.0-8.0	0.8 - 1.0	763.0 ± 3.4+7.0-9.0
1.0 - 1.2	762.6 ± 3.0+7.5-9.5	1.0 - 1.2	760.7 ± 3.2+5.5-7.5
1.2 - 1.4	760.7 ± 3.0+8.7-10	1.2 - 1.4	754.1 ± 3.0+6.7-10.
1.4 - 1.6	761.8 ± 2.7+10.-12.	1.4 - 1.6	761.4 ± 3.3+14.-13.
1.6 - 1.8	764.2 ± 3.3+12.-14.	1.6 - 1.8	767.7 ± 3.4+12.-12.
1.8 - 2.0	757.6 ± 3.7+14.-13.	1.8 - 2.0	775.8 ± 3.9+14.-13.
2.0 - 2.2	768.1 ± 4.0+6.0-6.4	2.0 - 2.2	771.2 ± 4.2+6.4-7.0
2.2 - 2.4	776.0 ± 6.0+8.3-6.0	2.2 - 2.4	767.6 ± 5.0+8.3-12.
2.4 - 2.6	771.9 ± 6.4+9.3-12.	2.4 - 2.6	764.8 ± 7.3+9.3-12.
2.6 - 2.8	770.5 ± 7.2+11.-13.	2.6 - 2.8	770.3 ± 7.7+11.-13.
2.8 - 3.0	771.6 ± 7.5+12.-13.	2.8 - 3.0	760.5 ± 7.9+12.-14.

Table 5.2: The ρ^0 mass for each p_T bin in 20-60% Cu+Cu collisions and 40-80% Au+Au collisions. The unit for p_T is GeV/c and the unit for mass is MeV/c^2. The mass values in Cu+Cu and Au+Au collisions are listed together with statistical uncertainties and systematic uncertainties. The first error corresponds to the statistical error and the last two errors are the asymmetric systematic errors.

5.1.1 In-Medium Effects and Mass Modification

In Figure 5.1 and Figure 5.2, a downward ρ^0 mass shift up to ~40 MeV/c^2 is observed in all the four collision systems, i.e. p+p, d+Au, Cu+Cu and Au+Au at $\sqrt{s_{NN}}$ = 200 GeV. Also, it has been observed that the mass shift is p_T dependent and it approaches towards the particle data book value with increasing p_T.

Dynamical interactions with the surrounding matter, interference between various $\pi^+\pi^-$ scattering channels, phase space distortions due to the re-scattering of the pions forming ρ^0, and Bose-Einstein correlations between the ρ^0 decay daughters and pions in the surrounding matter were previously given as the possible explanations for the downward mass shift [104]. It has been proposed [153] that the mass shift observed in p+p collisions is due to $\pi\pi$ re-scattering, which requires no medium. Since one also does not expect a medium to be formed in

d+Au collisions, if dynamical interactions are also the explanation for mass shift, then the re-scattering of the ρ^0 with the surrounding particles must exist.

In comparison to the in-medium ρ^0 production in hadronic Au+Au interactions, no modifications of the ρ^0 properties are expected for coherent ρ^0 production in ultra-peripheral heavy-ion collisions [162], where impact parameter $b > 2R_A$. In such collisions, a photon emitted by one gold ion fluctuates into a virtual ρ^0 meson state, which scatters diffractively from the other nucleus. The ρ^0 line shape in ultra-peripheral collisions measured with STAR detector is produced by a BW plus Söding interference term. The ρ^0 mass and width are consistent with their natural values reported in PDG [161].

5.2 Transverse Momentum Spectra

The transverse momentum (p_T) distributions of ρ^0 meson from Cu+Cu collisions at $\sqrt{s_{NN}}$ = 200 GeV are presented in Figure 5.3. For Cu+Cu collisions, the spectra are corrected for the detector efficiency and acceptance for various collision centralities. The statistical error bars are very small. The solid black lines shown are exponential fits to the data points, as given by

$$\frac{1}{2\pi p_T}\frac{d^2N}{dp_T dy} = \frac{dN/dy}{2\pi T(m_{\rho^0}+T)} exp[-(m_T - m_{\rho^0})/T] \tag{5.1}$$

The above fitting function has two free parameters, i.e. T and dN/dy. T is known as the inverse slope parameter and dN/dy is the ρ^0 yield per unit rapidity. The ρ^0 invariant yields ($d^2N/2\pi p_T dp_T dy$) at mid-rapidity in each p_T bin for different collision centralities in Cu+Cu system at $\sqrt{s_{NN}}$ = 200 GeV are listed in Table 5.3 and 5.4. For other systems, such as p+p, d+Au and Au+Au, only the ρ^0 raw spectra are discussed in section 3.6, without the detector acceptance and efficiency corrections.

The particle production at low p_T is primarily due to non-perturbative soft processes and thus the p_T distribution at this regime is expected to be exponential in nature. However, hard processes dominate particle production at high p_T

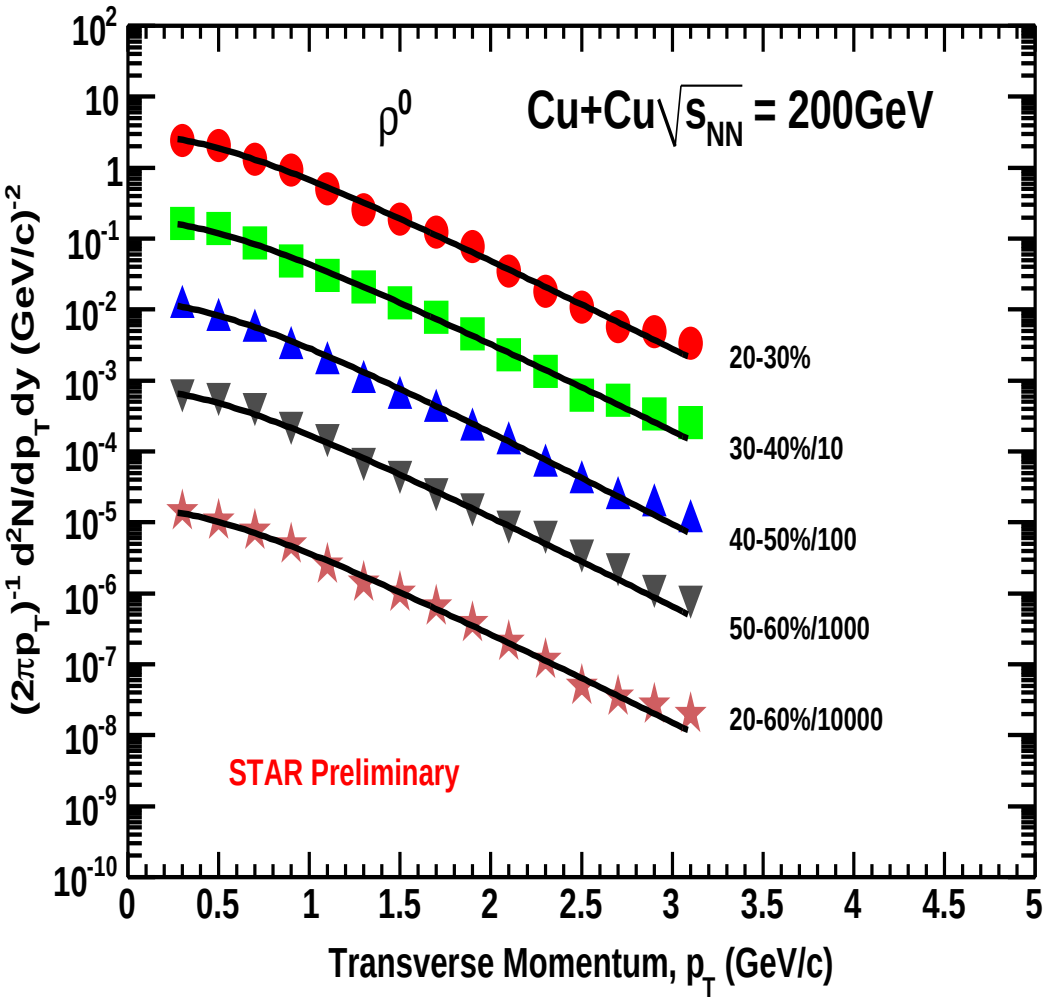

Figure 5.3: The detector efficiency and acceptance corrected ρ^0 vector meson transverse momentum spectra for different centralities in Cu+Cu collisions at $\sqrt{s_{NN}}$ = 200 GeV. The error bars shown are statistical only. The solid line represents an exponential function fit to the data points as given by Equation 5.1.

ρ^0 Invariant yield $(d^2N/2\pi p_T dp_T dy)$ in Cu+Cu collisions at $\sqrt{s_{NN}}$ = 200 GeV			
p_T **(GeV/c)**	**(20-30)% Cent.**	**(30-40)% Cent.**	**(40-50)% Cent.**
0.2 - 0.4	2.425± 0.1211	1.65735± 0.0708	1.29581 ± 0.0452
0.4 - 0.6	2.05915 ± 0.0727	1.38804± 0.0439	0.860342 ± 0.0270
0.6 - 0.8	1.30523± 0.0381	0.879889 ± 0.0288	0.604296 ± 0.0177
0.8 - 1.0	0.928404± 0.0243	0.482333± 0.0162	0.345862 ± 0.0109
1.0 - 1.2	0.498611± 0.0150	0.305142± 0.0098	0.210027 ± 0.0062
1.2 - 1.4	0.258041± 0.0086	0.209185 ± 0.0066	0.115067 ± 0.0036
1.4 - 1.6	0.1902± 0.0055	0.125511± 0.0041	0.0681062 ± 0.0023
1.6 - 1.8	0.123592± 0.0033	0.0778808± 0.0028	0.0452984 ± 0.0016
1.8 - 2.0	0.0771656± 0.0026	0.0452063± 0.0017	0.0242196 ± 0.0010
2.0 - 2.2	0.0346161± 0.0014	0.0232836 ± 0.0011	0.0156657 ± 0.0007
2.2 - 2.4	0.0180285± 0.0016	0.0135435± 0.0007	0.00764155 ± 0.0004
2.4 - 2.6	0.0107183± 0.0008	0.0062352± 0.00054	0.00436956 ± 0.0003
2.6 - 2.8	0.0057453 ± 0.0005	0.00525048± 0.00042	0.00266675 ± 0.0002
2.8 - 3.0	0.00493655± 0.0006	0.00336328± 0.0002	0.00207881 ± 0.0001
3.0 - 3.2	0.00337752± 0.0004	0.00257648± 0.0002	0.0012363 ± 0.0001

Table 5.3: The ρ^0 invariant yields $(d^2N/2\pi p_T dp_T dy)$ in different p_T bins and different centralities in Cu+Cu collisions at $\sqrt{s_{NN}}$ = 200 GeV. The errors are statistical only.

ρ^0 Invariant yield $(d^2N/2\pi p_T dp_T dy)$ in Cu+Cu at $\sqrt{s_{NN}}$ = 200 GeV		
p_T **(GeV/c)**	**(50-60)% Cent.**	**(20-60)% Cent.**
0.2 - 0.4	0.606191± 0.0272122	1.42834 ± 0.0315104
0.4 - 0.6	0.542537± 0.016900	1.06937 ± 0.0203099
0.6 - 0.8	0.390118 ± 0.0121507	0.761513 ± 0.0135052
0.8 - 1.0	0.212968 ± 0.00646184	0.482955 ± 0.00775297
1.0 - 1.2	0.142274± 0.00437899	0.252397 ± 0.00498305
1.2 - 1.4	0.0659414± 0.00223831	0.142444 ± 0.0030919
1.4 - 1.6	0.0428836± 0.00157285	0.102003 ± 0.0018155
1.6 - 1.8	0.0243108± 0.000991308	0.0652037 ± 0.00128203
1.8 - 2.0	0.0149868± 0.000690439	0.0376788 ± 0.00085387
2.0 - 2.2	0.00849927± 0.000491645	0.0206281 ± 0.000556129
2.2 - 2.4	0.00613939± 0.000340951	0.0114391 ± 0.000382478
2.4 - 2.6	0.0033351± 0.000224524	0.00498413 ± 0.000271572
2.6 - 2.8	0.00216003± 0.000160643	0.00350809 ± 0.00021989
2.8 - 3.0	0.00105714 ± 0.000118588	0.00269169 ± 0.000152891
3.0 - 3.2	0.000754329± 0.00009	0.00197942 ± 0.000115827

Table 5.4: The ρ^0 invariant yields $(d^2N/2\pi p_T dp_T dy)$ in different p_T bins in different centralities in Cu+Cu collisions at $\sqrt{s_{NN}}$ = 200 GeV. The errors are statistical only.

which is described by the perturbative QCD (pQCD) and a power-law like distribution is expected. But, in our analysis, we have observed a good fit with only exponential function and therefore it may be concluded that the ρ^0 production is mainly dominated by the soft processes. The contributions from hard processes are negligible in the covered p_T range. The two free parameters (T and dN/dy) obtained from the exponential fit to the data are tabulated in Table 5.5. The main contributions to the systematic uncertainties are from the tracking efficiency ($\sim$8%), and the normalization between the $M_{\pi\pi}$ and the like-sign reference distributions which is $\sim$ 23% for peripheral 20-60% Cu+Cu collisions.

Centrality	T (Inverse Slope) (MeV)	dN/dy
20-30%	344.4±2.1(stat.)±34(syst.)	6.7 ± 0.10 (stat.) ± 1.3 (syst.)
30-40%	339.0±2.3(stat.)±35(syst.)	4.4 ± 0.11 (stat.) ± 1.1 (syst.)
40-50%	321.2±2.8(stat.)±36(syst.)	2.9 ± 0.12 (stat.) ± 1.2 (syst.)
50-60%	329.4±3.1(stat.)±37(syst.)	1.8 ± 0.14 (stat.) ± 1.3 (syst.)
20-60%	334.1±1.1(stat.)±35(syst.)	4.0 ± 0.10 (stat.) ± 1.1 (syst.)

Table 5.5: The ρ^0 dN/dy at $|y| < 0.5$ and the inverse slope parameter (T) measured in Cu+Cu collisions at $\sqrt{s_{NN}}$ = 200 GeV for different centralities. Both statistical and systematic errors are shown.

5.3 Mean Transverse Momentum ($< p_T >$)

The ρ^0 mean transverse momentum ($< p_T >$), is calculated using the formula:

$$< p_T >= \frac{\int_0^\infty p_T \frac{1}{2\pi p_T} \frac{d^2N}{dydp_T} p_T dp_T}{\int_0^\infty \frac{1}{2\pi p_T} \frac{d^2N}{dydp_T} p_T dp_T}, \tag{5.2}$$

Now, plugging Equation 5.1 in Equation 5.2, we get

$$< p_T >= \frac{\int_0^\infty p_T^2 exp[-(\sqrt{p_T^2 + m_{\rho^0}^2} - m_{\rho^0})/T] dp_T}{\int_0^\infty p_T exp[-(\sqrt{p_T^2 + m_{\rho^0}^2} - m_{\rho^0})/T] dp_T} \tag{5.3}$$

where, m_{ρ^0} is the ρ^0 mass taken from the PDG (775.5 MeV/c^2). The obtained $< p_T >$ for different centralities in Cu+Cu collisions using Equation 5.3 are listed

in Table 5.6. The quoted error bars are the square root of the quadratic sums of the statistical and systematic errors. The main contributions to the systematic uncertainties quoted are from the tracking efficiency and the normalization between the $M_{\pi\pi}$ and the like-sign reference distributions.

Centrality	$< p_T >$**(GeV/**c**))**
20-30%	0.88±0.4
30-40%	0.87±0.37
40-50%	0.84±0.31
50-60%	0.85±0.23
20-60%	0.86±0.17

Table 5.6: The ρ^0 average transverse momentum ($< p_T >$) for different collision centralities at $\sqrt{s_{NN}}$ = 200 GeV Cu+Cu collisions.

Figure 5.4 shows $< p_T >$ of ρ^0 vector meson as a function of number of participants in different centralities and in various collision systems at $\sqrt{s_{NN}}$ = 200 GeV. The data points for $< p_T >$ of ρ^0 vector meson in p+p collisions is from the power-law fit to the p_T spectrum of ρ^0 vector meson [163]. The $< p_T >$ for $\bar{p}$, K^- and π^- [154] are also shown in Figure 5.4 for comparison. Also, in order to compare the $\rho^0 < p_T >$ with another short lived resonance, we have compared with the $K^* < p_T >$ [133]. All the results shown in Figure 5.4 are from $\sqrt{s_{NN}}$ = 200 GeV.

From Figure 5.4, we observe the mean transverse momentum, $< p_T >$, has no significant centrality and system size dependence in heavy-ion collisions (Au+Au and Cu+Cu). However, $< p_T >$ of ρ^0 and K^* in heavy-ion collisions is larger than the same in p+p collisions. This can be explained by arguing that in the hadronic phase, i.e. between chemical and kinetic freeze-out, the resonances with higher p_T have a greater chance to escape the hadronic medium. They decay outside the fireball and avoid the daughter particles' re-scattering effects. Therefore, high p_T resonances have a greater chance to be detected than low p_T resonances [133, 164]. That is why it is expected to observe higher $< p_T >$ distribution for ρ^0 and K^* in relativistic heavy-ion collisions than in elementary collisions, such as p+p. Also,

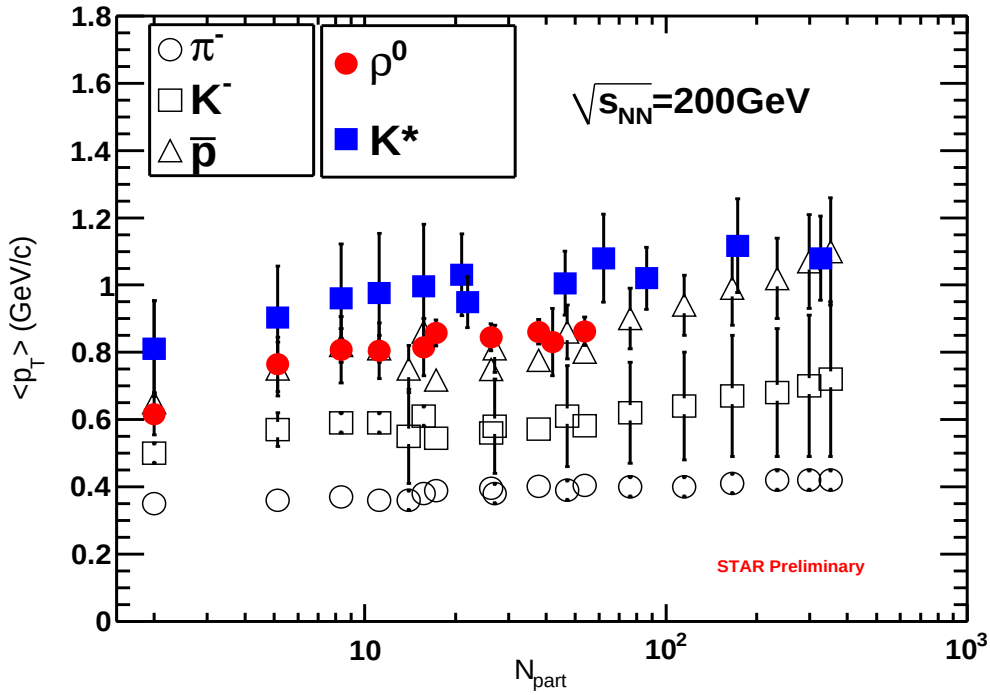

Figure 5.4: The mean transverse momentum, $< p_T >$, of different particles as a function of number of participants in different collision systems at 200 GeV.

it is seen that the $< p_T >$ is strongly dependent on the mass of the particles. The $< p_T >$ is higher for higher mass particles. In case of resonances, because of the final state effects, this argument of mass dependence is not valid and therefore, ρ^0 and K^* have higher $< p_T >$ than proton although they are of smaller masses than proton.

5.4 Particle Ratio

The yield ratio of the resonances to their stable particles such as kaon, pion and proton, produced in various collision systems can shed light on the particle production mechanisms during hadronization. These ratios can prove the dynamics involved in heavy- ion collisions and also help to constrain the predictions of thermal model calculations [101, 155–157].

Since ρ^0 lifetime is smaller than the lifetime formed in heavy- ion collisions, the ρ^0 vector meson is expected to decay, re-generate, and re-scatter all the way from chemical freeze-out to kinetic freeze-out. In the context of statistical models, the measured ρ^0 yield should reflect conditions at kinetic freeze-out rather than at chemical freeze-out where the inelastic interactions vanish [72, 73, 151, 152]. In p+p collisions, the ρ^0 vector meson is expected to be produced predominantly by string fragmentation. Therefore, the measurement of $\frac{\rho^0}{\pi^-}$ ratio in p+p and heavy-ion collisions at the same nucleon-nucleon c.m. energy can provide insight for understanding the dynamics of these systems.

In order to compare our results on ρ^0 to π^- yield ratio, we have taken the K^* to K^- yield ratio in different collision systems at the same $\sqrt{s_{NN}}$. The K^*/K^- data points are taken from [133]. Figure 5.5 shows the ratios of resonances such as ρ^0 and K^{*0} to their corresponding stable particles as a function of the number of participant nucleons in the collisions for various collision systems at $\sqrt{s_{NN}}$ = 200 GeV.

In case of $\frac{K^*}{K^-}$ ratio, it is observed that the ratio is smaller in heavy-ion (Cu+Cu and Au+Au) collisions compared to p+p collisions at the same beam energy. At

the same time, the $\frac{\rho^0}{\pi^-}$ ratio in heavy-ions has no significant difference from p+p collisions at the same beam energy. The $\frac{\rho^0}{\pi^-}$ ratios for p+p and Au+Au are taken from [104]. The observed decrease of $\frac{K^*}{K^-}$ ratios from p+p to Au+Au collisions has been explained by an extended lifetime of the hadronic phase where the re-scattering of the decay particles dominates over resonance re-generation [155–159]. As the $\frac{K^*}{K^-}$ ratios are similar in p+p and d+Au collisions, this would suggest the absence of an extended hadronic medium in d+Au collisions. The $\frac{\rho^0}{\pi^-}$ ratio in d+Au collisions is in agreement with the ratio measured in p+p collisions. This resonance ratio does not show any suppression from p+p to Au+Au collisions either. Hence, it is not sensitive to the lifetime of the hadronic medium, presumably due to its large re-generation cross-section. The data points for $\frac{\rho^0}{\pi^-}$ ratios in p+p, d+Au and peripheral Au+Au collisions are taken from [104, 110].

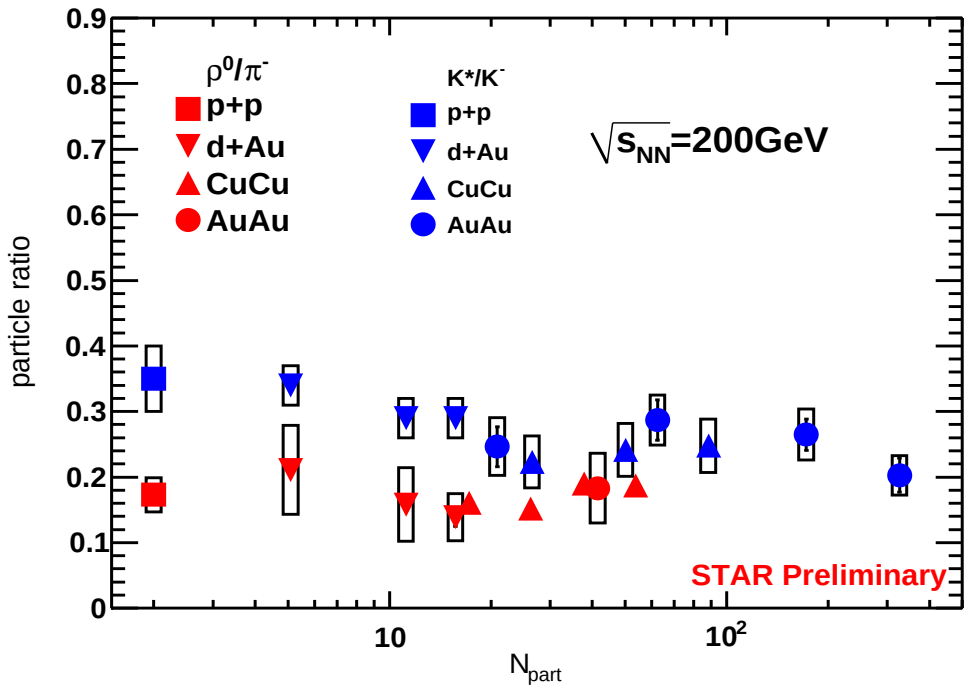

Figure 5.5: The ρ^0/π^- yield ratio at mid-rapidity as a function of N_{part} for different collision systems. The K^*/K^- yield ratio is plotted for comparison.

The $\frac{\rho^0}{\pi^-}$ ratio is independent of centrality, i.e from 20% to 60% in Cu+Cu and

from 40% to 80% in Au+Au collisions, and it is of the same order as the corresponding p+p measurement. In p+p collisions, it has been proposed that the mass shift is due to $\pi\pi$ re-scattering, even in the absence of a medium [153]. If this is the case, $\pi^+\pi^-$ re-scattering might re-generate the ρ^0. In addition, one of the decay daughters might also re-scatter with other hadrons which prevents the ρ^0 to be measured. Therefore, these two processes compete and balance with each other.

5.4.1 Re-Scattering and Re-Generation Effects and Evolution Properties

The ratio of resonance to stable particle can be used to understand the re-scattering and re-generation effects using a microscopic transport model (UrQMD) calculations [158, 165]. Different resonances decay into different daughters and different hadronic daughters may have different interaction cross sections with the pions which are the dominant hadrons in the medium created in heavy-ion collisions. Therefore, the relative yields of the resonances destroyed by the daughter particles re-scattering effect should be different for different resonances. Also because of the same reason, on the other hand, the amount of resonances signals re-produced by the re-generation effect in the hadronic medium should be different [134]. Now the question is whether both these effects (i.e. re-scattering and re-generation effects) depend on the interaction cross-section of the hadrons in the medium or not.

The upper panel of Figure 5.6 shows the $\pi^+\pi^-$ interaction cross section as a function of collision energy and the lower panel of Figure 5.6 shows the π^-K^+ interaction cross section as a function of $\sqrt{s}$ from UrQMD calculation [165]. From these two figures, it is seen that the total cross section for pion-pion interactions is higher than the total cross section for pion-kaon interactions. Therefore, the re-scattering effect should be more dominated by the pion-pion interaction than pion-kaon interaction.

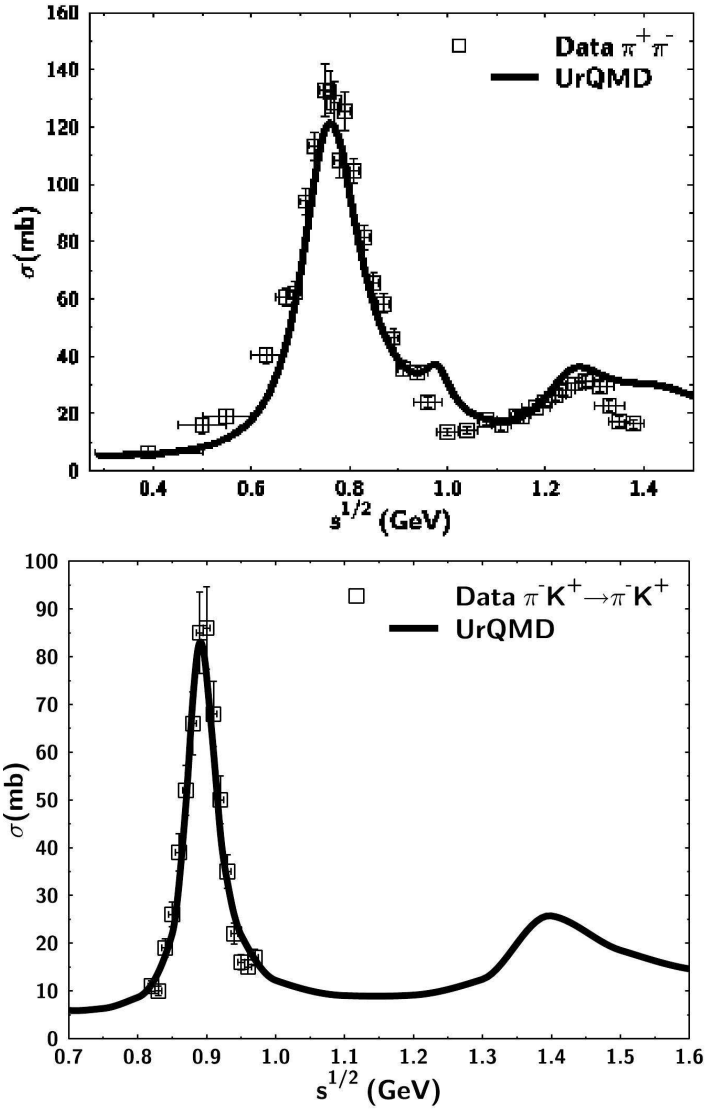

Figure 5.6: **Upper Panel**-The total $\pi^+\pi^-$ scattering cross section as a function of c.m. energy $\sqrt{s}$. Figure is taken from [165]. **Lower Panel**-The total cross section of π^-K^+ scattering as a function of c.m. energy $\sqrt{s}$. Figure is taken from [165].

In case of a K^{*0} decays to a kaon and pion, as long as one of its daughters is re-scattered by hadrons in the medium, one can loose the K^{*0} signal. Since pion is the dominating particle in the medium and pion-pion interaction cross section is more, therefore, there is a higher probability to loose the K^{*0} signal in the re-scattering of the daughters. On the other hand, the kaon-pion interaction to re-produce the K^* signal is relatively small to compensate the signal lost in re-scattering effect. Thus, we observe a suppression of K^*/K in Cu+Cu and Au+Au collisions compared to the p+p collisions.

In case of $\rho^0 \rightarrow \pi^+\pi^-$, the cross section for the decayed daughter pions re-scattered by the medium pions is same as the cross section for two medium pions scattered with each other to re-produce the ρ^0 signal. In this case, one can argue that the amount of ρ^0 signal lost by the re-scattering effect is compensated by the signal formed during the re-generation effect. Therefore, we should not expect any significant change in the $\frac{\rho^0}{\pi^-}$ ratio in heavy-ions in comparison to p+p collisions.

5.5 Azimuthal Anisotropy (v_2)

The measurement of ρ^0 elliptic flow (v_2) can probe the amount of hadronic final state interactions for ρ^0 at intermediate transverse momenta. This can be studied by looking at the systematic deviations of the measured elliptic flow coefficient, v_2, from the scaling law given by the quark recombination model at the intermediate transverse momentum. Also one of the very important motivations behind this study is to understand the production mechanism of ρ^0 vector meson. This study can be well understood through the number of constituent quark scaling of v_2 of ρ^0 in the intermediate p_T region. Our expectation for the above study is the following:

1) If v_2 of ρ^0 scales with $n_q = 2$ in the universal curve, then the $q\bar{q}$ coalescence mechanism for ρ^0 production is dominating.

2) If v_2 of ρ^0 scales with $n_q = 4$ (i.e. 2 for each pion and total 2+2=4), then the

hadronic $\pi^+\pi^-$ re-generation plays a dominating role for the ρ^0 production.

In this section, we present the result of ρ^0 elliptic flow (v_2) measurement in 40-80% Au+Au collisions at $\sqrt{s_{NN}}$ = 200 GeV. The results from $(\phi - \Psi_2)$ binning method and the v_2 vs. M_{inv} method are compared. In case of v_2 vs. M_{inv} method, the results from TPC event plane method and FTPC event plane method are compared. Dependencies of the elliptic flow coefficient (v_2) on transverse momentum (p_T), centrality and particle species are also presented. The ρ^0 elliptic flow measurement is done in large statistics data sample obtained in Au+Au collisions at $\sqrt{s_{NN}}$ = 200 GeV during RHIC Run VII.

5.5.1 Methods Comparison

As mentioned earlier, two different techniques are used to extract the differential elliptic flow coefficient $v_2\,(p_T)$ for the ρ^0 vector meson. The upper panel of Figure 5.7 shows the ρ^0 elliptic flow (v_2) in 40-80% centrality Au+Au collisions at $\sqrt{s_{NN}}$ = 200 GeV at mid-rapidity $(|\eta| < 1.0)$ measured in ($\phi - \Psi_2$ bin) and (v_2 vs $M_{inv.}$) methods. The v_2 values obtained in above two methods are tabulated in Table 5.7.

The v_2 values are obtained with the TPC event plane in $(\phi - \Psi_2)$ bin method as denoted by the open circle and the v_2 vs. M_{inv} method as denoted by the filled circle in the upper panel of Figure 5.7. The error bars are statistical only. It is shown that within the statistical error bars both the methods are consistent with each other. For the case of $(\phi - \Psi_2)$ bin method, we are making five bins of the $(\phi - \Psi_2)$ distribution in each transverse momentum bin. Therefore, we are running out of statistics and to overcome this problem we have merged two transverse momentum bins into one bin especially in the higher p_T region. That is why the number of data points are less for $(\phi - \Psi_2)$ binning method as shown in the upper panel of Figure 5.7.

The non-flow effects are studied for the ρ^0 elliptic flow measurement by comparing the v_2 results obtained with respect to the TPC event plane and the results obtained with respect to the FTPC event plane. However, the ρ^0s were recon-

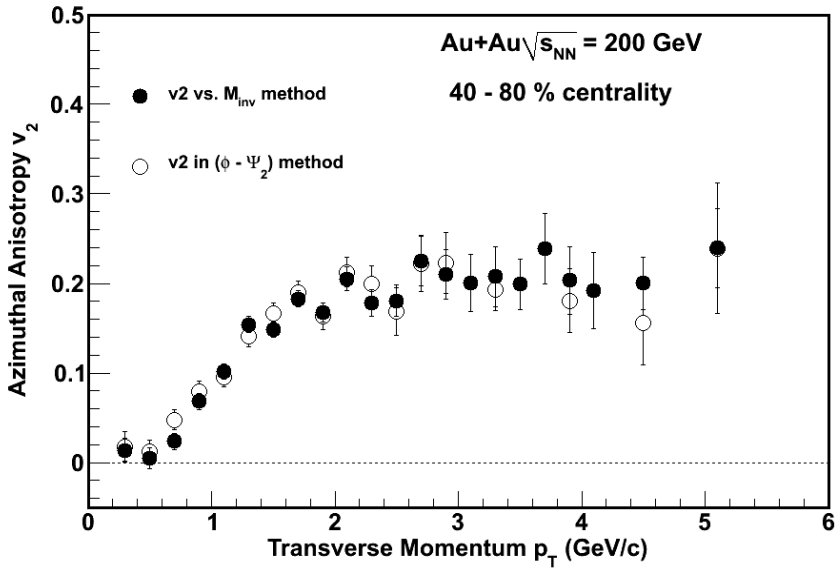

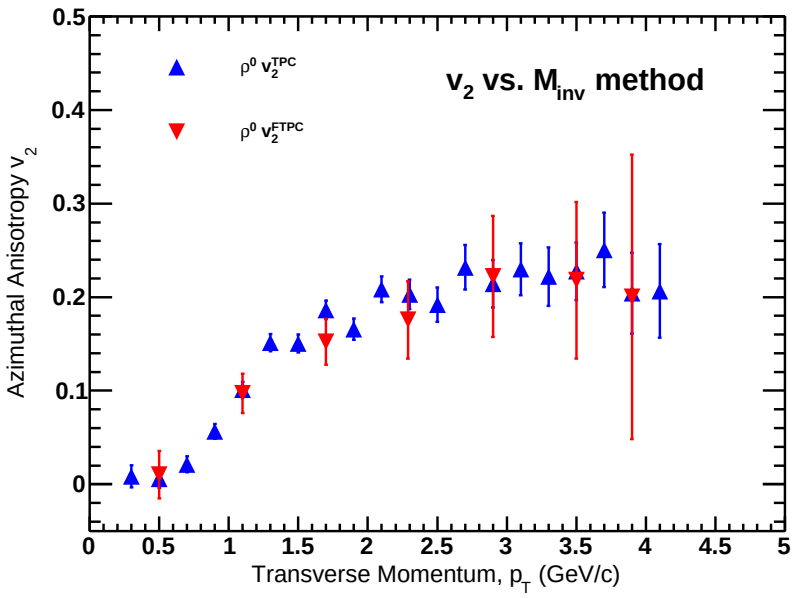

Figure 5.7: **Upper Panel**-The ρ^0 elliptic flow coefficient (v_2) as a function of p_T. The open circles correspond to the ($\phi - \Psi_2$) bin method and the filled circles correspond to the v_2 vs. M_{inv} method. The error bars shown are statistical only **Lower Panel**-The ρ^0 v_2 measured in TPC and FTPC event plane. Error bars are statistical only.

$\phi - \Psi_2$ **bin method**		v_2 **vs** $M_{inv.}$ **method**	
p_T	$v_2 \pm$ Stat.	p_T	$v_2 \pm$ Stat.
0.3	0.0177885 ± 0.016719	0.3	0.0135973 ± 0.013430
0.5	0.0124659 ± 0.013045	0.5	0.0084501 ± 0.006183
0.7	0.0477550 ± 0.011571	0.7	0.0235723 ± 0.009391
0.9	0.0795007 ± 0.011458	0.9	0.068091 ± 0.008549
1.1	0.0951547 ± 0.010822	1.1	0.1016070 ± 0.008661
1.3	0.1404320 ± 0.011394	1.3	0.153775 ± 0.009020
1.5	0.1666801 ± 0.011848	1.5	0.1485860 ± 0.008575
1.7	0.1902580 ± 0.012420	1.7	0.1829120 ± 0.009160
1.9	0.1636170 ± 0.014710	1.9	0.1678630 ± 0.010855
2.1	0.2125720 ± 0.016807	2.1	0.2052770 ± 0.012895
2.3	0.1991580 ± 0.020683	2.3	0.1785430 ± 0.014869
2.5	0.1682710 ± 0.026501	2.5	0.1807520 ± 0.017400
2.7	0.2220620 ± 0.030608	2.7	0.2254080 ± 0.028127
2.9	0.2228330 ± 0.033834	2.9	0.2103620 ± 0.027393
3.3	0.1927310 ± 0.023133	3.1	0.2004780 ± 0.031867
3.9	0.1807650 ± 0.035839	3.3	0.2076020 ± 0.033666
4.5	0.1558560 ± 0.047311	3.5	0.1989670 ± 0.028328
5.1	0.2391810 ± 0.072946	3.7	0.2385830 ± 0.039516
		3.9	0.2033630 ± 0.037860
		4.1	0.1921970 ± 0.042848
		4.5	0.2001780 ± 0.029519
		5.1	0.2395310 ± 0.044149

Table 5.7: The ρ^0 v_2 values obtained as a function of p_T in both the methods in Au+Au collisions at $\sqrt{s_{NN}}$ = 200 GeV. Only statistical error is mentioned.

structed from TPC tracks only. Since the FTPC covers a completely different pseudo-rapidity coverage, there is no auto-correlation in the determination of the FTPC event plane and the tracks that produce ρ^0 in the mid-rapidity. Hence, there is no need to further subtract the auto correlation between the tracks used for event plane calculation and the tracks used for the v_2 measurement. This is the advantage of using the FTPC event plane. Also, by using FTPC event plane one can minimize the possible non-flow contributions coming from jet like correlation in the final measured v_2 coefficient.

The lower panel of Figure 5.7 shows a comparison between the ρ^0 elliptic flow measured in v_2 vs. M_{inv} method using TPC as the event plane and FTPC as the

event plane for 40-80% centrality in Au+Au collisions at $\sqrt{s_{NN}}$ = 200 GeV. Because of the less possible non-flow effect in FTPC event plane than TPC event plane, one expects smaller v_2 values for FTPC event plane compared with TPC event plane. However, the large statistical error bars in the data points for the final v_2 measured in FTPC event plane forbid us to derive any such conclusion. Although we have quite large statistical error bars for the results with the FTPC event plane, but it is clear that the final v_2 results are consistent for both the cases. For this comparison, we have used only the v_2 vs. M_{inv} method.

Since the number of tracks detected in FTPC is less than TPC, the FTPC event plane has a poor resolution than the TPC event plane. For this reason, the ρ^0 final v_2 in FTPC event plane has large statistical error bars. In order to reduce the statistical error bars in each data points, we have combined p_T bins. Therefore, we have less number of data points for the results from FTPC event plane as shown in the lower panel of Figure 5.7.

5.5.2 v_2 vs. Transverse Momentum p_T

The transverse momentum dependency of ρ^0 elliptic flow (v_2) is shown in the upper panel of Figure 5.8 along with K_s^0 meson and Λ^0 baryon. The v_2 values for K_s^0 and Λ^0 were taken from [166]. The data points for ρ^0 is from the RHIC Run VII and for the two references (K_s^0 and Λ^0) the data points are from the RHIC Run IV. In case of ρ^0 data points, the error bars are statistical only.

It is shown in Figure 5.8 (Upper Panel) that v_2 first increases and then saturates in the intermediate p_T region. At low p_T, v_2 can be well described by hydrodynamics [144, 167]. However, the data points start deviating from ideal hydrodynamics at about 1.5 GeV/c [144]. It is believed that in this region ($1.5 \leq p_T < 5.0$ GeV/c) coalescence mechanism can be applied [144, 168].

It is also clear from the upper panel of Figure 5.8 that the v_2 of ρ^0 is following the same trend of the v_2 of K_s^0 meson in the intermediate p_T region, not the v_2 of Λ^0 baryon. This indicates that ρ^0 follows the trend of mesons, not baryons.

The elliptic flow (v_2) is plotted as a function of transverse kinetic energy in the

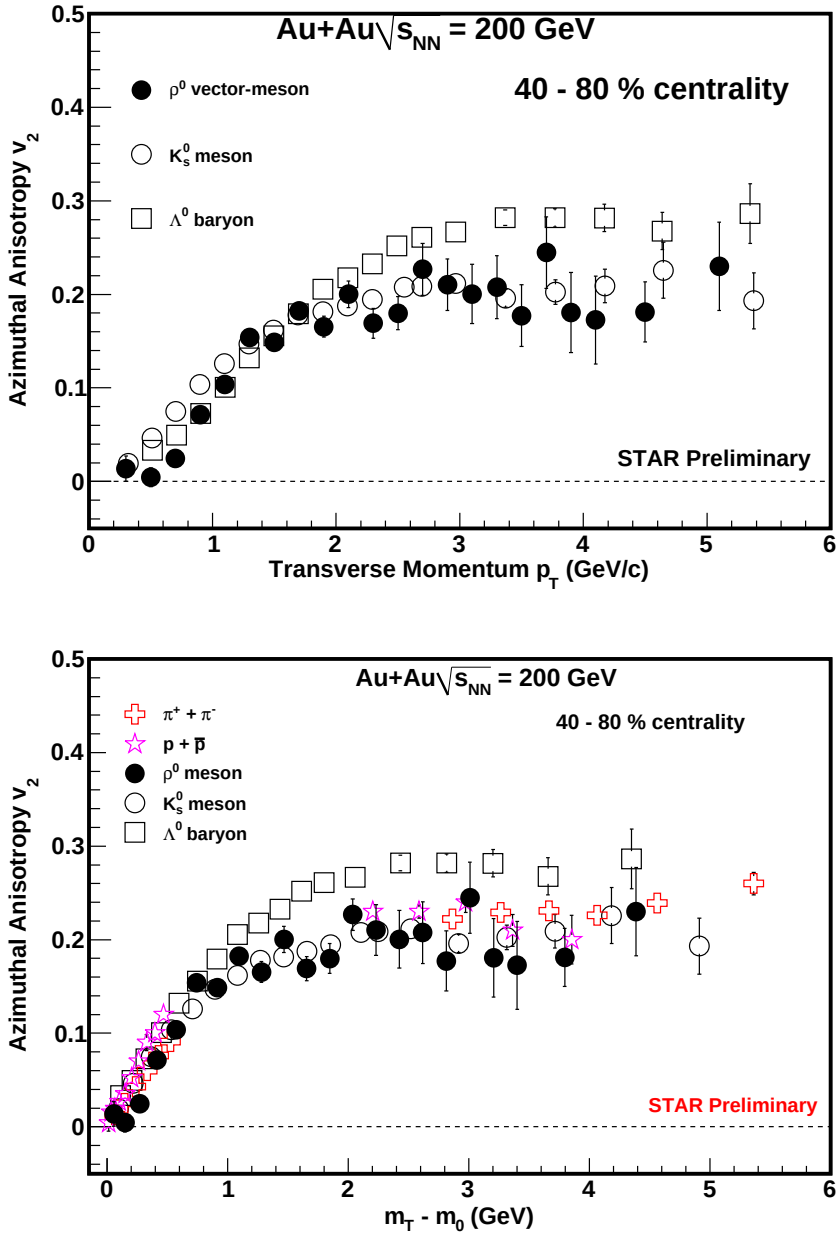

Figure 5.8: **Upper Panel**-Elliptic flow (v_2) as a function of transverse momentum. **Lower Panel**-Azimuthal anisotropy (v_2) vs. transverse kinetic energy ($m_T - m_0$) for ρ^0 vector meson compared with other particles from the same 40-80% hadronic cross-section at $\sqrt{s_{NN}}$ = 200 GeV in Au+Au collisions.

lower panel of Figure 5.8. The kinetic energy (KE_T) is defined as $m_T - m_0$, where $m_T = \sqrt{p_T^2 + m_0^2}$ and m_0 is the mass of the particle . From this figure, it is clear that the meson v_2 is different from the baryon v_2 in the intermediate p_T region.

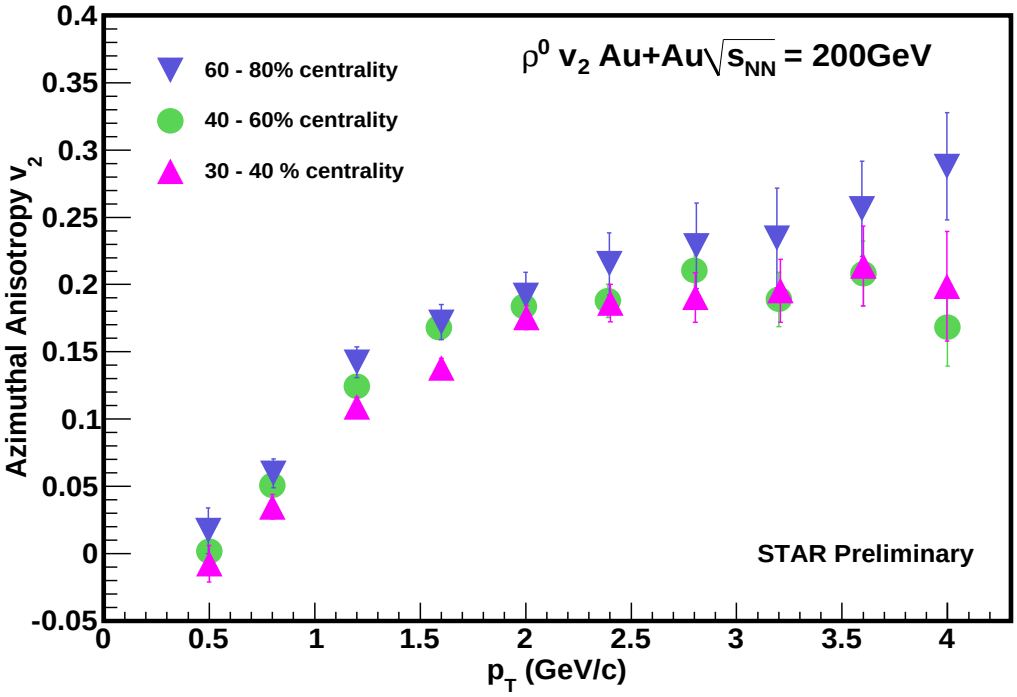

Figure 5.9: Centrality dependence of ρ^0 elliptic flow (v_2) in Au+Au at $\sqrt{s_{NN}}$ = 200 GeV collisions. The error bars are statistical only.

Figure 5.9 shows the v_2 of ρ^0 as a function of p_T for 30-40%, 40-60% and 60-80% centralities in Au+Au collisions at $\sqrt{s_{NN}}$ = 200 GeV. The error bars for all the three centralities are statistical only. Though, with the current statistics we cannot make a strong conclusive remark on the centrality dependence of elliptic flow of ρ^0 vector meson, but still it is clear that the ρ^0 v_2 is lower in 30%-40% centrality than the other two centralities, i.e. 40%-60% and 60%-80%. It is difficult to compare the v_2 values for 40%-60% and 60%-80% centralities because of the large error bars.

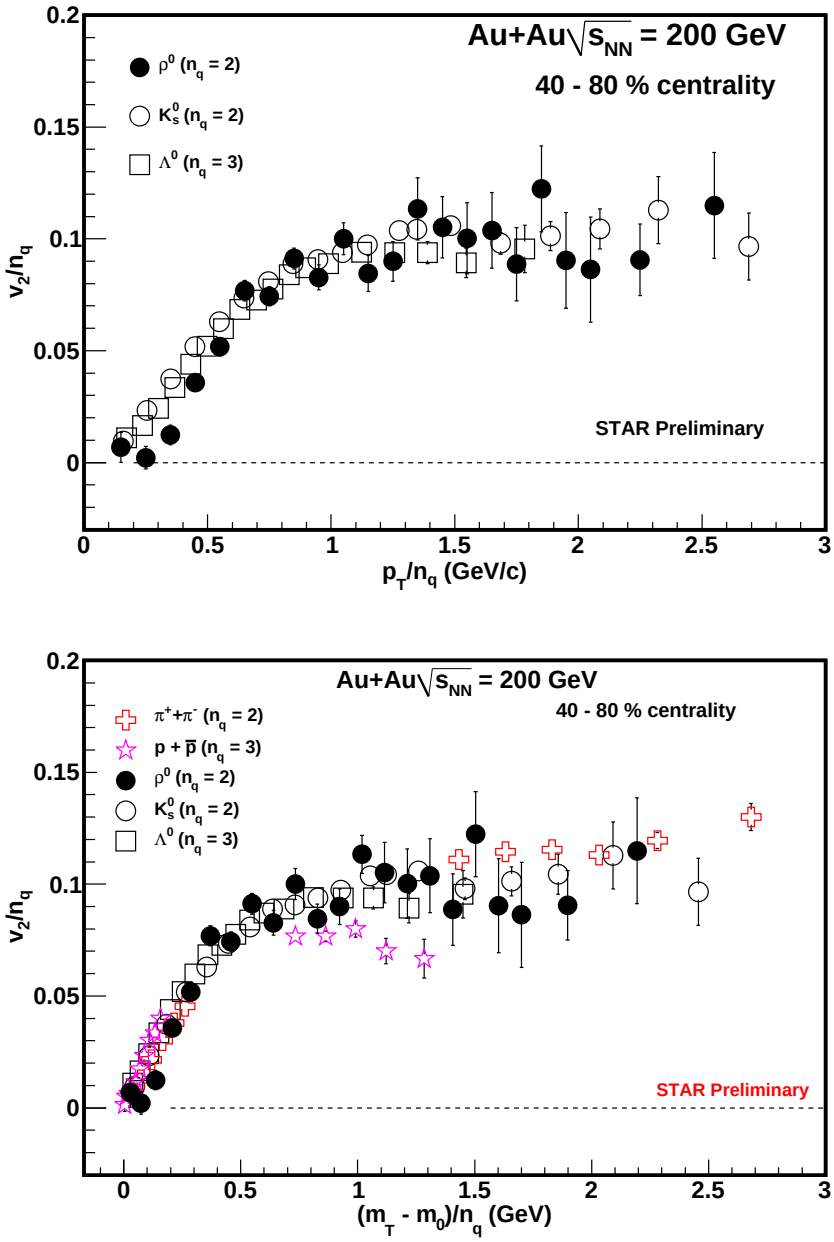

Figure 5.10: **Upper Panel**-Number of constituent quark scaling of v_2 (v_2/n_q vs. p_T/n_q) in 40-80% peripheral Au+Au collisions at $\sqrt{s_{NN}}$ = 200 GeV. ρ^0 v_2 scales with n=2 quarks. **Lower Panel**-Transverse kinetic energy scaling of v_2 (v_2/n_q vs. $(m_T - m_0)/n_q$) in 40-80% peripheral Au+Au collisions at $\sqrt{s_{NN}}$ = 200 GeV. ρ^0 v_2 scales with n=2 quarks.

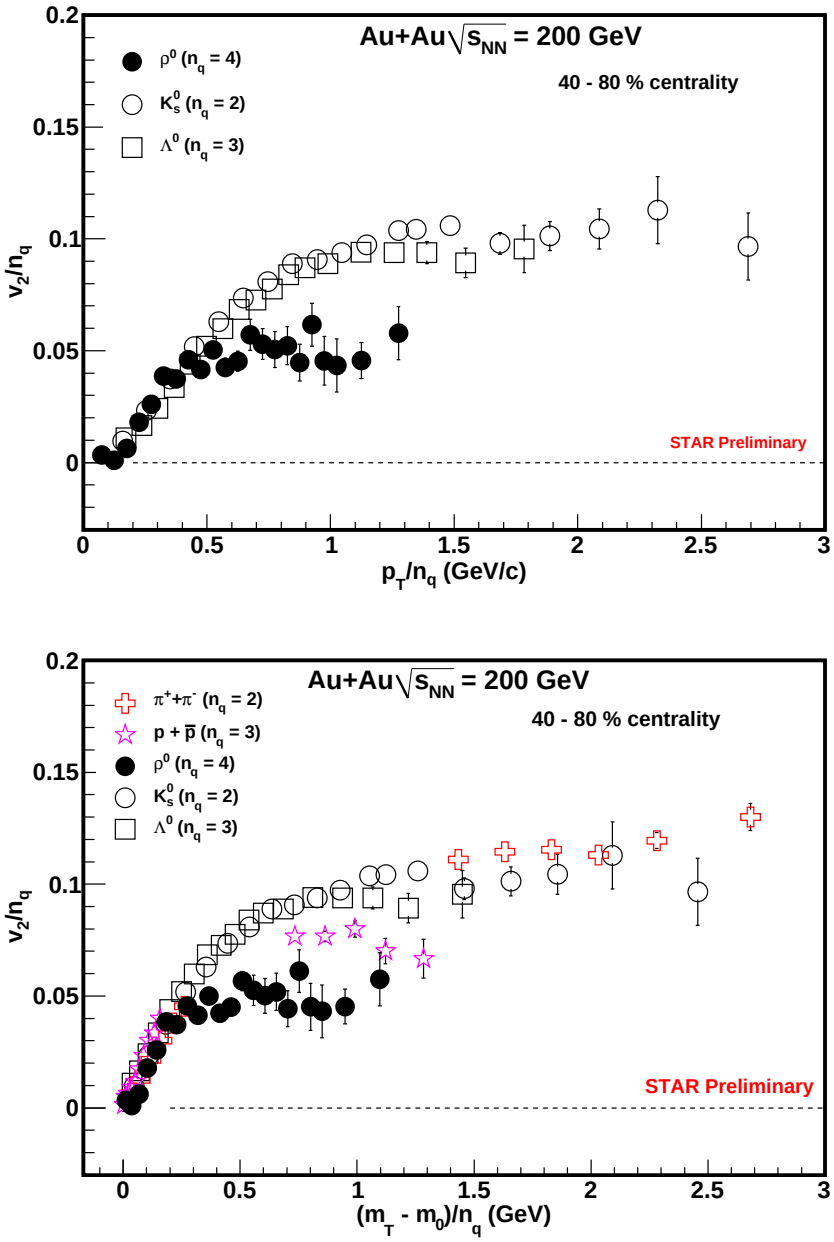

Figure 5.11: **Upper Panel**-Number of constituent quark scaling of v_2 (v_2/n_q vs. p_T/n_q) in 40-80% peripheral Au+Au collisions at $\sqrt{s_{NN}}$ = 200 GeV. ρ^0 v_2 scales with n=2 quarks. **Lower Panel**-Transverse kinetic energy scaling of v_2 (v_2/n_q vs. $(m_T - m_0)/n_q$) in 40-80% peripheral Au+Au collisions at $\sqrt{s_{NN}}$ = 200 GeV. ρ^0 v_2 scales with n=2 quarks.

5.5.3 Number of Constituent Quark Scaling of v_2

Elliptic flow of identified particles measured in Au+Au collisions at RHIC exhibits a remarkable scaling with the number of constituent quarks - an apparent dependence of hadron elliptic flow at intermediate transverse momentum, $p_T \sim 2 - 4$ GeV/c, on the the number of constituent quarks in the hadron [168]. This observation is of particular interest and importance as it indicates that the system is in a de-confined stage. It has been noted in Ref. [168] that if hadrons are formed via coalescence of the constituent quarks, then there should be a region in the transverse momentum space where particle yield would be proportional to the quark density to the power equal to the number of constituent quarks in the produced hadrons, i.e. 2 for mesons and 3 for baryons. According to the coalescence model [168], number of constituent quarks scaling suggests the creation of QGP with v_2^q characterizing the properties of the QGP.

Figure 5.10 shows the number of constituent quark scaling of ρ^0 elliptic flow (v_2), i.e. $\frac{v_2}{n_q}$ vs. $\frac{p_T}{n_q}$ in the upper panel and $\frac{v_2}{n_q}$ vs. $\frac{m_T - m_0}{n_q}$ in the lower panel. In Figure 5.10, both the plots are shown with the number of constituent quarks for ρ^0 equals to 2.

Figure 5.11 shows the number of constituent quark scaling of ρ^0 elliptic flow (v_2), i.e. $\frac{v_2}{n_q}$ vs. $\frac{p_T}{n_q}$ in the upper panel and $\frac{v_2}{n_q}$ vs. $\frac{m_T - m_0}{n_q}$ in the lower panel. In Figure 5.11, both the plots are shown with the number of constituent quarks for ρ^0 equals to 4.

From Figures 5.10 and 5.11, it is clear that the ρ^0 v_2 scales with n_q=2 quarks rather than n_q=4 in the intermediate transverse momentum ($1.5 \leq p_T < 5$ GeV/c). This simply suggests that the ρ^0s in the intermediate p_T region are produced from the de-confined phase of the matter, which could be a signature of the partonic degrees of freedom of the system formed in the heavy-ion collisions at RHIC.

Chapter 6

Summary and Outlook

6.1 Summary

The main objective of this thesis has been to study the evolution of the medium created in relativistic heavy-ion collisions through the measurement of ρ^0 vector meson production and it's elliptic flow (v_2). To study this, the data set of p+p, d+Au, Cu+Cu and Au+Au collisions at $\sqrt{s_{NN}}$ = 200 GeV have been analysed.

The ρ^0 vector meson production in the mid-rapidity has been studied through its hadronic decay channel $\rho^0 \rightarrow \pi^+\pi^-$. The decayed particles are detected in the STAR Time Projection Chamber (TPC). The mass of the ρ^0 vector meson has been extracted from the reconstructed invariant mass distributions of $\pi^+\pi^-$ as a function of p_T. Earlier, similar studies have been carried out in minimum bias p+p and peripheral Au+Au collisions at $\sqrt{s_{NN}}$ = 200 GeV. The statistics used in the earlier study is almost a factor of ∼20 times less than the statistics that we have used in the current study for heavy-ion collisions. In order to minimise the χ^2/ndf, hadronic cocktail function is suitably modified for the current analysis.

The ρ^0 mass obtained in this analysis is lower than the PDG value in the lower p_T region. In the higher p_T side, the ρ^0 mass approaches towards the PDG value. The centrality dependence and the system size dependence on the ρ^0 mass have been studied.

The ρ^0 vector meson invariant yields and the inverse slope parameter have

been measured in Cu+Cu collisions at $\sqrt{s_{NN}}$ = 200 GeV over a wide range of centralities using the STAR detector. The p_T spectra have been found to be well described by an exponential function for all the centralities. The exponential shape of the p_T spectrum implies a smaller contribution from hard pQCD processes to particle production. The average p_T ($\langle p_T \rangle$) values calculated from the above spectra are found to show no significant centrality dependence for a particular collision system. However, it is found to be systematically higher for Au+Au and Cu+Cu in comparison to p+p collisions at the same center of mass energy. The re-scattering effect is much reduced in elementary p+p collisions where no loss in low p_T particles occurs. The presence of low p_T particles lowers the mean value. That is why the $< p_T >$ ($\sim$0.616 GeV/c) in p+p collisions is smaller compared to the $< p_T >$ ($\sim$0.86 GeV/c) in heavy-ion collisions. Therefore, the mean decided by the higher p_T particles increases. Further, the $< p_T >$ of the ρ^0 vector mesons, is found to be higher than the proton.

We have also studied the ρ^0/π^- ratio in both Cu+Cu and Au+Au collisions. The measured ρ^0/π^- ratio is found to be almost consistent with the same measured in elementary p+p collisions. This is because of the daughter particles, coming from the ρ^0 decay, interact among other particles in the medium. Since, the daughters re-scattering effect compensates with the daughters re-generation effect, therefore, the ρ^0 signal lost in re-scattering will be filled by the signal formed by re-generation.

The ρ^0 vector meson differential elliptic flow ($v_2(p_T)$) was measured in peripheral Au+Au collisions at $\sqrt{s_{NN}}$ = 200 GeV. A significant amount of elliptic flow for the ρ^0 vector meson has been observed which is comparable to that of particles consisting of the lighter u and d quarks. Along with the standard event plane ($\phi - \Psi_2$ bin) method, a new measurement technique, the v_2 vs. m_{inv} method, was used to calculate the ρ^0 elliptic flow coefficient. Both the results are consistent within the error. In order to check the non-flow effects, we have also used the FTPC tracks to estimate the FTPC reaction plane to calculate the ρ^0 elliptic flow using the (v_2 vs. m_{inv}) method. Within the statistical error bars the v_2 results

obtained in the TPC event plane and the FTPC event plane are consistant with each other. The centrality dependance of the ρ^0 elliptic flow is studied for three different centrality bins in Au+Au collisions at $\sqrt{s_{NN}}$ = 200 GeV. Although, the large error bars do not allow us to make any final conclusion on the centrality dependance of the v_2 coefficient for the ρ^0 vector meson, but still it is clear from this analysis that the v_2 of ρ^0 is decreasing with increasing centrality as expected from the decreasing eccentricity in the initial nuclear overlap shape.

For 200 GeV Au+Au collisions, the peripheral (40-80% centrality) ρ^0 differential elliptic flow ($v_2(p_T)$) results are compared with other identified particles and with the resonances like K^0_S and Λ^0. It is found that the $v_2(p_T)$ results for the ρ^0 at low p_T ($<$ 1.3 GeV/c) are not consistent with a mass ordering trend and hydrodynamical expectations. Although, the exact reason for this mass ordering deviation for the ρ^0 vector meson is still not understood well, it can be explained through re-generation effects in this p_T region.

At intermediate transverse momentum ($1.5 < p_T < 5$ GeV/c), the ρ^0 elliptic flow scales with the constituent number of quarks. The ρ^0 vector meson $v_2(p_T)$ is comparable to that of particles composed of lighter u and d quarks and is also consistent with the number of quarks = 2 scaling. This strongly implies that there are a significant number of interactions between the quarks at the partonic stage and is, therefore, a strong evidence for partonic collectivity and de-confinement of the medium created in Au+Au collisions at RHIC. Also, the n=2 quarks scaling of v_2 of the ρ^0 vector meson implies that the ρ^0 production mechanism is mainly dominated by the quark and anti-quark coalescence at the early stage of the collisions and not from the $\pi^+\pi^-$ scattering at the hadronic stage.

6.2 Future Prospective

In the year 2010, STAR has already collected a large amount of data for Au+Au collisions at $\sqrt{s_{NN}}$ = 200 GeV. Also, by introducing Time of Flight (TOF) detector, STAR has now improved its particle identification capability up to higher p_T.

Therefore, in addition to the measurements which have been made to date of the ρ^0 vector meson at RHIC, there are yet further interesting aspects to study which will provide further information about the system created in heavy-ion collisions at RHIC.

The study of the ρ^0 vector meson via measurements of the di-electron decay channel ($\rho^0 \rightarrow e^+ + e^-$) with branching ratio $\sim 10^{-5}$ may help to disentangle contributions from hadronic re-scattering by comparing with hadronic decay channel of ρ^0. Electrons, being the electromagnetic particles, do not participate in the strong interactions. So it comes out of the fireball immediately. The ρ^0 vector meson reconstructed from the di-electron will be a good probe to study the in-medium mass and/or width modifications.

In addition to the measurement of ρ^0 invariant yield study through the di-electron channel, one can also study the elliptic flow of the ρ^0 vector meson via its di-electron decay. Due to the small branching ratio of ρ^0 compared to ω, the extraction of the ρ^0 signal from di-electron channel may not allow one to study its various properties. Therefore, instead of looking at the ρ^0 signal, one can always look at the ω meson signal which has a very closer mass (782 MeV/c^2) to ρ^0, and study the various properties and compare the same results obtained for the ρ^0 vector meson studied in the hadronic channel.

Appendix A

A.1 Rapidity and Pseudo-rapidity

One of the important observables commonly used to describe the kinematical condition of particles is called the rapidity, which is denoted by the variable y. In terms of its energy and momentum components, the rapidity is defined by the following equation:

$$y = \frac{1}{2} ln \left(\frac{E + p_L}{E - p_L} \right) \tag{A.1}$$

where p_L is the longitudinal momentum component along the beam direction and E is the total energy of the particle. Rapidity is a dimensionless quantity. It can be either positive or negative. Rapidity is a logarithmic measure of the longitudinal momentum and it depends on the frame of reference. It has the property of being Lorentz additive when one goes from one frame to another.

To calculate rapidity, one requires the information on energy and momentum. However, in many experiments the particle mass is a-priori not known and it is only possible to measure the angle of the particle relative to the beam axis. So in that case, to characterize a particle, a new variable, known as pseudo-rapidity is introduced, which is defined as follows:

$$\eta = -ln \left(tan \frac{\theta}{2} \right) \tag{A.2}$$

where θ is the angle between the particle direction and the beam axis. When a particle's momentum approaches the total energy ($p \rightarrow E$), pseudo-rapidity

tends to the rapidity variable ($\eta \rightarrow y$).

A.2 Energy Density

In heavy-ion collisions, the initial energy density is not known and also cannot be measured directly. Thus, it has to be calculated from the final state products. According to the Bjorken Model [169], the particles created at mid-rapidity can undergo re-scattering after some formation time, τ_0. These particles are referred to as quanta and the model does not distinguish whether they are hadrons or partons. The energy density can be calculated as follows:

$$\epsilon_{Bj} = \left(\frac{1}{\tau_0 A}\right)\frac{dE_T}{dy} \tag{A.3}$$

where $\frac{dE_T}{dy}$ is the total transverse energy carried by the particles per unit rapidity at $y = 0$, where $dE_T = < m_T > dN$. $< m_T >$ is the mean transverse mass and equals to $\sqrt{< p_T >^2 + m_0^2}$. Where, m_0 is the particle rest mass. In Equation A.3, A is the nuclear overlap area.

Appendix B

B.1 Systematic Uncertainty on the ρ^0 mass and yield

- Systematic error on the mass by fitting the signal to an exponential plus a BW $\times$ PS function: In order to evaluate the systematic uncertainty in the ρ^0 mass due to poorly known contributions in the hadronic cocktail, the ρ^0 mass was obtained by fitting the peak to a BW $\times$ PS function plus an exponential function representing these contributions. An example of such a fit is shown in Figure B.1 for a particular p_T bin in Cu+Cu collisions at $\sqrt{s_{NN}}$ = 200 GeV. This uncertainty is the main contributor to the systematic uncertainty, and it can be as large as ~20 MeV/c^2.

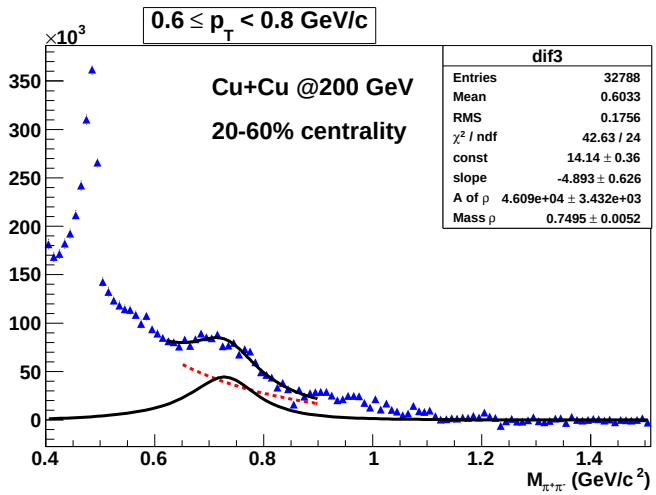

Figure B.1: The ρ^0 peak is fitted with an exponential plus the BW $\times$ PS function.

- Systematic error on the ρ^0 mass and yield due to normalization: Systematic

errors on the mass and yield were calculated by using the statistical error on the constant, which gives the best χ^2/ndf in the cocktail fit for the factor R and getting the mass and yield using the R_1 for $constant + E$ and R_2 for $constant - E$.

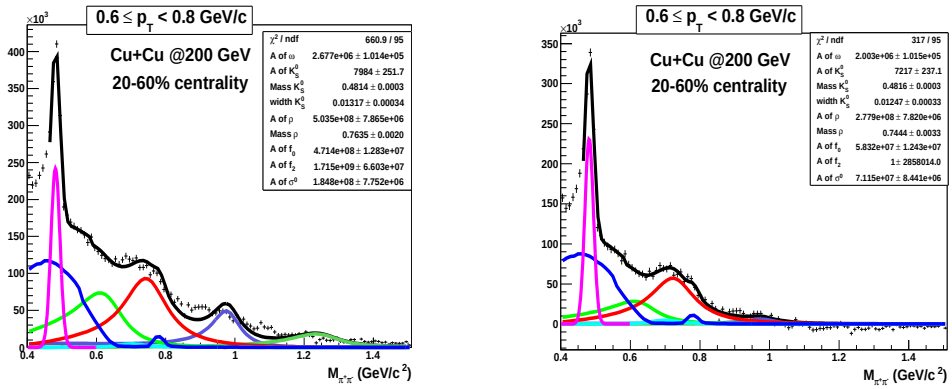

(a) $constant + E$ (b) $constant - E$

Figure B.2: Systematic error on the yield by varying the constant according to the statistical error on the constant that gives best χ^2/ndf.

Figure B.2 (a) and (b) show the error on the ρ^0 mass and yield by varying the ratio R according to the statistical error on the constant that gives the best χ^2/ndf of that particular p_T bin.

- Other sources: The other sources of systematic errors result from uncertainty in the measurement of particle momenta of $\sim$3 MeV$/c^2$ which leads to a mass resolution of $\sim$8 MeV$/c^2$ at the ρ^0 peak. These systematic uncertainties are common to all p_T bins.

Appendix C

C.1 Background flow

The v_2 of real pion pair (which is basically background dominated), is calculated here. The idea is to check the v_2 of the background, and how the background v_2 scales with other hadrons v_2 in different mass regions. Figure C.1 shows the $\pi^+\pi^-$ pair v_2 as a function of p_T calculated in different invariant mass regions.

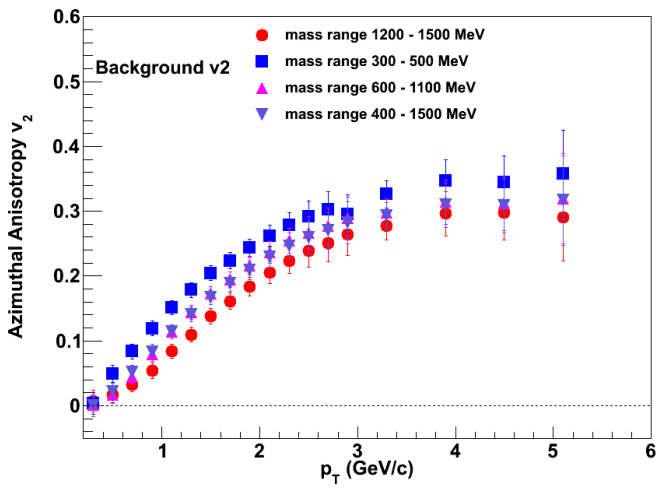

Figure C.1: $\pi^+\pi^-$ v_2 as a function of p_T in different mass window.

Bibliography

[1] R. K. Ellis, W. J. Stirling, and B. R. Webber, "QCD and Collider Physics," *Cambridge University Press.*

[2] F. Wilczek, "A crack in the Standard Model ?" *Nature.* **380**, (1996) 19-20.

[3] **UA1** Collaboration, "Experimental Observation of Isolated Large Transverse Energy Electrons with Associated Missing Energy at $\sqrt{s} = 540$ GeV, " *Physics Letters* **122B**, (1983) p103.

[4] **UA2** Collaboration, "Observation of Single Isolated Electrons of High Transverse Momentum in Events with Missing Transverse Energy at the CERN pp Collider, " *Physics Letters* **122B**, (1983) p476.

[5] **CDF** Collaboration, F. Abe *et al.*, "Observation of Top Quark Production in $\bar{p}p$ Collisions with the Collider Detector at Fermilab, " *Phys. Rev. Lett.* **74**, (1995) 2626.

[6] **D0** Collaboration, S. Abachi *et al.*, "Observation of the Top Quark, " *Phys. Rev. Lett.* **74**, (1995) 2632-2637.

[7] D. J. Gross and F. Wilczek, "Ultraviolet Behavior of Non-Abelian Gauge Theories," *Phys. Rev. Lett.* **30**, (1973) 1343.

[8] S. Bethke, "Experimental Tests of Asymptotic Freedom," *Prog. Part. Nucl. Phys.* **58**, (2007) 351-386.

[9] H. D. Politzer, "Reliable Perturbative Results for Strong Interactions," *Phys. Rev. Lett.* **30**, (1973) 1346.

[10] D. Griffiths, "Introduction to Elementary Particles," *Addison-Wesley Publishing Company Inc.*, 1987.

[11] Halzen and Martin, "Quarks and Leptons: An Introductory Course in Modern Particle Physics," *John Wiley and sons.*

[12] P. Zerwas, and H. Kastrup, "QCD - 20 Years Later," *World Scientific, Singapore*, (1993).

[13] F. Karsch, "Lattice results on QCD thermodynamics," *arXiv:hep-ph/0103314.* (2002) 199-208.

[14] F. Karsch, "Lattice QCD at High Temperature and Density," *Lech.Notes Phys.* **583**, (2002) 209-249.

[15] **STAR** Collaboration, M. M. Aggarwal *et al.*, "An Experimental Exploration of the QCD Phase Diagram: The search for the Critical Point and the Onset of De-confinement," *arXiv:nucl-ex/10072613.* (2010).

[16] **PHENIX** Collaboration, K. Adcox *et al.*, "Formation of dense partonic matter in relativistic nucleus-nucleus collisions at RHIC: Experimental evaluation by the PHENIX Collaboration," *Nucl. Phys.* **A 757**, (2005) 184-283.

[17] **STAR** Collaboration, J. Adams *et al.*, "Experimental and theoretical challenges in the search for the quark-gluon plasma: The STAR Collaboration's critical assessment of the evidence from RHIC collisions," *Nucl. Phys.* **A 757**, (2005) 102-183.

[18] S. Bethke, "α_s 2002," *Nucl. Phys. Proc. Suppl.* **121**, (2003) 7481,

[19] M. Creutz, "Quarks, gluons and Lattices," *Cambridge*, 1985.

[20] H. J. Rothe, "Lattice Gauge Theories: An Introduction," *World Scientific*, 1998.

[21] M. Creutz, "Quantum Fields On The Computer," *World Scientific Publishing Co. Pte. Ltd.*

[22] **PHOBOS** Collaboration, B.B. Back *et al.*, "The PHOBOS Perspective on Discoveries at RHIC," *Nucl. Phys.* **A 757**, (2005) 28-101.

[23] **BRAHMS** Collaboration, I. Arsene *et al.*, "Quark-gluon plasma and color glass condensate at RHIC? The perspective from the BRAHMS experiment," *Nucl. Phys.* **A 757**, (2005) 1.

[24] R. Hagedorn, *Riv. Nuovo Cim.* **6N10**, (1984) 1.

[25] G. Torrieri and J. Rafelski, "A comparison of statistical hadronization models," *Nucl. Part. Phys.* **S557**, (2004) 30.

[26] F. Retiere and M. Lisa, "Observable implications of geometrical and dynamical aspects of freeze-out in heavy ion collisions," *Phys. Rev.* **C 70** (2004) 044907.

[27] E. Schnedermann, J. Sollfrank, and U. Heinz, "Thermal phenomenology of hadrons from 200A GeV S+S collisions, " *Phys. Rev.* **C 48** (1993) 2462-2475.

[28] **STAR** Collaboration, O. Barannikova *et al.*, "Probing collision dynamics at RHIC," *nucl-ex/0403014.*

[29] J. Cleymans, B. Kampfer, M. Kaneta, S. Wheaton and N.Xu, "Centrality dependence of thermal parameters deduced from hadron multiplicities in Au+Au collisions at $\sqrt{s_{NN}}$=130 GeV," *Phys. Rev.* **C 71** (2005) 054901.

[30] P. Braun-Munzinger, K.Redlich, and J.Stachel , "Particle Production in Heavy Ion Collisions," *nucl-th/0304013.*

[31] J. Cleymans and K. Redlich, "Chemical and Thermal Freeze-out Parameters from 1 to 200 A. GeV.," *Phys. Rev.* **C 60**, (1999) 054908.

[32] R. S. Bhalerao, "Transport properties of the fluid produced at Relativistic Heavy-Ion Collider," *J. Physics* **75**, (2010) 247-257.

[33] S. A. Bass, M. Gyulassy, H. St*öcker*, W. Greiner, "Signatures of quark gluon plasma formation in high-energy heavy ion collisions: A Critical review," *J. Phys.* **G 25** (1997) R1-R57.

[34] H. St*öcker*, M. Gyulassy, J. Boguta, "Probing dense nuclear matter via nuclear collisions," *Phys. Lett.* **B 103**, (1981) 269.

[35] H. St*öcker* and W. Greiner, "High-Energy Heavy Ion Collisions: Probing the Equation of State of Highly Excited Hadronic Matter," *Phys. Rept.* **137**, (1986) 277.

[36] H. Sorge, "Highly Sensitive Centrality Dependence of Elliptic Flow: A Novel Signature of the Phase Transition in QCD," *Phys. Lett.* **B 402**, (1997) 251.

[37] J.-Y. Ollitrault, "Anisotropy as a signature of transverse collective flow," *Phys. Rev.* **D 46**, (1992) 229.

[38] **STAR** Collaboration, B. Alver *et al.*, "System Size, Energy, Psedorapidity, and Centrality Dependence of Elliptic Flow," *Phys. Rev. Lett.* **98**, (2007) 242302.

[39] S. Voloshin and Y. Zhang, "Flow study in relativistic nuclear collisions by Fourier expansion of Azimuthal particle distributions," *Z. Phys.* **C 70** (1996) 665.

[40] J.-Y. Ollitrault, "Determination of the reaction plane in ultra-relativistic nuclear collisions," *Phys. Rev.* **D 48** (1993) 1132.

[41] C. Alt *et al.*, "Directed and elliptic flow of charged pions and protons in Pb+Pb collisions at 40A and 158AGeV," *Phys. Rev.* **C 68**, (2003) 034903.

[42] **STAR** Collaboration, C. Adler *et al.*, "Elliptic flow from two-and four-particle correlations in Au+Au collisions at $\sqrt{s_{NN}}$=200 GeV," *Phys. Rev.* **C 66**, (2002) 034904.

[43] **STAR** Collaboration, J. Adams *et al.*, "Azimuthal anisotropy in Au+Au collisions at $\sqrt{s_{NN}}$= 200 GeV," *Phys. Rev.* **C 72**, (2005) 014904.

[44] S. A. Voloshin, "Transverse Radial Expansion and Directed Flow," *Phys.Rev.* **C 55**, (1997) 1630.

[45] S. A. Voloshin, A. M. Poskanzer, and R. Snellings, "Collective phenomena in non-central nuclear collisions," *arXiv:nucl-ex/08092949.*

[46] Z. W. Lin and D. Molnar, "Quark Coalescence and Elliptic Flow of Charm Hadrons," *Phys. Rev.* **C 68**, (2003) 044901.

[47] P. Huovinen, P. F. Kolb, U. W. Heinz, P. V. Ruuskanen and S. A. Voloshin, "Radial and elliptic flow at RHIC: further predictions," *Phys. Lett.* **B 503**, (2001) 58.

[48] **STAR** Collaboration, C. Adler *et al.*, "Identified Particle Elliptic Flow in Au+Au Collisions at $\sqrt{s_{NN}}$=130 GeV," *Phys. Rev. Lett.* **87**, (2001) 182301.

[49] **STAR** Collaboration, J. Adams *et al.*, "$K(892)^*$ Resonance Production in Au+Au and p+p Collisions at $\sqrt{s_{NN}}$ = 200 GeV at RHIC," *Phys. Rev.* **C 71**, (2005) 064902.

[50] S. A. Voloshin, "Anisotropic flow," *Nucl.Phys.* **A 715**, (2003) 379.

[51] **STAR and ALICE** Collaboration, R. Snellings *et al.*, "Anisotropic Flow from RHIC to the LHC," *Eur. Phys. J.* **C 49**, (2007) 87.

[52] **STAR** Collaboration, J. Adams *et al.*, "Azimuthal Anisotropy in Au+Au Collisions at $\sqrt{s_{NN}}$ = 200 GeV," *Phys. Rev.* **C 72**, (2005) 14904.

[53] D. Molnar and S. A. Voloshin, "Elliptic flow at large transverse momenta from quark coalescence," *Phys. Rev. Lett.* **91**, (2003) 092301.

[54] **STAR** Collaboration, B. I. Abelev *et al.*, "Mass, quark-number, and $\sqrt{s_{NN}}$ dependence of the second and fourth flow harmonics in ultra-relativistic nucleus-nucleus collisions," *Phys. Rev.* **C 75**, (2007) 054906.

[55] R. J. M. Snellings, A. M. Poskanzer and S. A. Voloshin, "Anisotropic Flow at STAR," *arXiv:nucl-ex/9904003* [STAR Note 388].

[56] M. Gyulassy and M. Plumer, "Jet quenching as a probe of dense matter," *Phys. Lett.* **B 243**, (1990) 432.

[57] X. N. Wang and M. Gyulassy, "Gluon shadowing and jet quenching in A+A collisions at $\sqrt{s_{NN}}$ =200A GeV," *Phys. Rev. Lett.* **68**, (1992) 1480.

[58] M. Gyulassy, I. Vitev, X. N. Wang and P. Huovinen, "Transverse Expansion and High p_T Azimuthal Asymmetry at RHIC," *Phys. Lett.* **B 526**, (2002) 301.

[59] **STAR** Collaboration, C. Adler *et al.*, "Azimuthal Anisotropy and Correlations in the Hard Scattering Regime at RHIC," *Phys. Rev. Lett.* **90**, (2003) 032301.

[60] R. Baier, D. Schiff and B. G. Zhakharov, "ENERGY LOSS IN PERTURBATIVE QCD," *Ann. Rev. Nucl. Part. Sci.* **50**, (2000) 37-69.

[61] **STAR** Collaboration, J. Adams *et al.*, "Evidence from d+Au Measurements for Final-State Suppression of High-p_T Hadrons in Au+Au Collisions at RHIC," *Phys. Rev. Lett.* **91**, (2003) 072304.

[62] **STAR** Collaboration, C. Adler *et al.*, "Disappearance of back-to-back high p_T hadron correlations in central Au+Au collisions at $\sqrt{s_{NN}}$ = 200-GeV," *Phys. Rev. Lett.* **90**, (2003) 082302.

[63] M. Alston *et al.*, "Resonance in the $\Lambda\pi$ system," *Phys. Rev. Lett.* **5**, (1960) 520.

[64] **STAR** Collaboration, J. Adams *et al.*, "Multi-strange baryon elliptic flow in Au+Au collisions at $\sqrt{s_{NN}}$= 200 GeV," *Phys. Rev. Lett.* **92**, (2004) 92301.

[65] **STAR** Collaboration, M. M. Aggarwal *et al.*, "K^{*0} production in Cu+Cu and Au+Au collisions at $\sqrt{s_{NN}}$ = 62.4 GeV and 200 GeV," *Phys. Rev.* **C 84**, (2011) 34909.

[66] **STAR** Collaboration, P. Fachini *et al.*, "ρ^0 and $f_0(980)$ Production in Au+Au and pp Collisions at $\sqrt{s_{NN}}$ = 200 GeV," *nucl-ex/0305034.*

[67] **STAR** Collaboration, B. Abelev *et al.*, "Measurements of ϕ meson production in relativistic heavy-ion collisions at RHIC," *Phys. Rev.* **C 79**, (2009) 64903.

[68] **STAR** Collaboration, B. Abelev *et al.*, "Hadronic resonance production in d+Au collisions at 200 GeV at RHIC," *Phys. Rev.* **C 78** (2008) 44906.

[69] S. Salur, Ph.D. Thesis, Yale University, 2006.

[70] **STAR** Collaboration, R. Witt *et al.*, *Internal STAR analysis meeting* 2003.

[71] **STAR** Collaboration, H. Zhang *et al.*, "Δ, K and ρ Resonance Production And Their Probing of Freeze-out Dynamics at RHIC," *arXiv:nucl-ex/0403010.*

[72] R. Rapp, "$\pi^+\pi^-$ Emission in High-Energy Nuclear Collisions," *Nucl. Phys.* **A 725** (2003) 254-268.

[73] E. Shuryak and G. Brown, "Matter-induced modification of resonances at RHIC freeze-out," *Nucl. Phys.* **A 717**, (2003) 322.

[74] M. Bleicher and J. Aichelin, "Strange Resonance Production: Probing Chemical and Thermal Freeze-out in Relativistic Heavy Ion Collisions," *Phys. Lett.* **B 530** (2002) 81-87.

[75] C. Adami and G. E. Brown, "Matter under extreme conditions," *Phys. Rep.* **234**, (1993) 1.

[76] R. Rapp and J. Wambach, "Chiral symmetry restoration and dileptons in relativistic heavy ion collisions," *Adv. Nucl. Phys.* **25**, (2000) 1.

[77] J. Schaffner-Bielich, "Effective Restoration of the UA(1) Symmetry in the SU(3) Linear Model," *Phys. Rev. Lett.* **84**, (2000) 3261.

[78] S. Pal, C. Ko and Z. Lin, "ϕ meson production in relativistic heavy ion collisions," *Nucl. Phys.* **A 707**, (2002) 525-539.

[79] **NA49** Collaboration, S. Afanasiev *et al.*, "Production of ϕ-mesons in p + p, p + Pb and central Pb + Pb collisions at Ebeam = 158 A GeV," *Phys. Lett.* **B 491**, (2000) 59.

[80] **CERES** Collaboration, A. Marin *et al.*, "Dilepton measurements with CERES," it arXiv:nucl-ex/0802.2679. (2008).

[81] M. Harrison, T. Ludlam, S. Ozaki, "RHIC project overview," *Nucl. Instrum. Meth.* **A 499** (2003) 235 - 244.

[82] $http://www.bnl.gov/rhic/RHIC_complex.htm.$

[83] H. Hahn *et al.*, "The RHIC design overview," *Nucl. Instrum. Meth.* **A 499** (2003) 245 - 263.

[84] **STAR** Collaboration, K. H. Ackermann *et al.*, "STAR Detector Overview," *Nucl. Instrum. Meth.* **A 499** (2003) 624.

[85] **STAR** Collaboration, F. Bergsma *et al.*, "The STAR detector magnet subsystem," *Nucl. Instrum. Meth.* **A 499** (2003) 633 - 639.

[86] **STAR** Collaboration, M. Anderson *et al.*, "The STAR Time Projection Chamber: A Unique Tool for Studying High Multiplicity Events at RHIC," *Nucl. Instrum. Meth.* **A 499** (2003) 659.

[87] **STAR** Collaboration, G. Van Buren *et al.*, "Correcting for Distortions due to Ionization in the STAR TPC," *Nucl. Instrum. Meth.* **A 566**, (2006) 22.

[88] **STAR** Collaboration, G. Van Buren *et al.*, "Precision Calibration of the STAR TPC," *Nucl. Inst. and Meth.* **A 566** (2006) 22.

[89] A. Timmins, Ph.D. Thesis, Birmingham University, 2008.

[90] W. R. Leo, "Techniques for Nuclear and Particle Physics Experiments."

[91] **STAR** Collaboration, M. Shao *et al.*, "Extensive Particle Identification with TPC and TOF at the STAR Experiment," *Nucl. Instrum. Meth.* **A 558** (2006) 419.

[92] **STAR** Collaboration, R. Bellwied *et al.*, "The STAR Silicon Vertex Tracker: A large area Silicon Drift Detector," *Nucl. Instrum. Meth.* **A 499** (2003) 640.

[93] **STAR** Collaboration, L. Arnold *et al.*, "The STAR silicon strip detector (SSD)," *Nucl. Instrum. Meth.* **A 499** (2003) 652.

[94] **STAR** Collaboration, M. Beddo *et al.*, "STAR Barrel Electromagnetic Calorimeter, " *Nucl. Instrum. Meth.* **A 499** (2003) 725.

[95] **STAR** Collaboration, C.E. Allgower *et al.*, "The STAR endcap electromagnetic calorimeter," *Nucl. Instrum. Meth.* **A 499** (2003) 740.

[96] **STAR** Collaboration, K.H. Ackermann *et al.*, "The forward time projection chamber in STAR," *Nucl. Instrum. Meth.* **A 499** (2003) 713.

[97] **STAR** Collaboration, M.M. Aggarwal *et al.*, "The STAR Photon Multiplicity Detector," *Nucl. Instrum. Meth.* **A 499** (2003) 751.

[98] **STAR** Collaboration, J.M. Landgraf *et al.*, "An overview of the STAR DAQ system," *Nucl. Instrum. Meth.* **A 499** (2003) 762.

[99] R. Pisarski, "Phenomenology of the chiral phase transition," *Phys. Lett.* **B 110** (1982) 155.

[100] G.E. Brown and M. Rho, "Scaling effective Lagrangian in a dense medium," *Phys. Rev. Lett.* **66** (1991) 2720.

[101] G.E. Brown and M. Rho, "Chiral Restoration in hot and/or dense matter," *Phys. Rep.* **269** (1996) 333.

[102] **PHENIX** Collaboration, S. Afanasiev *et al.*, "Enhancement of the dielectron continuum in $\sqrt{s_{NN}}$=200 GeV Au+Au collisions," *arXiv:0706.3034*.

[103] G. Chanfray, R. Rapp and J. Wambach, "Medium Modifications of the Rho Meson at CERN Super Proton Synchrotron Energies (200 GeV/nucleon)," *Phys. Rev. Lett.* **76** (1996) 368-371.

[104] **STAR** Collaboration, J. Adams *et al.*, "ρ^0 Production and Possible Modification in Au+Au and p+p Collisions at $\sqrt{s_{NN}}$=200 GeV," *Phys. Rev. Lett.* **92** (2004) 92301.

[105] H. Bichsel, "A method to improve tracking and particle identification in TPCs and silicon detectors," *Nucl. Instrum. Meth.* **A 562**, (2006) 154.

[106] H. Bichsel, "Straggling in thin silicon detectors, " *Rev. Mod. Phys.* **60**, (1988) 663-699.

[107] H. Bichsel, D.E. Groom, and S.R. Klein, "Passage of particles through matter," *Phys. Lett.* **B 592**, (2004) 242.

[108] **STAR** Collaboration, B.I. Abelev *et al.*, "Measurements of ϕ meson production in relativistic heavy-ion collisions at RHIC," *Phys. Rev.* **C 79**, (2009) 64903.

[109] **STAR** Collaboration, B.I. Abelev *et al.*, "Energy and system size dependence of ϕ meson production in Cu+Cu and Au+Au collisions," *Phys. Lett.* **B 673**, (2009) 183.

[110] **STAR** Collaboration, B.I. Abelev *et al.*, "Hadronic resonance production in d+Au collisions at 200 GeV at RHIC, " *Phys. Rev.* **C 78**, (2008) 44906.

[111] **STAR** Collaboration, M. M. Aggarwal *et al.*, "K^{*0} production in Cu+Cu and Au+Au collisions at $\sqrt{s_N N}$ = 62.4 GeV and 200 GeV," *Phys. Rev.* **C 84** (2011) 34909.

[112] X.N. Wang and M. Gyulassy, "hijing: A Monte Carlo model for multiple jet production in pp, pA, and AA collisions," *Phys. Rev.* **D 44**, (1991) 3501-3516.

[113] X.N. Wang and M. Gyulassy, "hijing: HIJING 1.0: A Monte Carlo Program for Parton and Particle Production in High Energy Hadronic and Nuclear Collisions," *Comput. Phys. Commun.* **83**, (1994) 307.

[114] **STAR** Collaboration, C. Adler *et al.*, "Coherent ρ^0 Production in Ultra-peripheral Heavy-Ion Collisions," *Phys. Rev. Lett.* **89**, (2002) 272302.

[115] **ZEUS** Collaboration, M. Derrick *et al.*, "Measurement of elastic ρ^0 photo-production at HERA," *Z. Phys.* **C 69**, (1995) 39.

[116] J.D. Jackson, "Remarks on the phenomenological analysis of resonances," *Nuova Cimento* **34**, (1964) 1644.

[117] G. Torrieri and J. Rafelski, "Strange hadron resonances as a signature of freeze-out dynamics," *Phys. Lett.* **B 509**, (2001) 239.

[118] G. Torrieri and J. Rafelski, "Statistical hadronization probed by resonances," *Phys. Rev.* **C 68**, (2003) 034912.

[119] **STAR** Collaboration, P. Fachini *et al.*, "ρ^0 and f_0 Production in Au+Au and p+p collisions at $\sqrt{s_{NN}}$=200 GeV," *J. Phys.* **G 30** (2004) S565.

[120] S. Vogel and M. Bleicher, "Resonance Production in Heavy Ion Collisions," *arXiv:hep-ph/0607242.*

[121] E.V. Shuryak and G.E. Brown, "MatterInduced Modification of Resonances at RHIC Freeze-out," *Nucl. Phys.* **A 717**, (2003) 322.

[122] P.F. Kolb and M. Prakash, "Spectroscopy of resonance decays in high-energy heavy-ion experiments," *nucl-th/0301007.*

[123] R. Rapp, "$\pi^+\pi^-$ Emission in High-Energy Nuclear Collisions," *Nucl. Phys.* **A 725**, (2003) 254-268.

[124] F. Becattini, "Statistical hadronization phenomenology," *Nucl. Phys.* **A 702**, (2002) 336-340.

[125] F. Becattini, "A thermodynamical approach to hadron production in e^+e^- collisions," *Z. Phys.* **C 69**, (1996) 485.

[126] F. Becattini and U. Heinz, "Thermal hadron production in pp and p $\bar{p}$ collisions," *Z. Phys.* **C 76**, (1997) 269.

[127] K. Hagiwara *et al.*, "Review of Particle Properties," *Phys. Rev.* **D 66**, (2002) 010001.

[128] **STAR** Collaboration, C. Adler *et al.*, "Multiplicity Distribution and Spectra of Negatively Charged Hadrons in Au+Au Collisions at $\sqrt{s_{NN}}$=200 GeV," *Phys. Rev. Lett.* **87**, (2001) 112303.

[129] A.K. Mazumder, J. Alam, B. D. Roy, and B. Sinha, "Dilepton Yield in Heavy-Ion Collisions with Bose Enhancement of Decay Widths," *Phys. Lett.* **B 396**, (1997) 264-268.

[130] H. Long, Ph.D. thesis, UCLA, 2002.

[131] "GEANT:Detector Description and Simulation Tool," *http://wwwasd.web.cern.ch/wwwasd/geant/.*

[132] P. Nevski, *http://www.star.bnl.gov/STARAFS/comp/simu/gstar/gstar.html.*

[133] S. Dash, Ph.D. thesis, Institute of Physics, BBSR, 2010.

[134] H. Zhang, Ph.D. thesis, Yale University, 2004.

[135] S.A. Bass, M. Gyulassy, H. St$\ddot{o}cker$ and W. Greiner, "Signatures of Quark-Gluon-Plasma formation in high energy heavy-ion collisions: A critical review," *J. Phys.* **G 25**, (1999) R1.

[136] H. St$\ddot{o}cker$, "Collective flow signals the quarkgluon plasma," *Nucl. Phys.* **A 121**, (2005) 750.

[137] H. Sorge, "Elliptical Flow: A Signature for Early Pressure in Ultra-relativistic Nucleus-Nucleus Collisions," *Phys. Rev. Lett.*, **78** (1997) 2309-2312.

[138] J.-Y. Ollitrault, "Anisotropy as a signature of transverse collective flow," *Phys. Rev.* **D 46**, (1992) 229.

[139] W. Reisdorf, H.G. Ritter, "Collective flow in heavy-ion collisions," *Ann. Rev. Nucl. Part. Sci.* **47**, (1997) 663-709.

[140] N. Borghini and J. -Y. Ollitrault, "Azimuthally sensitive correlations in nucleus-nucleus collisions," *Phys. Rev.* **C 70**, (2004) 064905.

[141] Roy A. Lacey and Arkadij Taranenko, "What do elliptic flow measurements tell us about the matter created in the little Bang at RHIC ?" *arXiv:nucl-ex/0610029.*

[142] C. Nonaka, B. Muller, M. Asakawa, S. A. Bass and R. J. Fries, "Elliptic flow of resonances in relativistic heavy ion collisions: Probing final state interactions and the structure of resonances," *Phys. Rev.* **C 69**, (2004) 031902.

[143] **STAR** Collaboration, P. Pujahari, "ρ^0 vector meson elliptic flow (v_2) in $Au+Au$ collisions at $\sqrt{s_{NN}}$ = 200 GeV in STAR at RHIC," *Nucl.Phys.* **A 862-863**, (2011) 297-300.

[144] **STAR** Collaboration, J. Adams *et al.*, "Azimuthal anisotropy in Au+Au collisions at $\sqrt{s_{NN}}$=200 GeV," *Phys. Rev.* **C 72**, (2005) 014904.

[145] A. M. Poskanzer and S. A. Voloshin, "Methods for analyzing anisotropic flow in relativistic nuclear collisions, " *Phys. Rev.* **C 58**, (1998) 3.

[146] J. Barrette *et al.*, "Proton and pion production relative to the reaction plane in Au + Au collisions at 11A GeV/c," *Phy. Rev.* **C 56**, (1997) 3254.

[147] A. Tang, Ph.D. thesis, Kent State University, 2002.

[148] R. Rapp and J. Wambach, "Chiral Symmetry Restoration and Dileptons in Relativistic Heavy-Ion Collisions," *Adv. Nucl. Phys.* **25**, (2002) 1.

[149] J. Wambach, "The Medium modification of hadrons," *Nucl. Phys.* **A 755**, (2005) 198-208.

[150] H.W. Barz, G. Bertsch, B.L. Friman, H. Schulz, and S. Boggs, "ρ thermometry in hot hadronic matter, " *Phys. Lett.* **B 265**, (1991) 219-222.

[151] W. Broniowski, Wojciech Florkowsk, and Brigitte Hiller, "Thermal analysis of production of resonances in relativistic heavy-ion collisions, " *nucl-th/0306034* (2003).

[152] S. Pratt and W. Bauer, "Thermal production of the ρ meson in the $\pi^+\pi^-$ channel," *Phys. Rev.* **C 68**, (2003) 064905.

[153] P. Fachini, R. S. Longacre, Z. Xu and H. Zhang, "Indication for $\pi^+\pi$ scattering in p + p collisions at $\sqrt{s_{\rm NN}}$ = 200 GeV," *J. Phys.* **G 34**, (2007) 431.

[154] **STAR** Collaboration, B. I. Abelev *et al.*, "Systematic Measurements of Identified Particle Spectra in pp, d+Au and Au+Au Collisions from STAR," *Phys. Rev.* **C 79** (2009) 34909.

[155] **STAR** Collaboration, C. Adler *et al.*, "K^{*0}(892) Production in Relativistic Heavy Ion Collisions at $\sqrt{s_{\rm NN}}$=130 GeV," *Phys. Rev.* **C 66**, (2002) 061901.

[156] **STAR** Collaboration, J. Adams *et al.*, "K^*0(892) production in Au+Au and p+p collisions at $\sqrt{s_{\rm NN}}$=200 GeV, " *Phys. Rev.* **C 71**, (2005) 064902.

[157] **STAR** Collaboration, B.I. Abelev *et al.*, "Strange Baryon Resonance Production in $\sqrt{s_{\rm NN}}$=200 GeV p+p and Au+Au Collisions," *Phys. Rev. Lett.* **97**, (2006) 132301.

[158] M. Bleicher and J. Aichelin, "Strange Resonance Production: Probing Chemical and Thermal Freeze-out in Relativistic Heavy Ion Collisions," *Phys. Lett.* **B 530**, (2002) 81.

[159] S. Vogel, J. Aichelin, M. Bleicher, "Resonances as a possible observable of hot and dense nuclear matter," *arXiv:1001.3260*

[160] **LEBC-EHS** Collaboration, M. Aguilar-Benitez *et al.*, "Inclusive particle production in 400 GeV/c pp-interaction," *Z. Phys.* **C 50**, (1991) 405.

[161] Particle Data Group, *J. Phys.* **G 33**, (2006) 1.

[162] **STAR** Collaboration, C. Adler *et al.*, "Coherent ρ^0 Production in Ultra-Peripheral Heavy Ion Collisions," *Phys. Rev. Lett.* **89**, (2002) 272302.

[163] **STAR** Collaboration, J. Adams *et al.*, "Identified Particle Distributions in pp and Au+Au Collisions at $\sqrt{s_{\rm NN}}$=200GeV," *Phys. Rev. Lett.* **92** (2004) 92301.

[164] S. Vogel and M. Bleicher, "Resonance Re-scattering and Absorption In Low Energy Heavy Ion Collisions," *Romanian Reports in Physics* **51**, (2006) 1.

[165] M. Bleicher *et al.*, "Relativistic hadron-hadron collisions in the ultra-relativistic quantum molecular dynamics model," *J. Phys.* **G 25**, (1999) 1859-1896.

[166] **STAR** Collaboration, B.I. Abelev *et al.*, "Centrality dependence of charged hadron and strange hadron elliptic flow from $\sqrt{s_{NN}}$=200 GeV Au+Au collisions," *Phys. Rev.* **C 77**, (2008) 54901.

[167] H. Holopainen, H. Niem, and K. J. Eskola, "Event-by-event hydrodynamics and elliptic flow from fluctuating initial states," *Phys. Rev.* **C 83**, (2011) 034901.

[168] S.A.Voloshin, "Anisotropic flow," *Nucl. Phys.* **A 715**, (2003) 379-388.

[169] J. D. Bjorken, "Highly relativistic nucleus-nucleus collisions: The central rapidity region," *Phys. Rev.* **D 27**, (1983) 140.

List of Publications

Publications:

- H. Agakishiev *et al.* [STAR Collaboration], *"Observation of the antimatter helium-4 nucleus"* Nature (2011).
- H. Agakishiev *et al.* [STAR Collaboration], *"High p_T non-photonic electron production in $p+p$ collisions at $\sqrt(s_{NN}) = 200$ GeV,"* Phys. Rev. D **83**, 52006 (2011).
- M. M. Aggarwal *et al.* [STAR Collaboration], *"Strange and Multi-strange Particle Production in $Au + Au$ collisions at $\sqrt{s_{NN}}$ = 62.4 GeV,"* Phys. Rev. C **83**, 24901 (2011).
- M. M. Aggarwal *et al.* [STAR Collaboration], *"Measurement of the parity-violating longitudinal single-spin asymmetry for the $W^{\pm}$ boson production in polarized proton-proton collisions at $\sqrt{s_{NN}} = 500$ GeV,"* Phys. Rev. Lett.**106** 62002 (2011).
- M. M. Aggarwal *et al.* [STAR Collaboration], *"Scaling properties at freeze-out in relativistic heavy ion collisions"* Phys. Rev. C**83** 34910 (2011).
- M. M. Aggarwal *et al.* [STAR Collaboration], *"Measurement of the Bottom contribution to non-photonic electron production in p+p collisions at sqrts=200 GeV "'* Phys. Rev. Lett.**105** 202301 (2010).
- M. M. Aggarwal *et al.* [STAR Collaboration], *"Balance Functions from Au+Au, d+Au, and p+p Collisions at $\sqrt{s_{NN}}$ = 200 GeV "'* Phys. Rev. C**82** 24905 (2010).
- M. M. Aggarwal *et al.* [STAR Collaboration], *"Higher Moments of Net-proton Multiplicity Distributions at RHIC "'* Phys. Rev. Lett.**105** 22302 (2010).
- M. M. Aggarwal *et al.* [STAR Collaboration], *"Azimuthal di-hadron correlations in d+Au and Au+Au collisions at $\sqrt{s_{NN}} = 200$ GeV from STAR"'* Phys. Rev. C**82** 24912 (2010).
- M. M. Aggarwal *et al.* [STAR Collaboration], *"Longitudinal scaling property of the charge balance function in Au + Au collisions at 200 GeV "'* Phys. Rev. B**690** 239 (2010).
- M. M. Aggarwal *et al.* [STAR Collaboration], *"Charged and strange hadron elliptic flow in Cu+Cu collisions at $\sqrt{s_{NN}}$ = 62.4 and 200 GeV "'* Phys. Rev. C**81** 44902 (2010).

- B. I. Abelev *et al.* [STAR Collaboration], *"Three-particle coincidence of the long range pseudorapidity correlation in high energy nucleus-nucleus collisions "'* Phys. Rev. Lett.**105** 22301 (2010):
- M. M. Aggarwal *et al.* [STAR Collaboration], *"Upsilon cross section in p+p collisions at sqrt(s) = 200 GeV "'* Phys. Rev. D**82** 12004 (2010).
- B. I. Abelev *et al.* [STAR Collaboration], *"Identified high-p_T spectra in Cu+Cu collisions at $\sqrt{s_{NN}}$=200 GeV"'* Phys. Rev. C**81** 54907 (2010).
- B. I. Abelev *et al.* [STAR Collaboration], *"Identified particle production, azimuthal anisotropy, and interferometry measurements in Au+Au collisions at $\sqrt{s}_{NN} =$ 9.2 GeV"* Phys. Rev. C**81** 24911 (2010).
- M. M. Aggarwal *et al.* [STAR Collaboration], *"$K*^0$ production in $Cu+Cu$ and $Au + Au$ collisions at $\sqrt{s_N N} =$ 62.4 GeV and 200 GeV "* Phys.Rev. C**84** 034909 (2011).

Publication in proceedings:

- P. R. Pujahari [for STAR Collaboration], *"ρ^0 vector- meson elliptic flow (v_2) in Au+Au collisions at $\sqrt{s_{NN}} = 200$ GeV in STAR at RHIC."* Nucl. Phys. A862-863, 297-300 (2011).
- ρ^0 elliptic flow in Au+Au collisions in STAR at RHIC (Poster)
  Quark Matter 2011, Annecy, France.
- ρ^0 production and elliptic flow in Cu+Cu collisions at $\sqrt{(s_{NN})}$ =62.4 and 200 GeV in STAR at RHIC. (Poster)
  Quark Matter 2009, Knoxville, Tennessee, March 30th to April 4th.
- ρ^0 vector-meson elliptic flow (v_2) in Au+Au collisions at $\sqrt{(s_{NN})} = 200$ GeV in STAR at RHIC. (Oral)
  The 6th International Conference on Physics and Astrophysics of Quark Gluon Plasma - Goa, India, Dec. 5-10, 2010.
- ρ^0 vector-meson elliptic flow in STAR at RHIC. (Oral)
  DAE-BRNS High Energy Physics Symposium, Dec. 13-18, 2010, Jaipur, India.
- ρ^0 vector-meson production in STAR at RHIC. (Oral)
  DAE-NP Symposium, Dec. 20-26, 2010, BITS Pilani, India.
- Resonance production in STAR at RHIC. (Oral)
  DAE-HEP Symposium, Dec. 14-20, 2008, Bhanaras Hindu University, India.

Acknowledgements

I would like to venerate the Almighty for giving me the strength and determination during the entire period and making my studies a success. There are a number of people without whom this thesis might not have been written, and to whom I am greatly indebted. I thank all those people who have inspired and helped me during my graduation.

Foremost, I would like to express my deep sense of gratitude to my thesis supervisor Prof. Basanta Kumar Nandi, for his guidance and supervision on my work throughout the study. I cannot forget his support, co-operation and advice to my life. I am indebted and obliged to him always. His wide knowledge and logical way of thinking have been of a great value to me. He is not only a good supervisor but also a very good friend of mine with whom I share all my thoughts at any time. Finally, I find no words to express my gratitude to him and would request him to be my guiding light throughout my life. Thank you sir and I owe the success to you.

I wish to express my warm and sincere thanks to Prof. Raghava Varma, for his invaluable advice and constructive criticism that he has extended to me throughout my research period. He is my friend, philosopher, guide and mentor. I will keep on learning taking inspiration and blessing from him throughout my life. Thank you Prof. Varma for your tremendous support and for all the opportunities you have given me during my graduation.

I am very glad for having an opportunity to work with Dr. Paul Sorensen from BNL. He suggested me the method of elliptic flow measurement for ρ^0 vector meson using the invariant mass technique which became a major part of my thesis. I would like to thank him for patiently helping me and for all the useful discussions. I would like to extend my sincere thanks to Dr. Patricia Fachini who has introduced me to the resonance analysis in the beginning of my Ph.D.

I had a great pleasure to discuss physics with Dr. Zhangbu Xu, Dr. James Dunlop, Dr. Bedanga Mohanty, Dr. Ron Longacre, Dr. Lijuan Runa, Dr. Anthony Timmins, Dr. Christina Markert, Dr. Nu Xu, Dr. Art Poskanzer, Prof. Huan

Huang, and Prof. Mike Lisa. I would like to thank all the STAR collaborators for many useful discussions and help on my data analysis. It was a learning and memorable experience with them all.

I would like to express my sincere thanks to Dr. Y. P. Viyogi, Dr. Tapan Nayak and Dr. Subhasis Chattopadhyay, for their support, advice and useful suggestions.

During my Ph.D., I have collaborated with many colleagues and seniors in PMD collaboration in India for whom I have great regards. I would like to extend my sincere thanks to my collaborators at IOP Bhubaneswar, Jammu University, Jammu, Panjab University, Chandigarh, Rajasthan University, Jaipur, and VECC Kolkata. I am really grateful and thank them all for their useful suggestions and encouragement. I have spent some very memorable time with them at various conferences, meetings, workshops etc. and during my stay at BNL. I wish to thank each and every member of the PMD collaboration for all their help and support.

During my stay at IIT Bombay, I have been blessed with a friendly and cheerful group of fellow students. I express my hearty thanks to my friends Satyajit, Himani, Neha, Kavita, Nirbhay, Anitha, Amal, Manoj, Greeshma, Siddesh, Jitendra for all their love and support.

I wish to express my sincere thanks to my seniors, Dr. Ankhi Roy, Dr. Sadhana Dash, Dr. Dipak Mishra, Dr. Raghunath Sahoo, Dr. Debashis Dash, for all their help and good wishes. Also, I would like to thank my friend Dhevan Gangadharan with whom I had lot of fun during my visit to UCLA and at various conferences.

Last but most importantly, I would like to express my due respect and sincere thanks to my parents for their immense patience and encouragement. Without their love and support, this thesis would not have been possible. I am indebted to them for giving me the freedom to choose my carrer and for constantly providing me the much needed moral support at every stage. Also, I am very thankful to my elder brothers Manoranjan and Chittaranjan and to my loving wife Sweta for their moral support to me throughout the writing of this thesis. It is only because of their love, affection and blessing that I could complete this thesis.